

*CONTROL STRATEGIES AND
APPLICATIONS OF THREE-PHASE DIRECT
MATRIX CONVERTERS*



Jianwei Zhang

**Faculty of Engineering and IT
University of Technology Sydney**

This dissertation is submitted for the degree of Doctor of Philosophy

September 2018

Title of Thesis:

CONTROL STRATEGIES AND APPLICATIONS OF THREE-PHASE DIRECT
MATRIX CONVERTERS

PhD Candidate:

Jianwei Zhang (Jianwei.Zhang@uts.edu.au)

Faculty of Engineering and IT | University of Technology Sydney | Australia

Principal Supervisor:

A/Prof. Li Li (Li.Li@uts.edu.au)

Faculty of Engineering and IT | University of Technology Sydney | Australia

Co-Supervisor:

A/Prof. Youguang Guo (Youguang.Guo-1@uts.edu.au)

Faculty of Engineering and IT | University of Technology Sydney | Australia

External Supervisor:

Prof. David G. Dorrell (d.g.dorrell@gmail.com)

Howard College Campus | University of KwaZulu-Natal | South Africa

DECLARATION

I declare that this thesis is submitted in fulfilment of the requirements for the ward of PhD degree in the Faculty of Engineering and Information Technology at the University of Technology Sydney. I certify that the work in this thesis has not been previously submitted, in part or whole, to any organizations for a degree or other qualifications.

This dissertation is the result of my own original work and the collaboration is fully acknowledged in this thesis. The literature and information sources used in this thesis are indicated.

Jianwei Zhang

Production Note:

Signed: _____ Signature removed prior to publication.

Date: _____ 10/07/2018

ACKNOWLEDGEMENTS

I would like to express my deepest gratitude to my supervisors A/Prof. Li Li, Prof. David Dorrell and A/Prof. Youguang Guo for their generous support, patient guidance and insightful advice on my project during my Ph.D life at University of Technology Sydney (UTS). I am also grateful to the support from A/Prof. Dylan Lu, Dr. Gang Lei, A/Prof. Peter Watterson, and engineers Russell Nicholson and Jiang Chen as well. I appreciate the generous financial support from the China Scholarship Council and UTS without which my study in Australia would be impossible.

I would also like to thank my friends Anton Tkachev, Linfeng Zheng, Tingting He, Haitao Yang, Tianshi Wang, Sayed Royal, Zahra Malekjamshidi, Mohammad Jafari, Shakil Ahamed Khan, Mahlagha Mahdavi Aghdam, Shuo Wang and Lei Zhang for their kind support and care during my study and daily life in Australia. In particular, I would like to thank Daai Zhang for her inimitable care, patience and support over the years since we met.

Finally, I would like to thank my family for their invaluable understanding, patience and support throughout my whole life.

ABSTRACT

AC-to-AC converters have been widely used in various areas in the real world. In industrial applications, the AC-to-AC power conversion is usually accomplished by indirect converters. In these traditional converters, AC power is firstly converted into DC power by a rectifier, and then the DC power is converted into AC power by an inverter. The rectifier and inverter are usually connected via an intermediate bulky DC-link capacitor. The use of the DC-link capacitor in these converters makes the equipment volume bulky, reduces the lifetime, increases the design complexity and decreases the system efficiency. Therefore, it is of great benefit to remove the bulky DC-link capacitor or propose new converter topologies. A matrix converter (MC) does not require large energy storage elements and it has emerged as a potential solution to AC-to-AC conversion.

A three-phase direct MC comprises nine bidirectional semiconductor switches arranged in a 3×3 matrix form to realize the direct AC-to-AC conversion. Thanks to benefits such as bidirectional power flow, compact volume, controllable input power factor and sinusoidal waveform, MCs have attracted research interests and plenty of projects on MC have been reported. MC is also regarded as an all-silicon converter. However, there are some drawbacks associated with MCs and they have very limited industrial applications. These drawbacks include low voltage transfer ratio (VTR), sensitivity to the grid variations and complex modulation. Some MC application areas need more exploration. The work in this thesis is carried out to contribute to possible solutions to some of the above issues by investigating some control strategies and applications of MCs.

The main contributions included in this work are summarized as follows:

- (1) A simple decoupling controller is designed for the MC-based unified power flow controller (UPFC) (MC-UPFC) to regulate the power flow in a transmission system. The controllable regions of the MC-UPFC are also analyzed. A design procedure for the closed-loop controller in the MC-UPFC is presented.
- (2) A modified PI controller is proposed for the improvement of the steady-state performance by including a current feedforward path. More control flexibility is provided because of the feedforward controller. A PR controller is designed for the MC and this has good performance.

(3) A hysteresis current controller is proposed for the MC to drive AC motors. Both fixed-band and sinusoidal-band hysteresis controllers are investigated, and their performance is compared. The hysteresis controller is a very simple and practical controller for the MC. For the MC-based motor drive, a direct torque control (DTC) technique is also investigated.

(4) Model predictive control (MPC) is investigated to control the MC. This scheme is used in an MC-based microgrid. In the islanded mode, predictive voltage control is employed to regulate the MC output voltages to supply various loads. An improved VTR is observed. When the microgrid is connected to the utility grid, power flow is the main objective. The performance of the controller is tested under various conditions including input disturbance and different loads.

(5) An MC prototype is built to support the research. The prototype hardware includes main circuit, drives, supplies, analog to digital conversion (ADC) conditioning circuits, and sensor board. The algorithm is implemented in Matlab Simulink with C2000 hardware support packages for TI DSP processors. Various experimental tests are carried out to support the proposed strategies.

TABLE OF CONTENTS

DECLARATION.....	i
ACKLEDGEMENTS.....	ii
ABSTRACT.....	iii
TABLE OF CONTENTS.....	v
LIST OF TABLES.....	viii
LIST OF FIGURES.....	ix
LIST OF APPENDICES.....	xv
PUBLICATIONS LIST.....	xvi
LIST OF ABBREVIATIONS AND ACRONYMS.....	xviii
1 INTRODUCTION.....	1
1.1 LITERATURE REVIEW	1
1.1.1 <i>The Switches for Matrix Converter</i>	3
1.1.2 <i>Matrix Converter Topologies</i>	4
1.1.3 <i>Modulation and Control Strategies</i>	9
1.1.4 <i>Potential Applications Areas</i>	12
1.2 OBJECTIVES AND SIGNIFICANCES	14
1.3 CONTRIBUTIONS AND ORGANIZATION.....	16
1.3.1 <i>Contributions</i>	16
1.3.2 <i>Organization of Thesis</i>	17
REFERENCES.....	17
2 MATRIX CONVERTER FUNDAMENTALS	23
2.1 MATRIX CONVERTER BASICS.....	23
2.2 SVM	24
2.2.1 <i>Direct SVM</i>	25
2.2.2 <i>Indirect SVM</i>	30
2.3 COMMUTATION TECHNIQUES.....	36
2.4 CLAMP CIRCUIT	40
2.5 SUMMARY.....	41
REFERENCES.....	41

3 D-Q COUPLING CONTROL FOR POWER FLOW CONTROL.....	43
3.1 INTRODUCTION.....	44
3.2 POWER FLOW CONTROL THEORY AND CONTROLLABLE REGIONS ANALYSIS	48
3.2.1 Power Flow Control Theory	48
3.2.2 MC-UPFC System in the Transmission Line	53
3.3 POWER FLOW CONTROLLER.....	54
3.3.1 Model Description.....	54
3.3.2 Controller Design.....	55
3.4 SIMULATION AND RESULTS.....	55
3.5 SUMMARY	60
REFERENCES	61
4 PI AND PR CONTROL FOR IMPROVING STEADY-STATE TRACKING PERFORMANCE	64
4.1 INTRODUCTION.....	65
4.2 PI CONTROLLER WITH CURRENT FEEDFORWARD.....	67
4.3 PR CONTROLLER DESIGN	69
4.3.1 PR Controller	69
4.3.2 PR Controller with Harmonics Compensator.....	72
4.4 SVM BASED PI AND PR CONTROLLER DIAGRAMS.....	73
4.5 SIMULATION TESTS	75
4.6 EXPERIMENTAL VALIDATION	81
4.7 SUMMARY	88
REFERENCES	88
5 HYSTERESIS AND DTC CONTROL FOR MOTOR DRIVES	92
5.1 HYSTERESIS CURRENT CONTROLLER FOR MOTOR DRIVES.....	92
5.1.1 Introduction.....	93
5.1.2 HB controller for the MC output currents	97
5.1.3 Overall modulation of MC.....	98
5.1.4 FOC with HB controller for PMSM	100
5.1.5 Simulation and Experimental Results.....	103
5.1.6 Conclusions.....	114
5.2 DTC FOR THE MATRIX CONVERTER-FED MOTOR DRIVE	115
5.2.1 Introduction.....	115

5.2.2 Matrix Converter and Space Vectors	116
5.2.3 Induction Motor Model and DTC Theory.....	117
5.2.4 DTC Control for Matrix Converter Drives.....	119
5.2.5 Simulation Results	122
5.2.6 Conclusions.....	124
5.3 SUMMARY	125
REFERENCES.....	125
6 PREDICTIVE CONTROL FOR MICROGRID AND OTHER CONVERSION	
POSSIBILITIES	127
6.1 PREDICTIVE CONTROL FOR MICROGRID	128
6.1.1 Introduction.....	129
6.1.2 Model Development.....	132
6.1.3 Observers Design	135
6.1.4 Predictive Voltage Controller Design.....	137
6.1.5 Simulation Results	139
6.1.6 Experimental Validation.....	145
6.1.7 Conclusions.....	151
6.2 PREDICTIVE CONTROL FOR OTHER CONVERSION POSSIBILITIES	152
6.2.1 Introduction.....	152
6.2.2 Versatile Conversion and Simulation Results.....	154
6.2.3 Conclusions.....	159
6.3 SUMMARY	160
REFERENCES.....	160
7 CONCLUSIONS	164
7.1 CONCLUSIONS	164
7.2 FUTURE WORK.....	165
APPENDICES.....	167

LIST OF TABLES

Table 1.1 Comparison of MCs.	8
Table 1.2 Comparison between some control techniques for MC.....	11
Table 1.3 Summarized information of some MC related commercial products.	12
Table 1.4 Summarized information of investigated applications areas of MC.	13
Table 2.1 Active states of MC switch states.....	26
Table 2.2 Zeros states and rotating states of MC switch states.	27
Table 2.3 Look-up table of the vector combinations to synthesize the output voltage and input currents.	28
Table 2.4 Possible switch combinations of the VSR.	31
Table 2.5 Possible switch combinations of the VSI.	33
Table 3.1 System parameters for the simulated transmission system.....	56
Table 3.2 Parameters of the PID power low controllers.	56
Table 4.1 Duty cycles distribution for symmetrical switching sequence.....	73
Table 4.2 Simulation system parameters.....	75
Table 4.3 Simulation comparison of PI-SVM, PICF-SVM, PR-SVM and PRHC-SCM.	81
Table 4.4 Comparison of low-order harmonics between PR-SVM and PRHC-SVM....	87
Table 4.5 Experimental comparison of PI-SVM, PICF-SVM, PR-SVM and PRHC- SVM.	87
Table 5.1 Switch states look-up table of F-HB control for MC.	99
Table 5.2 MC input power supply, filter and load parameters.	102
Table 5.3 PMSM system and controller parameters for F-HB based MC-PMSM drive.	103
Table 5.4 Comparative results for performances of F-HB and S-HB.....	103
Table 5.5 Modified switching look-up table for MC DTC.	121
Table 5.6 Induction machine simulation parameters.	122
Table 6.1 Simulation system and controller parameters.....	139
Table 6.2 Investigation of VTR versus output filter parameters	141
Table 6.3 Simulation system parameters.....	154

LIST OF FIGURES

Fig. 1.1 Back to back converter topology.	2
Fig. 1.2 Basic topology of the MC with filters.	2
Fig. 1.3 Topologies for bidirectional switches: (a) diode bridge arrangement, (b) reverse block arrangement, (c) common emitter arrangement, (d) common collector arrangement.	3
Fig. 1.4 Classification of AC-AC converters.	4
Fig. 1.5 Diagram for direct MC.	5
Fig. 1.6 Diagram for indirect MC proposed in [57].	6
Fig. 1.7 Indirect MC topology with auxiliary designs.	6
Fig. 1.8 Diagram for sparse MC.	7
Fig. 1.9 Diagram for very sparse MC.	7
Fig. 1.10 Diagram for ultra sparse MC.	8
Fig. 1.11 Classification of MC control strategies.	9
Fig. 2.1 A three-phase direct MC system with input filters.	24
Fig. 2.2 Space vector hexagons for known input voltages and output currents.	28
Fig. 2.3 Synthesis of the desired output voltage and input current vectors.	29
Fig. 2.4 Indirect SVM illustration with virtual DC link.	30
Fig. 2.5 (a) VSR current space vectors hexagon, (b) space vector synthesis.	32
Fig. 2.6 (a) VSI current space vectors hexagon, (b) space vector synthesis.	34
Fig. 2.7 Demonstration of commutation of current paths.	37
Fig. 2.8 Illustration diagram of the four-step commutation when load current is positive.	38
Fig. 2.9 Illustration diagram of the four-step commutation when load current is negative.	39
Fig. 2.10 The diode clamp protection circuit in the MC.	40
Fig. 3.1 Conventional UPFC system in a transmission line.	44
Fig. 3.2 Back-to-back converter topology in the UPFC.	45
Fig. 3.3 The MC system with the input filters and loads.	46
Fig. 3.4 Diagram for UPFC power-flow control.	47

Fig. 3.5 Transmission system inherent active power curves versus V_r and θ .	49
Fig. 3.6 Transmission system inherent reactive power curves versus V_r and θ .	49
Fig. 3.7 Phasor diagrams of the transmission line with UPFC under modes of (a) sending end voltage compensation, (b) transmission angle compensation and (c) comprehensive compensation.	50
Fig. 3.8 Controllable active power diagram as a function of UPFC's V_c and θ_c .	51
Fig. 3.9 Controllable reactive power diagram as a function of UPFC's V_c and θ_c .	51
Fig. 3.10 Full power controllable regions with the application of UPFC.	52
Fig. 3.11 MC-UPFC in double-line transmission system (simulation study case).	53
Fig. 3.12 D-Q decoupling PID controllers for MC-UPFC.	55
Fig. 3.13 Power diagrams as a result of voltage contribution (a) active power and (b) reactive power.	57
Fig. 3.14 Sending-end power ranges with the compensation of MC-UPFC (a) active power and (b) reactive power	57
Fig. 3.15 Response of the sending-end power to the step change in active and reactive power.	58
Fig. 3.16 Response of line current d and q components to the power changes.	59
Fig. 3.17 Transmission line sending-end currents and MC output currents.	59
Fig. 3.18 Injected phase voltage V_c by MC-UPFC and equivalent sending-end voltage ($V_L = V_s + V_c$).	59
Fig. 3.19 Three-phase voltages and currents of the supply source 1.	60
Fig. 3.20 Current spectrum analysis of the transmission line X.	60
Fig. 4.1 PI controller with a voltage feedforward path.	65
Fig. 4.2 Combined feedforward and feedback controller diagram.	66
Fig. 4.3 Frequency responses of $E(j\omega)$ for different values of K .	68
Fig. 4.4 Proposed PI current controller with current reference feedforward for MC.	68
Fig. 4.5 Cascaded ideal PR controllers with selective harmonic compensation.	70
Fig. 4.6 Frequency response of the ideal PR controllers with selective harmonics compensator ($K_P = 1$, $K_{Rn} = 1$, $\omega = 100\pi$ rad/s).	71
Fig. 4.7 Cascaded approximated PR controllers with harmonic compensation.	71
Fig. 4.8 Frequency response of the approximated PR controllers with selective harmonic compensator ($K_P = 1$, $K_{Rn} = 1$, $\omega = 100\pi$ rad/s, $\omega_c = 5, 10$, and 20 rad/s).	71
Fig. 4.9 Proposed PI controller diagram for the MC.	74

Fig. 4.10 PR controller diagram for the MC.	75
Fig. 4.11 Simulation results of the PI-SVM: (a) steady-state output currents and errors, (b) FFT analysis of the currents.	76
Fig. 4.12 Simulation results of the PICF-SVM: (a) steady-state output currents and errors, (b) FFT analysis of the current.	77
Fig. 4.13 MC input phase current and voltage (PICF-SVM).	77
Fig. 4.14 Transient performance of the PICF-SVM controller.	78
Fig. 4.15 Steady-state error performance of PRHC-SVM controlled output current ($K_{R4} = K_{R6} = 500, K_{R7} = 300$).	78
Fig. 4.16 FFT analysis of PR-SVM controlled MC output current (without harmonics compensator).	79
Fig. 4.17 FFT analysis of PRHC-SVM controlled MC output current (with harmonics compensator, $K_{R4} = K_{R6} = 500, K_{R7} = 300$).	80
Fig. 4.18 Dynamic response of the PR-SVM to a step reference ($K_{R4} = K_{R6} = 500, K_{R7} = 300$).	80
Fig. 4.19 MC prototype.	82
Fig. 4.20 Experimental results of SVM: (a) input voltage and current, (b) output currents (two phases).	83
Fig. 4.21 Experimental results of PI-SVM: (a) input voltage and current, (b) output currents, (c) output current harmonics spectrum and THD.	84
Fig. 4.22 Experimental results of PICF-SVM: (a) input voltage and current, (b) output currents, (c) output current harmonics spectrum and THD.	85
Fig. 4.23 Experimental results of PR-SVM: (a) output currents, (b) output current harmonics spectrum and THD.	86
Fig. 4.24 Experimental results of PRHC-SVM: (a) output currents, (b) output current harmonics spectrum and THD.	87
Fig. 5.1 The FOC controlled drive system with VSI or MC.	94
Fig. 5.2 HB current controller diagrams: (a) HB for the VSI, (b) HB for the MC, (c) F-HB band, (d) S-HB band.	96
Fig. 5.3 Illustration of overall modulation with virtual rectifier, inverter and DC link.	99
Fig. 5.4 HB-FOC controller diagram for MC based PMSM drive.	102
Fig. 5.5 Simulation results of HB current controller for MC: (a) F-HB controller currents dynamic performance, (b) S-HB controller currents dynamic performance, (c) FFT analysis of F-HB output current after 0.05 s, (d) FFT analysis of S-HB output current after 0.05 s, (e) F-HB average switching frequency, (f) S-HB average switching frequency.	106

Fig. 5.6 Simulation results of HB-FOC for MC based PMSM drive system in response to the speed change from +500 rpm to -300 rpm at 1 s when $T_L = 1.5$ N m. (a) F-HB, (b) S-HB.	107
Fig. 5.7 The experimental set up: (a) MC hardware board, (b) PMSM test bench.	108
Fig. 5.8 Experimental results of HB-FOC controlled MC based PMSM drive (steady-state results 1): (a) PMSM stator currents when $\omega = 10$ rpm and $T_L = 1.5$ N m, (b) PMSM stator line voltage when $\omega = 10$ rpm and $T_L = 1.5$ N m, (c) PMSM stator currents when $\omega = 50$ rpm and $T_L = 1.5$ N m, (d) PMSM stator line voltage when $\omega = 50$ rpm and $T_L = 1.5$ N m.	110
Fig. 5.9 Experimental results for HB-FOC controlled MC based PMSM drive (steady-state results 2): (a) PMSM stator currents when $\omega = 500$ rpm and $T_L = 1.5$ N m, (b) PMSM stator line voltage when $\omega = 500$ rpm and $T_L = 1.5$ N m, (c) MC input phase voltage and current when $\omega = 300$ rpm and $T_L = 1.5$ N m, (d) PMSM torque performance when $\omega = 300$ rpm and $T_L = 1.5$ N m.	111
Fig. 5.10 Experimental results of HB-FOC controlled MC based PMSM drive (transient results 1): (a) PMSM stator currents, rotor speed and q -axis component current responses to command speed step change from 50 rpm to 300 rpm when $T_L = 1.5$ N m, (b) PMSM stator currents, rotor speed and q -axis current component to load torque step change from 0 to 1.5 N m when $\omega = 500$ rpm.	113
Fig. 5.11 Experimental results of HB-FOC controlled MC based PMSM drive (transient results 2): (a) PMSM stator current and MC input current response, (b) PMSM rotor speed and q -axis current component response to command speed step change from 350 rpm to 250 rpm (deceleration) when $T_L = 1.5$ N m.	114
Fig. 5.12 MC (a) input voltage and (b) output current vectors hexagon (Fig. 2.2 repeated).	117
Fig. 5.13 DTC illustration diagram with the MC vectors.	118
Fig. 5.14 Block diagram of DTC for motor drive with inverter or MC.	119
Fig. 5.15 Redefined input voltage vector sector for deciding the amplitudes of output voltage vectors.	121
Fig. 5.16 Motor steady-state stator current when speed is 1000 rpm and load torque is 10 N m.	122
Fig. 5.17 Motor steady-state electromagnetic torque when speed is 1000 rpm and load torque is 10 N m.	123
Fig. 5.18 Steady-state stator flux locus when speed is 1000 rpm and load torque is 10 N m.	123
Fig. 5.19 Torque transient response to a step change at 0.65s.	124
Fig. 5.20 Stator current for a torque step change at 0.65s.	124
Fig. 6.1 Diagram of an interconnected power system example involving renewable DGs.	129

Fig. 6.2 AC microgrid with renewable DGs and MC.....	130
Fig. 6.3 Output filter model in block diagram and its Bode plots for different values of L_{oa} and C_{oa} (mH, μ F).....	135
Fig. 6.4 Luenberger observer design diagram and the simplified diagram.....	136
Fig. 6.5 The predictive voltage controller scheme for MC in an islanded microgrid...	138
Fig. 6.6 Simulation results: (a) regulated output line-to-line voltages, (b) FFT analysis result and harmonic spectrum for v_{ab} , (c) source voltage and current waveforms, (d) estimated and measured load currents. ($\lambda_1=1$, $\lambda_2=0$, $\lambda_3=0$, $\lambda_4=0$).....	141
Fig. 6.7 Simulation results: output voltage waveforms corresponding to the parameter combinations listed in Table 6.2.....	142
Fig. 6.8 Simulation results: (a) source voltage and current with controlled power factor with $\lambda_2=0.0067$, (b) uncontrolled and controlled common mode voltage with $\lambda_3=25$, (c) uncontrolled and controlled average switching frequencies with $\lambda_4=0.09$, (d) simulated intermittent source voltages and controlled output voltages.	144
Fig. 6.9 Hardware setup for verifying the proposed scheme: (a) MC system comprising ① MC prototype, ② IGBT drivers power supply, ③ microprocessor control card, ④ ADC conditioning circuits, ⑤ sensors boards, ⑥ input filter inductors, ⑦ output LC filters, ⑧ inductive loads, ⑨ clamp circuit, ⑩ input filter capacitors, (b) nonlinear load with $R=30\Omega$ and $C=1700\mu$ F.	145
Fig. 6.10 Experimental waveforms: (a) output voltage and currents when $f_o=25$ Hz, (b) output voltage and currents when $f_o=100$ Hz, (c) output voltage and currents when $f_o=50$ Hz, (d) source voltage and current when $f_o=50$ Hz, (e) output voltage and current responses to load connection, (f) output voltage and current responses to load disconnection. ($\lambda_1=1$, $\lambda_2=0$, $\lambda_3=0$, $\lambda_4=0$).	148
Fig. 6.11 Experimental waveforms: (a) uncontrolled and controlled input power factor with $\lambda_2=0.0067$, (b) uncontrolled and controlled common mode voltage with $\lambda_3=25$	149
Fig. 6.12 Experimental waveforms: (a) output voltages and currents for nonlinear load test, (b) output voltages and currents for unbalanced load test, (c) input voltages and currents for unbalanced input test, (d) output voltages and currents for unbalanced input test.....	151
Fig. 6.13 Diagram for AC/AC conversion using MC.....	155
Fig. 6.14 Diagram for AC/DC conversion using MC.....	155
Fig. 6.15 AC/DC conversion (a) input voltages, (b) output voltages and (c) unity input power factor operation for the input phase A	156
Fig. 6.16 Diagram for DC/AC conversion using MC.....	157
Fig. 6.17 DC/AC conversion (a) output voltages, (b) unregulated common-mode voltage and (c) regulated common-mode voltage.....	158

Fig. 6.18 Diagram for DC/DC conversion using MC.....	158
Fig. 6.19 DC/DC conversion (a) output voltages and (b) average switching frequencies of 9 switches in the MC.....	159

LIST OF APPENDICES

APPENDIX A	168
APPENDIX B	172

PUBLICATIONS LIST

1. Published Journal Papers

- [1] **J. Zhang**, H. Yang, T. Wang, L. Li, D. G. Dorrell, D.D.C. Lu, "Field-Oriented Control based on Hysteresis Band Current Controller for a Permanent Magnet Synchronous Motor driven by a Direct Matrix Converter," *IET Power Electronics*, vol. 11, no. 7, pp. 1277-1285, 2018.
- [2] **J. Zhang**, L. Li, D. G. Dorrell, Y. Guo, "Decoupling Controller Design and Controllable Regions Analysis for the Space Vector Modulated Matrix Converter-Unified Power Flow Controller in Transmission Systems," *Electric Power Components and Systems*, vol. 46, no. 1, pp. 1-14, 2018.
- [3] **J. Zhang**, L. Li, D. G. Dorrell, "Control and Applications of Direct Matrix Converters: A Review," *Chinese Journal of Electrical Engineering*, vol. 4, no. 2, pp. 18-27, 2018.

2. Submitted Journal Papers

- [4] **J. Zhang**, L. Li, D. G. Dorrell, M. Norambuena, and J. Rodriguez, "Predictive Voltage Control of Direct Matrix Converter with Improved Output Voltage for the Renewable Microgrid Applications," *IEEE Journal of Emerging and Selected Topics in Power Electronics*, under review, 2018.
- [5] **J. Zhang**, L. Li, D. G. Dorrell, "Improved Steady-State Performance by Modified PI Controller and Comparison with PR Controller on Direct Matrix Converters," *IET Power Electronics*, under review, 2018.
- [6] **J. Zhang**, M. Norambuena, L. Li, J. Rodriguez, D. G. Dorrell, "Sequential Model Predictive Control of Three-Phase Direct Matrix Converter," *IEEE Access*, under review. 2018.

3. Published Conference Papers

- [7] **J. Zhang**, L. Li, L. Zhang, D. G. Dorrell, "Hysteresis Band Current Controller based Field-Oriented Control for an Induction Motor driven by a Direct Matrix Converter," 43rd Annual Conference of the IEEE Industrial Electronics Society (IECON 2017), Beijing, China, pp. 4633-4638, November 2017.
- [8] **J. Zhang**, L. Li, T. He, M. M. Aghdam, D. G. Dorrell, "Investigation of Direct Matrix Converter Working as a Versatile Converter (AC/AC, AC/DC, DC/AC, DC/DC Conversion) with Predictive Control," 43rd Annual Conference of the IEEE Industrial Electronics Society (IECON 2017), Beijing, China, pp. 4644-4649, November 2017.
- [9] **J. Zhang**, L. Li, Z. Malekjamshidi and D. G. Dorrell, "Predictive Voltage Control of Direct Matrix Converter with Reduced Number of Sensors for the Renewable Energy and

- Microgrid Applications," 2017 IEEE Energy Conversion Congress and Exposition (ECCE 2017), Cincinnati, U.S., pp. 3309-3315, October 2017.
- [10] **J. Zhang**, L. Li, D. G. Dorrell and Y. Guo, "Space Vector Modulation based Proportional Resonant Current Controller with Selective Harmonics Compensation for Matrix Converter Systems," 20th International Conference on Electrical Machines and Systems (ICEMS 2017), Sydney, Australia, August 2017.
- [11] **J. Zhang**, L. Li, D. G. Dorrell and Y. Guo, "A PI Controller with Current Feedforward to Improve the Steady-State Error Performance for the Current Controlled Direct Matrix Converter," 20th International Conference on Electrical Machines and Systems (ICEMS 2017), Sydney, Australia, August 2017.
- [12] **J. Zhang**, L. Li, D. G. Dorrell and Y. Guo, "Direct Torque Control with a Modified Switching Table for a Direct Matrix Converter based AC Motor Drive System," 20th International Conference on Electrical Machines and Systems (ICEMS 2017), Sydney, Australia, August 2017.
- [13] **J. Zhang**, L. Li and D. G. Dorrell, "D-q coupling suppressed pid controller for the transmission line power flow control using a matrix converter," The 42nd Annual Conference of IEEE Industrial Electronics Society (IECON 2016), pp. 6249 – 6254, Florence, Italy, October 2016.
- [14] **J. Zhang**, D. G. Dorrell and L. Li, "Applications of the Direct Space Vector Modulation Controlled Matrix Converter as the Unified Power Flow Controller," The 8th International Conference on Power Electronics, Machines and Drives (PEMD 2016), pp. 1-6, Glasgow, UK, 2016.
- [15] **J. Zhang**, D. G. Dorrell, L. Li and A. Argha, "A novel sliding mode controller for DC-DC boost converters under input/load variations," The 41st Annual Conference of IEEE Industrial Electronics Society (IECON 2015), pp. 1698-1703, Yokohama, Japan, 2015.

4. Submitted Conference Papers

- [16] **J. Zhang**, L. Li, D. G. Dorrell, J. Rodriguez and M. Norambuena, "Investigation of Grid-Connected and Islanded Direct Matrix Converter for the Renewable Microgrid Applications with Model Predictive Control," 2018 IEEE Energy Conversion Congress and Exposition (ECCE 2018), Portland, U.S., accepted, 2018.
- [17] **J. Zhang**, L. Li, D. G. Dorrell, J. Rodriguez and M. Norambuena, "Sequential Model Predictive Control of Direct Matrix Converter without Weighting Factors," 44th Annual Conference of the IEEE Industrial Electronics Society (IECON 2018), Washington, U.S., accepted, 2018.

LIST OF ABBREVIATIONS AND ACRONYMS

AC	=	Alternating Current
ADC	=	Analog to Digital Converter
DC	=	Direct Current
DSP	=	Digital Signal Processor
DTC	=	Direct Torque Control
ePWM	=	Enhanced Pulse Width Modulator
eQEP	=	Enhanced Quadrature Encoder Pulse
FACTS	=	Flexible Alternating Current Transmission System
FFT	=	Fast Fourier Transform
F-HB	=	Sinusoidal Hysteresis Band
FOC	=	Field Oriented Control
HB	=	Hysteresis Band
IGBT	=	Insulated Gate Bipolar Transistor
KCL	=	Kirchhoff Current Law
KCL	=	Kirchhoff Current Law
MC	=	Matrix Converter
MC-UPFC	=	Matrix Converter based Unified Power Flow Controller
MPC	=	Model Predictive Control
PI	=	Proportional Integral
PICF	=	Proportional Integral Controller with Current Feedforward
PI-SVM	=	Proportional Integral Controller based on Space Vector Modulation
PLL	=	Phase Locked Loop
PMSM	=	Permanent Magnet Synchronous Machine
PR	=	Proportional Resonant
PRHC-SVM	=	Proportional Resonant Controller with Harmonics Compensator based on Space Vector Modulation
PR-SVM	=	Proportional Resonant Controller based on Space Vector Modulation
PWM	=	Pulse Width Modulation
SCI	=	Serial Communications Interface

S-HB	=	Fixed Hysteresis Band
SMC	=	Sliding Mode Control
SSSC	=	Static Synchronous Series Compensator
STATCOM	=	Static Synchronous Compensator
SVM	=	Space Vector Modulation
THD	=	Total Harmonic Distortion
UPFC	=	Unified Power Flow Controller
VSI	=	Voltage Source Inverter
VSR	=	Voltage Source Rectifier
VTR	=	Voltage Transfer Ratio

1 INTRODUCTION

A matrix converter (MC) is composed of an array of controlled bidirectional switches that perform direct energy conversion without any bulky energy storage elements as an intermediate link. A three-phase direct MC comprises nine bidirectional semiconductor switches arranged in a 3×3 matrix form to realize the direct AC-to-AC conversion. MCs have several advantageous characteristics, such as compact volume, bidirectional power flow, controllable input power factor and sinusoidal waveforms, MCs have attracted research interest and many MC projects have been reported. The MC is regarded as an all-silicon converter. This chapter reviews the development of MC technology, including topologies, control issues and application areas, and presents the background of this project.

1.1 Literature Review

AC-to-AC converters have been widely applied in various areas in the real world including motor drives, renewable generation, grid interface, unified power flow controller (UPFC). In industrial applications, AC-to-AC power conversion is usually accomplished by indirect converters. In these converters, the AC power is firstly converted into DC power by a rectifier, and then the DC power is converted into AC power by an inverter. The rectifier and inverter are usually connected via an intermediate bulky DC-link capacitor. A typical example of these converters is the back-to-back converter as shown in Fig. 1.1. The use of the DC-link capacitor in these

converters makes the equipment volume high, reduces the lifetime of the device, increases the design complexity and decreases the system efficiency. Therefore, it is of great benefit to remove the DC link capacitor or propose new converter topologies. Some research works have been dedicated to addressing this issue. It is believed that the AC-to-AC converters should be equipped with the following desirable features: sinusoidal input and output waveforms, low harmonic component, bidirectional power flow, small volume energy-storage devices, controllable power factor [1]. MCs appear to be a possible solution since they can fulfill the above requirements.

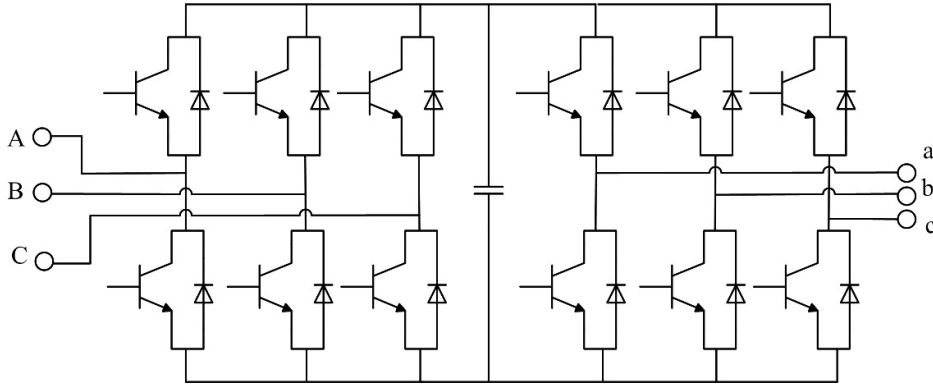


Fig. 1.1 Back to back converter topology.

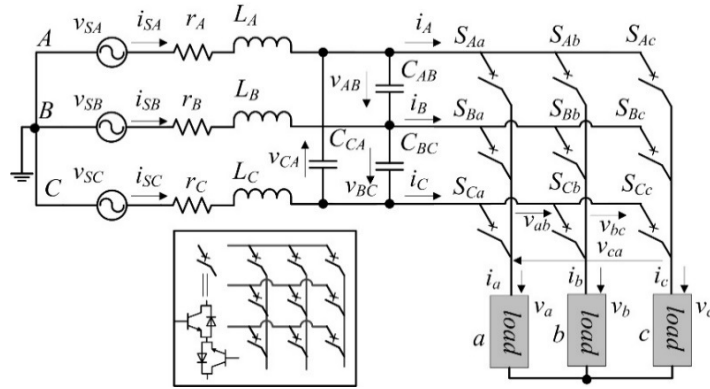


Fig. 1.2 Basic topology of the MC with filters.

The concept of direct MC circuit appeared in the literature as early as in the 1970s [2][3]. There has been extensive research since the work published by Venturini and Alesina in the 1980s [4]-[6]. A developed three-phase direct MC is shown in Fig. 1.2. In contrast to the conventional AC-DC-AC conversion, the MC does not require the DC

capacitor and completes the power conversion in one stage. The absence of the DC capacitor reduces the volume, enhances the efficiency, increases the lifetime and simplifies the control schemes. In the MC, nine semiconductor switches are arranged in a 3×3 matrix form. MCs only require capacitors in the filters to suppress the ripples generated by the switching actions [7] and these are smaller in size. MCs have received attention because of their advantages: sinusoidal input and output waveforms, controllable power factor, bidirectional power flow and the compact feature [4].

1.1.1 The Switches for Matrix Converter

The MC switches have to be bidirectional semiconductor devices because bidirectional current flow occurs, and this has to be controlled in both directions. However, a single device that can conduct current and block the voltage in both directions is currently not commercially available [8]. Therefore, the bidirectional switches are usually formed from several devices which are appropriately connected. For MCs, typical bidirectional switching devices are usually implemented using: (a) a diode bridge arrangement [1][8][9], (b) a reverse block arrangement [8][10], (c) a common emitter arrangement, or (d) a common collector structure [1][8][9][11], as shown in Fig 1.3. Here, insulated gate bipolar transistors (IGBTs) are used to represent the controlled switches.

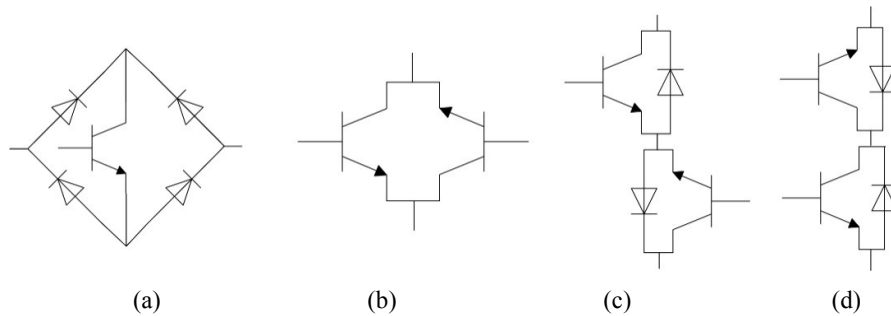


Fig. 1.3 Topologies for bidirectional switches: (a) diode bridge arrangement, (b) reverse block arrangement, (c) common emitter arrangement, (d) common collector arrangement.

The configuration in (a) requires nine independent drive power supplies, i.e., only one driver supply for each switch cell. The losses are relatively high since there are three devices in the conduction path. It is also difficult to control the current direction through the switch.

The arrangement (b) only requires two controlled switches. The anti-parallel diodes that are usual in these power devices are removed. Six independent drive supplies are required.

The structures in (c) and (d) facilitate the bidirectional control. These structures are good for four-quadrant commutation control. In the common emitter structure, nine independent driver supplies are needed to control the IGBTs; while in the common collector configuration, only six power supplies are required [12]. The configuration in (c) can provide an inherent auxiliary commutating current path, which enables the application of advanced commutation techniques [13].

The development of semiconductor device technology influences the properties (switching frequency, voltage blocking capability, voltage and power ratings, etc.) of converters. Fast and high-speed power switches are desirable as the filter volume may be reduced by increasing the frequency [14]. The development of novel semiconductor devices such as SiC (silicon carbide) or GaN (gallium nitride) switches can potentially improve the performance of converters.

1.1.2 Matrix Converter Topologies

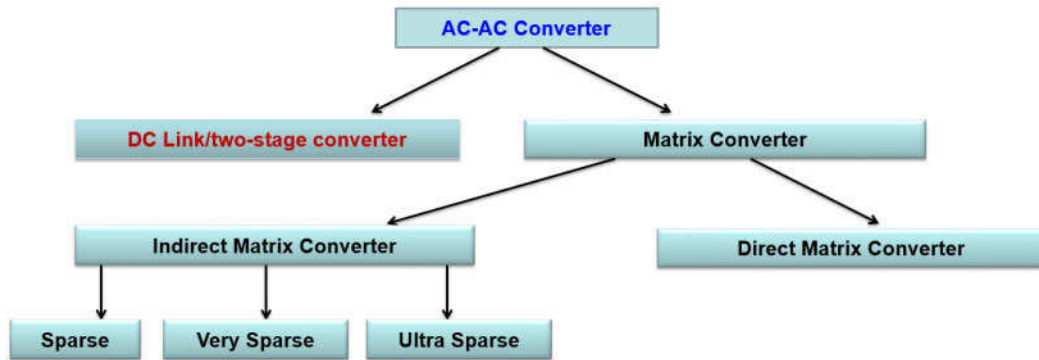


Fig. 1.4 Classification of AC-AC converters.

MC topologies have been researched to expand the control range of the output voltage, reduce the number of semiconductor devices, improve the waveform quality, eliminate the common mode voltage and decrease the switching losses [15]. As summarized in Fig. 1.4, The most notable MC topologies include the direct MC, indirect MC, sparse

MC, very sparse MC, ultra-sparse MC, hybrid MC and multilevel MC. Many have a maximum voltage transfer ratio of 0.866, such as the sparse, ultra-sparse, very sparse and inverting link MCs [16].

In addition to the three-phase to three-phase MC, other categories such as single-phase MC [17], single to two-phase MC [18], three to five-phase MC [19], and three to seven-phase MC [20][21], have been explored in the literature.

A direct MC with the switch cells arranged in the common emitter configuration is shown in Fig. 1.5. In this topology, there are nine bidirectional switches and they are composed of eighteen controlled switches (IGBTs) and eighteen diodes. This topology is also known as the traditional MC.

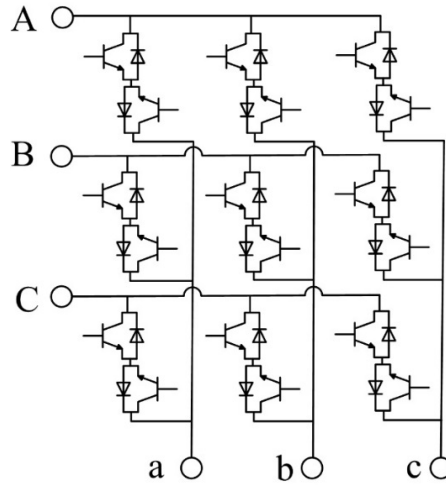


Fig. 1.5 Diagram for direct MC.

The indirect MC proposed in [22] is shown in Fig 1.6. As seen from this topology, the AC-to-AC power conversion is performed indirectly, but the DC energy storage element is not required. This topology consists of eighteen IGBTs and eighteen diodes. It is possible to reduce the number of semiconductor devices further to derive other MC topologies [1]. As suggested in [23], this topology enables improvement of the voltage transfer ratio and immunity against disturbances from supply sources by embedding an auxiliary design into the intermediate stage as shown in Fig. 1.7. The indirect MC can be regarded as a combination of a voltage source rectifier (VSR) and a voltage source inverter (VSI). Therefore, various modulation schemes can be used in both stages [4]. It

is easier and simpler to implement the switching modulation compared with the single-state topology [24].

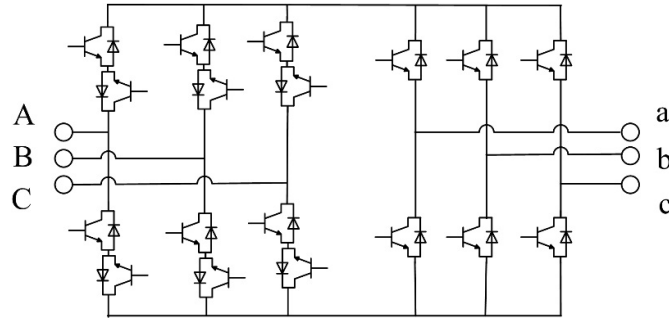


Fig. 1.6 Diagram for indirect MC proposed in [57].

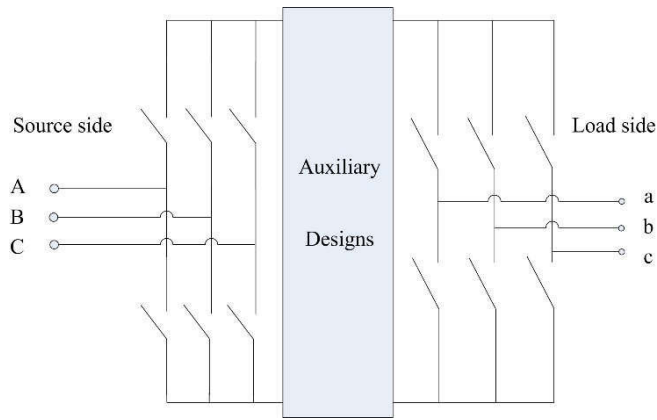


Fig. 1.7 Indirect MC topology with auxiliary designs.

The sparse MC, as shown in Fig. 1.8, consists of fifteen IGBTs and eighteen diodes. At least seven independent drive supplies are required in this configuration. This topology is equivalent to the indirect MC in function while less implementation efforts are needed [16]. The sparse MC contains fewer IGBTs compared to the indirect MC. However, a significant disadvantage is the higher power losses because there are more semiconductor switches in the conduction path [15].

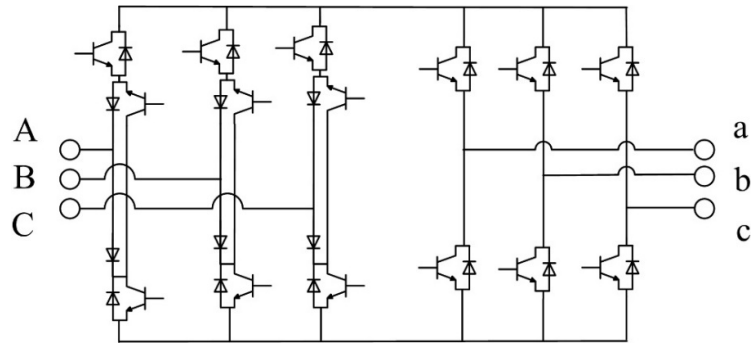


Fig. 1.8 Diagram for sparse MC.

To reduce the number of IGBTs further, the very sparse converter, as shown in Fig. 1.9, was proposed. This topology is composed of twelve IGBTs and thirty diodes, and ten independent driver supplies are required. The number of controlled switches is reduced; however, the losses are increased, and the control range is reduced [15].

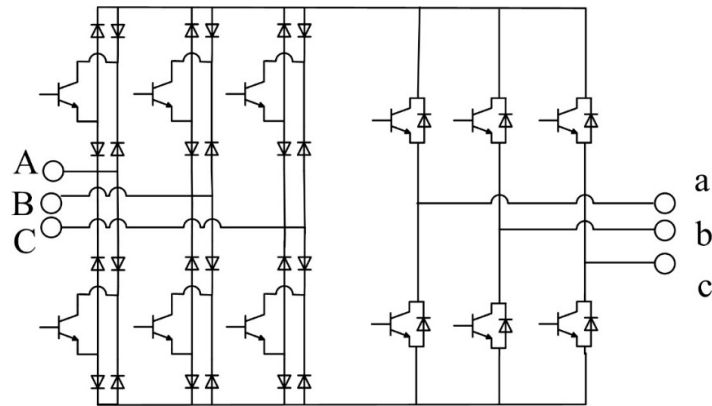


Fig. 1.9 Diagram for very sparse MC.

If only unidirectional power flow is required, the ultra-sparse MC, as shown in Fig. 1.10, can be obtained. This topology has a sparser structure and it requires nine IGBTs and eighteen diodes [16]. This structure requires seven independent driver supplies.

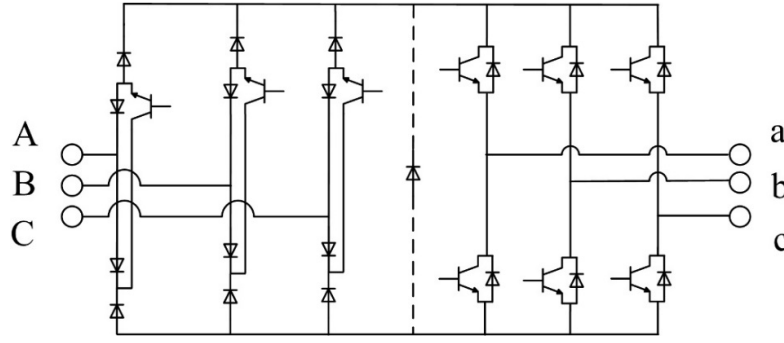


Fig. 1.10 Diagram for ultra sparse MC.

Table 1.1 Comparison of MCs.

Converter Topology	No. of Transistors	No. of Diodes	No. of Drives
Direct MC	18	18	6
Indirect MC	18	18	8
Sparse MC	15	18	7
Very Sparse MC	12	30	10
Ultra Sparse MC	9	18	7

A comparison of the above topologies is presented in Table 1.1. The sparse, very sparse and ultra-sparse MCs can be regarded as indirect MCs. These indirect topologies have the same second stage for DC to AC conversion. The power conversion of indirect MCs is still performed indirectly with two conversion stages.

As a derivative of the MC, the multilevel MC has been proposed by incorporating the concept of multilevel converter with an MC [1][25][26]. The multilevel MC can produce better power quality because of its multilevel outputs. It also has the potential to provide a solution for high-power energy conversion [27]. However, the semiconductor requirement and modulation complexity are increased [16].

Another derivative is the hybrid MC which combines an MC with another converter type such as an inverter. The hybrid MC was proposed to address the limitations of the output voltage. Hybrid MCs are capable of enlarging the control range of the output voltage and are even able to operate under unbalanced grid conditions. However, the topology structure is complicated and intricate control strategies are required [6][10].

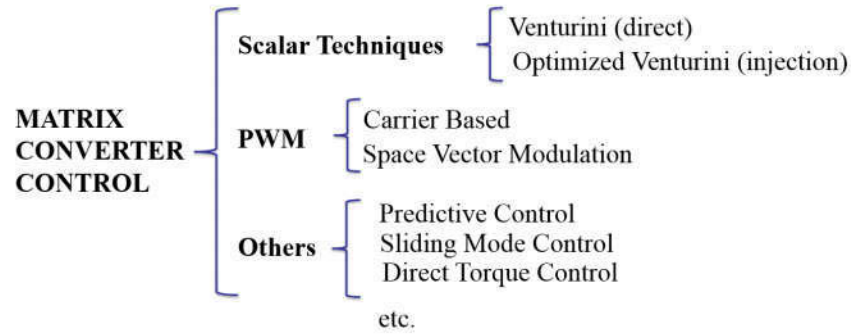


Fig. 1.11 Classification of MC control strategies.

1.1.3 Modulation and Control Strategies

Many modulation and control strategies have been proposed for MCs [28]. Generally, the modulation strategies can be classified into: 1) pulse width modulation (PWM) methods (carrier based and space vector modulation (SVM)) [7], 2) scalar techniques (e.g., Venturini method [29]), and 3) other control strategies (such as hysteresis band [30][31], predictive control [32], sliding mode control [33], direct torque control (DTC) [34], fuzzy method [35] and neural networks [36]). These are summarized in Fig. 1.11. In addition, proportional-integral (PI) and proportional-resonant (PR) controllers based on the SVM have been investigated for the MC [37][38].

The Venturini method is a direct modulation technique. Using the direct transfer function approach, switch timings are directly calculated from input voltages and target output voltages. The calculation of these timings is cumbersome for practical implementation. Another significant drawback of this method is that the voltage transfer ratio cannot exceed 0.5 [39]. To improve the voltage transfer ratio, the optimized Venturini method was proposed. In this method, the voltage transfer ratio is improved from 0.5 to 0.866 by the third harmonic injection [12].

PWM modulation techniques include carrier-based and SVM. In the carrier-based modulation, the input power factor can be regulated using the offset voltage and changing the slope of carrier [40][41]. SVM is a more popular method and it has the potential to make best use of input voltage, to reduce the number of commutation, to control the input power factor, and to provide better power quality [39][42]. Based on the space vector representation, SVM combines two adjacent vectors and zero state vectors to generate the desired reference [24]. It has been proved that SVM can

generalize the modulation issue of MCs. There are direct and indirect SVMs for MCs which will be explained in detail in the next chapter.

Indirect conversion is capable of controlling output frequency, amplitude and input current phase displacement [7][43]. This method can decouple the modulation of the virtual rectifier stage and the virtual inverter stage, thus making it possible to combine different modulation strategies of two stages [44]. In addition, the indirect conversion scheme facilitates the analysis of input voltage unbalance [45]. However, indirect conversion tends to be replaced by the direct conversion since the direct scheme provides a better understanding of operation and modulation process due to the absence of a fictitious DC link [12].

Using SVM, closed-loop controllers, such as PI, PR and sliding mode controllers, have been investigated for the MC [37][38]. These controllers are simple and independent of the system model. PI controllers are industry-mature, and they have been used in a wide range of areas. However, there are significant steady-state errors when PI controllers are used to track sinusoidal variables. Otherwise, frame transformations are required to convert the sinusoidal variables into constant values, which results in a complex design and heavy computational burden. A modified PI controller with current feedforward is proposed in this thesis to address this issue. Another possible solution is the PR controller. These topics will be discussed in detail in Chapter 4.

Sliding mode control has been developed for the three-phase MC [46]. Sliding mode control can provide advantages such as stability against large disturbances, fast dynamic response and simple implementation [47]. It has improved robustness in terms of providing fast transient responses over a wide range of operating conditions [48]. Sliding mode based direct power control was proposed for control of the power flow in a transmission line [33]. It enables the real-time selection of adequate state space vectors to regulate the input and output variables. It exhibits robust behaviour and immunity against power system nonlinearity [33].

Another popular control tool for power electronic converters including MCs is model predictive control (MPC) [49]. With the development of microprocessors, MPC has become an increasingly researched topic in recent decades [50]. MPC utilizes a system model to predict future behaviour and selects an optimum switch action based on a user-defined cost function. This controller can provide flexibility for the control of different

variables, and the constraints can be considered in the controller. In the literature, several MC predictive control studies have been reported. However, most focus on the control of sinusoidal output current [51][52]. In this thesis, predictive control is used to regulate the sinusoidal output voltage and power flow. This work is presented in Chapter 6.

DTC is especially relevant when an MC is used to drive an AC motor [34][53]-[55]. This controller has been widely used in high-performance motor drives because of its fast torque dynamic response and robustness. A DTC of an MC-fed induction motor is presented in Chapter 5. In addition, a hysteresis current controller is designed for the MC in order to drive an AC motor. Both fixed-band and sinusoidal-band hysteresis controller are evaluated. The proposed controller is simple in structure and provides good performance. This controller is explained in detail in Chapter 5.

A performance comparison of some MC control strategies is shown in Table 1.2. Among these controllers, investigation of the hysteresis controller for MCs remains underexplored. At present, the Venturini method is not attracting very much attention. However, research on SVM, DTC and predictive control is still very active. Predictive control appears to be a promising control tool because of its simplicity, good performance and flexibility. It can include additional control objectives and system constraints. The derivatives of predictive control for power converters and drives includes predictive current control, predictive voltage control, predictive power control and predictive torque control.

Table 1.2 Comparison between some control techniques for MC.

	Venturini	SVM	DTC	Predictive Control	Hysteresis Control
Complexity	low	high	medium	low	very low
Sampling Frequency	very low	low	very high	high	high
Switching Frequency	very low	low	high	high	high
Dynamic Response	good	good	fast	very fast	very fast
Range of Application Area	narrow	wide	narrow	very wide	medium

1.1.4 Potential Applications Areas

The MC can be applied in a wide range of areas and it is particularly suitable for applications that require a compact volume, low weight and reliability [56]. However, they have only been used in a low number of industry applications so far [15]. There are some commercially available MC products and modules. Some examples of these products are Yaskawa FSDrive-MX1S series, U1000, AC7, Eupec ECONOMAC FM35R12KE3ENG and Fuji FRENIC-Mx. Table 1.3 summarizes the current availability of MC related commercial products. In this table, only the maximum available rating is listed for voltage and capacity, although products with lower ratings are available. In addition to MC products, there are plenty of commercially available power switch modules that can be used to construct an MC. As observed from Table 1.3, most MC manufacturers target motor drive applications.

Table 1.3 Summarized information of some MC related commercial products.

Manufacturers	Product/Model	Max. Voltage	Max. Power	Target Application	Other Information/Feature
Yaskawa	FSDrive-MX1S	6.6 kV	6 MVA	motor drive	energy-saving
Yaskawa	U1000	480 V	800 HP	motor drive	full regeneration, ultra-low harmonics
Yaskawa	AC7	480 V	250 HP	motor drive	legacy product
Yaskawa	Z1000U	480 V	350 HP	HVAC applications	low input distortion
Eupec	ECONOMAC FM35R12KE3ENG	1200 V	42 kVA	unspecified	module
Fuji	FRENIC-Mx	400 V	45 kW	general industrial machines	best suitable for elevators and cranes

In the literature, the motor drive is the most widely investigated application area of MCs [36][57]-[59]. The MC has also been proposed for the applications such as UPFC [60]-[63], mobile utility power supply [64]-[66] and wind turbine applications [67]-[70]. The summarized information of these application areas is provided in Table 1.4.

Table 1.4 Summarized information of investigated applications areas of MC.

	Input and Output Frequency	Applied Control Methods	Investigation Breadth	Comments
Motor Drive	very different	DTC, MPC, FOC	very wide	promising and developed
UPFC	same	SVM, SMC	wide	developing
Wind Turbine	very different	SVM, SMC, SVD ¹	medium	developing
Utility Supply	different	SVM, genetic algorithm, repetitive control	medium	developing
Grid Interface (Smart Grid)	same or similar	MPC	narrow	promising and underexplored

1 SVD – Singular Value Decomposition

The area in which the MC has most potential, both in industry and academia, is the motor drive [36][57]-[59], hence it is already used in this area. At the moment, motor drive applications are dominated by VSIs. For a high inertia system that requires dynamic braking, the VSI based drive system usually requires a rectifier stage to supply the DC voltage and a braking chopper to absorb the kinetic energy generated from the motor deceleration, or back-to-back inverters are required for bidirectional power flow. Bidirectional MC power flow means that an MC-based drive system does not require the braking chopper for motor deceleration. Therefore, the efficiency is improved and maintenance is alleviated. In the literature, several MC-fed motor drive control methods have been investigated. These include DTC, field-oriented control (FOC) and model predictive control (MPC). The tested motor types include the induction motor and permanent magnet synchronous motor (PMSM).

The MC has been investigated as a UPFC in flexible alternating current transmission systems (FACTS) [60]-[63]. The traditional UPFC employs a back-to-back converter that can fulfill the AC-to-AC conversion indirectly. The traditional UPFC combines a static synchronous compensator (STATCOM, shunt controller) and a static synchronous series compensator (SSSC, series controller). These two controllers are connected by a DC capacitor link. A UPFC can improve the capacity of a transmission system. However, the capacitor in the traditional UPFC produces losses, increases the weight and volume, reduces equipment lifetime and requires DC voltage control. No DC capacitor needed in an MC based UPFC (MC-UPFC). This structure has advantages such as compact configuration, less weight, bidirectional power flow, high efficiency,

controllable input power factor, and longer life cycle. Some research on the MC-UPFC has been carried out to test the performance and some good results have been reported.

In terms of application in wind turbines, the MC has been used to regulate the performance of a wind generator and achieve the maximum power extraction [67]-[70]. The wind turbine generation is controlled to produce power over a wide range of wind speeds. A cage induction generator or a doubly-fed induction generator can be used with the latter utilizing a reduced-size converter between the grid and the rotor windings. In the conventional scheme, the DC-link capacitor almost separates the control of the generator and grid. For the MC system, the generator and grid-side quantities are controlled simultaneously. Therefore, a better cooperative control can be achieved. The grid-side reactive power can be effectively regulated, which is desirable in a grid-connected wind turbine. Many control strategies have been studied in this area.

Another potential application area that has been investigated is the mobile power supply [64]-[66]. In this application, an MC is integrated with a variable speed diesel generator to create a supply. There is growing interest in utilizing static power converters to supply high-performance AC power in the uninterrupted power supplies, programmable AC sources and mobile supply units. An MC based mobile AC ground supply unit has been proposed for the aircraft servicing [66]. The use of this unit removes the auxiliary power unit on the aircraft that is supplied by burning jet fuel. Therefore, the noise, air pollution, and maintenance are reduced.

MCs can also be applied in microgrids for interfacing distributed renewable generation to the utility grid. However, this application area has not been investigated to any great extent. In terms of microgrid applications, there are two operation modes, i.e., islanded and grid-connected mode. In each mode, the main control objectives are different. In this thesis, the MC is used in a smart grid and MPC is employed as the control technique. This is a significant application that needs more research attention and further investigation.

1.2 Objectives and Significances

The topic of interest of this thesis is the three-phase direct MC. Although this converter has many advantages, there are some noticeable shortcomings such as low voltage

transfer ratio, sensitivity to the grid variations and complex modulation. Operational improvements in the MC have been studied and these include the expansion of the output voltage control range [11][13][23][39], control methods [28][29], commutation strategies [12][71]-[73], improvement of the waveforms quality [1][16][43][56], reduction of the number of devices [24][74][75], reduction of the common mode voltage [15][45] and the reduction of switching losses [42][45][76]-[78]. This thesis aims at finding possible solutions to some of the above issues.

The theoretical analysis of output voltage limitation was investigated in [6] and it was concluded that the three-phase direct AC to AC converter has the maximum intrinsic output voltage limit of $0.866 (\sqrt{3}/2)$. This drawback hinders the wide application of MCs. A transformer can be used to increase the voltage transfer ratio (VTR) either at the source or load side, but it would operate at either the grid or drive frequency, i.e., a relatively low frequency so that the transformer volume is relatively high, and the compactness of MC is affected. In addition, the overall system efficiency is reduced. Therefore, it is desirable to increase the VTR by modifying the topology or by revising the modulation strategies.

Any distortion or the imbalance at the input terminals will be directly reflected at the output terminals because of the absence of an intermediate energy storage unit [79]. The MC is then sensitive to input variations, which is undesirable. Therefore, it is of great benefit to reduce the influence of the input variations on the MC performance. Although some work has tried to address this problem, there is still a lot of room for improvement.

The improvement of power quality is beneficial. With increasing penetration of renewable energy systems into the grid, standards and codes impose more stringent requirements on the current quality and harmonic content. Therefore, if it can be demonstrated that the MC can make a contribution to power quality improvement, and MC applications are likely to be expanded.

With regards to applications, the focus of this thesis is the power flow controller, motor drive and smart grid. For motor drives, most control methods in the literature are not very practical to implement considering the processing capability of currently available microprocessors. Therefore, it is beneficial to propose simple methods with low computational burden.

With the development of distributed generation technology and the smart grid, AC-to-AC converters may have a wide range of applications in the future; they can be employed to link renewable energy resources and distributed energy generators to the grid. This field needs further investigation. The solutions to these issues will result in the improved performance and wider applications of MC.

1.3 Contributions and Organization

1.3.1 Contributions

The main contributions of this work are summarized as follows:

- (1) A simple decoupling controller is designed for the matrix converter-based UPFC to regulate the power flow in a transmission system. The controllable regions of the MC-UPFC are also analyzed. A design procedure for the closed-loop controller in the MC-UPFC is presented.
- (2) A modified PI controller is proposed for the improvement of the steady-state performance by including a current feedforward path. More control flexibility is provided because of the feedforward controller. A PR controller is designed for the MC and this has good performance.
- (3) A hysteresis current controller is proposed for the MC to drive AC motors. Both fixed-band and sinusoidal-band hysteresis controllers are investigated, and their performance is compared. The hysteresis controller is a very simple and practical controller for MC. For the MC-base motor drive, a DTC technique is also investigated.
- (4) MPC is investigated to control the MC. This scheme is used in an MC based microgrid. In the islanded mode, predictive voltage control is employed to regulate the MC output voltages to supply various loads. An improved VTR is observed. When the microgrid is connected to the utility grid, power flow is the main objective. The performance of the controller is tested under various conditions including input disturbance and different loads.
- (5) An MC prototype is built to support the research. The prototype hardware includes main circuit, drives, supplies, analog to digital conversion (ADC) conditioning circuits, and sensor board. The algorithm is implemented in Matlab Simulink with C2000

hardware support packages for TI DSP processors. Various experimental tests are carried out to support the proposed strategies.

1.3.2 Organization of Thesis

This thesis consists of eight chapters in total. This chapter introduces the MC, summarises the literature review and outlines the contributions and organization of the thesis. In Chapter 2, the fundamentals of a direct MC are introduced as a foundation for the work reported in this thesis. Chapter 3 presents the MC based UPFC. The MC is used to control the power flow in a transmission system. In Chapter 4, PI and PR controllers are proposed for the improvement of the steady-state tracking performance. These controllers are used to control the output current of a direct MC. In Chapter 5, the work on the MC fed AC motor drives is presented. Chapter 6 presents the predictive control based MC for microgrid applications.

References

- [1] M. Y. Lee, P. Wheeler, and C. Klumpner, "Space-vector modulated multilevel matrix converter," *IEEE Trans. Ind. Electron.*, vol. 57, no. 10, pp. 3385-3394, 2010.
- [2] L. Gyugi and B. Pelly, *Static Power Frequency Changers: Theory, Performance and Applications*. New York: Wiley, 1976.
- [3] A. Daniels and D. Slattery, "New power convertor technique employing power transistors," *Proc. IEE*, vol. 125, no. 2, pp. 146-150, Feb. 1978.
- [4] M. Venturini, A. Alesina. "The generalized transformer: A new bidirectional sinusoidal waveform frequency converter with continuously adjustable input power factor," *PESC'80 Power Electron. Specialists Conf.*, vol. 1, pp. 242-252, 1980.
- [5] M. Venturini, "A new sine wave in sine wave out, conversion technique which eliminates reactive elements," in *Proc. Powercon 7*, pp. E3/1-E3/15, 1980.
- [6] A. Alesina, and M. G. B. Venturini, "Analysis and design of optimum-amplitude nine-switch direct AC-AC converters," *IEEE Trans. Power Electron.*, vol. 4, no. 1, pp. 101-112, 1989.
- [7] L. Huber, D. Borojovic, "Space vector modulated three-phase to three-phase matrix converter with input power factor correction," *IEEE Trans. Ind. Applicat.*, vol. 31, no. 6, pp. 1234-1246, 1995.
- [8] L. Empringham, J. W. Kolar, J. Rodríguez, P. W. Wheeler, and J. C. Clare, "Technological issues and Ind. application of matrix converters: A review," *IEEE Trans. Ind. Electron.*, vol. 60, no. 10, pp. 4260-4271, 2013.
- [9] P. Wheeler, J. Rodríguez, Jon C. Clare, Lee Empringham, and Alejandro Weinstein. "Matrix converters: a technology review," *IEEE Trans. Ind. Electron.*, vol. 49, no. 2, pp. 276-288, 2002.

- [10] J. Itoh, A. Odaka, and I. Sato, "High efficiency power conversion using a matrix converter," *Fuji Electric Review*, vol. 50, no. 3, pp. 94-98, 2004.
- [11] A. Jahangiri, and A. Radan, "Indirect matrix converter with unity voltage transfer ratio for AC to AC power conversion," *Electric Power Systems Research*, 96, pp. 157-169, 2013.
- [12] Z. Luca, "Control of Matrix Converters," PhD dissertation, Department of electrical engineering, University of Bologna, Italy, 2007.
- [13] J. Chang, T. Sun, and A. Wang, "Highly compact AC-AC converter achieving a high voltage transfer ratio," *IEEE Trans. Ind. Electron.*, vol. 49, no. 2, pp. 345-352, 2002.
- [14] J. Oyama, T. Higuchi, E. Yamada, T. Koga, and T. Lipo, "New control strategy for matrix converter," 20th Annu. IEEE Power Electron. Specialists Conf., PESC'89, pp. 360-367, 1989.
- [15] J. Kolar, T. Friedli, J. Rodriguez, and P. Wheeler, "Review of three-phase PWM AC-AC converter topologies," *IEEE Trans. Ind. Electron.*, vol. 58, no.11, pp. 4988-5006, 2011.
- [16] P. Szczechniak, *Three-Phase AC-AC Power Converters Based on Matrix Converter Topology*, Springer London Heidelberg New York Dordrecht, 2012.
- [17] M. Raghuram, and A. Agarwal, "Simulation of single phase matrix converter as all in one converter," *IEEE Int. Conf. on Power Signals Control and Computations (EPSCICON)*, pp. 1-6., 2014.
- [18] Y. Kudoh, K. Mizutani, N. Otsuka, D. Ueda, S. Takahashi, M. Inamori, H. Yamagiwa et al, "Single to two-phase matrix converter using GaN-based monolithic bidirectional switch for driving symmetrical two-phase motor," *IEEE Energy Conversion Congress and Exposition (ECCE)*, 2014, pp. 3186-3191, 2014.
- [19] A. Iqbal, S. M. Ahmed, and H. Abu-Rub, "Space vector PWM technique for a three-to-five-phase matrix converter," *IEEE Trans. Ind. Appl.*, vol. 48, no. 2, pp. 697-707, 2012.
- [20] S. M. Ahmed, H. Abu-Rub, and Z. Salam, "Model predictive control of a direct three-to-seven phase matrix converter," *IEEE Energy Conversion Congress and Exposition (ECCE)*, 2014, pp. 1059-1063, 2014.
- [21] S. M. Ahmed, Z. Salam, and H. Abu-Rub, "An improved space vector modulation for a three-to-seven-phase matrix converter with reduced number of switching vectors," *IEEE Trans. Ind. Electron.*, vol. 62, no. 6, pp. 3327-3337, 2015.
- [22] K. Iimori, K. Shinohara, O. Tarumi, Z. Fu, and M. Muroya, "New current-controlled PWM rectifier-voltage source inverter without DC link components," *IEEE Power Conversion Conf.-Nagaoka*, vol. 2, pp. 783-786, 1997.
- [23] C. Klumpner, "A hybrid indirect matrix converter immune to unbalanced voltage supply, with reduced switching losses and improved voltage transfer ratio," 21st IEEE Applied Power Electron. Conf. Expo., APEC'06, pp. 1-7, 2006.
- [24] C. Klumpner, M. Lee, and P. Wheeler, "A new three-level sparse indirect matrix converter," *IECON-32nd Annu. Conf. on IEEE Ind. Electron.*, pp. 1902-1907, 2006.
- [25] Y. Deng, Y. Wang, K. H. Teo, and R. G. Harley, "Space Vector Modulation Method for Modular Multilevel Converters," *IECON*, 2014.

- [26] Y. Shi, X. Yang, Q. He, and Z. Wang, "Research on a novel capacitor clamped multilevel matrix converter," *IEEE Trans. Power Electron.*, vol. 20, no. 5, pp. 1055-1065, 2005.
- [27] M. Diaz, R. Cardenas, B. M. Espinoza, A. Mora, and F. Rojas, "A novel LVRT control strategy for Modular Multilevel Matrix Converter based high-power Wind Energy Conversion Systems," *IEEE 2015 Tenth Int. Conf. on Ecological Vehicles and Renewable Energies (EVER)*, pp. 1-11, 2015.
- [28] J. Rodriguez, M. Rivera, J. W. Kolar, and P. W. Wheeler, "A review of control and modulation methods for matrix converters," *IEEE Trans. Ind. Electron.*, vol. 59, no. 1, pp. 58-70, 2012.
- [29] M. Venturini, "A new sine wave in, sine wave out conversion technique eliminates reactive elements," *Proc. POWERCON*, pp. E3-1, 1980.
- [30] J. Zhang, H. Yang, T. Wang, L. Li, D. G. Dorrell, "Field-Oriented Control based on Hysteresis Band Current Controller for a Permanent Magnet Synchronous Motor driven by a Direct Matrix Converter," *IET Power Electronics*, vol. 11, no. 7, pp. 1277-1285, 2018.
- [31] J. Zhang, L. Li, L. Zhang, D. G. Dorrell, "Hysteresis Band Current Controller based Field-Oriented Control for an Induction Motor driven by a Direct Matrix Converter," *43rd Annual Conference of the IEEE Ind. Electron. Society (IECON 2017)*, Beijing, China, pp. 4633-4638, November 2017.
- [32] R. Vargas, U. Ammann, J. Rodríguez, and J. Pontt, "Predictive strategy to control common-mode voltage in loads fed by matrix converters," *IEEE Trans. Ind. Electron.*, vol. 55, no. 12, pp. 4372-4380, 2008.
- [33] J. Monteiro, J. F. Silva, S. F. Pinto, and J. Palma, "Linear and sliding-mode control design for matrix converter-based unified power flow controllers," *IEEE Trans. Power Electron.*, vol. 29, no. 7, pp. 3357-3367, 2014.
- [34] D. Casadei, G. Serra, A. Tani, "The use of matrix converters in direct torque control of induction machines," *IEEE Trans. Ind. Electron.*, vol. 48, no. 6, pp. 1057-1064, 2001.
- [35] H. Karaca, R. Akkaya, and H. Dogan, "A novel compensation method based on fuzzy logic control for matrix converter under distorted input voltage conditions," *18th IEEE Int. Conf. on Electrical Machines (ICEM)*, pp. 1-5, 2008.
- [36] P. Q. Dzung, "A new artificial neural network-Direct torque control for matrix converter fed three-phase induction motor," *IEEE Int. Conf. on Power Electron. and Drives Systems (PEDS)*, pp. 78-83, 2005.
- [37] J. Zhang, L. Li, D. G. Dorrell and Y. Guo, "A PI Controller with Current Feedforward to Improve the Steady-State Error Performance for the Current Controlled Direct Matrix Converter," *20th Int. Conf. on Electrical Machines and Systems (ICEMS 2017)*, Sydney, Australia, August 2017.
- [38] J. Zhang, L. Li, D. Dorrell and Y. Guo, "SVM based Proportional Resonant Current Controller with Selective Harmonics Compensation for Matrix Converter Systems," *20th Int. Conf. on Electrical Machines and Systems (ICEMS)*, Sydney, 2017.
- [39] D. Casadei, Domenico, G. Serra, A. Tani, and L. Zarri, "Matrix converter modulation strategies: a new general approach based on space-vector representation of the switch state," *IEEE Trans. Ind. Electron.*, vol. 49, no. 2, pp. 370-381, 2002.
- [40] Y. Yoon and S. K. Sul, "Carrier-based modulation technique for matrix converter," *IEEE Trans. Power Electron.*, vol. 21, no. 6, pp. 1691-1703, 2006.

- [41] P. C. Loh, R. Rong, F. Blaabjerg, and P. Wang, "Digital carrier modulation and sampling issues of matrix converters," *IEEE Trans. Power Electron.*, vol. 24, no. 7, pp. 1690–1700, 2009.
- [42] F. Gao, and M. R. Iravani, "Dynamic model of a space vector modulated matrix converter," *IEEE Trans. Power Del.*, vol. 22, no. 3, pp. 1696-1705, 2007.
- [43] T. Friedli, J. W. Kolar, J. Rodriguez, and P. W. Wheeler, "Comparative evaluation of three-phase AC–AC matrix converter and voltage DC-link back-to-back converter systems," *IEEE Trans. Ind. Electron.*, vol. 59, no. 12, pp. 4487-4510, 2012.
- [44] H. J. Cha, and P. N. Enjeti, "An approach to reduce common-mode voltage in matrix converter," *IEEE Trans. Ind. Appl.*, vol. 39, no. 4, pp. 1151-1159, 2003.
- [45] P. Nielsen, F. Blaabjerg, and J. K. Pedersen, "Space vector modulated matrix converter with minimized number of switchings and a feedforward compensation of input voltage unbalance," *IEEE Proceedings of the 1996 Int. Conf. on Power Electronics, Drives and Energy Systems for Industrial Growth*, vol. 2, pp. 833-839., 1996.
- [46] S. F. Pinto, and J. Fernando Silva, "Robust Sliding Mode Control of Matrix Converters with Unity Power Factor," *9th Int. Conf. on Power Electron. and Motor Control*, Kosice, PP. 157-162, 2000.
- [47] P. Mattavelli, L. Rossetto, G. Spiazzi, and P. Tenti, "General-purpose sliding-mode controller for DC/DC converter applications," *24th Annu. IEEE Specialists Conf. Power Electron.*, 1993, pp. 609-615, 1993.
- [48] S.-C. Tan, Y.-M. Lai and C. K. Tse, "General design issues of sliding-mode controllers in DC–DC converters," *IEEE Trans. Ind. Electron.*, vol. 55, no. 3, pp. 1160-1174, 2008.
- [49] S. Kouro, P. Cortés, R. Vargas, U. Ammann, and J. Rodríguez, "Model predictive control—A simple and powerful method to control power converters," *IEEE Trans. Ind. Electron*, vol. 56, no. 6, pp. 1826-18386, 2009.
- [50] P. Correa, J. Rodríguez, M. Rivera, J. R. Espinoza, and J. W. Kolar, "Predictive control of an indirect matrix converter," *IEEE Trans. Ind. Electron.*, vol. 56, no. 6, pp. 1847-1853, 2009.
- [51] M. Rivera, C. Rojas, J. Rodriguez, P. Wheeler, B. Wu, and J. Espinoza, "Predictive current control with input filter resonance mitigation for a direct matrix converter," *IEEE Trans. Power Electron.*, no. 99, 2011.
- [52] L. Wang, H. Dan, Y. Zhao, Q. Zhu, T. Peng, Y. Sun, and P. Wheeler, "A finite control set model predictive control method for matrix converter with zero common-mode voltage," *IEEE J. Emerging and Selected Topics in Power Electron.*, vol. 6, no. 1, pp. 327-338, 2018.
- [53] Y. Yan, J. Zhao, C. Xia, and T. Shi, "Direct torque control of matrix converter-fed permanent magnet synchronous motor drives based on master and slave vectors," *IET Power Electronics*, vol. 8, no. 2, pp.288-296, 2014.
- [54] K. B. Lee, and F. Blaabjerg, "Sensorless DTC-SVM for induction motor driven by a matrix converter using a parameter estimation strategy," *IEEE Trans. Ind. Electron.*, vol. 55, no. 2, pp. 512-521, 2008.
- [55] J. Zhang, L. Li, D. G. Dorrell, Y. Guo, "Direct Torque Control with a Modified Switching Table for a Direct Matrix Converter based AC Motor Drive System," *20th Int. Conf. on Electrical Machines and Systems (ICEMS 2017)*. Sydney, Australia, 2017.

- [56] P. Wheeler, J. Clare, and L. Empringham, "Enhancement of matrix converter output waveform quality using minimized commutation times," *IEEE Trans. Ind. Electron.*, vol. 51, no. 1, pp. 240-244, 2004.
- [57] M. Jussila, and H. Tuusa, "Comparison of direct and indirect matrix converters in induction motor drive," *IECON 2006-32nd Annu. Conf. on IEEE Ind. Electron.*, pp. 1621-1626, 2006.
- [58] M. Melaku, *Modelling stability analysis and control of a direct ac/ac matrix converter based systems*, Tennessee Technical University, US, 2011.
- [59] M. Imayavaramban, A. V. Krishna Chaithanya, and B. G. Fernandes, "Analysis and mathematical modelling of matrix converter for adjustable speed AC drives," *IEEE PES-PSCE'06.*, pp. 1113-1120, 2006.
- [60] R. Strzelecki, A. Noculak, H. Tunia, K. Sozanski, and Z. Fedyczak, "UPFC with matrix converter," *EPE conf.*, Graz, Austria, Sep. 2001.
- [61] B.-T. Ooi, and M. Kazerani, "Unified power flow controller based on matrix converter," *27th Annu. IEEE Power Electron. Specialists Conf. (PESC'96)*, pp. 502-507, 1996.
- [62] J. Monteiro, J. Fernando Silva, S. F. Pinto, and J. Palma, "Matrix converter-based unified power-flow controllers: Advanced direct power control method," *IEEE Trans. Power Del.*, vol. 26, no. 1, pp. 420-430. 2011.
- [63] J. Monteiro, J. Fernando Silva, J. Palma, and S. Pinto, "Unified Power Flow Controllers Without Energy Storage: Designing Power Controllers for the Matrix Converter Solution," *Energy Storage in the Emerging Era of Smart Grids*, INTECH Open Access Publisher, 2011.
- [64] P. Wheeler, P. Zanchetta, J. C. Clare, L. Empringham, M. Bland, and D. Katsis, "A utility power supply based on a four-output leg matrix converter," *IEEE Trans. Ind. Appl.* vol. 44, no. 1, pp. 174-186, 2008.
- [65] P. Zanchetta, P. W. Wheeler, J. C. Clare, M. Bland, L. Empringham, and D. Katsis, "Control design of a three-phase matrix-converter-based AC-AC mobile utility power supply," *IEEE Trans. Ind. Electron.*, vol. 55, no. 1, 209-217, 2008.
- [66] S. Arevalo, P. Zanchetta, P. W. Wheeler, A. Trentin, and L. Empringham, "Control and implementation of a matrix-converter-based AC ground power-supply unit for aircraft servicing," *IEEE Trans. on Ind. Electron.*, vol 57, no. 6, 2076-2084, 2010.
- [67] K. Inomata, H. Hara, S. Morimoto, J. Fujii, K. Takeda, and E. Yamamoto, "Application of modular matrix converter to wind turbine generator," *IEEE Int. Power Electron. Conf. (IPEC-Hiroshima, ECCE-ASIA)*, pp. 1654-1659, 2014.
- [68] D. G. Dorrell, "Understanding and modeling of matrix converters for application in renewable energy and micro grid applications," *IECON 2014-40th IEEE Annu. Conf. of the Ind. Electron. Society*, pp. 4409-4415, 2014.
- [69] H. J. Cha, and P. N. Enjeti, "A three-phase AC/AC high-frequency link matrix converter for VSCF applications," *IEEE 34th Annu. Power Electron. Specialist Conf. (PESC'03)*, 2003, vol. 4, pp. 1971-1976, 2003.
- [70] A. Escobar-Mejia, "Indirect Matrix Converter as Standard Power Electronic Interface," PhD diss., UNIVERSITY OF ARKANSAS, 2014.

- [71] H. She, H. Lin, B. He, X. Wang, L. Yue, and X. An, "Implementation of voltage-based commutation in space-vector-modulated matrix converter," *IEEE Trans. Ind. Electron.*, vol. 59, no. 1, pp. 154-166, 2012.
- [72] L. Wei, and T. A. Lipo, "A novel matrix converter topology with simple commutation," *IEEE Thirty-Sixth IAS Annu. Meeting Conf. Industry Applications Conf.*, vol. 3, pp. 1749-1754, 2001.
- [73] L. Huber and D. Borojevic, "Space vector modulator for forced commutated cycloconverters," *Ind. Applicat. Soc. Annu. Meeting Conf. Rec.*, pp. 871-876, 1989.
- [74] T. Friedli, S. D. Round, and J. W. Kolar, "A 100 kHz SiC sparse matrix converter," *IEEE Power Electron. Specialists Conf. (PESC 2007)*, pp. 2148-2154, 2007.
- [75] J. Schönberger, T. Friedli, S. D. Round, and J. W. Kolar, "An ultra sparse matrix converter with a novel active clamp circuit," *IEEE Power Conversion Conf.-Nagoya (PCC'07)*, pp. 784-791, 2007.
- [76] P. Wheeler, P., and D. Grant, "Optimized input filter design and low-loss switching techniques for a practical matrix converter," *IEE Proceedings-Electric Power Applications*, vol. 144, no. 1, pp. 53-60, 1997.
- [77] P. Himamshu, "Analysis and Comparison of Space Vector Modulation schemes for Three-Leg and Four-Leg Voltage Source inverters," *Master Thesis, Virginia Polytechnic Institute and State University, US*, May 1997.
- [78] D. Neacsu, "Space vector modulation-an introduction," *In IECON*, vol. 1, pp. 1583-1592. 2001.
- [79] H. Karaca, and R. Akkaya, "Control of Venturini method based matrix converter in input voltage variations." *In Proceedings of the Int. Multi Conf. of Engineers and Computer Scientists IMECS, Hong Kong*, vol. 2. 2009.

2 MATRIX CONVERTER FUNDAMENTALS

In this Chapter, the fundamentals of the matrix converter (MC) are introduced. Both indirect and direct space vector modulation (SVM) techniques are described. SVM is based on pulse width modulation (PWM) theory to synthesize the instantaneous space vector representation of the desired output voltages and input currents. It is a developed and commonly used control strategy for MCs and other converters. Then the four-step commutation technique is introduced followed by the clamp circuit to protect the MC from the harmful overvoltage.

2.1 Matrix Converter Basics

A three-phase direct MC is shown in Fig. 2.1. It consists of nine bidirectional semiconductor switches. The switch matrix is arranged so that any output can be connected to any input. The arrangement of these switches forms a 3×3 switch matrix as expressed by

$$\begin{bmatrix} v_a \\ v_b \\ v_c \end{bmatrix} = \begin{bmatrix} S_{Aa} & S_{Ba} & S_{Ca} \\ S_{Ab} & S_{Bb} & S_{Cb} \\ S_{Ac} & S_{Bc} & S_{Cc} \end{bmatrix} \begin{bmatrix} v_A \\ v_B \\ v_C \end{bmatrix} = S \begin{bmatrix} v_A \\ v_B \\ v_C \end{bmatrix} \quad (2.1)$$

$$\begin{bmatrix} i_A \\ i_B \\ i_C \end{bmatrix} = \begin{bmatrix} S_{Aa} & S_{Ab} & S_{Ac} \\ S_{Ba} & S_{Bb} & S_{Bc} \\ S_{Ca} & S_{Cb} & S_{Cc} \end{bmatrix} \begin{bmatrix} i_a \\ i_b \\ i_c \end{bmatrix} = S^T \begin{bmatrix} i_a \\ i_b \\ i_c \end{bmatrix} \quad (2.2)$$

$$\sum_{X=A,B,C} S_{Xx} = 1, (x = a, b, c) \quad (2.3)$$

where S and its transpose S^T are switch matrices. These can be used to control the MC output voltages and input currents. The elements S_{Xx} in the switch matrix can be assigned a value of one for the ON state and zero for the OFF state. As a result, there are $2^9 = 512$ switch combinations in total in a three-phase direct MC. Based on the measurement of v_A, B, C and i_a, b, c , the voltages and currents v_a, b, c and i_A, B, C can be calculated respectively, which will be used in the prediction models.

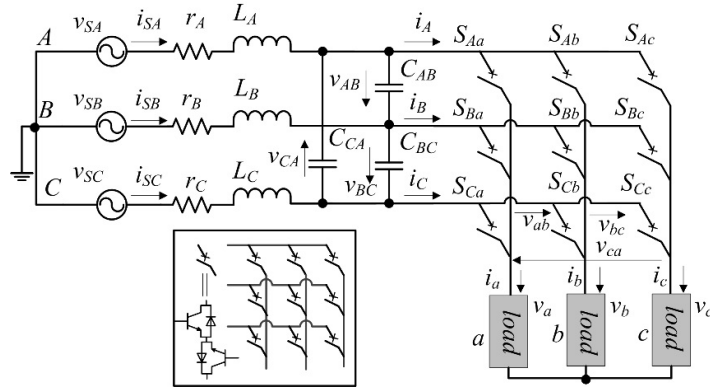


Fig. 2.1 A three-phase direct MC system with input filters.

The conditions (2.3) are used to exclude switch states that short-circuit the inputs (usually voltage sources) and open-circuit the outputs (usually inductive loads). Otherwise, overcurrent and overvoltage will be generated which can damage devices. Therefore, there are 27 switch states allowable in the matrix and they correspond to 27 control actions. This is a finite control set for the model predictive control.

2.2 SVM

SVM is a PWM technique for synthesizing the instantaneous space vector representation of the desired output voltages and input currents by selecting the

appropriate available input voltage and output current vectors [1]. There are two types of SVM for the MC; i.e., direct and indirect SVM.

2.2.1 Direct SVM

In SVM, the voltages and currents are expressed in space vector form. Consider the balanced three-phase input voltages applied to an MC:

$$\begin{aligned} v_A &= V_i \sin(\omega_i t) \\ v_B &= V_i \sin(\omega_i t - 2\pi/3) \\ v_C &= V_i \sin(\omega_i t + 2\pi/3) \end{aligned} \quad (2.4)$$

where V_i is the amplitude of input phase voltages and $\omega_i = 2\pi f_i$ is the input angular frequency. The MC output current can be expressed as

$$\begin{aligned} i_a &= I_o \sin(\omega_o t - \varphi_o) \\ i_b &= I_o \sin(\omega_o t - \varphi_o - 2\pi/3) \\ i_c &= I_o \sin(\omega_o t - \varphi_o + 2\pi/3) \end{aligned} \quad (2.5)$$

where I_o is the amplitude of output currents, $\omega_o = 2\pi f_o$ the output angular frequency and φ_o the angle difference between the output voltage and output current. The three-phase system can be expressed by space vectors by using the transformation:

$$x_s = \frac{2}{3} (x_1 + \alpha x_2 + \alpha^2 x_3) \quad (2.6)$$

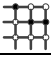
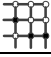
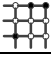
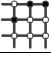
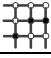
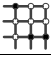
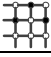
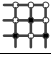
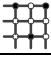
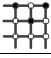
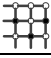
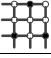
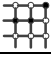
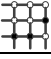
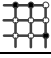
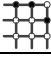
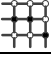

where $x_{1,2,3}$ are the variables in the three-phase system, $\alpha = e^{j(2\pi/3)}$, and x_s is the corresponding space vector after the transformation. The desired output voltages and input currents are

$$\begin{aligned} v_a &= V_o \sin(\omega_o t + \varphi) \\ v_b &= V_o \sin(\omega_o t + \varphi - 2\pi/3) \\ v_c &= V_o \sin(\omega_o t + \varphi + 2\pi/3) \end{aligned} \quad (2.7)$$

$$\begin{aligned} i_A &= I_i \sin(\omega_i t - \varphi_i) \\ i_B &= I_i \sin(\omega_i t - \varphi_i - 2\pi/3) \\ i_C &= I_i \sin(\omega_i t - \varphi_i + 2\pi/3) \end{aligned} \quad (2.8)$$

They are transformed using (2.6) to determine the location of the desired vectors at any instant. Here V_o and I_i are the amplitudes of the expected output voltages and input currents, φ_i the input power factor angle and φ the expected output voltage phase angle.

Table 2.1 Active states of MC switch states.

No.	Switch states	Output voltage vectors	Input current vectors	Group
+1		$V_{+1} = \frac{2}{\sqrt{3}} V_i \sin\left(\omega t + \frac{\pi}{6}\right) e^{j\omega t}$	$I_{+1} = \frac{2}{\sqrt{3}} I_o \sin(\omega_o t - \varphi_o) e^{j\omega_o t - \frac{\pi}{6}}$	active states
+2		$V_{+2} = \frac{2}{\sqrt{3}} V_i \sin\left(\omega t - \frac{\pi}{2}\right) e^{j\omega t}$	$I_{+2} = \frac{2}{\sqrt{3}} I_o \sin(\omega_o t - \varphi_o) e^{j\omega_o t - \frac{\pi}{2}}$	
+3		$V_{+3} = \frac{2}{\sqrt{3}} V_i \sin\left(\omega t + \frac{5\pi}{6}\right) e^{j\omega t}$	$I_{+3} = \frac{2}{\sqrt{3}} I_o \sin(\omega_o t - \varphi_o) e^{j\omega_o t - \frac{7\pi}{6}}$	
-1		$V_{-1} = -\frac{2}{\sqrt{3}} V_i \sin\left(\omega t + \frac{\pi}{6}\right) e^{j\omega t}$	$I_{-1} = -\frac{2}{\sqrt{3}} I_o \sin(\omega_o t - \varphi_o) e^{j\omega_o t - \frac{\pi}{6}}$	
-2		$V_{-2} = -\frac{2}{\sqrt{3}} V_i \sin\left(\omega t - \frac{\pi}{2}\right) e^{j\omega t}$	$I_{-2} = -\frac{2}{\sqrt{3}} I_o \sin(\omega_o t - \varphi_o) e^{j\omega_o t - \frac{\pi}{2}}$	
-3		$V_{-3} = -\frac{2}{\sqrt{3}} V_i \sin\left(\omega t + \frac{5\pi}{6}\right) e^{j\omega t}$	$I_{-3} = -\frac{2}{\sqrt{3}} I_o \sin(\omega_o t - \varphi_o) e^{j\omega_o t - \frac{7\pi}{6}}$	
+4		$V_{+4} = \frac{2}{\sqrt{3}} V_i \sin\left(\omega t + \frac{\pi}{6}\right) e^{j\frac{2\pi}{3}}$	$I_{+4} = \frac{2}{\sqrt{3}} I_o \sin\left(\omega_o t - \varphi_o - \frac{2\pi}{3}\right) e^{j\omega_o t - \frac{\pi}{6}}$	
+5		$V_{+5} = \frac{2}{\sqrt{3}} V_i \sin\left(\omega t - \frac{\pi}{2}\right) e^{j\frac{2\pi}{3}}$	$I_{+5} = \frac{2}{\sqrt{3}} I_o \sin\left(\omega_o t - \varphi_o - \frac{2\pi}{3}\right) e^{j\omega_o t - \frac{\pi}{2}}$	
+6		$V_{+6} = \frac{2}{\sqrt{3}} V_i \sin\left(\omega t + \frac{5\pi}{6}\right) e^{j\frac{2\pi}{3}}$	$I_{+6} = \frac{2}{\sqrt{3}} I_o \sin\left(\omega_o t - \varphi_o - \frac{2\pi}{3}\right) e^{j\omega_o t - \frac{7\pi}{6}}$	
-4		$V_{-4} = -\frac{2}{\sqrt{3}} V_i \sin\left(\omega t + \frac{\pi}{6}\right) e^{j\frac{2\pi}{3}}$	$I_{-4} = -\frac{2}{\sqrt{3}} I_o \sin\left(\omega_o t - \varphi_o - \frac{2\pi}{3}\right) e^{j\omega_o t - \frac{\pi}{6}}$	
-5		$V_{-5} = -\frac{2}{\sqrt{3}} V_i \sin\left(\omega t - \frac{\pi}{2}\right) e^{j\frac{2\pi}{3}}$	$I_{-5} = -\frac{2}{\sqrt{3}} I_o \sin\left(\omega_o t - \varphi_o - \frac{2\pi}{3}\right) e^{j\omega_o t - \frac{\pi}{2}}$	
-6		$V_{-6} = -\frac{2}{\sqrt{3}} V_i \sin\left(\omega t + \frac{5\pi}{6}\right) e^{j\frac{2\pi}{3}}$	$I_{-6} = -\frac{2}{\sqrt{3}} I_o \sin\left(\omega_o t - \varphi_o - \frac{2\pi}{3}\right) e^{j\omega_o t - \frac{7\pi}{6}}$	
+7		$V_{+7} = \frac{2}{\sqrt{3}} V_i \sin\left(\omega t + \frac{\pi}{6}\right) e^{j\frac{4\pi}{3}}$	$I_{+7} = \frac{2}{\sqrt{3}} I_o \sin\left(\omega_o t - \varphi_o + \frac{2\pi}{3}\right) e^{j\omega_o t - \frac{\pi}{6}}$	
+8		$V_{+8} = \frac{2}{\sqrt{3}} V_i \sin\left(\omega t - \frac{\pi}{2}\right) e^{j\frac{4\pi}{3}}$	$I_{+8} = \frac{2}{\sqrt{3}} I_o \sin\left(\omega_o t - \varphi_o + \frac{2\pi}{3}\right) e^{j\omega_o t - \frac{\pi}{2}}$	
+9		$V_{+9} = \frac{2}{\sqrt{3}} V_i \sin\left(\omega t + \frac{5\pi}{6}\right) e^{j\frac{4\pi}{3}}$	$I_{+9} = \frac{2}{\sqrt{3}} I_o \sin\left(\omega_o t - \varphi_o + \frac{2\pi}{3}\right) e^{j\omega_o t - \frac{7\pi}{6}}$	
-7		$V_{-7} = -\frac{2}{\sqrt{3}} V_i \sin\left(\omega t + \frac{\pi}{6}\right) e^{j\frac{4\pi}{3}}$	$I_{-7} = -\frac{2}{\sqrt{3}} I_o \sin\left(\omega_o t - \varphi_o + \frac{2\pi}{3}\right) e^{j\omega_o t - \frac{\pi}{6}}$	
-8		$V_{-8} = -\frac{2}{\sqrt{3}} V_i \sin\left(\omega t - \frac{\pi}{2}\right) e^{j\frac{4\pi}{3}}$	$I_{-8} = -\frac{2}{\sqrt{3}} I_o \sin\left(\omega_o t - \varphi_o + \frac{2\pi}{3}\right) e^{j\omega_o t - \frac{\pi}{2}}$	
-9		$V_{-9} = -\frac{2}{\sqrt{3}} V_i \sin\left(\omega t + \frac{5\pi}{6}\right) e^{j\frac{4\pi}{3}}$	$I_{-9} = -\frac{2}{\sqrt{3}} I_o \sin\left(\omega_o t - \varphi_o + \frac{2\pi}{3}\right) e^{j\omega_o t - \frac{7\pi}{6}}$	

As discussed previously, there are 27 switch combinations allowable in a three-phase direct MC. These combinations can establish different vectors and they can be classified into the following three groups, as shown in Tables 2.1 and 2.2.

Group I (Active vectors): two outputs are connected to the same input while the remaining output is connected to one of the other inputs. These 18 active vectors have

fixed direction, but their amplitudes vary with an instantaneous value equal to the input voltage.

Group II (Zero vectors): all three outputs are connected to the same input. These 3 vectors have zero amplitude and arbitrary directions.

Group III (Rotating vectors): all three outputs are connected to different inputs. These 6 rotating vectors rotate with fixed amplitudes.

Table 2.2 Zeros states and rotating states of MC switch states.

No.	Switch states	Output voltage vector	Input voltage vector	Group
01		$V_{01} = 0$	$I_{01} = 0$	zero states
02		$V_{02} = 0$	$I_{02} = 0$	
03		$V_{03} = 0$	$I_{03} = 0$	
r1		$V_{r1} = V_i e^{j \cdot \arctan(-\cot(\omega_i t))}$	$I_{r1} = I_o e^{j \cdot \arctan(-\cot(\omega_o t - \phi_o))}$	rotating states
r2		$V_{r2} = V_i e^{j \cdot \arctan(\cot(\omega_i t))}$	$I_{r2} = I_o e^{j \cdot \arctan(\cot(\omega_o t - \phi_o))}$	
r3		$V_{r3} = -V_i e^{j \cdot \arctan(\cot(\omega_i t + \frac{\pi}{3}))}$	$I_{r3} = -I_o e^{j \cdot \arctan(\cot(\omega_o t - \phi_o + \frac{\pi}{3}))}$	
r4		$V_{r4} = -V_i e^{j \cdot \arctan(-\cot(\omega_i t + \frac{\pi}{3}))}$	$I_{r4} = -I_o e^{j \cdot \arctan(-\cot(\omega_o t - \phi_o + \frac{\pi}{3}))}$	
r5		$V_{r5} = -V_i e^{j \cdot \arctan(\cot(\omega_i t + \frac{\pi}{3}))}$	$I_{r5} = -I_o e^{j \cdot \arctan(\cot(\omega_o t - \phi_o + \frac{\pi}{3}))}$	
r6		$V_{r6} = -V_i e^{j \cdot \arctan(-\cot(\omega_i t + \frac{\pi}{3}))}$	$I_{r6} = -I_o e^{j \cdot \arctan(-\cot(\omega_o t - \phi_o + \frac{\pi}{3}))}$	

In the Switch states column of Tables 2.1 and 2.2, a solid circle means the corresponding switches are turned on, for example, S_{Aa} , S_{Bb} and S_{Bc} are turned on in the case of switch No. +1. Among the 27 available states, only 21 states (18 active and 3 zero states) are considered useful in SVM to synthesize the desired output voltage vectors and input current vectors [2], which limits the flexibility. The rotating vectors cannot be usefully utilized since it is difficult to locate them. In contrast, all 27 states can be involved in model predictive control (MPC) [3], so the flexibility can be improved further using this simple control method. The active vectors are plotted in Fig. 2.2 and they form hexagons.

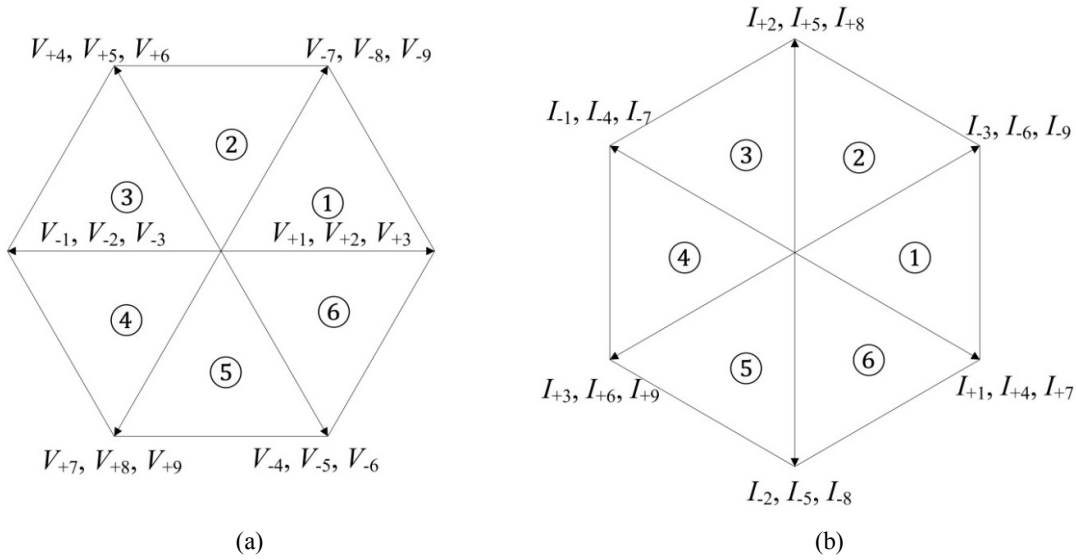
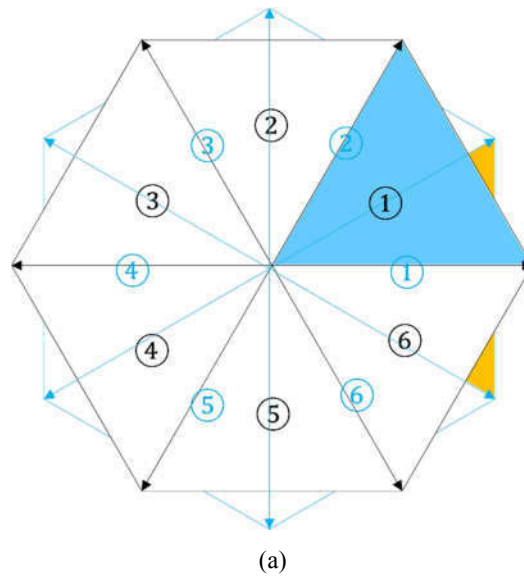


Fig. 2.2 Space vector hexagons for known input voltages and output currents.

Table 2.3 Look-up table of the vector combinations to synthesize the output voltage and input currents.

Sector number of the output voltage vector													
Sector number of input current vector	1, 4				2, 5				3, 6				
	1, 4	+9, +7, +3, +1			+6, +4, +9, +7				+3, +1, +6, +4				
	2, 5	+8, +9, +2, +3			+5, +6, +8, +9				+2, +3, +5, +6				
	3, 6	+7, +8, +1, +2			+4, +5, +7, +8				+1, +2, +4, +5				
Times		t_{x1}	t_{x2}	t_{y1}	t_{y2}	t_{x1}	t_{x2}	t_{y1}	t_{y2}	t_{x1}	t_{x2}	t_{y1}	t_{y2}



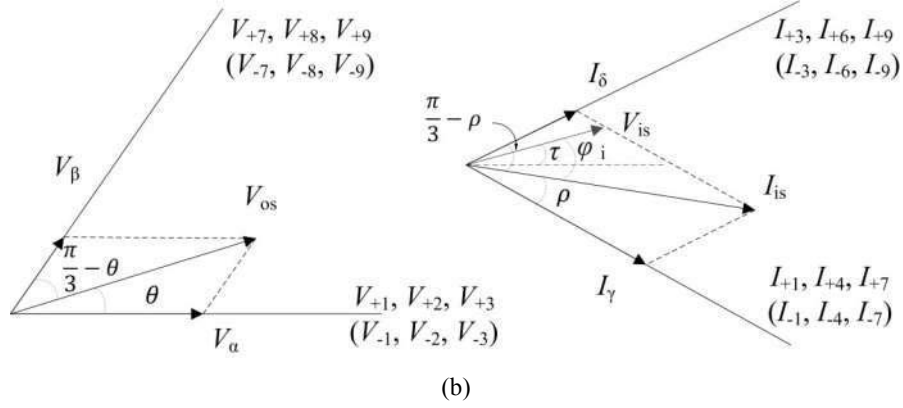


Fig. 2.3 Synthesis of the desired output voltage and input current vectors.

In an SVM scheme, the adjacent vectors nearest to the required vector are utilized to synthesize the required vectors. The use of non-adjacent vectors may produce higher total harmonic distortion (THD) and switching losses [4]. The chosen vectors must accomplish the synthesis of both output voltages (2.7) and input currents (2.8) at the same time, and they are summarized and tabulated in Table 2.3.

To explain the algorithm, without loss of generality, it is assumed that, at a given time instant, both the desired output voltage and input current vectors appear in sector ① of each hexagon shown in Fig. 2.3. The expected output voltage and input current space vectors can be decomposed into V_{α} and V_{β} , I_{γ} and I_{δ} respectively as shown in Fig. 2.3. Once the switch states are determined (Table 2.3), the corresponding working times for each switch are calculated. According to Figs. 2.2, 2.3 and Table 2.3, the working times for applied vectors are formulated as (more details can be found in Appendix A)

$$t_{x1} = (-1)^{m+n} \frac{2}{\sqrt{3}} T_s q \frac{\sin(\theta)\sin(\rho)}{\cos(\varphi_i)} \quad (2.9)$$

$$t_{x2} = (-1)^{m+n+1} \frac{2}{\sqrt{3}} T_s q \frac{\sin(\theta)\sin(\pi/3 - \rho)}{\cos(\varphi_i)} \quad (2.10)$$

$$t_{y1} = (-1)^{m+n+1} \frac{2}{\sqrt{3}} T_s q \frac{\sin(\pi/3 - \theta)\sin(\rho)}{\cos(\varphi_i)} \quad (2.11)$$

$$t_{y2} = (-1)^{m+n} \frac{2}{\sqrt{3}} T_s q \frac{\sin(\pi/3 - \theta)\sin(\pi/3 - \rho)}{\cos(\varphi_i)} \quad (2.12)$$

$$t_0 = T_s - (|t_{x1}| + |t_{x2}| + |t_{y1}| + |t_{y2}|) \quad (2.13)$$

$$q = \frac{V_o}{V_i} \leq \left| \frac{\sqrt{3}\cos(\varphi_i)}{2\sin(\theta + \pi/3)\sin(\rho + \pi/3)} \right| \quad (2.14)$$

where $0 \leq \theta \leq \pi/3$ is the angular difference between the desired output space vector V_{os} and its corresponding right-hand adjacent vector V_a . $0 \leq \rho \leq \pi/3$ is the angle between the desired input space vector I_{is} and its corresponding right-hand adjacent vector I_γ . t_{x1} , t_{x2} and t_{y1} , t_{y2} are working times for the selected vectors and T_s is the cycle period. m and n denote ($m, n = 1, 2, 3, 4, 5, 6$) the m^{th} output voltage vector sector and the n^{th} input current vector sector. If any of the working times are negative, then the corresponding negative vector should be selected instead of the assumed positive vector as shown in Table 2.3. Note that correct commutation techniques and switching sequences are necessary to improve waveforms quality and avoid contingencies caused by unexpected short or open circuits. However, they are not discussed here.

2.2.2 Indirect SVM

In indirect SVM, the virtual DC link, shown in Fig. 2.4, is used to divide the modulation into a voltage source rectifier (VSR) stage and a voltage source inverter (VSI) stage [5]. It is worth noting that the virtual DC link does not really exist in the MC. It is only used for explaining the modulation technique. By applying SVM to each stage, and then combining them, the overall indirect SVM is obtained.

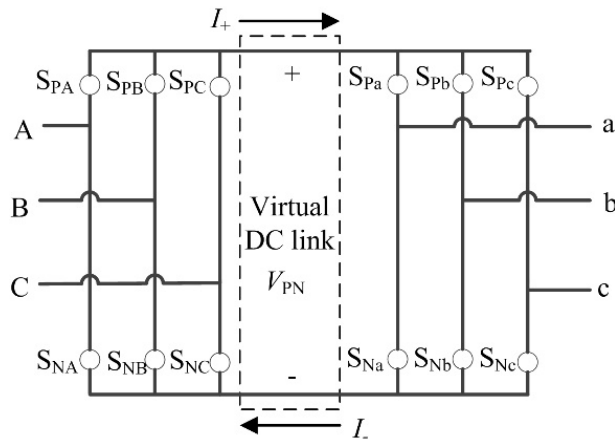


Fig. 2.4 Indirect SVM illustration with virtual DC link.

(a). SVM for the Virtual Rectifier

In the virtual VSR, the main objective is to synthesize the input currents. The input currents generated from the DC-link currents can be transformed into space vectors using (2.5). There are nine possible switch combinations, including 6 non-zero vectors and three zero vectors (Table 2.4), generated by the available current in the DC link. These switch combinations correspond to VSR current vectors as plotted in Fig. 2.5(a).

From Fig. 2.4, the input currents can be controlled by controlling the switch matrix:

$$\begin{bmatrix} i_A \\ i_B \\ i_C \end{bmatrix} = \begin{bmatrix} S_{PA} & S_{NA} \\ S_{PB} & S_{NB} \\ S_{PC} & S_{NC} \end{bmatrix} \begin{bmatrix} I_+ \\ I_- \end{bmatrix} \quad (2.15)$$

$$\begin{bmatrix} V_+ \\ V_- \end{bmatrix} = \begin{bmatrix} S_{PA} & S_{PB} & S_{PC} \\ S_{NA} & S_{NB} & S_{NC} \end{bmatrix} \begin{bmatrix} v_A \\ v_B \\ v_C \end{bmatrix} \quad (2.16)$$

In (2.15) and (2.16), each switch element can have two different values (1 for ON state and 0 for OFF state). In order to exclude the switch states that short circuit the input voltage sources, the constraints of $S_{PA}+S_{PB}+S_{PC} = 1$ and $S_{NA}+S_{NB}+S_{NC} = 1$ have to be applied; otherwise, an overcurrent will be generated at the input terminals.

Table 2.4 Possible switch combinations of the VSR.

No.	on-state switches	rectifier current vectors	DC voltages	group
R1	S_{PA}, S_{NC}	$I_{R1} = \frac{2\sqrt{3}}{3} I_+ e^{j\frac{\pi}{6}}$	$V_+ = V_A$ $V_- = V_C$	non zero
R2	S_{PB}, S_{NC}	$I_{R2} = \frac{2\sqrt{3}}{3} I_+ e^{j\frac{\pi}{2}}$	$V_+ = V_B$ $V_- = V_C$	
R3	S_{PB}, S_{NA}	$I_{R3} = \frac{2\sqrt{3}}{3} I_+ e^{j\frac{5\pi}{6}}$	$V_+ = V_B$ $V_- = V_A$	
R4	S_{PC}, S_{NA}	$I_{R4} = \frac{2\sqrt{3}}{3} I_+ e^{j\frac{7\pi}{6}}$	$V_+ = V_C$ $V_- = V_A$	
R5	S_{PC}, S_{NB}	$I_{R5} = \frac{2\sqrt{3}}{3} I_+ e^{j\frac{3\pi}{2}}$	$V_+ = V_C$ $V_- = V_B$	
R6	S_{PA}, S_{NB}	$I_{R6} = \frac{2\sqrt{3}}{3} I_+ e^{j\frac{11\pi}{6}}$	$V_+ = V_A$ $V_- = V_B$	
R7	S_{PA}, S_{NA}	$I_{R7} = 0$	$V_+ = V_A$ $V_- = V_A$	zero
R8	S_{PB}, S_{NB}	$I_{R8} = 0$	$V_+ = V_B$ $V_- = V_B$	
R9	S_{PC}, S_{NC}	$I_{R9} = 0$	$V_+ = V_C$ $V_- = V_C$	

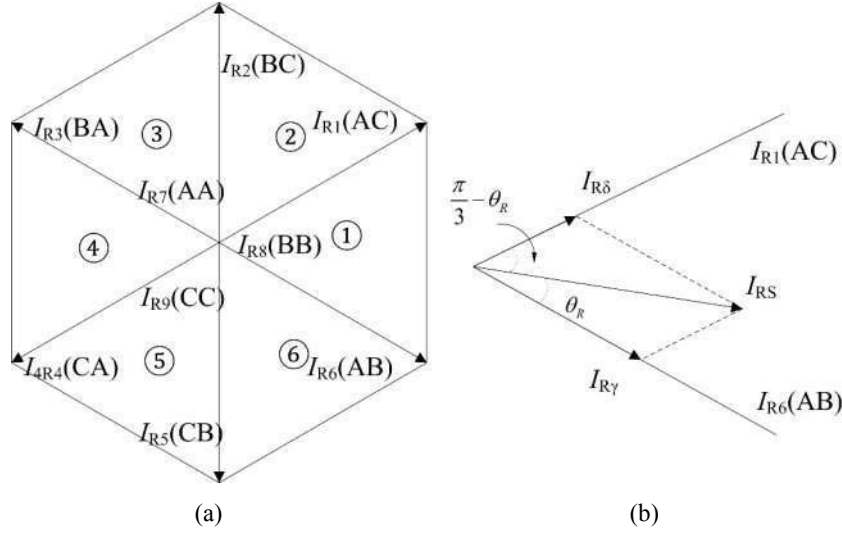


Fig. 2.5 (a) VSR current space vectors hexagon, (b) space vector synthesis.

The nine VSR current vectors described above are used to synthesize the desired input currents. The desired input current vectors are synthesized with a combination of these vectors depending on its sector location. In each sector, two adjacent non-zero vectors and one zero vector are used to synthesize the desired vector as shown in Fig. 2.5(b). For example, if the desired current vector is located in sector ①, then I_{R1} , I_{R6} and a zero vector will be selected in the corresponding switching cycle. The prescribed working time for each vector is calculated using

$$t_{R\gamma} = \frac{2}{\sqrt{3}} \frac{I_i}{I_+} \sin\left(\frac{\pi}{3} - \theta_R\right) T_s \quad (2.17)$$

$$t_{R\delta} = \frac{2}{\sqrt{3}} \frac{I_i}{I_+} \sin(\theta_R) T_s \quad (2.18)$$

$$t_{R0} = T_s - (t_{R\gamma} + t_{R\delta}) \quad (2.19)$$

$$m_i = \frac{2}{\sqrt{3}} \frac{I_i}{I_+} \quad (2.20)$$

where $t_{R\delta}$ and $t_{R\gamma}$ are the times for the application of non-zero vectors; t_{R0} is the time for the application of zero vectors; T_s is the switching period; and m_i is the VSR modulation index.

(b). SVM for the Virtual Inverter

In the virtual VSI, the control objective is to synthesize the output voltages. The output voltages generated from the DC-link voltages can be described as space vectors using (2.4). Eight vectors are obtained including six non-zero and two zero vectors. They are summarized in Table 2.5. These VSI voltage vectors form a hexagon as plotted in Fig. 2.6(a).

As shown in Fig. 2.4, the output voltages can be regulated by controlling the switch matrix in:

$$\begin{bmatrix} v_a \\ v_b \\ v_c \end{bmatrix} = \begin{bmatrix} S_{Pa} & S_{Na} \\ S_{Pb} & S_{Nb} \\ S_{Pc} & S_{Nc} \end{bmatrix} \begin{bmatrix} V_+ \\ V_- \end{bmatrix} \quad (2.21)$$

$$\begin{bmatrix} I_+ \\ I_- \end{bmatrix} = \begin{bmatrix} S_{Pa} & S_{Pb} & S_{Pc} \\ S_{Na} & S_{Nb} & S_{Nc} \end{bmatrix} \begin{bmatrix} i_a \\ i_b \\ i_c \end{bmatrix} \quad (2.22)$$

Here the constraints of $S_{Pa}+S_{Na} = 1$, $S_{Pb}+S_{Nb} = 1$ and $S_{Pc}+S_{Nc} = 1$, are applied to avoid the switch states that open-circuit the inductive loads; otherwise, overcurrent will be generated at the output terminals.

Table 2.5 Possible switch combinations of the VSI.

No.	on-state switches	inverter voltage vectors	DC currents	group
11	S_{Pa}, S_{Nb}, S_{Nc}	$V_{11} = \frac{2}{3} V_{PN} e^{j0}$	$I_s = I_a$ $I_z = I_b + I_c$	non zero
12	S_{Pa}, S_{Pb}, S_{Nc}	$V_{12} = \frac{2}{3} V_{PN} e^{j\frac{\pi}{3}}$	$I_s = I_a + I_b$ $I_z = I_c$	
13	S_{Na}, S_{Pb}, S_{Nc}	$V_{13} = \frac{2}{3} V_{PN} e^{j\frac{2\pi}{3}}$	$I_s = I_b$ $I_z = I_a + I_c$	
14	S_{Na}, S_{Pb}, S_{Pc}	$V_{14} = \frac{2}{3} V_{PN} e^{j\pi}$	$I_s = I_b + I_c$ $I_z = I_a$	
15	S_{Na}, S_{Nb}, S_{Pc}	$V_{15} = \frac{2}{3} V_{PN} e^{j\frac{4\pi}{3}}$	$I_s = I_c$ $I_z = I_a + I_b$	
16	S_{Pa}, S_{Nb}, S_{Pc}	$V_{16} = \frac{2}{3} V_{PN} e^{j\frac{5\pi}{3}}$	$I_s = I_a + I_c$ $I_z = I_b$	
17	S_{Na}, S_{Nb}, S_{Nc}	$V_{17} = 0$	$I_s = 0$ $I_z = 0$	zero
18	S_{Pa}, S_{Pb}, S_{Pc}	$V_{18} = 0$	$I_s = 0$ $I_z = 0$	

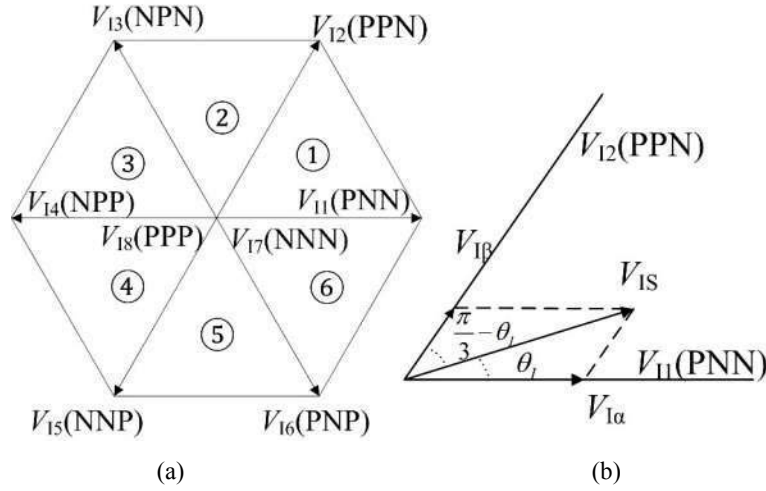


Fig. 2.6 (a) VSI current space vectors hexagon, (b) space vector synthesis.

The eight VSI voltage vectors are employed to synthesize the desired output voltage. In a similar manner to the VSR, the working times for the vectors are calculated using

$$t_{1\alpha} = \frac{2}{\sqrt{3}} \frac{V_o}{V_{PN}} \sin\left(\frac{\pi}{3} - \theta_i\right) T_s \quad (2.23)$$

$$t_{1\beta} = \frac{2}{\sqrt{3}} \frac{V_o}{V_{PN}} \sin(\theta_i) T_s \quad (2.24)$$

$$t_{10} = T_s - (t_{1\alpha} + t_{1\beta}) \quad (2.25)$$

$$m_v = \frac{2}{\sqrt{3}} \frac{V_o}{V_{PN}} \quad (2.26)$$

where $t_{1\alpha}$ and $t_{1\beta}$ are the times for the applications of non-zero vectors; t_{10} is the time for the application of zero vectors and m_v is the VSI modulation index. The selection of zero vectors in both SVMs should benefit the reduction of switching actions, thus switching losses.

(c). Overall Modulation

Combining the VSR and VSI stages, the overall SVM for the whole MC can be obtained. Based on (2.15), (2.16), (2.21) and (2.22), the switch matrix S can be derived as:

$$\begin{aligned}
 S &= \begin{bmatrix} S_{PA} & S_{NA} \\ S_{PB} & S_{NB} \\ S_{PC} & S_{NC} \end{bmatrix} \begin{bmatrix} S_{Pa} & S_{Pb} & S_{Pc} \\ S_{Na} & S_{Nb} & S_{Nc} \end{bmatrix} \\
 &= \begin{bmatrix} S_{PA}S_{Pa} + S_{NA}S_{Na} & S_{PA}S_{Pb} + S_{NA}S_{Nb} & S_{PA}S_{Pc} + S_{NA}S_{Nc} \\ S_{PB}S_{Pa} + S_{NB}S_{Na} & S_{PB}S_{Pb} + S_{NB}S_{Nb} & S_{PB}S_{Pc} + S_{NB}S_{Nc} \\ S_{PC}S_{Pa} + S_{NC}S_{Na} & S_{PC}S_{Pb} + S_{NC}S_{Nb} & S_{PC}S_{Pc} + S_{NC}S_{Nc} \end{bmatrix} \quad (2.27) \\
 &= \begin{bmatrix} S_{Aa} & S_{Ba} & S_{Ca} \\ S_{Ab} & S_{Bb} & S_{Cb} \\ S_{Ac} & S_{Bc} & S_{Cc} \end{bmatrix}
 \end{aligned}$$

$$\begin{bmatrix} v_a \\ v_b \\ v_c \end{bmatrix} = S \begin{bmatrix} v_A \\ v_B \\ v_C \end{bmatrix} \quad (2.28)$$

$$\begin{bmatrix} i_A \\ i_B \\ i_C \end{bmatrix} = S^T \begin{bmatrix} i_a \\ i_b \\ i_c \end{bmatrix} \quad (2.29)$$

where S_{ij} ($i = P, N, j = A, B, C, a, b, c$ or $i = A, B, C, j = a, b, c$) are the switches as shown in Figs. 2.1 and 2.4.

Every element in the 3 by 3 matrix in (2.27) corresponds to one switch in the MC. For example, the first element S_{Aa} indicates the connection of the input phase A to the output phase a . This is equivalent to the connection of A to a through (S_{PA} and S_{Pa}) or through (S_{NA} and S_{Na}), as shown in Fig. 2.4. Applying the same rule, the MC switch states can be determined. Hence the corresponding times $t_{\gamma\alpha}$, $t_{\delta\alpha}$, $t_{\gamma\beta}$, $t_{\delta\beta}$ and t_0 in the MC are given by

$$t_{\gamma\alpha} = t_{R\gamma} \cdot t_{I\alpha} = m \sin\left(\frac{\pi}{3} - \theta_R\right) \sin\left(\frac{\pi}{3} - \theta_I\right) \quad (2.30)$$

$$t_{\delta\alpha} = t_{R\delta} \cdot t_{I\alpha} = m \sin(\theta_R) \sin\left(\frac{\pi}{3} - \theta_I\right) \quad (2.31)$$

$$t_{\gamma\beta} = t_{R\gamma} \cdot t_{I\beta} = m \sin\left(\frac{\pi}{3} - \theta_R\right) \sin(\theta_I) \quad (2.32)$$

$$t_{\delta\beta} = t_{R\delta} \cdot t_{I\beta} = m \sin(\theta_R) \sin(\theta_I) \quad (2.33)$$

$$t_0 = T_s - (t_{\gamma\alpha} + t_{\delta\alpha} + t_{\gamma\beta} + t_{\delta\beta}) \quad (2.34)$$

where $0 \leq \theta_R (\theta_I) \leq \pi/3$ is the angle between the desired space vector $I_{RS} (V_{IS})$ and the right-hand adjacent vector $I_{Ry} (V_{I\alpha})$; $m = m_i \times m_v$ is the modulation index and T_s is the cycle period. Therefore, the input currents and output voltages of the MC can be controlled.

2.3 Commutation Techniques

For the safe operation of an MC, the issue of commutating the current path between the bidirectional switches should be considered. As presented earlier, the constraint (2.3) has to be applied in an MC to prevent overvoltage and overcurrent. However, this constraint can be violated during the transitioning from one switch state to another in practical systems. To demonstrate current commutation in an MC, it is sufficient to consider a two-phase to single-phase converter, as shown in Fig. 2.7. The commutation rules explained below apply to all scenarios of the three-phase MC.

As an example, consider the case where the input phase A is supplying current to the load connected to the output phase a , as shown in Fig. 2.7(a). The switches S_{Aa1} and S_{Aa2} are turned on while S_{Aa2} is not conducting the current. The switches S_{Ba1} and S_{Ba2} are turned off. If a command to change the connection to input phase B is requested, the connection shown in Fig. 2.7(b) should be achieved. Without a proper commutation strategy, the short circuit at the input terminal or the open circuit at the output terminal will occur. These will result in overcurrent and overvoltage that can cause switch breakdown, since the input sources are usually voltage sources and the loads are usually inductive loads.

To change the current path, assume the switches S_{Ba1} and S_{Ba2} are turned on first, a short-circuit path appears between input phase A and B . An overcurrent will be generated. In comparison, if the switches S_{Aa1} and S_{Aa2} are turned off first, the load current path is cut off, which leads to an overvoltage. Therefore, an appropriate commutation strategy should be designed and applied.

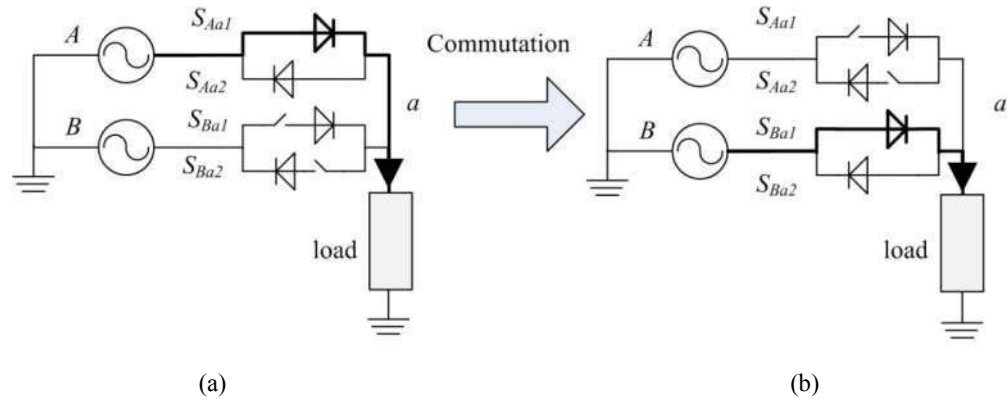


Fig. 2.7 Demonstration of commutation of current paths.

The commutation in an inverter is normally achieved by applying a dead time between the switching of devices in each output leg; however, this is not available in an MC. There is no freewheeling path in MCs; therefore, the current commutation becomes a difficult task [6]. The commutation in MCs can be implemented based on the relative value of input voltages or the direction of output currents. To avoid a short circuit at the input side and open circuit at the output side, an appropriate commutation scheme should be employed. If the commutation time can be reduced, the power quality of output waveform can be improved [7]. An appropriate commutation strategy can reduce the switching losses and improve the efficiency.

Bidirectional switches make it possible to commute from one phase to another without causing overcurrent from short-circuiting the input lines or causing overvoltage from open-circuiting output lines in an MC. Various commutation approaches have been designed by researchers [7]-[10]. The current-direction-based commutation strategy needs to detect the direction of output currents. This is usually difficult because of the uncertainties, especially during the zero crossings. In terms of voltage-based commutation, the relative amplitude of input voltages is needed to determine the switching states [8]. Incorrect information about the output current direction and relative magnitude of the input voltage can lead to wrong switch actions that can generate harmful overvoltage or overcurrent. The hybrid commutation approach requires both output current and input voltage information, which obviously demands more measurement devices.

The output-current-based commutation method has an obvious advantage over the input-voltage-based commutation strategy. The required commutation time in output-current-based commutation is considerably lower than that in input-voltage-based commutation. This is because turning on the incoming device is faster than turning off the outgoing device. The four-step, three-step, two-step and single-step commutation methods based on the input voltage magnitude and the output current direction are explained in [7]. Here the current-direction-based four-step commutation is explained.

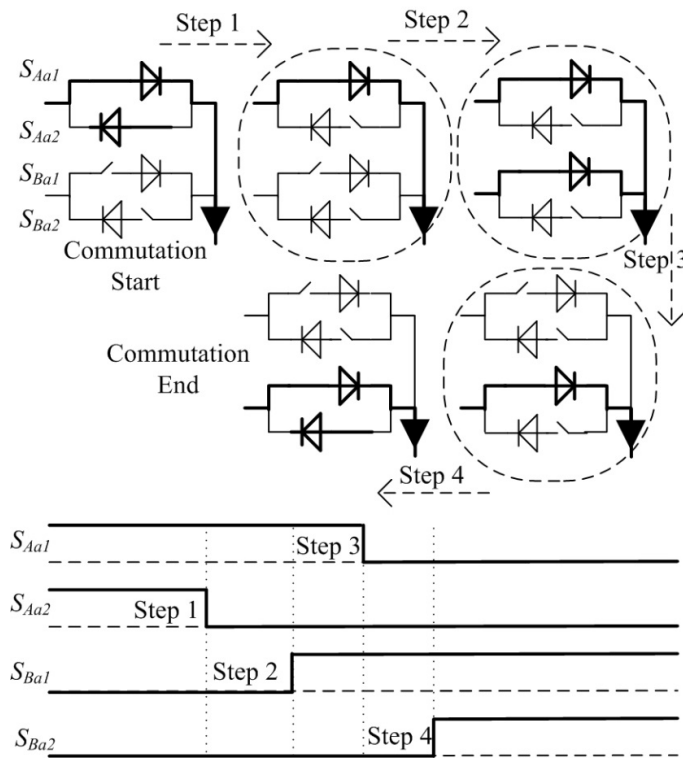


Fig. 2.8 Illustration diagram of the four-step commutation when load current is positive.

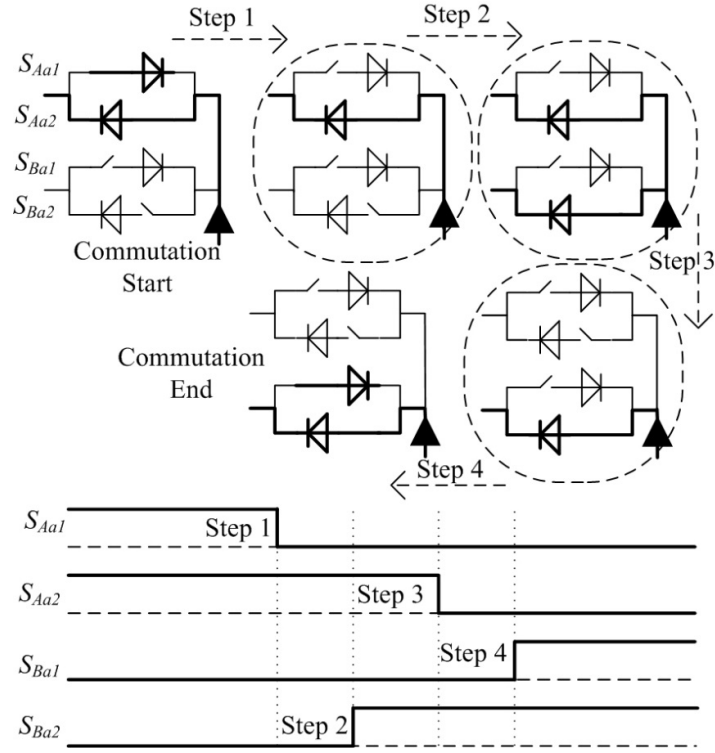


Fig. 2.9 Illustration diagram of the four-step commutation when load current is negative.

As shown in Fig. 2.8, if the load current is positive as indicated by the arrow in the current path, four-step commutation is performed as follows. Step 1: switch S_{Aa2} is turned off first. The current path is not cut off since S_{Aa2} does not conduct current at this moment. Step 2: switch S_{Ba1} is turned on. This does not produce the short-circuit current path because both S_{Aa1} and S_{Ba1} conduct current in the same direction. Step 3: switch S_{Aa1} is turned off. By doing this, the current path changes from phase A to B . The current path is maintained. Step 4: switch S_{Ba2} is finally turned on. Bidirectional capability is maintained. The timing diagram for these steps is shown at the bottom of Fig. 2.8.

Similarly, if the current direction is reversed as shown in Fig. 2.9. The four steps to perform the commutation are as follows. Step 1: switch S_{Aa1} is turned off first. Step 2: switch S_{Ba2} is turned on. Step 3: switch S_{Aa2} is turned off. Step 4: switch S_{Ba1} is finally turned on. The timing diagram is shown at the bottom of Fig. 2.9.

As mentioned earlier, output-current-direction-based commutation can reduce the commutation time. Ideally, the commutation time can be reduced to zero. As a result, four-step commutation can be amended to two-step commutation. This is achieved by

combining steps 1 and 2 into one step and combining steps 3 and 4 into the other step. This is because turning on the incoming device is faster than turning off the outgoing device. However, this disables the bidirectional path of the switch in steady state.

2.4 Clamp Circuit

A detrimental overvoltage can be generated at the output terminal by a control malfunction, commutation failure, switch breakdown or intentional emergency shut-down of the converter. A diode clamp circuit is usually used in the MC to protect the switches from the destructive overvoltage. A typical clamp circuit used in the direct MC to protect the devices from the harmful overvoltage is shown in Fig. 2.10. This clamp circuit is simple, and it consists of two diode bridge rectifiers that are connected in a back-to-back structure, and a capacitor and resistor. The diodes are fast-recovery diodes. The capacitor is used to absorb energy caused by the overvoltage and the resistor is used to discharge the capacitor. A parameter design of the clamp circuit can be found in [11].

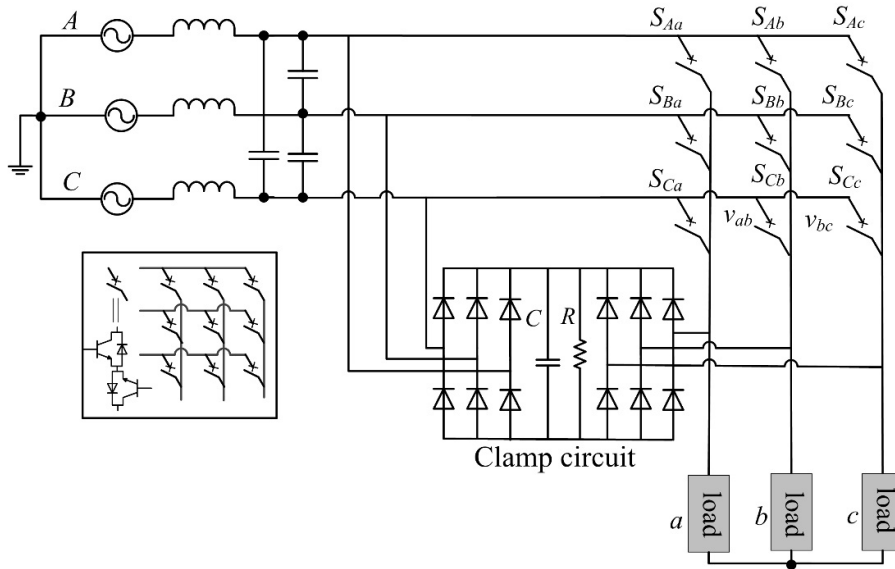


Fig. 2.10 The diode clamp protection circuit in the MC.

Under normal conditions, the amplitude of the output voltage is lower than the input voltage in the MC. Therefore, only the left-hand-side rectifier works while the right-hand-side rectifier is blocked. However, if overvoltage is generated at the output

terminal, the right-hand-side rectifier will work while the other rectifier is blocked. A freewheeling path is provided via the rectifier. Therefore, the energy at the output side can be absorbed by the capacitor. Once the overvoltage disappears, the capacitor discharges through the resistor, and then the clamp circuit works under normal conditions.

2.5 Summary

This chapter introduces the basic operation of the MC including switch matrices, direct and indirect SVMs, the four-step commutation technique and the clamp circuit. Direct and indirect SVM have very similar performance while the direct SVM provides a better understanding of MC principles. For safe operation, a commutation technique and protection devices are necessary. These operating principles will be used in the following chapters for the controller implementation and hardware development.

References

- [1] J. Zhang, L. Li, and D. G. Dorrell, "DQ Coupling Suppressed PID Controller for the Transmission Line Power Flow Control Using a Matrix Converter," *IEEE Ind. Electron. Soc. Annu. Meeting (IECON16)*, Florence, Italy, pp. 6249 – 6254, October 2016.
- [2] J. Kolar, T. Friedli, J. Rodriguez, and P. Wheeler, "Review of three-phase PWM AC–AC converter topologies," *IEEE Trans. Ind. Electron.*, vol. 58, no.11, pp. 4988-5006, 2011.
- [3] S. Kouro, P. Cortés, R. Vargas, U. Ammann, and J. Rodríguez, "Model predictive control—A simple and powerful method to control power converters," *IEEE Trans. Ind. Electron.*, vol. 56, no. 6, pp. 1826-1838, 2009.
- [4] V. Prasad, "Analysis and Comparison of Space Vector Modulation schemes for Three-Leg and Four-Leg Voltage Source inverters," *Master Thesis, Virginia Polytechnic Institute and State University*, 1997.
- [5] L. Huber, D. Borjovic, "Space vector modulated three-phase to three-phase matrix converter with input power factor correction," *IEEE Trans. Ind. Applicat.*, vol. 31, no. 6, pp. 1234-1246, 1995.
- [6] Z. Luca, "Control of Matrix Converters," PhD dissertation, Department of electrical engineering, University of Bologna, Italy, 2007.
- [7] P. Wheeler, J. Clare, and L. Empringham, "Enhancement of matrix converter output waveform quality using minimized commutation times," *IEEE Trans. Ind. Electron.*, vol. 51, no. 1, pp. 240-244, 2004.

- [8] H. She, H. Lin, B. He, X. Wang, L. Yue, and X. An, "Implementation of voltage-based commutation in space-vector-modulated matrix converter," *IEEE Trans. Ind. Electron.*, vol. 59, no. 1, pp. 154-166, 2012.
- [9] J. Mahlein, J. Igney, J. Weigold, M. Braun, and O. Simon, "Matrix converter commutation strategies with and without explicit input voltage sign measurement," *IEEE Trans. Ind. Electron.*, vol. 49, no. 2, pp. 407-414, 2002.
- [10] P. W. Wheeler, J. C. Clare, L. Empringharn, M. Bland, and M. Apap, "Gate drive level intelligence and current sensing for matrix converter current commutation," *IEEE Trans. Ind. Electron.*, vol. 49, no. 2, pp. 382-389, 2002.
- [11] P. Nielsen, F. Blaabjerg, and J. K. Pedersen, "New protection issues of a matrix converter: Design considerations for adjustable-speed drives," *IEEE Trans. Ind. Appl.*, vol. 35, no. 5, 1150-1161, 1999.

3 D-Q COUPLING CONTROL FOR POWER FLOW CONTROL

Flexible alternating current transmission system (FACTS) devices are essential components of a modern transmission system. They can enhance the controllability and elevate the transfer capacity of an electrical network. The unified power flow controller (UPFC) is known as the most versatile device in the FACTS family. This chapter studies a matrix converter (MC) based UPFC (MC-UPFC) structure to regulate active and reactive power in a transmission system. In contrast to the conventional UPFC, there is no requirement for an energy storage element in this structure. This results in various benefits including: decreased system volume, improved efficiency, prolonged lifetime, reduced maintenance and removal of the DC-link control. The controllable regions are analyzed and graphically obtained for the MC-UPFC, which facilitates the selection of correct UPFC ratings. The working principles and a model of the MC-UPFC are put forward and discussed. Direct space vector modulation (SVM), as explained in Chapter 2, is used here. Using SVM, PID controllers are developed to control power flow in a double-line transmission system. In addition, decoupling controllers are derived by feeding back the coupling components into controllers. Numerical simulation results for a double-line transmission system corroborate the feasibility and effectiveness of the control.

3.1 Introduction

FACTS devices are able to control power flow efficiently, enhance system reliability, mitigate congestion and increase transmission capacity. This can alleviate the problem of continuously increasing electricity demand and provide potential solutions to multi-objective problems in modern power industries [1, 2]. A UPFC uses power electronic technology to control transmission system parameters, such as voltage amplitude, phase angle and line equivalent impedance, either simultaneously or selectively [3]. It has been recognized as the most versatile FACTS device [4, 5]. Unlike other FACTS devices, a UPFC can control active and reactive power, or adjust system parameters by injecting a series voltage with the desired amplitude and phase angle into the transmission line. The theoretical transmission capacity potential can be realized, thus increasing the practical capacity of existing systems with an essential stability level. System stability can be enhanced by injecting or compensating the required active and reactive power. The UPFC was designed to solve power delivery problems, such as real-time control, dynamic compensation, and multifunctional flexibility [6]. Current active research on the UPFC mainly addresses new controller design [1], optimal location and size determination [7, 8], impacts on system devices [9], and new topology development such as transformerless UPFCs [10, 11] and MC-UPFCs [12-14]. A back-to-back converter is the core of UPFC and its linear operating regions have been evaluated recently in [15]. The MC-UPFC is a promising technology and more work is needed for its development.

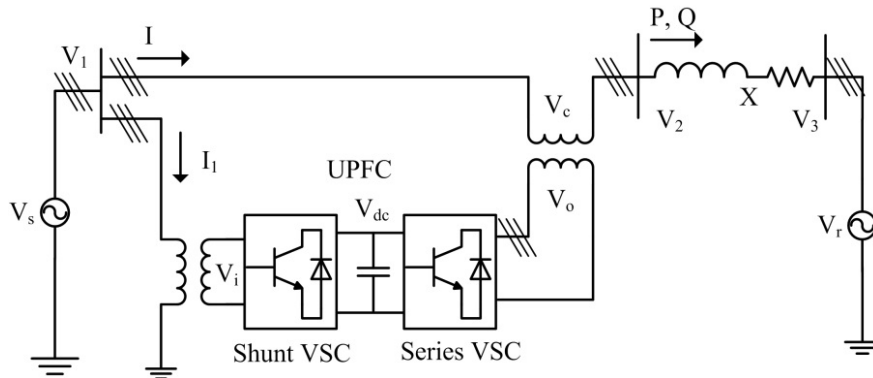


Fig. 3.1 Conventional UPFC system in a transmission line.

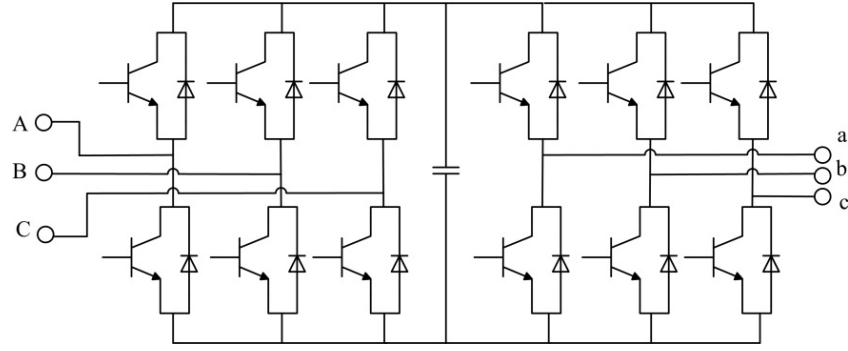


Fig. 3.2 Back-to-back converter topology in the UPFC.

The traditional UPFC system in a transmission line is shown in Fig. 3.1. It employs a back-to-back converter (as shown in Fig. 3.2.) which can fulfill indirect AC-to-AC conversion (AC/DC/AC). This structure usually consists of two voltage source converters (VSCs): a shunt VSC, which acts as a static synchronous compensator (STATCOM); and a series VSC, which acts as a static synchronous series compensator (SSSC). They are back-to-back connected with a capacitor across the DC link for energy storage. The STATCOM is connected in parallel with the transmission line by a transformer and it can work as a controllable current source, thus giving dynamic compensation of the reactive power. The SSSC is connected in series with the system and it can generate a series voltage with controlled amplitude and phase angle in order to adjust the system parameters, thereby facilitating active power exchange between the transmission line buses and the control of reactive power. Therefore, the power transfer capacity of a transmission line can be controlled in a flexible manner. However, the capacitor in the conventional UPFC introduces extra losses, increases the weight and volume, requires DC voltage control and deteriorates with time [16]. Work has been carried out aimed at the removal of the DC-link capacitor [17]. However, the DC link still exists resulting in the requirement for DC voltage control.

Energy storage elements are not required in the MC, as illustrated in Fig. 3.3 (simplified from Fig. 1.2). This arrangement has attracted research because of its compact configuration, bidirectional power-flow capability, high efficiency, controllable input power factor, and longer life cycle [18]. The MC gives direct AC-to-AC conversion and it can be regarded as a competitive alternative to the back-to-back converter in various applications [19]. In fact, the MC and its derivatives have found applications [20-22], and they are especially attractive for applications where the system volume is a

significant issue, e.g., in aerospace applications [23]. There are examples of the industrial application of MCs. Several manufacturers, such as Yaskawa [24], Eupec [18][25] and Fuji [26], have produced commercial MC modules and products. For the Yaskawa MX1S series of MCs, the nominal power capacity can reach 6 MVA. Hence, the MC is a promising candidate for industrial applications such as motor drives, interfacing different systems, microgrid and power flow control.

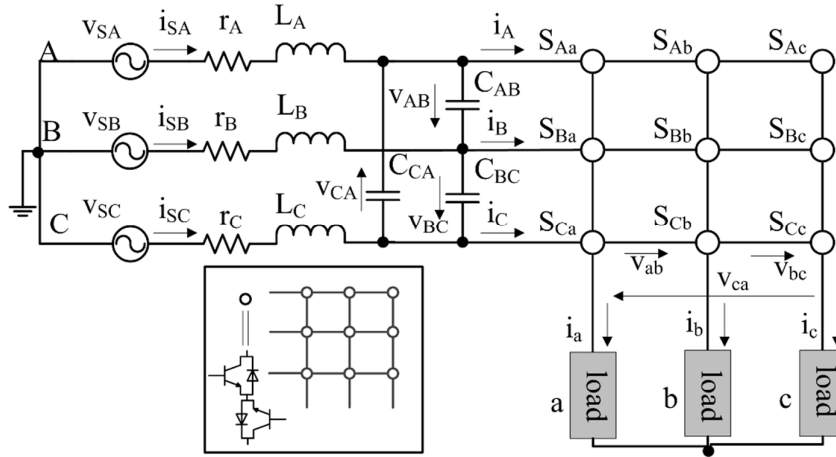


Fig. 3.3 The MC system with the input filters and loads.

Since the concept of MC-UPFC was reported in [27], further work has developed the understanding of its controller. Although existing literature is limited, they have adequately demonstrated the ability of the MC to work as a power flow controller [28]. A two-stage control design is needed in this application; the first stage is the MC modulation and the second stage is power flow control. These stages are closely related to the controllable system regions. In terms of the first stage, SVM [29] can make the best use of the input voltage while reducing the number of commutations, controlling the input power factor independently and providing better power quality; therefore, this work adopts direct SVM for the MC modulation. Regarding the MC-UPFC, one significant contribution is from [16], in which a direct power controller was designed, and good results were obtained, although the controller is complex due to the nonlinear sliding mode controller involved in the control scheme. A complex vector synchronous frame PI current regulator was proposed in [30] in order to improve the transient response, which is limited in traditional PI current controllers due to its dependence on

system synchronous frequency. The obtained results showed that the overshoot is restrained, and the transient response is slightly improved. Nevertheless there is increased complexity because six PI controllers have to be employed in the controller design. None of these studies has investigated the controllable power regions for the MC-UPFC. In this chapter, controllable regions are analyzed for the MC-UPFC, and then a simple decoupling controller scheme involving only two PID controllers is designed for controlling active and reactive power flow in a MC-UPFC.

The main contributions of the work in this chapter include: (1) the full controllable regions of transmission system without and with MC-UPFC are analyzed, and the source contributions to the power controllability are investigated; (2) effective and simple PID controllers are developed using SVM for controlling the power flow in a transmission system; and (3) this work presents a method for closed-loop controller design for the MC-UPFC. This chapter is organized as follows. In Section 3.2, power-flow control theory and complete controllable power-flow regions are detailed. Section 3.3 illustrates the PID controller design. Simulation results are presented in Section 3.4 followed by the summary in Section 3.5.

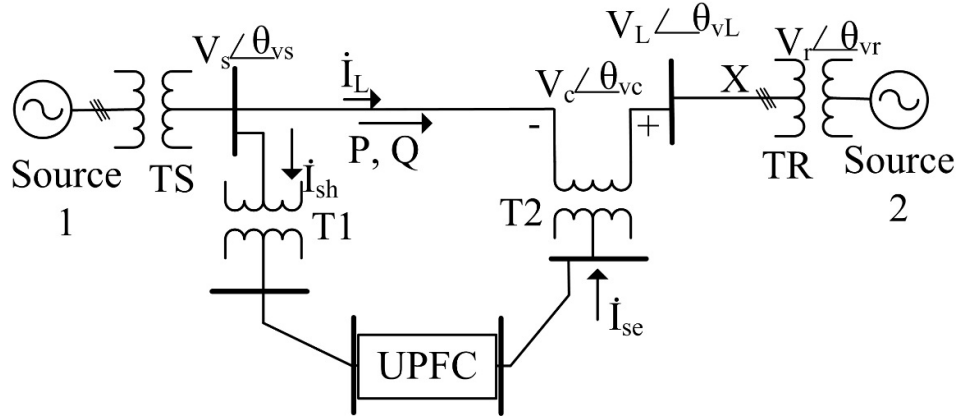


Fig. 3.4 Diagram for UPFC power-flow control.

3.2 Power Flow Control Theory and Controllable Regions Analysis

3.2.1 Power Flow Control Theory

The UPFC, when deployed in a transmission system, is shown in Fig. 3.4 and the complex power \dot{S} through the transmission line X can be expressed as

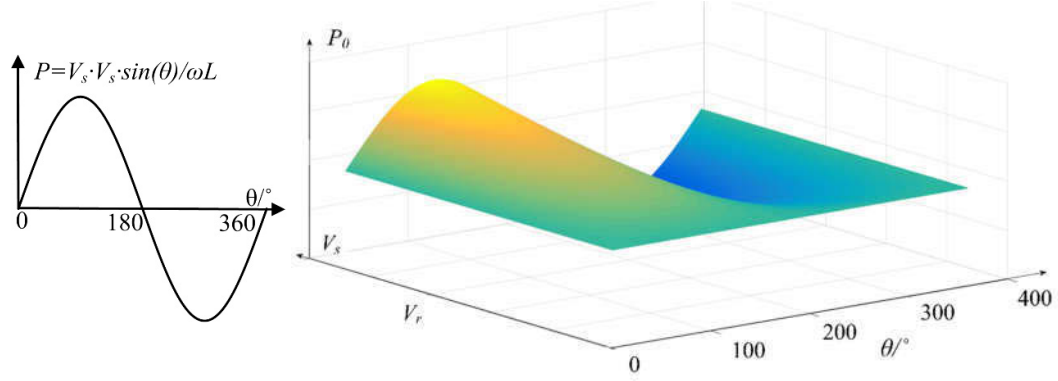
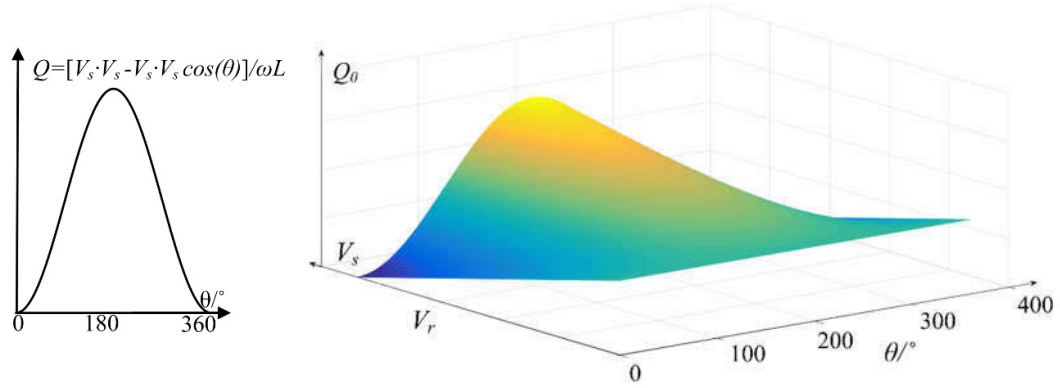
$$\dot{S} = P + jQ = \dot{V}_L \left(\frac{\dot{V}_L - \dot{V}_r}{Z} \right)^* \quad (3.1)$$

where $Z = R_L + j\omega L_L$ ($\omega = 2\pi f$ is the angular frequency, R_L and L_L the resistance and inductance respectively) is the transmission line impedance. The resistance can be neglected for high voltage applications because the ratio of ωL_L to R_L is sufficiently large [31]. Here V^* denotes the conjugate of phasor V , and the phasors $V_L = V_s + V_c$ and V_r are shown in the Fig. 3.4.

From Fig. 3.4, if the compensation voltage from the UPFC is zero, i.e., $V_c = 0$, then the result is $V_s = V_L$, and (3.1) becomes

$$P_0 + jQ_0 = \dot{V}_s \left(\frac{\dot{V}_s - \dot{V}_r}{j\omega L} \right)^* = \frac{V_s V_r \sin \theta}{\omega L} + j \frac{V_s (V_s - V_r \cos \theta)}{\omega L} \quad (3.2)$$

where $\theta = \theta_{vs} - \theta_{vr}$ is the transmission angle of the system, being the phase difference between the sending and receiving end voltages. According to (3.2), with an assumption of $V_r \leq V_s$, the system power operating regions can be obtained for different amplitudes ($0 \sim V_s$) and phase angles ($0 \sim 360^\circ$) of the receiving end voltage. They are shown in Figs. 3.5 and 3.6, from which we can see that the mesh cross sections with $V_r = V_s$ will result in typical system power curves as displayed on the left-hand sides of the figures.


 Fig. 3.5 Transmission system inherent active power curves versus V_r and θ .

 Fig. 3.6 Transmission system inherent reactive power curves versus V_r and θ .

Similarly, when the injected voltage $V_c \neq 0$, the transmission line active and reactive power before the compensation point are obtained from

$$\begin{aligned}
 P + jQ &= \dot{V}_s \dot{I}_L^* = \dot{V}_s \left(\frac{\dot{V}_s + \dot{V}_c - \dot{V}_r}{j\omega L} \right)^* \\
 &= \frac{1}{\omega L} \left\{ \left[V_s V_r \sin \theta + j(V_s^2 - V_s V_r \cos \theta) \right] + \left[V_c V_s \sin(\theta_{vc} - \theta_{vs}) + jV_c V_s \cos(\theta_{vc} - \theta_{vs}) \right] \right\} \\
 &= (P_0 + jQ_0) + (\Delta P_1 + j\Delta Q_1)
 \end{aligned} \tag{3.3}$$

According to (3.3), the active and reactive power through the lines are divided into the uncontrollable part (3.2) and the controllable part (P_1 and Q_1). By controlling the amplitude and phase angle of V_c , the active and reactive power through the transmission

line can be regulated. In steady state, the MC-UPFC does not consume any real power, except the losses. DC-link losses do not exist in the MC-UPFC.

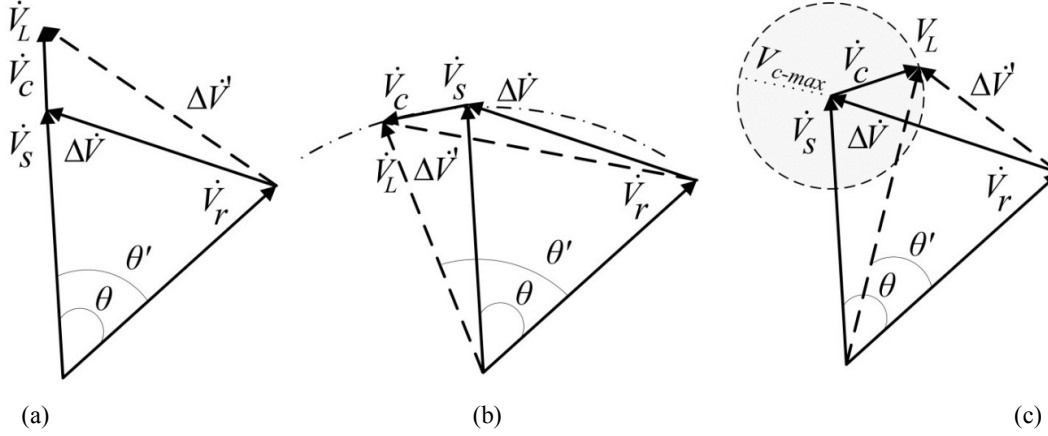
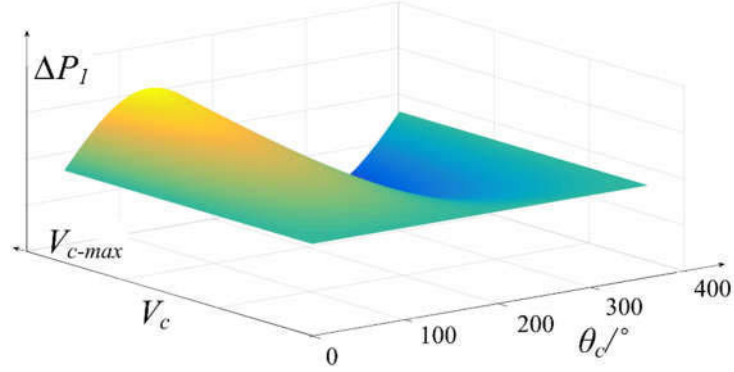
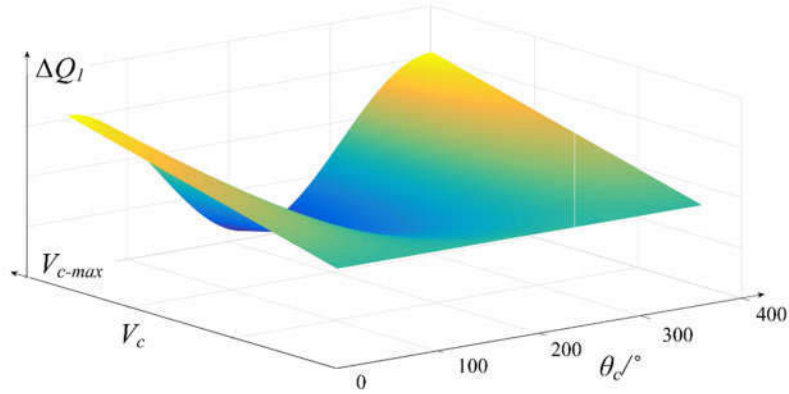


Fig. 3.7 Phasor diagrams of the transmission line with UPFC under modes of (a) sending end voltage compensation, (b) transmission angle compensation and (c) comprehensive compensation.

The system phasor diagrams are shown in Fig. 3.7. The UPFC can operate in voltage, transmission angle, impedance and comprehensive compensation modes. The compensated voltage V_c can have a maximum voltage V_{c-max} which is only determined by the UPFC rated capacity while phase angles have a range of 360° as shown by the shaded circle in Fig. 3.7(c). With a given UPFC capacity, the controllable active power

P_1 and reactive power Q_1 can be obtained as a function of the compensated voltage amplitudes V_c and phase angles θ_c , as shown in Figs. 3.8 and 3.9. These controllable regions are only limited by the designed UPFC capacity. Combining the system inherent active and reactive power (Figs. 3.5 and 3.6) with these controllable power (Figs. 3.8 and 3.9), we can get the total sending-end transmitting power which is enhanced in a flexible manner by the UPFC.


 Fig. 3.8 Controllable active power diagram as a function of UPFC's V_c and θ_c .

 Fig. 3.9 Controllable reactive power diagram as a function of UPFC's V_c and θ_c .

It is assumed that the receiving-end voltage amplitude range is $0 \leq V_r \leq V_s$, and the transmission angle range is $0 \leq \theta \leq 360^\circ$. With a UPFC of the fixed capacity, the full achievable power regions for the sending end of the system can be derived, as shown in Fig. 3.10. In this figure, if V_r is fixed while θ is varying, the angle loci are obtained, and they are denoted by two adjacent parallel lines. They are only drawn for angles of $60^\circ/240^\circ$, $90^\circ/270^\circ$ and $150^\circ/330^\circ$ for the purpose of clear visibility. If θ is fixed while V_r is varying, the loci denoted by the cyan circles are obtained. Only two loci are sketched here, i.e. $V_r = V_s$ and $V_r = 0.5V_s$.

In the Fig. 3.10, the small bold circles represent the UPFC rated controllable region at different values of V_r and θ . Each circle corresponds specifically to the system original operating point, being the center point of that circle. For example, the small blue circle shown in the figure has the center point located on the $V_r = 0.5V_s$ locus and it lies in the $\theta = 150^\circ$ loci, these indicate the blue circle is the UPFC controllable region for the

operating point of $(V_r = 0.5V_s, \theta = 150^\circ)$. Only a limited number of operating points and their corresponding UPFC controllable regions are shown here. The outermost red dashed circle is the fully achievable power region of the transmission system with the UPFC compensation. Again, from this figure, it is evident that the system power controllability becomes more flexible and the power transfer capacity can be improved.

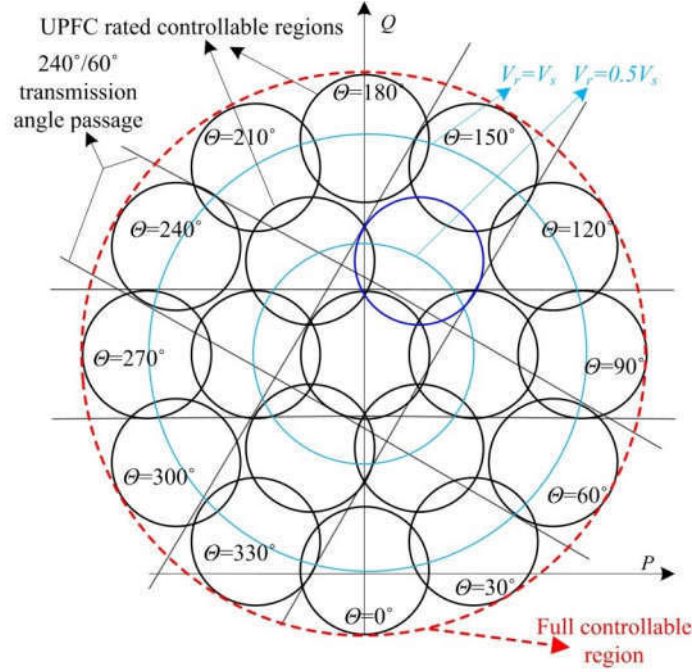


Fig. 3.10 Full power controllable regions with the application of UPFC.

In addition to the contribution of power controllability from the point before compensation (which is a result of current compensation), the UPFC can directly compensate the active and reactive power. This is obtained from voltage compensation. Therefore, there are two sources of contribution for power controllability in the transmission line X , as compensated by a UPFC. The total complex power flowing through the transmission line X after the compensation point is

$$\begin{aligned}
 P + jQ &= \dot{V}_L \dot{I}_L^* = \left(\dot{V}_s + \dot{V}_c \right) \left(\frac{\dot{V}_s + \dot{V}_c - \dot{V}_r}{j\omega L} \right)^* \\
 &= \frac{1}{\omega L} \left\{ \left[V_s V_r \sin \theta + j(V_s^2 - V_s V_r \cos \theta) \right] \right. \\
 &\quad \left. + V_c V_r \sin(\theta_{vc} - \theta_{vr}) + jV_c^2 + j2V_c V_s \cos(\theta_{vs} - \theta_{vc}) - jV_c V_r \cos(\theta_{vc} - \theta_{vr}) \right\} \\
 &= (P_0 + jQ_0) + (\Delta P_2 + j\Delta Q_2)
 \end{aligned} \tag{3.4}$$

and the power provided by the UPFC injected voltage (voltage contribution) becomes:

$$\begin{aligned}
 \Delta S &= \Delta P + j\Delta Q = \Delta P_2 - \Delta P_1 + j(\Delta Q_2 - \Delta Q_1) \\
 &= \frac{1}{\omega L} \left[V_c V_s \sin(\theta_{vs} - \theta_{vc}) + V_c V_r \sin(\theta_{vc} - \theta_{vr}) \right. \\
 &\quad \left. + jV_c^2 + jV_c V_s \cos(\theta_{vc} - \theta_{vs}) - jV_c V_r \cos(\theta_{vc} - \theta_{vr}) \right]
 \end{aligned} \tag{3.5}$$

Hence, the mesh curves for P and Q , as transferred by the power flow controller due to the voltage compensation, can be derived. This is studied in the simulation study case in the simulation section (Figs. 3.13 and 3.14).

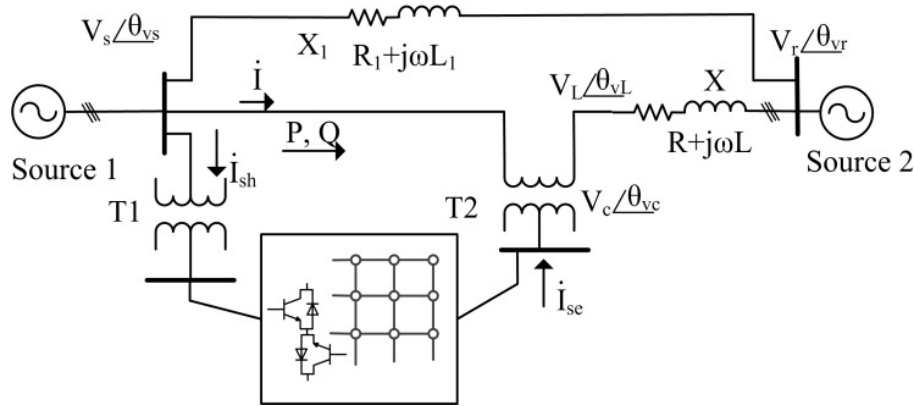


Fig. 3.11 MC-UPFC in double-line transmission system (simulation study case).

3.2.2 MC-UPFC System in the Transmission Line

A UPFC based on a direct SVM controlled MC is shown in Fig. 3.11 for one branch in a double-line transmission system. Transformers T1 and T2 are employed to connect the input and output terminals of the MC-UPFC to the transmission line. The input and output sides are connected in shunt and series with the transmission line respectively.

The MC-UPFC is proposed for power compensation through one of the lines in a double-line system. The simulation studies are based on this system.

3.3 Power Flow Controller

3.3.1 Model Description

The MC-UPFC circuit for the simulation study is given in Fig. 3.11. A mathematical model of the transmission line X can be described by

$$\frac{dI_x}{dt} = \frac{V_{sx} + V_{cx} - V_{rx}}{L} - \frac{R}{L} I_x \quad (3.6)$$

where $x = a, b, c$ is the index of three phases. Using a rotating d - q reference frame transformation, the three-phase quantities can be represented in the d - q frame as

$$\frac{dI_d}{dt} = -\frac{R}{L} I_d - \omega I_q + \frac{V_{sd} + V_{cd} - V_{rd}}{L} \quad (3.7)$$

$$\frac{dI_q}{dt} = -\frac{R}{L} I_q + \omega I_d + \frac{V_{sq} + V_{cq} - V_{rq}}{L} \quad (3.8)$$

As we can see from equations (3.7) and (3.8), the d and q components are coupled to each other and this will cause coupling effects in the system. The Laplace transforms for (3.7) and (3.8) are

$$V_{cd} = (Ls + R)I_d + L\omega I_q - V_{sd} + V_{rd} \quad (3.9)$$

$$V_{cq} = (Ls + R)I_q - L\omega I_d - V_{sq} + V_{rq} \quad (3.10)$$

If the reference frame is synchronized with a source voltage $V_{sq} = 0$ and the active and reactive power through the transmission line can be expressed as

$$P = \frac{3}{2} V_{sd} I_d, \text{ and } Q = -\frac{3}{2} V_{sd} I_q \quad (3.11)$$

Consequently, I_d and I_q references corresponding to the P and Q references are obtained from

$$I_d = \frac{2}{3} \frac{P}{V_{sd}}, \text{ and } I_q = -\frac{2}{3} \frac{Q}{V_{sd}} \quad (3.12)$$

3.3.2 Controller Design

To design the PID controllers for power flow control purposes, the d and q component references for the line current are obtained from the required active and reactive power using (3.11) and (3.12). These current references are passed through the PID controllers (shown in Fig. 3.12) to deliver d and q component references for the series voltage generation. These two references can be converted into three-phase quantities, and then direct SVM utilizes these references to provide the derived voltages for the MC. To address the d - q coupling effects, the d and q components are introduced to each PID controller with coefficients k_1 and k_2 . In a manner similar to the parameter selection in a PID controller, the selection of these two coefficients is based on empirical methods. As a result, the d - q coupling suppressed PID controllers are shown in Fig. 3.12. As can be seen, the proposed controller is simple and only two PID controllers are required. A phase locked loop (PLL) is used to detect the ramp for the frame transformation. The PID parameters are tuned based on a trial-and-error process. This can be improved using some developed tuning techniques existing in the literature [32][33].

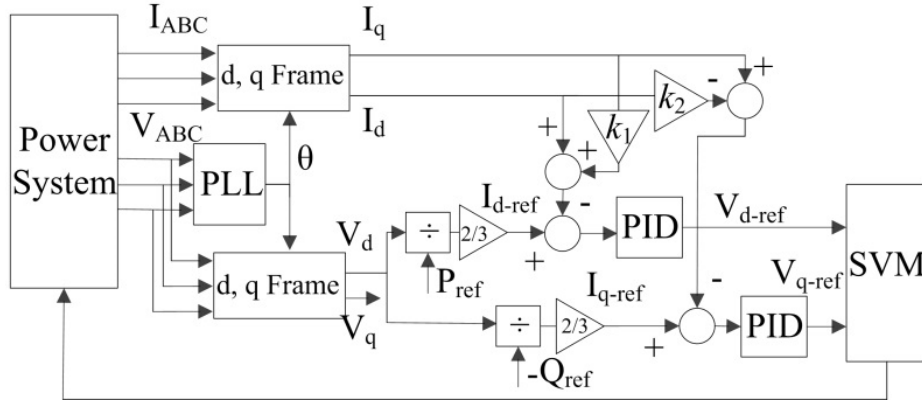


Fig. 3.12 D-Q decoupling PID controllers for MC-UPFC.

3.4 Simulation and Results

The simulation study is implemented for the 11 kV double-circuit transmission system shown in Fig. 3.11. The system parameters and controller parameters are given in Tables 3.1 and 3.2 respectively. The PID parameters used are consistent throughout the simulation work, but they may need to be adjusted for different system ratings and load

conditions. All simulation results are shown in per unit (p.u.) values and the base values can be found in Table 3.1. Small RLC filters are normally necessary at the input terminals of MC to filter high-frequency harmonics in the current waveform. The maximum available voltage provided by the MC-UPFC is set to 0.24 p.u. and the inherent transmission angle of the system is 15° .

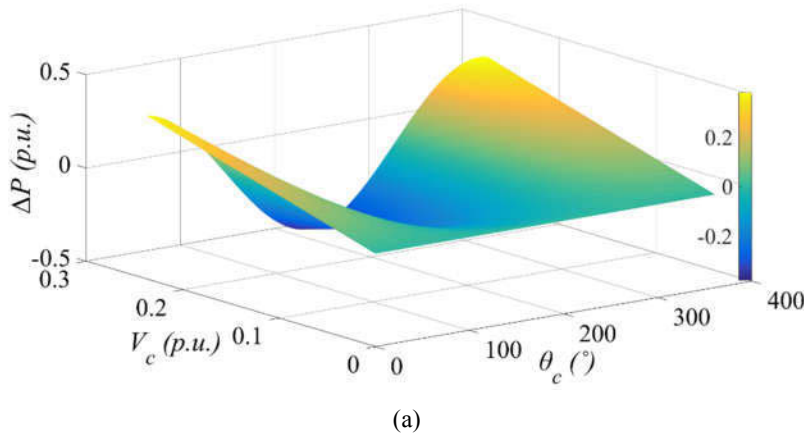
Table 3.1 System parameters for the simulated transmission system.

S_{base} (MVA)	V_{base} (kV)	V_s (p.u.)	f (Hz)	V_r (p.u.)	Z (p.u.)	Z_1 (Ω)
10	11	1	60	$0.9659-j0.2588$	$0.1102+j0.5193$	$0.0207+j0.1947$

Table 3.2 Parameters of the PID power low controllers.

k_{p1}	k_{i1}	k_{d1}	k_{p2}	k_{i2}	k_{d2}	k_1	k_2
3	0.03	0	11	0.06	0.05	0.09	0.001

Fig. 3.13 shows the active and reactive power contributed by the MC-UPFC due to series voltage compensation. As mentioned earlier, the other contribution to the power compensation is from the line current. Therefore, the total available active and reactive power ranges at the sending end are obtained and shown in Fig. 3.14. In this case, with the parameters given above, it is concluded that the approximate active and reactive power range from 0 to 4 p.u. and -2 to 2 p.u. respectively, which can be verified using (3.3).



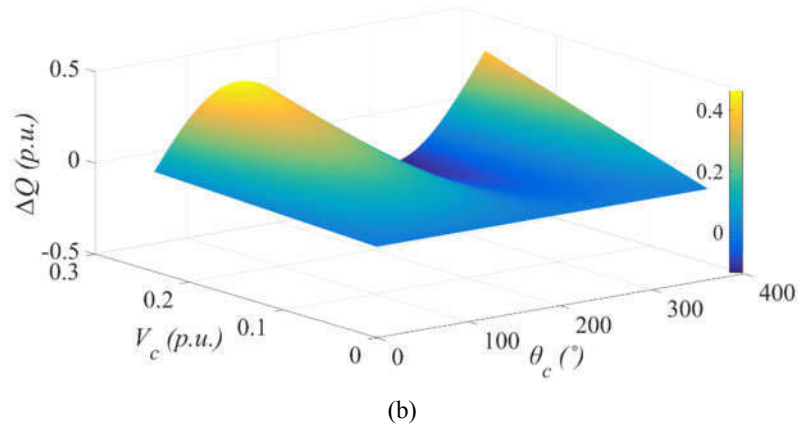


Fig. 3.13 Power diagrams as a result of voltage contribution (a) active power and (b) reactive power.

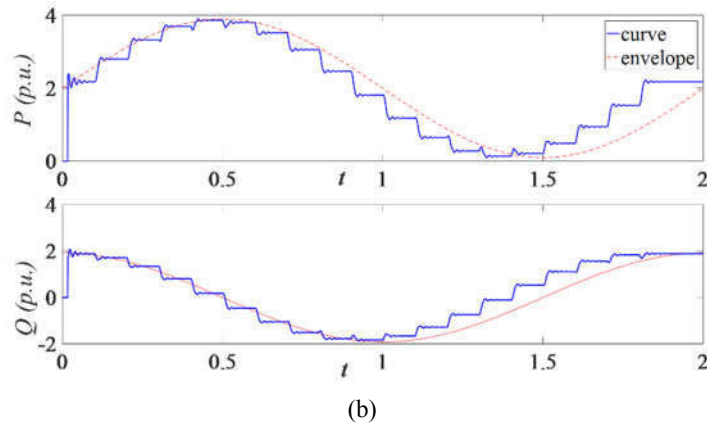
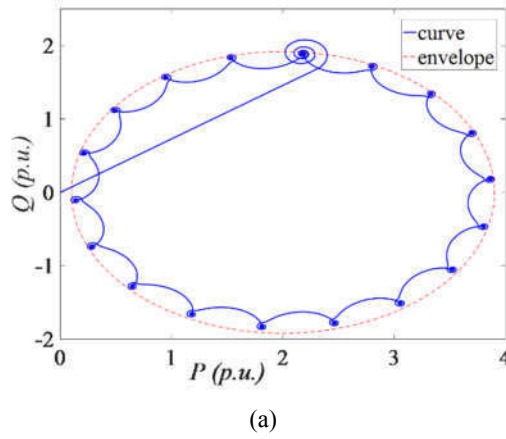


Fig. 3.14 Sending-end power ranges with the compensation of MC-UPFC (a) active power and (b) reactive power

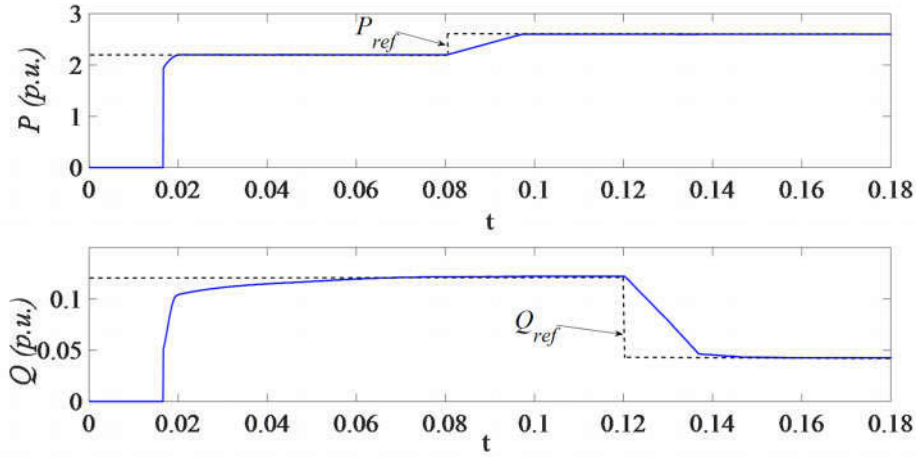


Fig. 3.15 Response of the sending-end power to the step change in active and reactive power.

Fig. 3.15 shows the active and reactive power flowing through the line at the sending end. The active power reference is set as 2.2 p.u. before 0.08 s and 2.6 p.u. after 0.08 s, while the reactive power reference is set as 0.12 p.u. before 0.12 s and 0.04 p.u. after 0.12 s. As observed from the figure, the output can be regulated to follow the references effectively, and the d - q coupling effects are suppressed. d and q components of the compensated bus current react in accordance with the power demand as shown in Fig. 3.16. Fig. 3.17 shows the sending-end currents of transmission line X and MC output. Fig. 3.18 shows the injected voltages and equivalent sending-end voltages where the relationship of $V_L = V_s + V_c$ holds as described in (3.3). The voltages and currents of the supply source 1 are shown in Fig. 3.19, and the total harmonic distortion (THD) analysis for the line X current is illustrated in Fig. 3.20. It can be seen from the simulation results that the proposed controllers are effective in controlling transmission power and improving the transfer capacity of the transmission system. Flexibility of the transmission system is enhanced.

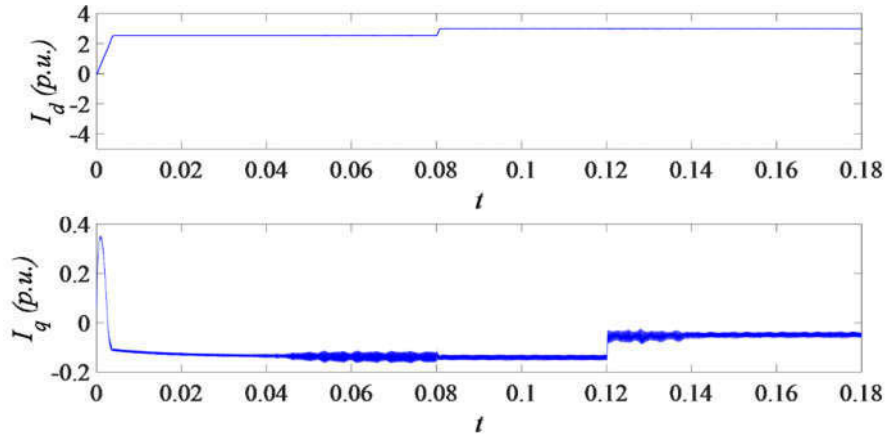


Fig. 3.16 Response of line current d and q components to the power changes.

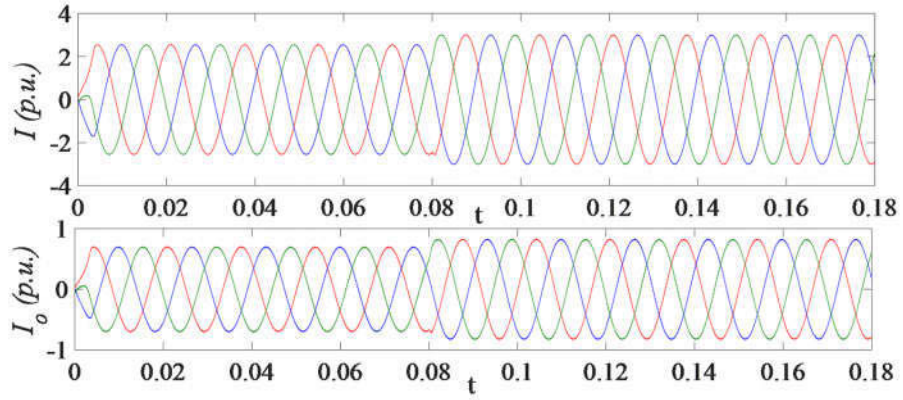


Fig. 3.17 Transmission line sending-end currents and MC output currents.

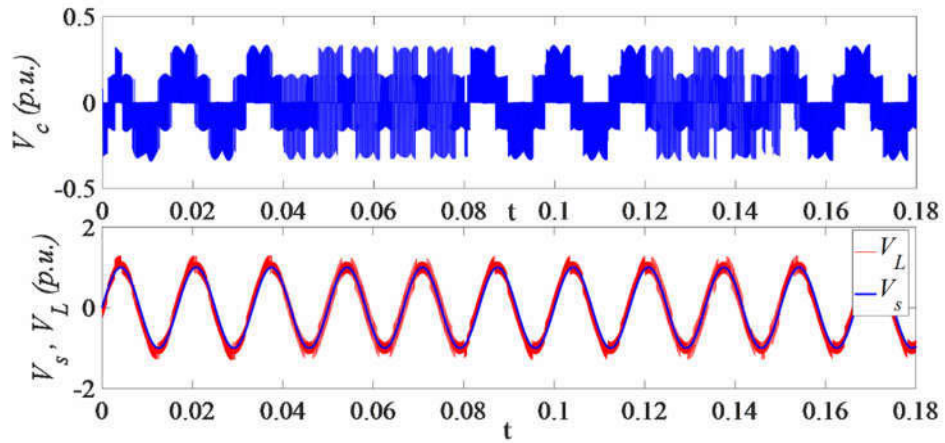


Fig. 3.18 Injected phase voltage V_c by MC-UPFC and equivalent sending-end voltage ($V_L = V_s + V_c$).

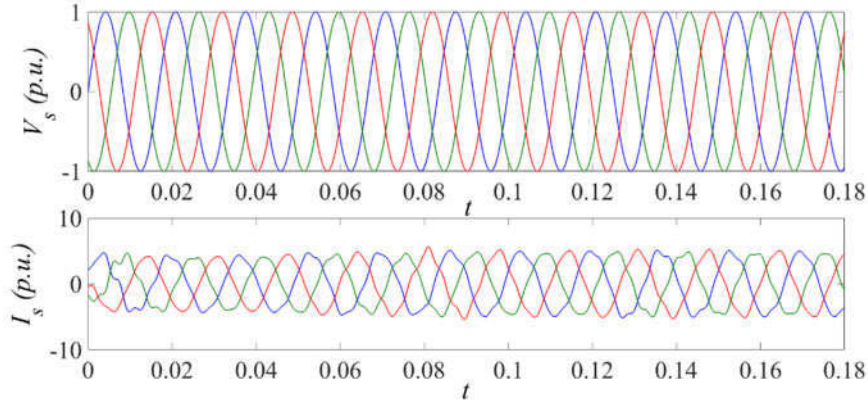


Fig. 3.19 Three-phase voltages and currents of the supply source 1.

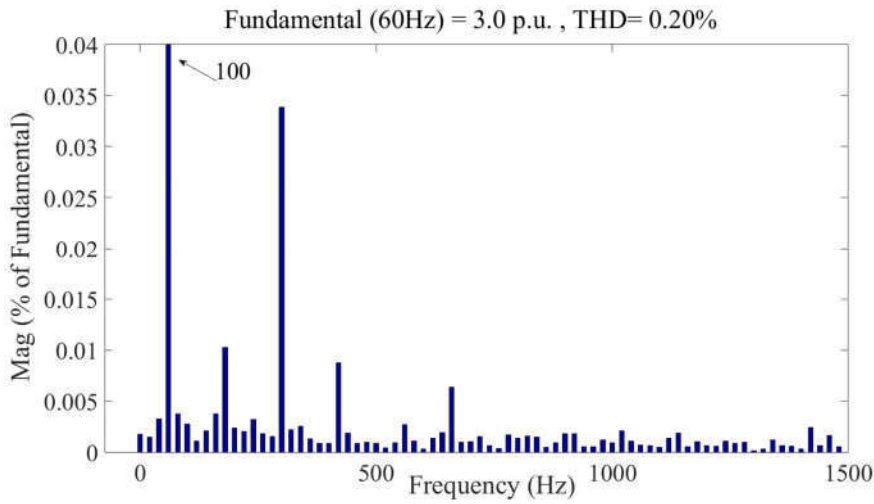


Fig. 3.20 Current spectrum analysis of the transmission line X.

3.5 Summary

The UPFC is an essential component in a transmission system. The bulky energy storage element in the traditional UPFC increases the volume and weight, reduces the lifetime of the device, and decreases the efficiency. The MC has been proposed as a potential alternative to the back-to-back converter in various applications including UPFC. In this chapter, the fully controllable regions of transmission system without and with the MC-UPFC are analyzed, and the contribution of MC-UPFC to power controllability is investigated. Effective and simple PID controllers are developed involving SVM for controlling power flow in a transmission system. The decoupling control of MC-UPFC is detailed and the coupling effects are suppressed. The work in

this chapter presents a design procedure for the closed-loop controller in the MC-UPFC. The MC-UPFC is proved able to provide good flexibility in terms of controlling active and reactive power and increasing the power transfer capability. The proposed controllers can follow the references effectively with good dynamics. The steady state errors are negligible. The simulation results validate the effectiveness and feasibility of the proposed scheme and controllers.

The work presented in this chapter and other related work have been published in [13], [14] and [34].

References

- [1] H. Xie, Y. H. Song, A. Yokoyama, and M. Goto, "Integrated linear and nonlinear control of unified power flow controllers for enhancing power system stability," *Elec. Power Compon. Syst.*, vol. 31, no. 4, pp. 335-347, 2003.
- [2] S. P. Singh, "Congestion mitigation using UPFC," *IET Generation, Transmission & Distribution*, vol. 10, no. 10, pp. 2433-2442, 2016.
- [3] L. Gyugyi, "Unified power-flow control concept for flexible AC transmission systems," *IEE proceedings C (generation, transmission and distribution)*, vol. 139, no. 4, pp. 323-331, 1992.
- [4] J. Verveckken, F. Silva, D. Barros, and J. Driesen, "Direct power control of series converter of unified power-flow controller with three-level neutral point clamped converter," *IEEE Trans. Power Del.*, vol. 27, no. 4, pp. 1772-1782, 2012.
- [5] T. Al-Awami Ali, Y. L. Abdel-Magid, M. A. and Abido, "Simultaneous stabilization of power system using UPFC-based controllers," *Elec. Power Compon. Syst.*, vol. 34, no. 9, pp. 941-959, 2006.
- [6] N. G. Hingorani, and L. Gyugyi, "Combined compensators: unified power flow controller (UPFC) and interline power flow controller (IPFC)", in: *Understanding FACTS: concepts and technology of flexible AC transmission systems*, Wiley-IEEE press, pp. 297-352, 2000.
- [7] M. Reddy, Y. Balasubba, P. Obulesh, S. Sivanagaraju, C. V. Suresh, "Mathematical modelling and analysis of generalised interline power flow controller: an effect of converter location," *J. Experimental & Theoretical Artificial Intelligence*, vol. 28, no. 4, pp. 655-671, 2016.
- [8] S. Ali Al-Mawsawi, "Optimal Location of UPFC Applied to Nonlinear Load Model," *Elec. Power Compon. Syst.*, vol. 32, no. 1, pp. 1-12, 2004.
- [9] L. N. Tripathy, S. R. Samantaray, and P. K. Dash, "A fast time–frequency transform based differential relaying scheme for UPFC based double-circuit transmission line," *Int. J. Electr. Power Energy Syst.*, vol. 77, pp. 404-417, 2016.
- [10] F. Z. Peng, Y. Liu, S. Yang, S. Zhang, D. Gunasekaran, and U. Karki, "Transformer-Less Unified Power-Flow Controller Using the Cascade Multilevel Inverter," *IEEE Trans. Power Electron.*, vol. 31, no. 8, pp. 5461-5472, 2016.

- [11] S. Yang, Y. Liu, X. Wang, D. Gunasekaran, U. Karki, and F. Z. Peng, "Modulation and Control of Transformerless UPFC," *IEEE Trans. Power Electron.*, vol. 31.2, pp. 1050-1063, 2016.
- [12] J. Monteiro, J. Fernando Silva, and S. Pinto, "Matrix converter as unified power flow controller: design and implementation of decoupled direct power controllers," 9th Int. Conf. Compatibility Power Electron. (CPE), Lisbon, Portugal, pp. 197-201, June 2015.
- [13] J. Zhang, D. Dorrell, L. Li "Applications of the Direct Space Vector Modulation Controlled Matrix Converter as the Unified Power Flow Controller," The 8th Int. Conf. on Power Electron., Machines & Drives (PEMD 2016), Glasgow, pp.1- 6, 2016.
- [14] J. Zhang, L. Li, and D. Dorrell, "DQ Coupling Suppressed PID Controller for the Transmission Line Power Flow Control Using a Matrix Converter," *IEEE Ind. Electron. Soc. Annu. Meeting (IECON16)*, Florence, Italy, pp. 6249 – 6254, October 2016.
- [15] J. Alcalá, V. Cárdenas, J. Espinoza, and M. Durán, "Investigation on the limitation of the BTB-VSC converter to control the active and reactive power flow," *Electr. Power Syst. Res.*, vol. 143, pp. 149-162, 2017.
- [16] J. Monteiro, J. F. Silva, S. F. Pinto, and J. Palma, "Matrix converter-based unified power-flow controllers: Advanced direct power control method," *IEEE Trans. Power Del.*, vol. 26, no. 1, pp. 420-430, 2011.
- [17] B. Geethalakshmi, and P. Dananjayan, "Investigation of performance of UPFC without DC link capacitor," *Electr. Power Syst. Res.*, vol. 78, no. 4, pp. 736-746, 2008.
- [18] P. W. Wheeler, J. Rodriguez, J. C. Clare, L. Empringham, and A. Weinstein, "Matrix converters: a technology review," *IEEE Trans. Ind. Electron.*, vol. 49, no. 2, pp. 276-288, 2002.
- [19] H. Hojabri, H. Mokhtari, L. and Chang, L., "Stand Alone Performance of Permanent Magnet Synchronous Wind Power Generator with Current Source Matrix Converter," *Elec. Power Compon. Syst.*, vol. 43, no. 8-10, pp. 1018-1027, 2015.
- [20] A. Yousefi-Talouki, S. Asghar Gholamian, M. Yousefi-Talouki, and M. Yazdani-Asrami, "A new direct power control of doubly-fed induction generator using matrix converter," *Australian J. Electrical and Electronics Engineering*, vol. 10, no. 3, pp. 307-320, 2013.
- [21] F. Jurado, M. Ortega, and A. Cano, "Predictive control of matrix converter-based micro-turbine," *Elec. Power Compon. Syst.*, vol. 36, no. 4, pp. 409-431, 2008.
- [22] R. Cárdenas, R. Peña, P. Wheeler, J. Clare, and C. Juri, "Control of a matrix converter for the operation of autonomous systems," *Renewable Energy*, vol. 43, PP. 343-353, 2012.
- [23] S. L. Arevalo, P. Zanchetta, P. W. Wheeler, A. Trentin, A. and L. Empringham, "Control and implementation of a matrix-converter-based ac ground power-supply unit for aircraft servicing," *IEEE Trans. Ind. Electron.*, vol. 57, no. 6, pp. 2076-2084, 2010.
- [24] E. Yamamoto, J. K. Kang, and H. P. Krug, "Development of Matrix Converter for Industrial Applications," *Yaskawa White Paper*, 2007.
- [25] M. Munzer, "EconoMac – the First All In One IGBT Module for Matrix Converters“, *Drives and Control Conference*, Section 3, London, 2001.
- [26] J. Itoh, A. Odaka, I. and Sato, "High efficiency power conversion using a matrix converter." *Fuji Electric Review*, vol. 50, no. 3, pp. 94-98, 2004.

- [27] R. Strzelecki, A. Noculak, H. Tunia, K. Sozanski, Z. and Fedyczka, "UPFC with matrix converter," EPE conf., Graz, Austria, pp. 1-9, September 2001.
- [28] A. Dasgupta, P. Tripathy, and P. Sarathi Sensarma, P., "Matrix converter as UPFC for transmission line compensation," 7th Int. Conf. Power Electron., Daegu, Korea, pp. 1050-1055, October 2007.
- [29] L. Huber and D. Borojevic, "Space vector modulator for forced commutated cycloconverters," Ind. Applicat. Soc. Annu. Meeting Conf. Rec., pp. 871-876, October 1989.
- [30] S. Zhang, R. Guo, and K. Li, "Modeling and design of matrix converter based unified power flow controller with implementation of complex vector synchronous frame PI current regulators," Int. Conf. Electrical Machines and Systems (ICEMS), Busan, Korea, pp. 1619-1623, October 2013.
- [31] S. D. Round, Q. Yu, L. E. Norum, T. M. and Undeland, "Performance of a unified power flow controller using a dq control system," 6th Int. Conf. AC and DC Power Transmission, pp. 357-362, April 1996.
- [32] Q. G. Wang, T. H. Lee, H. W. Fung, Q. Bi, and Y. Zhang, "PID tuning for improved performance," IEEE Trans. Control Syst. Tech., vol. 7, no. 4, pp. 457-465, 1999.
- [33] P. Cominos and N. Munro, "PID controllers: recent tuning methods and design to specification," IEE Proceedings-Control Theory and Applications, vol. 149, no. 1, pp. 46-53, 2002.
- [34] J. Zhang, L. Li, D. Dorrell, and Y. Guo, "Decoupling Controller Design and Controllable Regions Analysis for the Space Vector Modulated Matrix Converter-Unified Power Flow Controller in Transmission Systems," Elec. Power Compon. Syst., vol. 46, no. 1, pp. 1-14, 2018.

4 PI AND PR CONTROL FOR IMPROVING STEADY-STATE TRACKING PERFORMANCE

This chapter proposes a modified proportional-integral (PI) controller for a three-phase direct matrix converter (MC). This involves current feedforward together with space vector modulation (SVM) to control the MC output currents. This controller provides extra control flexibility in terms of the current regulation, and it gives improved steady-state tracking performance. The total harmonic distortion (THD) is also reduced. As part of the work, a proportional-resonant (PR) controller is designed and compared. The PR controller shows improved performance in terms of steady-state error, selective harmonic compensation and the ability to handle sinusoidal quantities, compared with traditional PI controllers. These improvements enhance the tracking performance of a converter and improve the current quality. Both the proposed PI and PR controllers are implemented in the natural frame (abc) in a straightforward manner. This removes the coordinate transformations that are required in the stationary ($\alpha\beta$) and synchronous (dq) reference frame-based strategies. A constant switching frequency is maintained because of the SVM modulation stage. The experimental and simulation results verify the feasibility and effectiveness of the proposed controllers.

4.1 Introduction

PI controllers are simple, easy to implement and have been widely used in power electronic converters and other industrial applications [1][2]. A PI controller, when used in a power electronic converter, generally uses one of three reference frames in its control strategy: the synchronous reference frame (dq system), the stationary reference frame ($\alpha\beta$ system), or the natural frame (abc system) [3]. Both $\alpha\beta$ and dq based control methods require multiple frame transformations (Clark and/or Park) leading to an increased computational burden. Stationary frame PI controllers are considered as unsatisfactory controllers due to significant amplitude and phase tracking errors, especially when tracking sinusoidal variables. The reason for steady-state errors in a stationary PI controller is because the stationary controller only offers a limited gain at non-zero frequencies [4]-[6]. In contrast, the synchronous PI controller is commonly used because it can achieve zero steady-state error due to the infinite gain of the DC signal provided by the integral term.

However, the synchronous frame controller is more complex than the stationary frame controller due to several transformations being required ($abc \leftrightarrow dq$) to convert the controlled signals to DC quantities. The controllers are also error-prone because of noise in the synchronous reference signal detection. The reference signal is usually captured using a phase locked loop (PLL). This introduces extra errors which become even worse for a single-phase system.

Several modified PI controllers are described in the literature. Some of these involve a feedforward controller. Feedforward control is simple in concept, robust and has good dynamic performance [7]. It is especially effective in handling a disturbance that can be measured. A stationary PI controller with a grid voltage feedforward path (shown in Fig. 4.1) was proposed in [8] for a grid-tied converter. This strategy improved the transient and disturbance rejection performance. However, this scheme suffers from voltage background harmonics and stability problems [9].

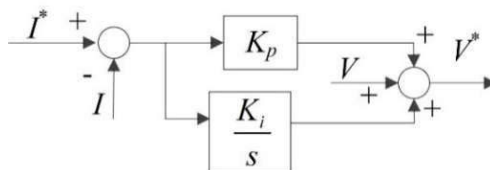


Fig. 4.1 PI controller with a voltage feedforward path.

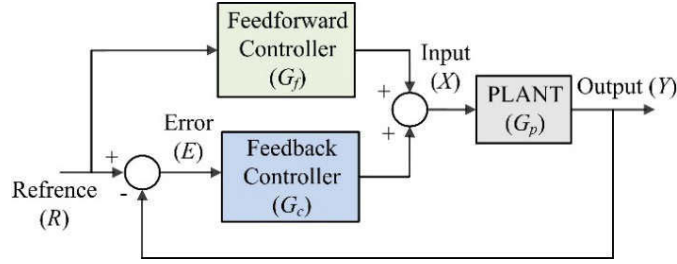


Fig. 4.2 Combined feedforward and feedback controller diagram.

A combined feedforward-feedback controller, as shown in Fig. 4.2, was proposed in [3] in order to improve the overall performance of the whole control system. The control strategy described in Fig. 4.2 has been used in other fields such as chemistry and mechanical systems [10]-[13]. However, it has drawn little attention in terms of the power electronic converter. In this chapter, a modified PI controller with a current feedforward path is proposed for a three-phase direct MC.

One of the other possible solutions for improving the steady-state tracking performance is the proportional-resonant (PR) controller. The PR offers excellent steady-state error performance and provides specific-order harmonic compensation with reasonable computational burden [5][14][15]. Resonant controllers have proved to be a good alternative to conventional PI controllers for current loop control. With increasing grid penetration of renewable energy systems, standards and codes impose more stringent requirements on current quality and harmonic distortion [16]. Traditional PI controllers are not able to deal with low-order harmonics efficiently. Instead, a high proportional gain is required, which pushes the system stability to a critical level [17]. In contrast, PR controllers are efficient in terms of compensating for selective current harmonics. The PR controller has been proposed for some converters and good performance has been reported [18]-[21]. However, it has not been investigated for MCs.

The three-phase direct MC is a possible option for AC/AC conversion. It has several advantageous features, such as compact volume, bidirectional power flow, sinusoidal waveforms, and controllable input power factor [22]-[24]. MCs have been proposed for various applications [3][5][25]. In industry, manufacturers such as Yaskawa [26][27], Eupec [22][28] and Fuji [29][30] have produced MC products or modules; e.g., the Yaskawa U1000, the AC7, the Eupec ECONOMAC FM35R12KE3ENG, and the Fuji

FRENIC-MX1S. The power ratings have reached 6.3 MVA in the Yaskawa MX1S series MC [31][32].

To improve the steady-state tracking performance of a power electronic converter, this work proposes a combined feedforward-feedback PI controller and investigates the PR controller for a three-phase direct MC. Both controllers demonstrate reduced steady-state tracking error and THD. A fast Fourier transform (FFT) is performed to obtain the THD to illustrate these improvements. In Sections 4.2 and 4.3, the PI and PR controllers are introduced. The indirect SVM described previously in Chapter 2 is used in this work. The controller diagrams are presented in Section 4.4. The simulation results and experimental verification are presented in Sections 4.5 and 4.6, followed by the summary in Section 4.7.

4.2 PI Controller with Current Feedforward

The proposed combined feedforward-feedback controller is shown in Fig. 4.2, where the current reference is fed forward as an additional control signal. This will improve the steady-state error. The transfer function $E(s)/R(s)$ is given by

$$\frac{E(s)}{R(s)} = \frac{1 - G_f(s)G_p(s)}{1 + G_c(s)G_p(s)} \quad (4.1)$$

where G_c is the PI controller, G_f is the feedforward controller (proportional controller), and G_p is the inductive load plant. These are given by

$$G_c(s) = \frac{K_p s + K_i}{s}, \quad G_f(s) = K, \quad G_p(s) = \frac{1}{R + Ls}$$

This is a two-degrees-of-freedom control system in which the closed-loop characteristics and the feedback characteristics can be regulated independently to improve the overall response performance of the whole control system [33]. By rearranging (4.1), the error in the frequency domain is

$$E(s) = \frac{1 - G_f(s)G_p(s)}{1 + G_c(s)G_p(s)} \cdot R(s) \quad (4.2)$$

The reference R in the natural frame is usually a sinusoidal function $R(t) = I_r \sin(\omega_c t)$ and its frequency domain expression (Laplace transform) is

$$R(s) = I_r \frac{\omega_c}{s^2 + \omega_c^2} \quad (4.3)$$

where I_r is the reference amplitude and $\omega_c = 2\pi f$ is the reference angular frequency. By substituting (4.3) into (4.2):

$$E(s) = \frac{Ls^2 + (R - K)s}{Ls^2 + (K_p + R)s + K_i} \cdot I_r \frac{\omega_c}{s^2 + \omega_c^2} \quad (4.4)$$

In order to derive the amplitude and phase responses of the error $E(s)$, s is substituted by $j\omega$. Therefore, the amplitude and phase angles are obtained from:

$$|E(j\omega)| = \sqrt{\frac{\omega^2 L^2 + (R - K)^2}{(K_i - \omega^2 L)^2 + (K_p + R)^2 \omega^2}} \cdot \frac{I_r \omega \omega_c}{-\omega^2 + \omega_c^2} \quad (4.5)$$

$$\angle E(j\omega) = \begin{cases} \tan^{-1} \frac{(R - K)}{-L\omega} - \tan^{-1} \frac{(K_p + R)\omega}{K_i - L\omega^2}, & \omega < \omega_c \\ \tan^{-1} \frac{(R - K)}{-L\omega} - \tan^{-1} \frac{(K_p + R)\omega}{K_i - L\omega^2} + \pi, & \omega > \omega_c \end{cases} \quad (4.6)$$

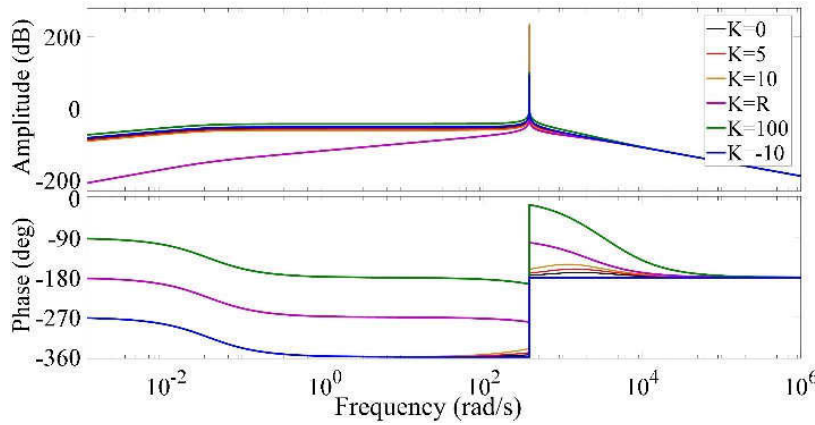


Fig. 4.3 Frequency responses of $E(j\omega)$ for different values of K .

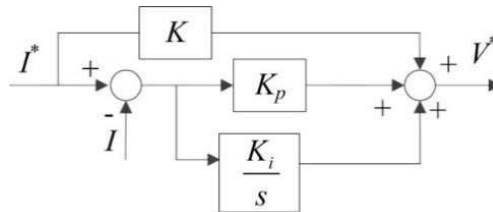


Fig. 4.4 Proposed PI current controller with current reference feedforward for MC.

According to (4.5) and (4.6), the error amplitude will have the minimum value when $K = R$ and other parameters are fixed. Introduction of the feedforward controller K offers an extra flexibility to tune the steady-state error performance. The amplitude and phase responses for different values of K are shown in Fig. 4.3. Here, the parameters used are: $K_p = 10$, $K_i = 1$, $R = 20 \Omega$, $L = 15 \text{ mH}$, $\omega_c = 120\pi \text{ rad/s}$. As can be seen from the figure, the amplitude response for $K = R$ is particularly distinct from others and it has the minimum level of amplitude response for the whole frequency domain. This illustrates that an appropriate selection of K can help reduce the steady-state error. Fig. 4.4 shows the proposed PI controller with current feedforward for controlling the MC output currents.

This controller is implemented in the natural abc frame (stationary) which does not require any frame transformation. Therefore, the complexity and computation burden is reduced. The controller generates the voltage references which will be utilized in the SVM control to control the MC. The description of SVM control can be found in Chapter 2.

4.3 PR Controller Design

The PR controller, compared with the more common PI controller, has better steady-state error performance, specific harmonic compensation capability, and the ability to handle sinusoidal quantities. The design of PR controller is straightforward. Briefly, the PR controller provides an infinite gain at the targeted frequencies to eliminate the steady-state error at these frequencies, and to provide harmonic compensation by cascading multiple PR controllers.

4.3.1 PR Controller

The derivation of an ideal PR controller can be achieved by transforming a synchronous reference frame based PI controller into a stationary frame based controller. The ideal PR controller is:

$$G_{PR}(s) = K_p + \frac{2K_R s}{s^2 + \omega^2} \quad (4.7)$$

This is shown in Fig. 4.5. It provides an infinite gain at the AC frequency ω and causes no phase shift at other frequencies (as shown in Fig. 4.6). K_P and K_R are the proportional and resonant gains respectively.

However, the implementation of an ideal PR controller is not practical due to the infinite quality factor [34]. Therefore, an approximated PR controller is usually adopted where:

$$G_{PR}(s) = K_P + \frac{2K_R\omega_c s}{s^2 + 2\omega_c s + \omega^2} \quad (4.8)$$

Here $\omega_c \ll \omega$ is the cut-off frequency, which affects the bandwidth around the resonance frequencies.

The approximated PR controller has wider bandwidth around the targeted frequencies which leads to less sensitivity. This means it is more robust to frequency variations around these targeted frequencies (as seen in Fig. 4.7).

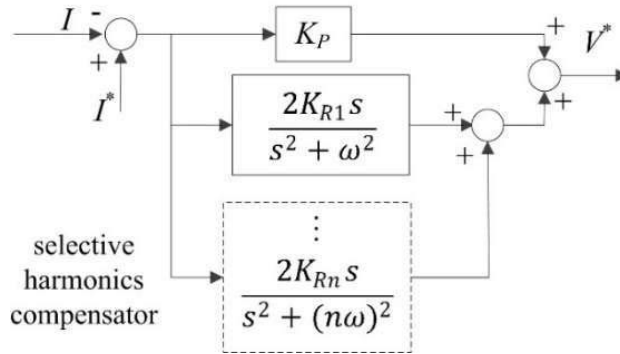


Fig. 4.5 Cascaded ideal PR controllers with selective harmonic compensation.

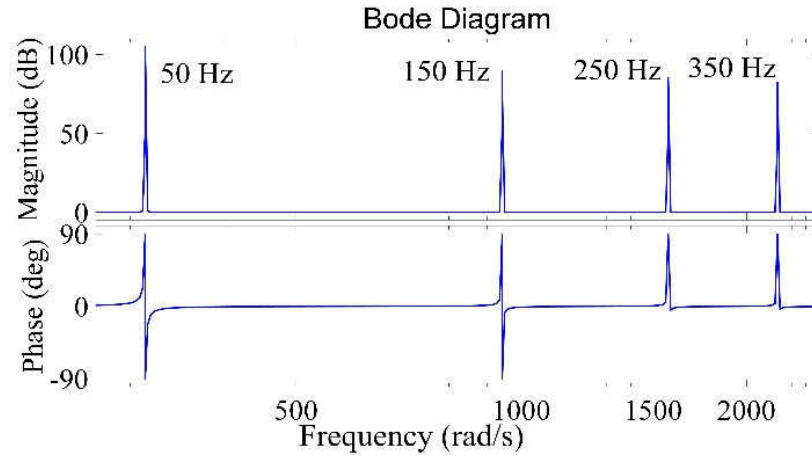


Fig. 4.6 Frequency response of the ideal PR controllers with selective harmonics compensator ($K_P = 1$, $K_{Rn} = 1$, $\omega = 100\pi$ rad/s).

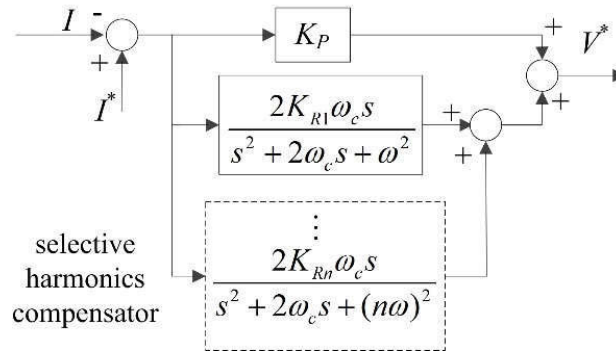


Fig. 4.7 Cascaded approximated PR controllers with harmonic compensation.

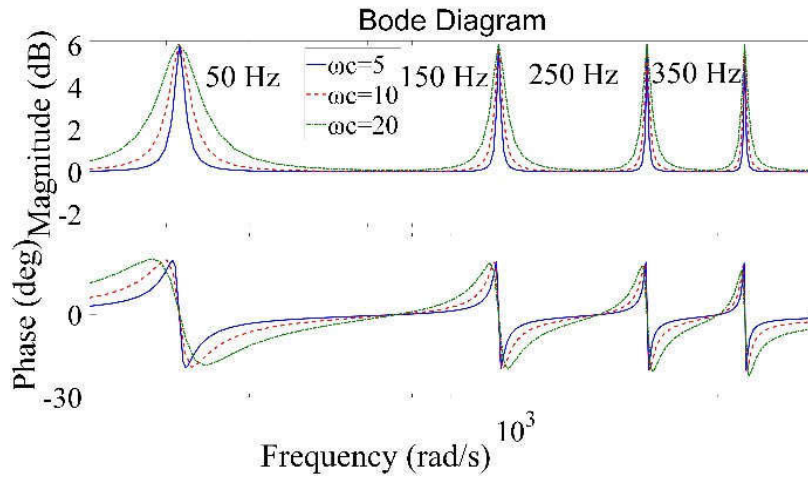


Fig. 4.8 Frequency response of the approximated PR controllers with selective harmonic compensator ($K_P = 1$, $K_{Rn} = 1$, $\omega = 100\pi$ rad/s, $\omega_c = 5, 10$, and 20 rad/s).

4.3.2 PR Controller with Harmonics Compensator

By cascading several PR controllers with different resonant frequencies, the ideal PR controller becomes

$$G_{PR}(s) = K_P + \sum_{n=1,3,5,7} \frac{2K_{Rn}s}{s^2 + (n\omega)^2} \quad (4.9)$$

and the approximated PR controller is

$$G_{PR}(s) = K_P + \sum_{n=1,3,5,7} \frac{2K_{Rn}\omega_c s}{s^2 + 2\omega_c s + (n\omega)^2} \quad (4.10)$$

where n is the harmonic order and K_{Rn} represents the individual resonant gain for the n^{th} harmonic. Thus, the ideal and approximated selective harmonic compensators (4.9) and (4.10) can be obtained as the block systems shown in Figs. 4.5 and 4.7 respectively. Their frequency responses (Bode plots) are shown in Figs. 4.6 and 4.8 respectively. It is worth noting that the gains at resonant frequencies can be tuned. Here, for simplicity, $K_P = K_{Rn} = 1$ is used.

For the harmonic compensator, the targeted frequencies can be designed according to specific applications. However, the 3rd, 5th, and 7th order harmonics are usually considered since they are regarded as the most prominent harmonics in a typical current spectrum [35].

From Figs. 4.6 and 4.8, it can be observed that the PR controller and harmonic compensator provide large gains only at the targeted frequencies and they do not introduce a phase shift to other frequencies. Compared with the ideal PR controller, the approximated PR controller has a wider bandwidth around the targeted frequencies, which results in improved robustness to frequency variations.

The output current error of an MC passes through the PR controllers (with harmonic compensators) to provide the voltage references. These references are then delivered to the SVM controller to generate the gating pulses for the MC. The MC input currents are also controlled by this scheme and the input power factor can be regulated to be unity. Controller parameters should be tuned appropriately to obtain the desired results. The tuning may be carried out in the same way as in a PI controller.

Table 4.1 Duty cycles distribution for symmetrical switching sequence.

	$t_{\gamma\alpha}/2$	$t_{\delta\alpha}/2$	$t_{\delta\beta}/2$	$t_{\gamma\beta}/2$	$t_0/2$	$t_0/2$	$t_{\gamma\beta}/2$	$t_{\delta\beta}/2$	$t_{\delta\alpha}/2$	$t_{\gamma\alpha}/2$
S_{Aa}	1	1	1	1	0	0	1	1	1	1
S_{Ba}	0	0	0	0	0	0	0	0	0	0
S_{Ca}	0	0	0	0	1	1	0	0	0	0
S_{Ab}	0	1	1	0	0	0	0	1	1	0
S_{Bb}	1	0	0	0	0	0	0	0	0	1
S_{Cb}	0	0	0	1	1	1	1	0	0	0
S_{Ac}	0	0	0	0	0	0	0	0	0	0
S_{Bc}	1	1	0	0	0	0	0	0	1	1
S_{Cc}	0	0	1	1	1	1	1	1	0	0

In order to reduce the switching transitions between each switch state, a symmetrical switching sequence is employed in each sampling interval T_s . This is achieved using the location information (k_i and k_v) of the input current and output voltage space vectors. An example is given in Table 4.1 for $k_i = k_v = 1$. In this table, a value of “1” indicates that the corresponding switch is turned on for the designated time segments, and vice versa. As seen in this table, only one switching transition is required between each state in one sampling period. An exhaustive switching look-up table with all combinations of k_i and k_v can be obtained in a similar manner. The table is presented in Appendix B. Taking advantage of this, enhanced pulse width modulator (ePWM) can be implemented by assigning the compare registers appropriate values.

4.4 SVM based PI and PR Controller Diagrams

SVM has been developed for the MC and it is a common control technique. However, it is ineffective when the load is unknown since this method requires the output current in the modulation. A synchronous frame based PI controller using SVM was proposed in [36] and [37] for an MC to control the power flow in a transmission system. However, the issues associated with synchronous PI controllers persisted.

Indirect SVM control is adopted here as a modulation stage to generate the firing pulses for the proposed controllers. There are two ways to implement the SVM method for the controller: direct and indirect methods [5].

In the direct method, the PI controller forms a current loop and generates output voltage references based on the output current errors (the difference between the reference and actual). The MC input current references are specified according to the system requirements. The output voltage and input current references are directly used in the SVM control to generate gating pulses for the semiconductor switches in the MC [37].

In the indirect method, the SVM control is divided into virtual inversion and rectification modulation stages. In the virtual inversion modulation stage, the PI controller and SVM (for the inverter only) are used to generate gating pulses for the semiconductor switches in the virtual inverter. SVM (for the rectifier only) is used in the virtual rectification modulation stage to generate gating pulses for the semiconductor switches in the virtual rectifier. Then the two virtual modulation stages are combined to control the MC [36]. In this work the indirect method is employed because of easy experimental implementation.

According to above analyses of the proposed controllers and SVM, the proposed PI and PR controllers for the SVM modulated MC can be designed. These are shown in Figs. 4.9 and 4.10 respectively. These controller structures are simple and no frame transformations are required since they are implemented in the natural abc system. In order to control the input power factor, a PLL is used to detect the location of the input voltages.

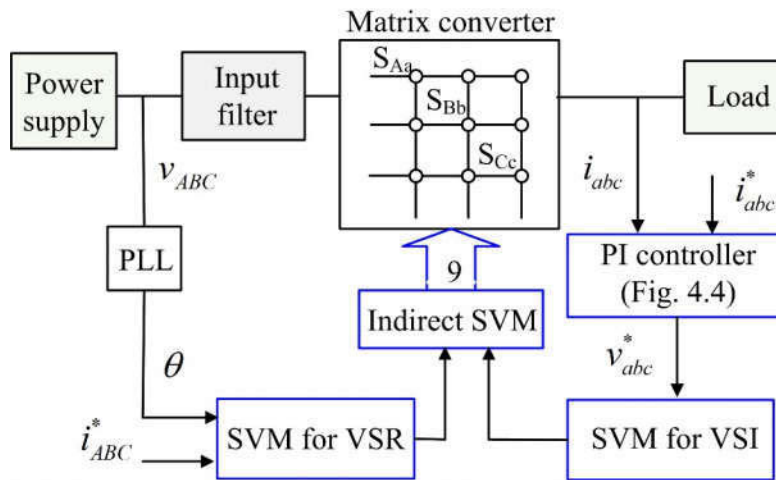


Fig. 4.9 Proposed PI controller diagram for the MC.

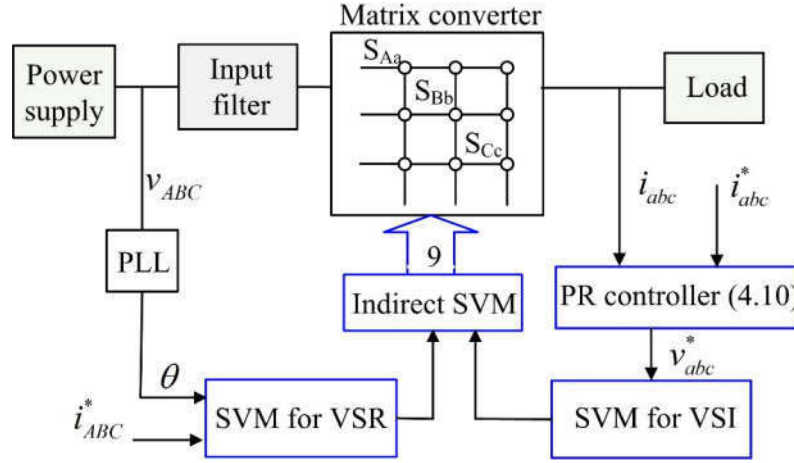


Fig. 4.10 PR controller diagram for the MC.

4.5 Simulation Tests

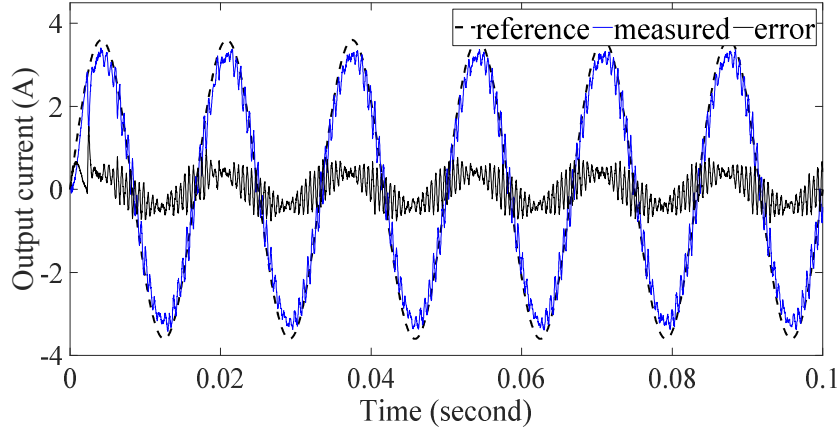
The parameters of simulation system are tabulated in Table 4.2. The output frequency can be a wide range and 60 Hz is used in this work. The input frequency is 50 Hz so that frequency conversion can be carried out. For simple and explicit figure captions, the tested controllers are abbreviated as follows: open loop SVM (SVM), PI based SVM (PI-SVM), PI with current feedforward based SVM (PICF-SVM), PR based SVM (PR-SVM) and PR with harmonic compensation based SVM (PRHC-SVM).

Table 4.2 Simulation system parameters.

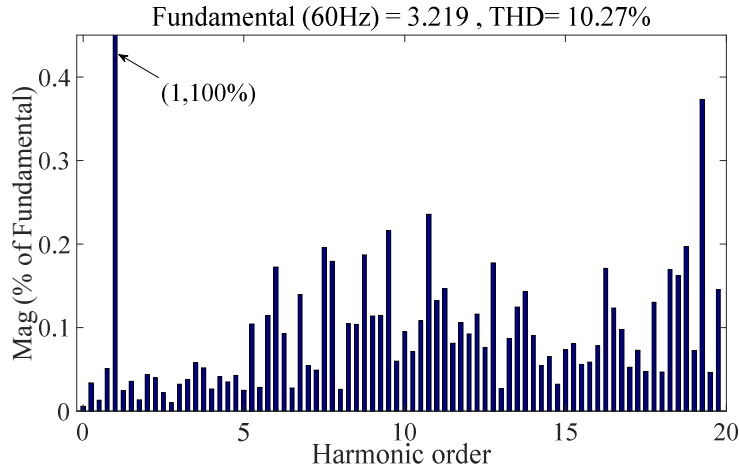
V_i [V]	f_i [Hz]	L_A [mH]	r_A [Ω]	C_{AB} [μ F]	L [mH]	R [Ω]	T_s [μ s]
100	50	4.8	30	10	14	20.3	100

Comparative simulation results for the PI controller with current feedforward are presented in Figs. 4.11 to 4.14. The parameters used in the PI controller are $K_p = 200$ and $K_i = 10$. The simulation results for the traditional PI controller are shown in Fig. 4.11. The obvious steady-state error appears in the waveform. The fundamental reference current amplitude is 3.6 A while the regulated fundamental current amplitude only reaches 3.22 A with a THD of 10.27 %. In contrast, the steady-state error performance is significantly improved with the proposed PI controller with current feedforward ($K = R = 20.3$ while K_p and K_i are the same as before), as shown in Fig.

4.12. The steady-state current amplitude reaches 3.53 A and the THD is reduced to 7.80 % at the same time. The MC input voltage and current of phase *A* are shown in Fig. 4.13. As can be seen, the MC input current is almost in phase with the input voltage. A small phase shift is caused by the input filters since the input current is controlled in the open loop approach.

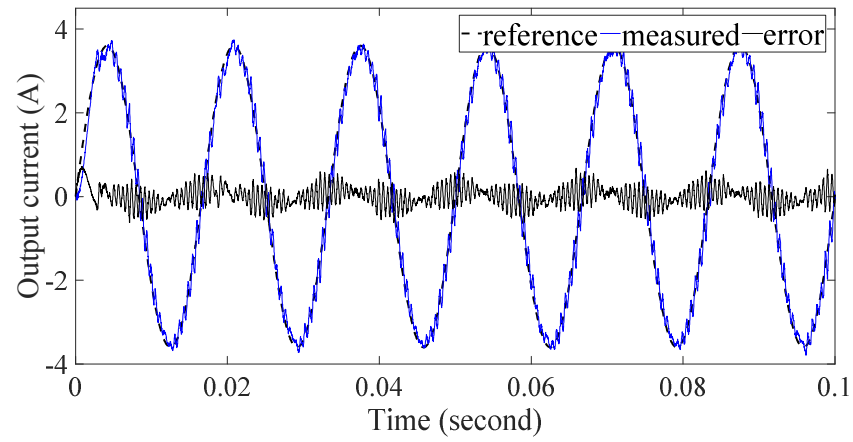


(a)

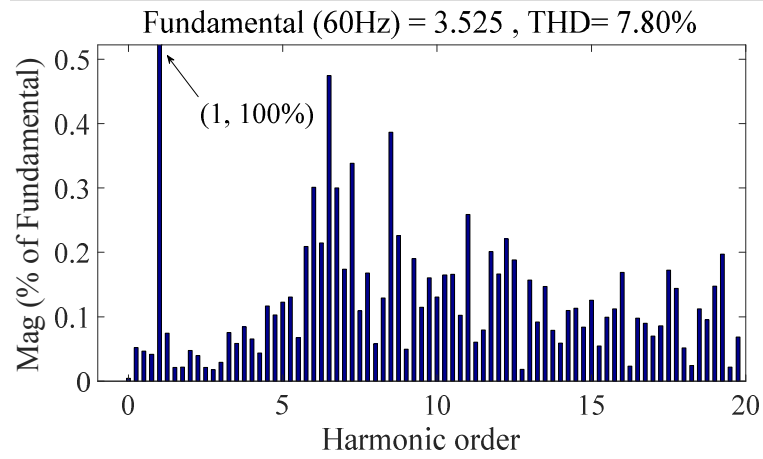


(b)

Fig. 4.11 Simulation results of the PI-SVM: (a) steady-state output currents and errors, (b) FFT analysis of the currents.



(a)



(b)

Fig. 4.12 Simulation results of the PICF-SVM: (a) steady-state output currents and errors, (b) FFT analysis of the current.

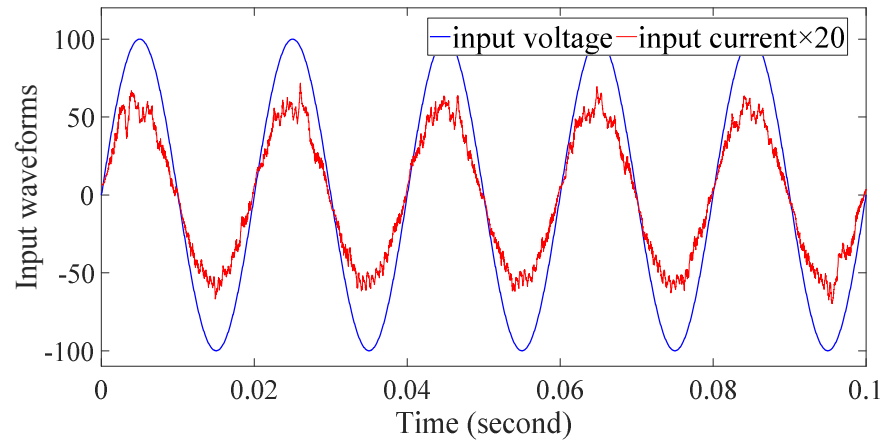


Fig. 4.13 MC input phase current and voltage (PICF-SVM).

The dynamic response of the proposed controller to a current amplitude change from 2.8 A to 3.6 A at 0.05 s is shown in Fig. 4.14. This result shows the fast transient response of the proposed controller. It is worth mentioning that the modulation index of the MC also influences the controller performance. This can be observed in Fig. 4.14 where different current amplitudes correspond to different modulation indices.

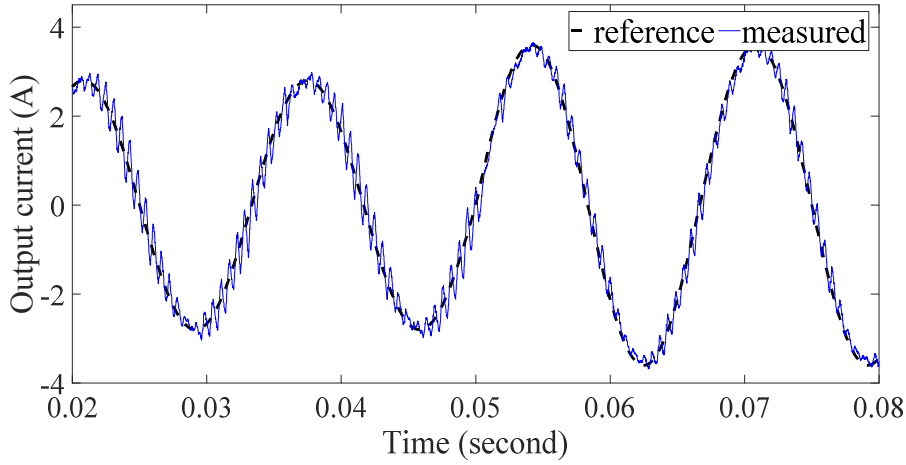


Fig. 4.14 Transient performance of the PICF-SVM controller.

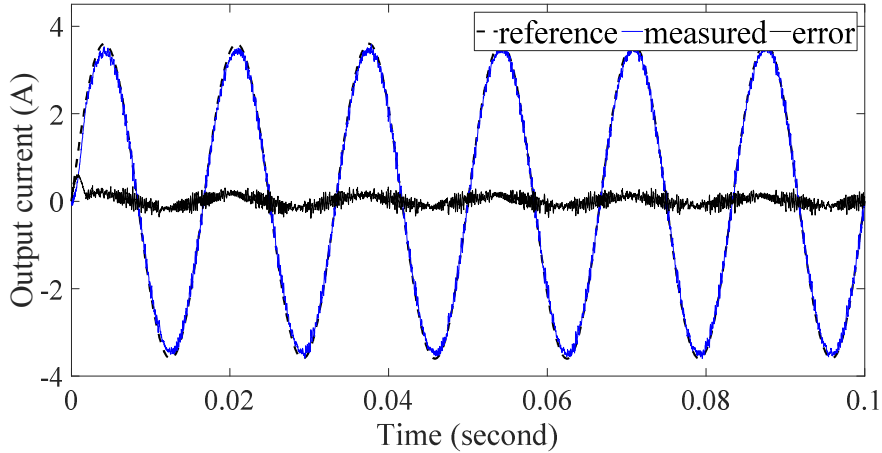


Fig. 4.15 Steady-state error performance of PRHC-SVM controlled output current ($K_{R4} = K_{R6} = 500$, $K_{R7} = 300$).

The simulation results for the PR controller are shown in Figs. 4.15 to 4.18. The controller parameters are (unless otherwise specified): $K_P = 350$, $K_{Rl} = 600$, K_{Rn} ($n=1, 2, 3, 4, 5, 6, 7$) = 0, $\omega = 120\pi$ rad/s, $\omega_c = 2\pi$ rad/s.

Fig. 4.15 shows the steady-state error of the PRHC-SVM controller. The simulation results for PR-SVM are not shown here because they are very similar to the PRHC-SVM. As shown in Fig. 4.15, the steady-state tracking error is not significant. Figs. 4.16 and 4.17 compare the FFT analysis results of PR-SVM and PRHC-SVM. As seen in Fig. 4.16, the 4th, 6th and 7th harmonics are significant in PR-SVM; therefore these harmonics are compensated for in the PRHC-SVM. The FFT analysis results for the PRHC-SVM are shown in Fig. 4.17. It is evident that specific harmonics (6th and 7th) are suppressed appreciably and the controller is effective. The gain of each compensator determines the corresponding control effectiveness. The reduction of specific harmonics may result in an increase in other harmonics; therefore, a compromise needs to be achieved when designing the controller. Fig. 4.17 presents a compromised result and this is why there is a slight increase in the 4th order harmonic distortions.

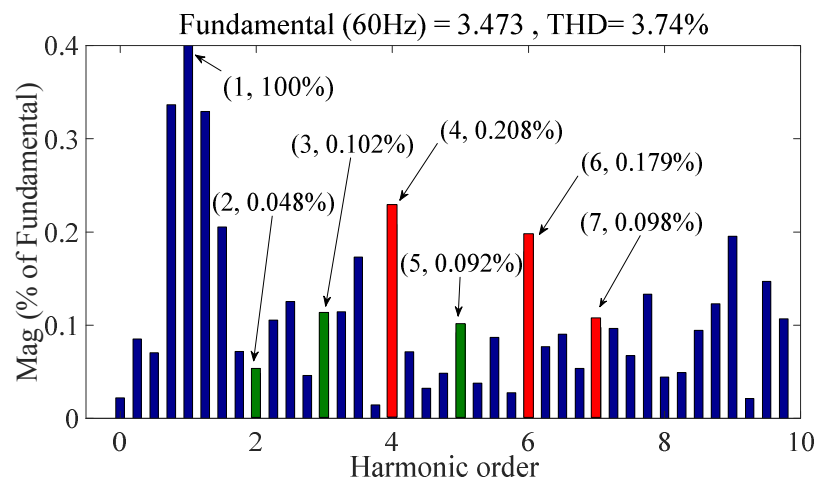


Fig. 4.16 FFT analysis of PR-SVM controlled MC output current (without harmonics compensator).

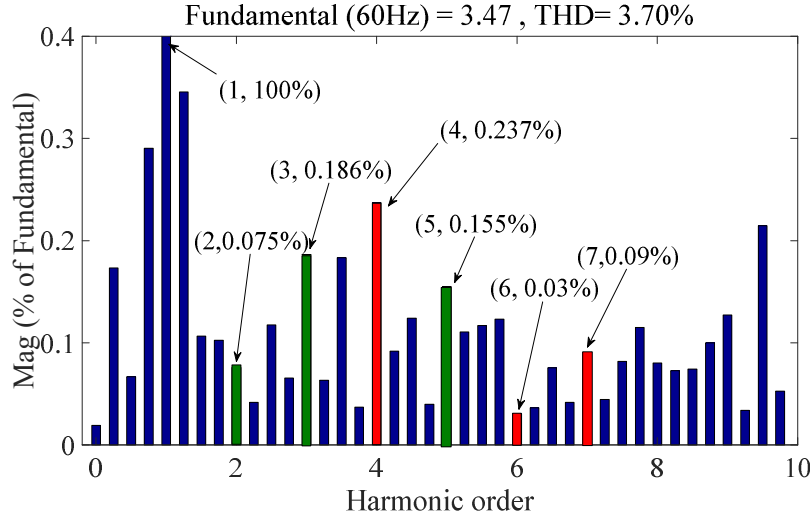


Fig. 4.17 FFT analysis of PRHC-SVM controlled MC output current (with harmonics compensator, $K_{R4} = K_{R6} = 500$, $K_{R7} = 300$).

It is worth noting that the harmonic compensator does not necessarily improve the overall THD performance. In fact, it affects the harmonic spectrum since it causes a gain reduction at the frequencies near the resonant frequencies when it compensates for the targeted harmonics as shown in Fig. 4.8. The THD of MC output currents is influenced by the voltage transfer ratio. With the PR-SVM and PRHC-SVM control schemes, the input power factor can also be regulated (being able to reach a unity power factor).

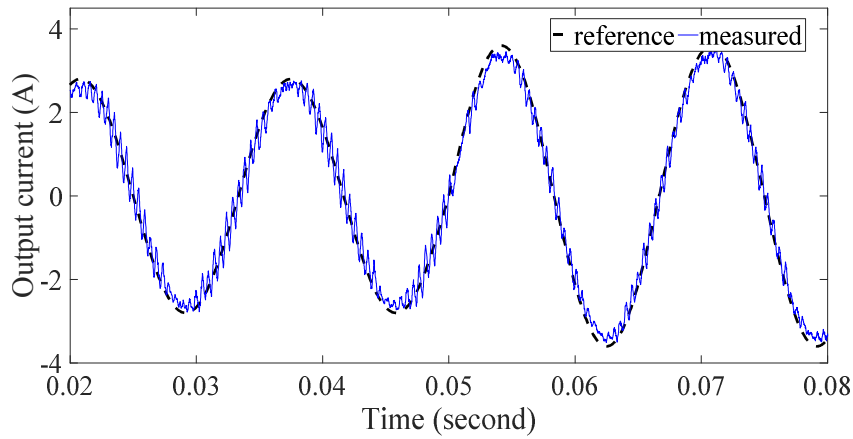


Fig. 4.18 Dynamic response of the PR-SVM to a step reference ($K_{R4} = K_{R6} = 500$, $K_{R7} = 300$).

In Fig. 4.18, the dynamic response of controller to a step change in the reference signal from 2.8 A to 3.6 A is evaluated. It can be seen that the controller exhibits a good dynamic response and tracks the prescribed reference effectively.

The above steady-state simulation results are summarized in Table 4.3. As seen in this table, the modified PI controller shows an improved steady-state performance especially in terms of error while the PR controller has better performance in terms of the THD.

Table 4.3 Simulation comparison of PI-SVM, PICF-SVM, PR-SVM and PRHC-SCM.

Method	PI-SVM	PICF-SVM	PR-SVM	PRHC-SVM
Error	0.381	0.075	0.127	0.13
THD	10.27%	7.8%	3.74%	3.7%

4.6 Experimental Validation

In order to validate the feasibility and effectiveness of the proposed strategies, an MC was built and experimental work was carried out. The experimental set up is shown in Fig. 4.19. A clamp circuit was used in the hardware to protect devices from overvoltage. The bidirectional switches (IGBTs) were arranged in a common collector configuration. As a result, only six independent driver power supplies were required to drive eighteen IGBTs. The control card is a TI TMS320F28377D series DSP board. The real-time control implementation was carried out in MATLAB/Simulink with C2000 hardware support packages. A serial communications interface was used for the communication between the host computer and DSP card. The analog to digital conversion (ADC) and peripheral circuits were employed to process the signals from the voltage and current sensors. The carrier waveform used in the modulation stage was generated from the ePWM blocks, which facilitates the implementation of the symmetrical switching sequence.

In the experimental tests, the parameters of controllers were set to the same value as those used in the simulation for each corresponding controller, unless otherwise stated. The steady-state experimental results are presented in Figs. 4.20 to 4.24 and Tables 4.4 and 4.5.

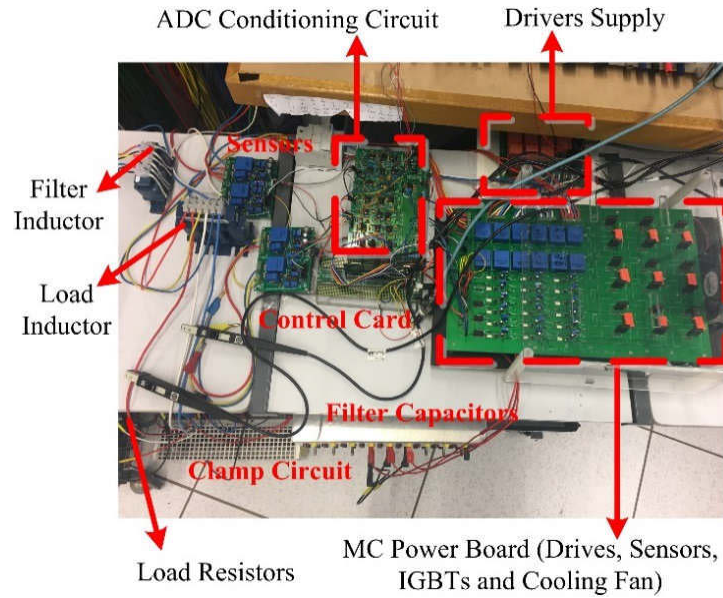
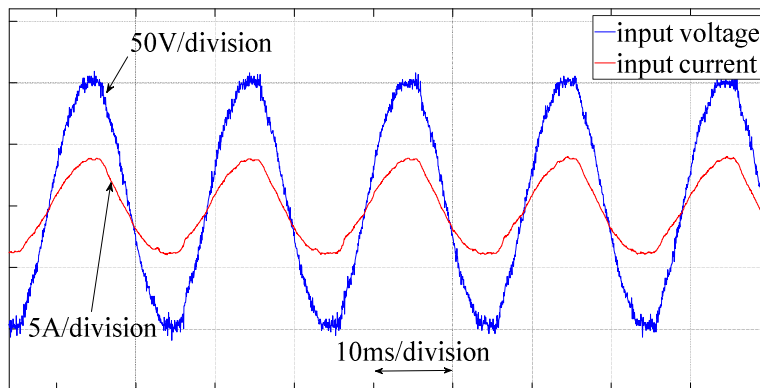
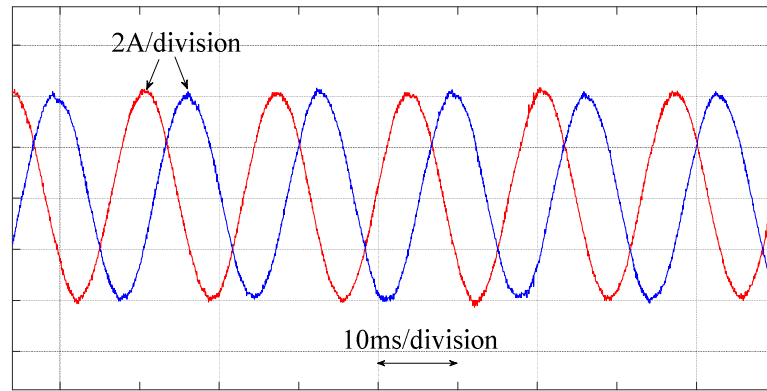


Fig. 4.19 MC prototype.

The experimental waveforms for SVM are presented in Fig. 4.20. As can be seen, the SVM controlled MC can generate sinusoidal waveforms. However, the open-loop SVM becomes ineffective in controlling the output currents to the desired values when the load is unknown.

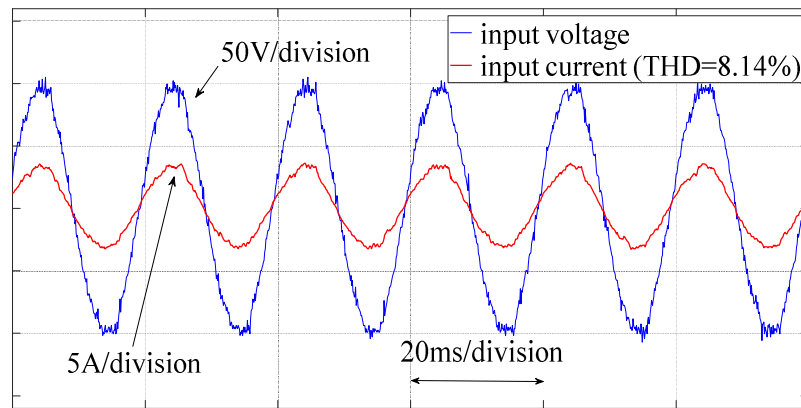


(a)

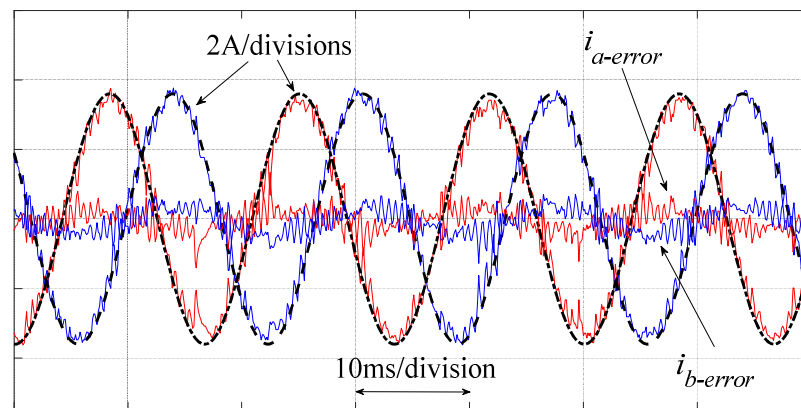


(b)

Fig. 4.20 Experimental results of SVM: (a) input voltage and current, (b) output currents (two phases).



(a)



(b)

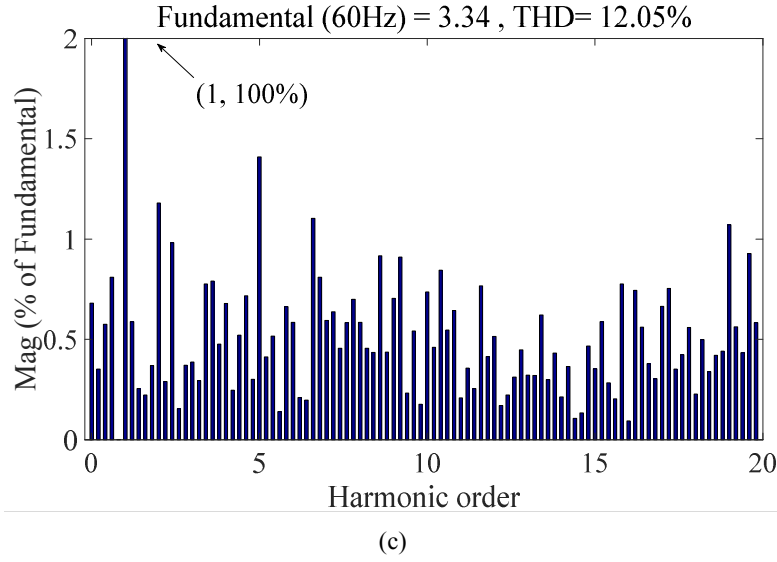
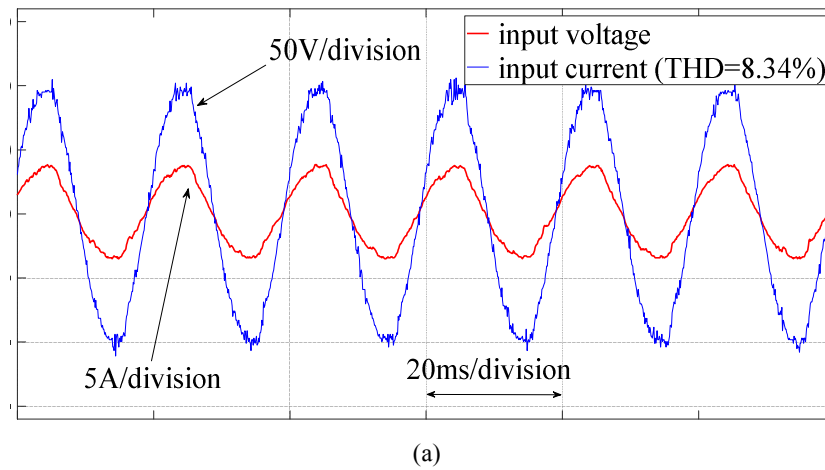
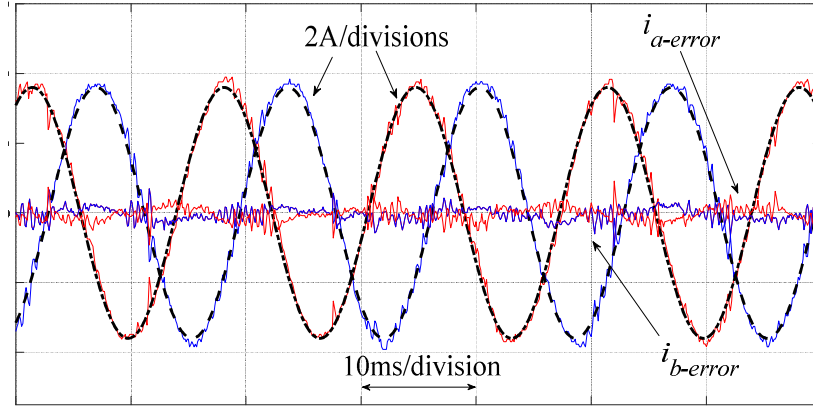


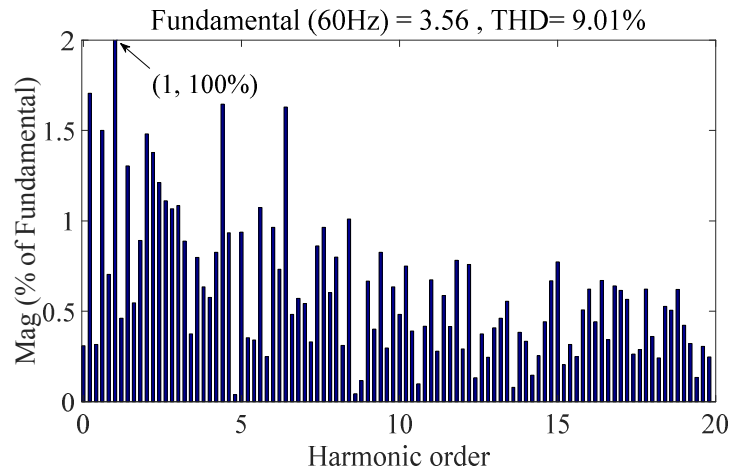
Fig. 4.21 Experimental results of PI-SVM: (a) input voltage and current, (b) output currents, (c) output current harmonics spectrum and THD.

Fig. 4.21 shows the experimental results for PI-SVM. As observed in Figs. 4.21(b) and (c), the steady-state tracking error is significant. However, for the proposed PICF-SVM controller, the fundamental current amplitude is improved from 3.34 A to 3.56 A when the reference is 3.6 A. At the same time the THD is reduced from 12.05 % to 9.01 %. These can be observed in Figs. 4.21(b)-(c) and Figs. 4.22(b)-(c). The PI-SVM and PICF-SVM controls have very similar performance in terms of the input current regulation. The input power factor is regulated to be close to one.





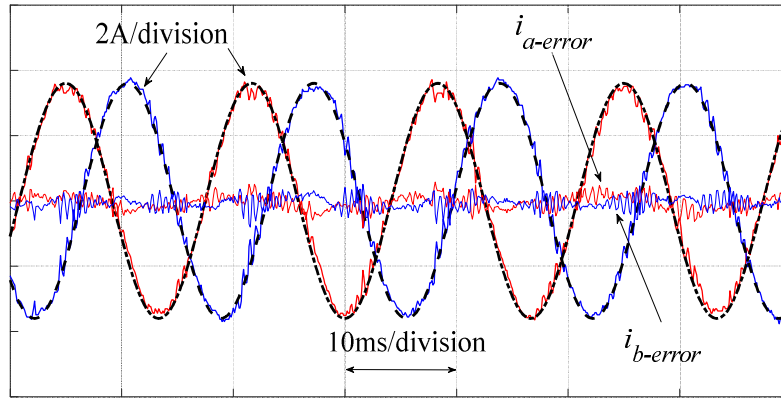
(b)



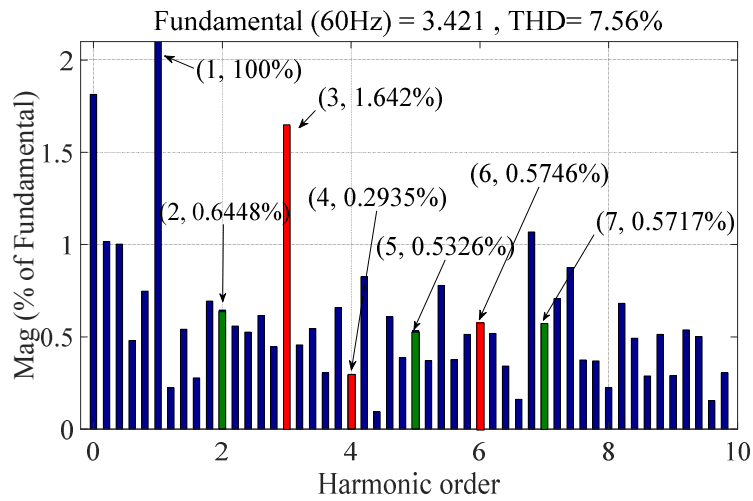
(c)

Fig. 4.22 Experimental results of PICF-SVM: (a) input voltage and current, (b) output currents, (c) output current harmonics spectrum and THD.

In the following part, the comparative experimental results for PR-SVM and PRHC-SVM are illustrated in Figs. 4.23 and 4.24, and in Table 4.3. The performance of the input current regulation is quite similar to that presented for PICF-SVM, and therefore they are not presented here. The experimental waveforms of PR-SVM controlled output currents and FFT analysis are shown in Figs. 4.23(a) and (b) respectively. Here, the 3rd harmonic, together with non-harmonic higher frequency components which are 4.2 and 6.8 time the main frequency (252 Hz and 408 Hz), are relatively more significant; therefore the 3rd, 4th and 6th harmonics are compensated for in the PRHC-SVM scheme.

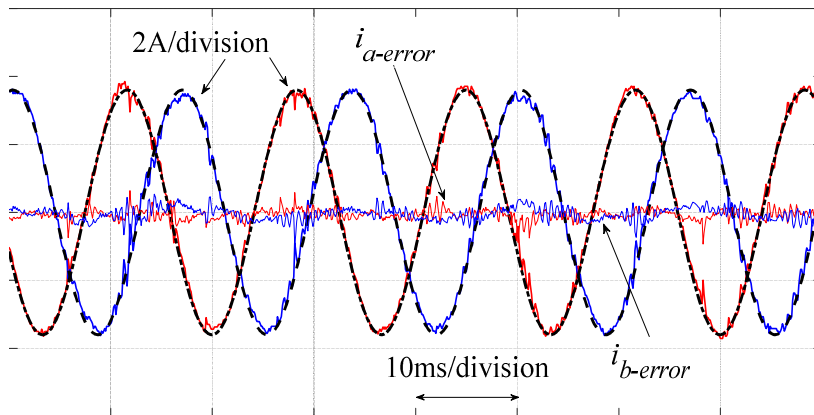


(a)



(b)

Fig. 4.23 Experimental results of PR-SVM: (a) output currents, (b) output current harmonics spectrum and THD.



(a)

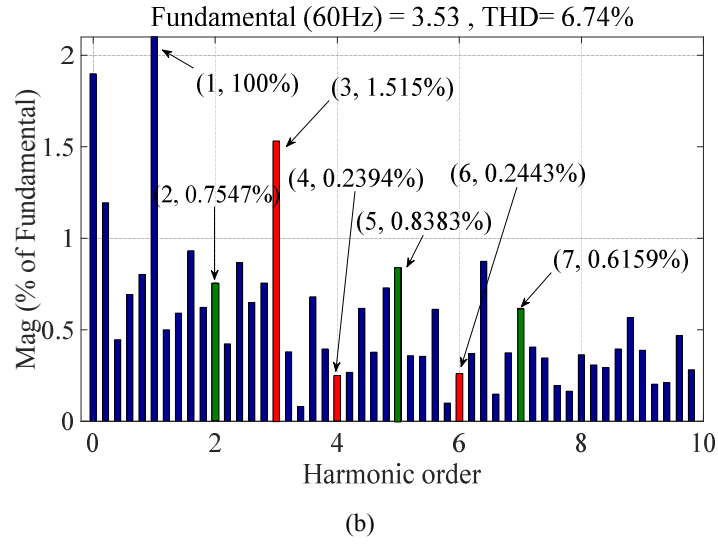


Fig. 4.24 Experimental results of PRHC-SVM: (a) output currents, (b) output current harmonics spectrum and THD.

Fig. 4.24 shows the PRHC-SVM controlled output currents and FFT analysis. Table 4.4 compares the low-order harmonics between PR-SVM and PRHC-SVM. From these results, the PRHC-SVM control can be seen to compensate selective-orders harmonics effectively.

Table 4.4 Comparison of low-order harmonics between PR-SVM and PRHC-SVM.

Harmonic	2 nd	3 rd	4 th	5 th	6 th	7 th
PR-SVM	0.6448	1.642	0.2935	0.5326	0.5764	0.5717
PRHC-SVM	0.7547	1.515	0.2394	0.8383	0.2443	0.6159

Table 4.5 Experimental comparison of PI-SVM, PICF-SVM, PR-SVM and PRHC-SVM.

Method	PI-SVM	PICF-SVM	PR-SVM	PRHC-SVM
Error	0.26	0.04	0.179	0.07
THD	12.05%	9.01%	7.56%	6.74%

Table 4.5 compares the steady-state experimental results. These results are consistent with the simulation results in Table 4.3. The modified PI controller is especially effective in reducing errors while the PR controllers have less THD.

4.7 Summary

In order to improve the steady-state tracking performance of direct MCs, this chapter proposes a combined feedforward-feedback PI controller and investigates the PR controller. Both controllers demonstrate reduced steady-state tracking error and THD. Firstly, a modified PI controller with current feedforward is proposed. The introduction of feedforward control provides extra freedom to improve the steady-state error performance. The analysis indicates that the minimum tracking error can be achieved when the coefficient of current feedforward is equal to the load resistor ($K = R$). Then a PR controller with the capability of compensating selective-order harmonics is investigated for the MC. Both of the proposed controllers are simple, easy to implement, and do not require reference frame transformations. This is because they can be implemented in the natural abc frame in a straightforward manner. The computational burden is thus reduced. A constant switching frequency is achieved because of the SVM modulation stage. In comparison, the proposed PI controller is relatively easier to implement and it demonstrates less steady-state error while the PR controller is more effective in reducing distortions.

Simulation and experimental results verify the effectiveness of the proposed controllers. These controller schemes can be readily extended to other power electronic converters and applied in relevant applications such as grid synchronization and microgrid.

The work in this chapter and other related work have been published in [3] and [5].

References

- [1] J. Rocabert, A. Luna, F. Blaabjerg, and P. Rodriguez, "Control of power converters in AC microgrids," *IEEE Trans. Ind. Electron.*, vol. 27, no. 11, pp. 4734-4749, 2012.
- [2] T. Ye, N. Dai, C. Lam, M. Wong, and J. M. Guerrero, "Analysis, Design, and Implementation of a Quasi-Proportional-Resonant Controller for a Multifunctional Capacitive-Coupling Grid-Connected Inverter," *IEEE Trans. Ind. Appl.*, vol. 52, no. 5, pp. 4269-4280, 2016.
- [3] J. Zhang, L. Li, D. G. Dorrell and Y. Guo, "A PI Controller with Current Feedforward to Improve the Steady-State Error Performance for the Current Controlled Direct Matrix Converter," 20th Int. Conf. on Electrical Machines and Systems (ICEMS 2017), Sydney, Australia, August 2017.
- [4] Y. Han, P. Shen, and J. M. Guerrero, "Stationary frame current control evaluations for three-phase grid-connected inverters with PVR-based active damped LCL filters," *J. Power Electron.*, vol. 16, no. 1, pp. 297-309, 2016.

- [5] J. Zhang, L. Li, D. Dorrell and Y. Guo, "SVM based Proportional Resonant Current Controller with Selective Harmonics Compensation for Matrix Converter Systems," 20th Int. Conf. on Electrical Machines and Systems (ICEMS), Sydney, 2017.
- [6] X. Yuan, W. Merk, H. Stemmler and J. Allmeling, "Stationary-frame generalized integrators for current control of active power filters with zero steady-state error for current harmonics of concern under unbalanced and distorted operating conditions." IEEE Trans. Ind. Appl., vol. 38, no. 2, pp. 523-532, 2002.
- [7] R. Redl, "Feedforward control of switching regulators," in Analog Circuit Design, Springer Netherlands, pp. 321-338., 2012.
- [8] G. Shen, D. Xu, L. Cao, and X. Zhu, "An improved control strategy for grid-connected voltage source inverters with an LCL filter," IEEE Trans. Power Electron., vol. 23, no. 4, pp. 1899-1906, 2008.
- [9] R. Teodorescu, F. Blaabjerg, M. Liserre, and P. C. Loh, "Proportional-resonant controllers and filters for grid-connected voltage-source converters," IEE Proc. Electric Power Appl., vol. 153, no. 5, pp. 750-762, 2006.
- [10] H. Zhang, and J. Wang, "Combined feedback–feedforward tracking control for networked control systems with probabilistic delays," J. the Franklin Institute, vol. 351, no. 6, pp. 3477-3489, 2014.
- [11] A. Koerber, and R. King, "Combined feedback–feedforward control of wind turbines using state-constrained model predictive control," IEEE Trans. Control Syst. Tech., vol. 21, no. 4, pp.1117-1128, 2013.
- [12] L. Y. Pao, J. A. Butterworth, and D. Y. Abramovitch, "Combined feedforward/feedback control of atomic force microscopes," In American Control Conf. (ACC'07), pp. 3509-3515, 2007.
- [13] R. Guo, "Modeling and simulation of run-out table cooling control using feedforward-feedback and element tracking system," IEEE Trans. Ind. Appl., vol. 33, no. 2, pp. 304-311, 1997.
- [14] H. Cha, T. K. Vu, and J. E. Kim, "Design and control of Proportional-Resonant controller based Photovoltaic power conditioning system," IEEE Energy Conversion Congr. Exposition (ECCE), pp. 2198-2205, 2009.
- [15] A. Timbus, M. Liserre, R. Teodorescu, P. Rodriguez, and F. Blaabjerg, "Evaluation of current controllers for distributed power generation systems," IEEE Trans. Power Electron., vol. 24, no. 3, pp. 654-664, 2009.
- [16] X. Liang, "Emerging power quality challenges due to integration of renewable energy sources," IEEE Trans. Ind. Appl., vol. 53, no. 2, pp. 855-866, 2017.
- [17] A. Timbus, M. Ciobotaru, R. Teodorescu, and F. Blaabjerg, "Adaptive resonant controller for grid-connected converters in distributed power generation system," 21st IEEE Applied Power Electron. Conf. and Exposition (APEC'06), pp. 6, 2006.
- [18] A. Hasanzadeh, O. C. Onar, H. Mokhtari, and A. Khaligh, "A proportional-resonant controller-based wireless control strategy with a reduced number of sensors for parallel-operated UPSs," IEEE Trans. Power Del., vol. 25, no. 1, pp. 468-478, 2010.
- [19] F. Blaabjerg, R. Teodorescu, M. Liserre, and A. V. Timbus, "Overview of control and grid synchronization for distributed power generation systems," IEEE Trans. Ind. Electron., vol. 53, no. 5, pp. 1398-1409, 2006.

- [20] A. Vidal, F. D. Freijedo, A. G. Yepes, P. Fernandez-Comesana, J. Malvar, Ó. López, and J. Doval-Gandoy, "Assessment and optimization of the transient response of proportional-resonant current controllers for distributed power generation systems," *IEEE Trans. Ind. Electron.*, vol. 60, no. 4, pp. 1367-1383, 2013.
- [21] G. Shen, X. Zhu, J. Zhang, and D. Xu, "A new feedback method for PR current control of LCL-filter-based grid-connected inverter," *IEEE Trans. Ind. Electron.*, vol. 57, no. 6, pp. 2033-2041, 2010.
- [22] P. Wheeler, J. Rodriguez, J. Clare, L. Empringham, and A. Weinstein, "Matrix converters: a technology review," *IEEE Trans. Ind. Electron.*, vol. 49, no. 2, pp. 276-288, 2002.
- [23] J. Zhang, L. Li, Z. Malekjamshidi and D. G. Dorrell, "Predictive Voltage Control of Direct Matrix Converter with Reduced Number of Sensors for the Renewable Energy and Microgrid Applications," *IEEE Energy Conversion Congress and Exposition (ECCE 2017)*, Cincinnati, U.S., pp. 3309-3315, October 2017.
- [24] A. Trentin, L. Empringham, L. Lillo, P. Zanchetta, P. Wheeler, and J. Clare, "Experimental Efficiency Comparison Between a Direct Matrix Converter and an Indirect Matrix Converter Using Both Si IGBTs and SiC mosfets," *IEEE Trans. Ind. Appl.*, vol. 52, no. 5, pp. 4135-4145, 2016.
- [25] J. Zhang, L. Li, T. He, M. Aghdam, D. G. Dorrell, " Investigation of Direct Matrix Converter Working as a Versatile Converter (AC/AC, AC/DC, DC/AC, DC/DC Conversion) with Predictive Control," *43rd Ann. Conf. of the IEEE Ind. Electron. Society (IECON 2017)*, Beijing, China, pp. 4644-4649, November 2017.
- [26] Yaskawa, Low Harmonics Regenerative Matrix Converter U1000. [online]. <http://www.pillar.com.mx/Varios/CATALOGO%20TECNICO%20U1000.pdf>
- [27] Yaskawa, AC7 Matrix Drive. [online]. <https://www.yaskawa.com/products/drives/industrial-ac-drives/general-purpose-drives/ac7-matrix-drive>
- [28] M. Munzer, "EconoMac – the First All In One IGBT Module for Matrix Converters“, *Drives and Control Conf.*, Section 3, London, 2001.
- [29] J. Itoh, A. Odaka, and I. Sato, "High efficiency power conversion using a matrix converter." *Fuji Electric Review*, vol. 50, no. 3, pp. 94-98, 2004.
- [30] Fuji Electric, Fuji Electric FA Components & Systems Releases Next Generation Matrix Converter FRENIC-Mx Series, [online]. <http://www.fujielectric.com/company/news/2006/06030601.html>.
- [31] E. Yamamoto, J. Kang, and H. Krug, "Development of Matrix Converter for Industrial Applications," *Yaskawa White Paper*, 2007.
- [32] Yaskawa, FSdrive-MX1S - Super Energy Saving Medium Voltage Matrix Converter with Power Regeneration. [online]. <http://www.yaskawa.com.sg/product/converter-2/fsdrive-mx1s---super-energy-saving-medium-voltage-matrix-converter-with-power-regeneration>.
- [33] K. Ogata, "PID controllers and modified PID controllers," in *Modern Control Engineering*, fifth edition, PEARSON, pp. 577-651, 2010.
- [34] J. Rocabert, A. Luna, F. Blaabjerg, and P. Rodriguez, "Control of power converters in AC microgrids," *IEEE Trans. Ind. Electron.*, vol. 58, no. 11, pp. 4734-4749, 2012.

- [35] R. Teodorescu, F. Blaabjerg, and M. Liserre, "Proportional-resonant controllers. A new breed of controllers suitable for grid-connected voltage-source converters," OPTIM, Brasov, Romania. 2004.
- [36] J. Zhang, L. Li, and D. Dorrell, "DQ Coupling Suppressed PID Controller for the Transmission Line Power Flow Control Using a Matrix Converter," 42nd Ann. Conf. of the IEEE Ind. Electron. Society (IECON16), Florence, Italy, pp. 6249 – 6254, October 2016.
- [37] J. Zhang, D. Dorrell, and L. Li, "Applications of the Direct Space Vector Modulation Controlled Matrix Converter as the Unified Power Flow Controller," 8th Int. conf. power electron. motor drives (PEMD2016), Glasgow, UK, pp. 1-6, April 2016.

5 HYSTERESIS AND DTC CONTROL FOR MOTOR DRIVES

The AC motor drive is a potential application area where the MC can be used. Compared with the traditional AC motor drives, MC based motor drives have some benefits. It is particularly suitable for the application areas where the size and volume are limited. In this chapter, two control strategies, the hysteresis band (HB) and direct torque control (DTC) strategies, are investigated for the MC-fed AC motor drive.

5.1 Hysteresis Current Controller for Motor Drives

The HB controller offers excellent dynamic performance. It has been widely researched and used in voltage source inverters (VSIs) and inverter-fed drives; however, it has not been investigated within the context of an MC or an MC-based motor drive. In this chapter, both fixed-band and sinusoidal-band hysteresis current controllers are proposed and developed for a direct MC. A comprehensive comparative evaluation of the two methods is carried out. Both methods have fast dynamic performance and they inherently integrate the line modulation technique of the virtual rectifier stage into the overall modulation. Surge currents are prevented with the proposed scheme. The sinusoidal-band hysteresis controller has lower THD at the expense of higher average

switching frequency, which is only significantly observable at very high sampling frequencies. The proposed controller is integrated with field-oriented control to drive an MC-fed permanent magnet synchronous machine. The proposed methods are simple and incur a light computational burden, which advances the practical applications of MCs in AC motor drives. The simulation and experiment results demonstrate the effectiveness and feasibility of the proposed scheme.

5.1.1 Introduction

Field-oriented control (FOC) is a classical control approach for electrical machines and it is a commonly used linear control strategy for medium- and low-power motor drives [1]. FOC-based electrical drive systems are mature and utilized extensively in high-performance drives [2]. Current controllers are vital components in the FOC method. Modern electrical drive systems use an induction motor, brushless permanent magnetic motor or other motor. They are controlled from a VSI, which are prevalent in industrial adjustable speed drives [3]. For a VSI based drive system, current controllers are preferred for the high-performance drives because of their excellent dynamic behaviour. Among these current controllers, the HB current controller features inherent current limiting capability, robustness, no modulation stage, and simple implementation. These are in addition to excellent dynamic and tracking performance [4]. The HB control has been mainly constrained to the VSI, and active research on this includes constant switching frequency control [5], online computation of bands [6], and multi-band hysteresis control [7][8]. In [9], a comparative study for fixed-band and sinusoidal-band hysteresis current controllers (F-HB and S-HB) was carried out for VSIs; however, hysteresis bands are impractical, and the comparison needs further evaluation for various band widths and sampling frequencies. In the literature, there is no detailed published research on either F-HB or S-HB control for a direct MC [10].

In VSI-fed motor drive systems, a dynamic braking chopper is often used to absorb the kinetic energy generated from motor deceleration; otherwise, for generator operation mode, back-to-back converters are used. These will make the system bulkier, decrease the efficiency and increase the complexity.

These problems can be addressed with the MC based drive system using F-HB and S-HB control techniques. A 3×3 direct MC is a flexible power converter which is capable of bidirectional power flow, sinusoidal waveform, regenerative ability, controllable

input power factor and compact volume [11]-[13]. With an MC based drive system, one significant benefit is that the braking chopper is removed as shown in Fig. 5.1. Therefore four-quadrant operation is enabled. In addition to motor drive applications, the MC and its derivatives have been proposed for numerous applications including aerospace systems [14], microgrids [15], flexible alternating current transmission systems [16] and electric vehicles [17].

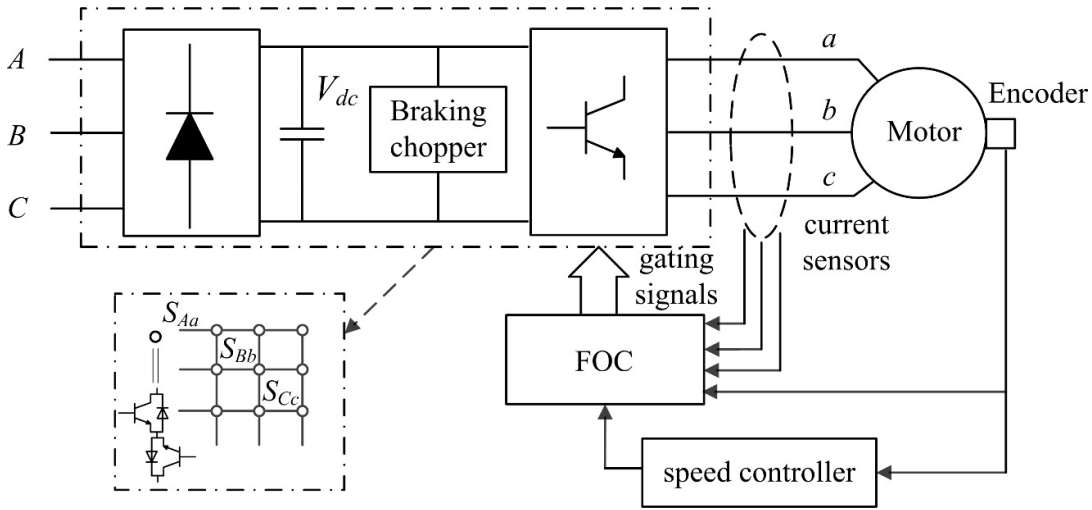


Fig. 5.1 The FOC controlled drive system with VSI or MC.

In terms of MC-fed motor drives, the most common drive applications use the induction machine [18]-[20] while only few use the brushless permanent magnet machine. For the brushless permanent machine, these can be split up in the brushless permanent magnet DC machine (trapezoidal current) or brushless permanent magnet synchronous machine (PMSM) which has sinusoidal current; the latter is suitable for MC control [21]. PMSMs are more efficient compared with the induction motor since they do not have rotor current so the field requires no external current to support it. Other merits of the PMSM include high torque-to-current ratio, low inertia and compact design. Because of these, the PMSM is gaining increasing interest and popularity in high-performance variable-speed drives. However, they use rare earth magnet material which makes them more expensive compared to an induction motor and they require synchronization, so a shaft encoder is usually required. In an MC based PMSM drive system, the favourable features of the MC and PMSM can be combined for a high-performance drive application.

For the control of MC based drives, many methods have been proposed. DTC and predictive torque control have been investigated [18]-[24]. With regards to DTC control, the known issues of large torque ripple especially in low-speed operation, persist. In the case of predictive control, the computing burden is heavy because of the high number of switch actions (27 possibilities) of the MC. Another standard control strategy is the space vector modulation (SVM) based proportional-integral (PI) controller. This controller requires an SVM modulation stage and has more demands in terms of parameter tuning. This is because of an extra current PI controller in addition to the speed PI controller. This controller requires multiple synchronous reference frame transformations ($abc \leftrightarrow dq$). In fact, the FOC based method is rarely investigated for MC based motor drives. HB and HB-based FOC for a 3×3 direct MC in an MC-based drive remain unexplored even though the HB controller is simple and has a low computational burden.

This work proposes and studies the HB current controller and HB based FOC for an MC-fed PMSM drive. Several features of the MC and PMSM can be integrated into one system. Compared with SVM based control strategies [25], the proposed controller does not require an extra modulation stage but includes the modulation of the virtual rectifier stage of the MC. The proposed HB controller requires only one synchronous frame transformation ($dq \rightarrow abc$) when used in an MC-fed motor drive. This reduces the complexity and computational burden. Both F-HB and S-HB current controllers are developed and compared. Both methods demonstrate good dynamic features. Comparative results show that the S-HB controller has less low-order harmonics and lower THD at the cost of higher average switching frequency. However, according to comparative studies, improved performance of the S-HB in terms of THD is only appreciably observable when the sampling interval is very short. Furthermore, HB current controllers are integrated with the FOC to drive a PMSM with an MC. S-HB shows slightly lower stator current and torque ripple. The braking chopper is not required in this structure. The proposed method is very simple, effective and practical to implement; which is an advancement with respect to industrial applications of an MC based drive system.

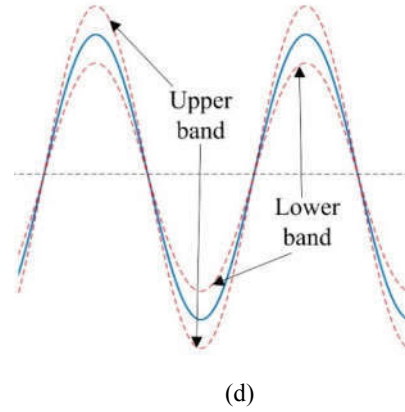
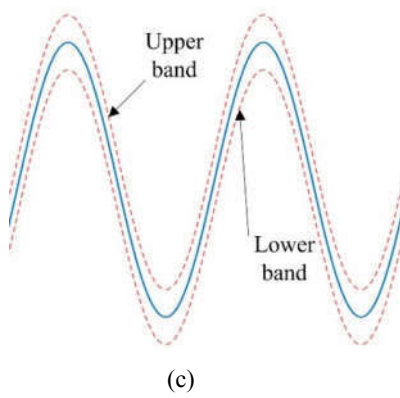
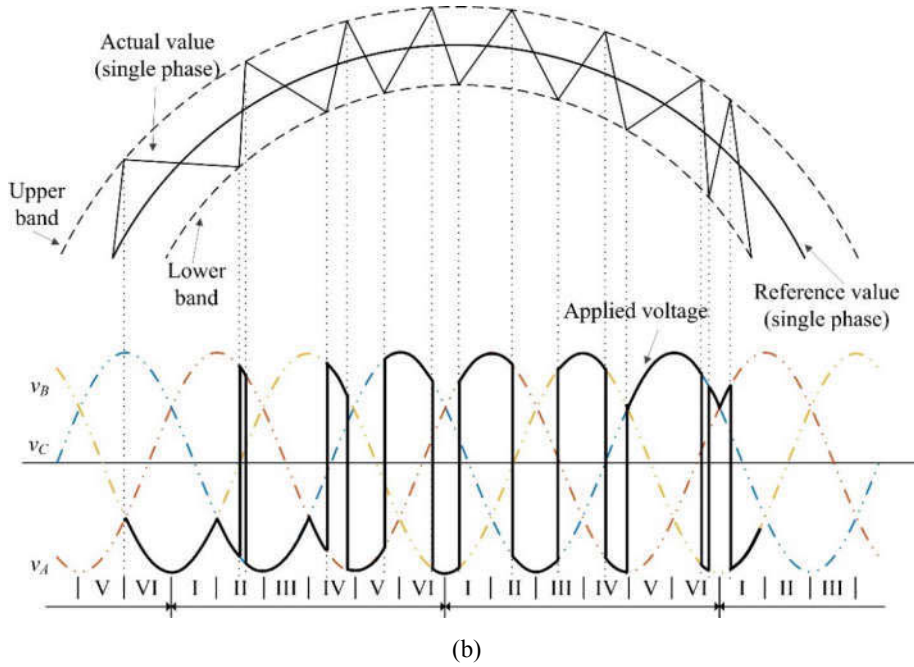
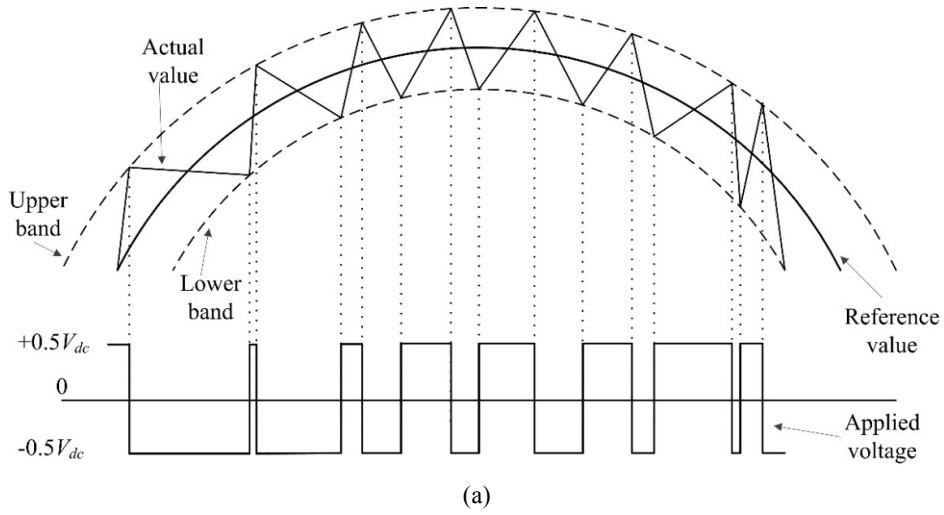


Fig. 5.2 HB current controller diagrams: (a) HB for the VSI, (b) HB for the MC, (c) F-HB band, (d) S-HB band.

5.1.2 HB controller for the MC output currents

(a). Fixed-Band Hysteresis Control for MC

The rationale of an HB controller is simple. The HB current controller for the VSI is illustrated in Fig. 5.2(a) for one of the phases and described by

$$\begin{aligned} i_{upper} &= I_{ref} \sin(\omega_{ref}t + \theta_{ref}) + \frac{h}{2} \\ i_{lower} &= I_{ref} \sin(\omega_{ref}t + \theta_{ref}) - \frac{h}{2} \end{aligned} \quad (5.1)$$

$$\begin{aligned} \text{If } i_a > i_{upper}, v_{ao} &= -0.5V_{dc} \\ \text{if } i_a < i_{lower}, v_{ao} &= +0.5V_{dc} \end{aligned} \quad (5.2)$$

where I_{ref} is the reference current amplitude and h is the hysteresis controller band width and it is fixed (F-HB, Fig. 5.2(c)). θ_{ref} and ω_{ref} are the initial phase angle and angular frequency of the phase a reference current. i_{upper} and i_{lower} are the upper and lower bands of the HB current controller. i_a is the actual current of phase a . V_{dc} is the DC link voltage and v_{ao} is the applied voltage across output phase a and the neutral point of DC link. The control law in (5.2) is straightforward. When the actual current exceeds the upper band, the upper/lower leg is turned off/on to reduce the current and vice versa. Therefore, in theory, the actual currents will always be regulated to stay within the prescribed boundaries. Similarly the HB current controllers for an MC can be developed.

In terms of the MC, the upper and lower bands in (5.1) for the F-HB are shown in Fig. 5.2(b). The controller law is obtained in a manner similar to a VSI but with further modification. In Fig. 5.2(b), the single-phase current control is shown and the maximum or minimum voltage is selected to increase or decrease the currents where:

$$\begin{aligned} \text{If } i_a > i_{upper}, v_a &= \text{minimum}(v_A, v_B, v_C) \\ \text{if } i_a < i_{lower}, v_a &= \text{maximum}(v_A, v_B, v_C) \end{aligned} \quad (5.3)$$

It is worth noting that the MC offers more flexibility compared with VSI as it offers more voltage choices. In general, there are three levels of voltages available in MC rather than two in VSI. This flexibility benefits the implementation of multi-band HB control [26].

(b). Sinusoidal-Band Hysteresis Control for MC

The sinusoidal bands are shown in Fig. 5.2(d) and can be expressed as

$$\begin{aligned} i_{upper} &= \left(I_{ref} + \frac{h}{2} \right) \sin(\omega_{ref}t + \theta_{ref}) \\ i_{lower} &= \left(I_{ref} - \frac{h}{2} \right) \sin(\omega_{ref}t + \theta_{ref}) \end{aligned} \quad (5.4)$$

With S-HB, the control law is slightly modified as the relative locations of upper and lower bands are alternated every half cycle, for the a -phase:

$$\begin{aligned} \text{For } i_{ref} > 0, \text{ if } i_a > i_{upper}, v_a &= \text{minimum}(v_A, v_B, v_C) \\ \text{if } i_a < i_{lower}, v_a &= \text{maximum}(v_A, v_B, v_C) \end{aligned} \quad (5.5)$$

$$\begin{aligned} \text{For } i_{ref} < 0, \text{ if } i_a > i_{upper}, v_a &= \text{maximum}(v_A, v_B, v_C) \\ \text{if } i_a < i_{lower}, v_a &= \text{minimum}(v_A, v_B, v_C) \end{aligned} \quad (5.6)$$

where $i_{ref} = I_{ref} \sin(\omega_{ref}t + \theta_{ref})$ is the reference current. If the reference current is in the positive half cycle and when the actual current exceeds the upper band, the voltage that enables current reduction is selected; when the actual current reaches the lower band, the voltage that drives current increase is selected; see (5.5). Alternatively, if the reference current is in the negative half cycle and when the actual current exceeds the upper band, the maximum voltage that can increase the current is employed; when the actual current reaches the lower band, the minimum voltage that can decrease the current is used; see (5.6). Therefore, the actual currents can be theoretically controlled to be within the region with the predefined band-width. The above methods are demonstrated for a single-phase case and it can be readily extended to the three-phase case because of symmetry.

5.1.3 Overall modulation of MC

A switching look-up table for the F-HB can be derived which is shown in Table 5.1. It is based on the hysteresis controller and input voltage sectors (Fig. 5.2(b)). The F-HB hysteresis comparator outputs, which are used as indices in the look-up Table 5.1, are described by

$$\begin{cases} HB_x = 0, \text{ if } I_x < I_{x-lower} \\ HB_x = 1, \text{ if } I_x > I_{x-upper} \end{cases} \quad x = a, b, c \quad (5.7)$$

The output values in (5.7) correspond to the digits of the first column in Table 5.1. For example, the index 001 indicates $i_a < i_{a-lower}$, $i_b < i_{b-lower}$ and $i_c > i_{c-upper}$. The input voltage sectors, which show the amplitude relationships of the input voltages, are used to determine the switch states. For instance, if the input voltages are in Sector I, switches S_{Aa} , S_{Ab} and S_{Bc} are turned on since v_A is maximum and v_B is minimum; see Fig. 5.2(b). Therefore, i_a and i_b will increase while i_c will decrease. A switching look-up table can also be obtained for the S-HB controller in a very similar manner, and therefore it is not shown here to avoid repetition. There are 18 MC switch states in Table 5.1; they correspond to 18 active MC vectors.

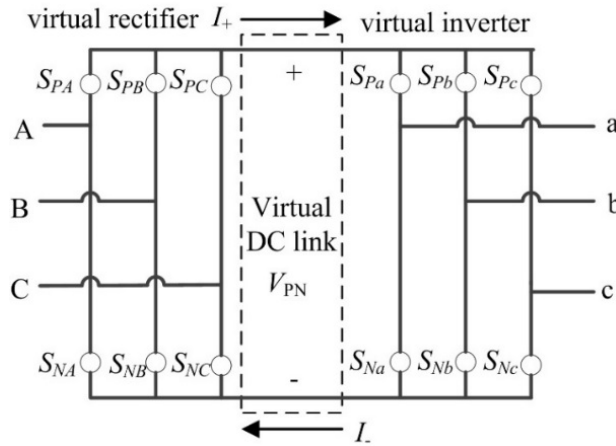


Fig. 5.3 Illustration of overall modulation with virtual rectifier, inverter and DC link.

Table 5.1 Switch states look-up table of F-HB control for MC.

	I	II	III	IV	V	VI
001	S_{Aa}, S_{Ab}, S_{Bc}	S_{Aa}, S_{Ab}, S_{Cc}	S_{Ba}, S_{Bb}, S_{Cc}	S_{Ba}, S_{Bb}, S_{Ac}	S_{Ca}, S_{Cb}, S_{Ac}	S_{Ca}, S_{Cb}, S_{Bc}
010	S_{Aa}, S_{Bb}, S_{Ac}	S_{Aa}, S_{Cb}, S_{Ac}	S_{Ba}, S_{Cb}, S_{Bc}	S_{Ba}, S_{Ab}, S_{Bc}	S_{Ca}, S_{Ab}, S_{Cc}	S_{Ca}, S_{Bb}, S_{Cc}
011	S_{Aa}, S_{Bb}, S_{Bc}	S_{Aa}, S_{Cb}, S_{Cc}	S_{Ba}, S_{Cb}, S_{Cc}	S_{Ba}, S_{Ab}, S_{Ac}	S_{Ca}, S_{Ab}, S_{Ac}	S_{Ca}, S_{Bb}, S_{Bc}
100	S_{Ba}, S_{Ab}, S_{Ac}	S_{Ca}, S_{Ab}, S_{Ac}	S_{Ca}, S_{Bb}, S_{Bc}	S_{Aa}, S_{Bb}, S_{Bc}	S_{Aa}, S_{Cb}, S_{Cc}	S_{Ba}, S_{Cb}, S_{Cc}
101	S_{Ba}, S_{Ab}, S_{Bc}	S_{Ca}, S_{Ab}, S_{Cc}	S_{Ca}, S_{Bb}, S_{Cc}	S_{Aa}, S_{Bb}, S_{Ac}	S_{Aa}, S_{Cb}, S_{Ac}	S_{Ba}, S_{Cb}, S_{Bc}
110	S_{Ba}, S_{Bb}, S_{Ac}	S_{Ca}, S_{Cb}, S_{Ac}	S_{Ca}, S_{Cb}, S_{Bc}	S_{Aa}, S_{Ab}, S_{Bc}	S_{Aa}, S_{Ab}, S_{Cc}	S_{Ba}, S_{Bb}, S_{Cc}

The above methods integrate the line-commutated modulation of the MC input currents. To explain this, the overall MC modulation is divided into a virtual rectifier and a virtual inverter stage as shown in Fig. 5.3. These two virtual stages can be modulated independently using different methods. The output current of the virtual inverter stage is modulated with the VSI HB control, while the input current of the virtual rectifier stage is regulated with a line-commutated approach. For example, in F-HB, if the output phase a current i_a reaches the lower band ($i_a < i_{a-lower}$) and the maximum input voltage is v_B at this moment, then S_{Pa} and S_{PB} in Fig. 5.3 are turned on to increase the current i_a . Turning on the switches S_{Pa} and S_{PB} results in the connection between the output phase a and input phase B . Therefore, the equivalent switch S_{Ba} in the direct MC is switched on. The same rule applies to other situations. Therefore, the input currents are controlled automatically. An equivalent look-up table can be tabulated based on this. It is worth noting that different modulation techniques, such as SVM, for the virtual rectifier stage, can be incorporated into the overall modulation scheme to control the input currents.

5.1.4 FOC with HB controller for PMSM

(a). PMSM Model Description

In this section, FOC is implemented for the MC based PMSM drive system using the HB current controller. The FOC converts the AC motor dynamics so they are similar to an equivalent DC motor where the torque and flux are decoupled. FOC relies upon the fact that the motor rotor flux and torque can be controlled through the d and q components of the stator current which are usually provided by a current-controlled PWM inverter.

This is achieved by using the abc to dq fame transformation,

$$\begin{bmatrix} i_d \\ i_q \\ i_0 \end{bmatrix} = \begin{bmatrix} \cos(\theta_s) & \cos\left(\theta_s - \frac{2\pi}{3}\right) & \cos\left(\theta_s + \frac{2\pi}{3}\right) \\ -\sin(\theta_s) & -\sin\left(\theta_s - \frac{2\pi}{3}\right) & -\sin\left(\theta_s + \frac{2\pi}{3}\right) \\ 0.5 & 0.5 & 0.5 \end{bmatrix} \begin{bmatrix} i_a \\ i_b \\ i_c \end{bmatrix} \quad (5.8)$$

and the reverse transformation,

$$\begin{bmatrix} i_a \\ i_b \\ i_c \end{bmatrix} = \begin{bmatrix} \cos(\theta_s) & -\sin(\theta_s) & 1 \\ \cos\left(\theta_s - \frac{2\pi}{3}\right) & -\sin\left(\theta_s - \frac{2\pi}{3}\right) & 1 \\ \cos\left(\theta_s + \frac{2\pi}{3}\right) & -\sin\left(\theta_s + \frac{2\pi}{3}\right) & 1 \end{bmatrix} \begin{bmatrix} i_d \\ i_q \\ i_0 \end{bmatrix} \quad (5.9)$$

where $i_{a,b,c}$ are the three phase currents in the abc system and $i_{d,q,0}$ are the currents in dq system. $i_0 = 0$ for a balanced three-phase system. θ_s is the synchronous reference angle which can be obtained from an encoder.

Using synchronous reference frame transformations, the PMSM model equations can be obtained for the FOC control [27] and they can be expressed as

$$\frac{di_d}{dt} = \frac{v_d}{L_d} - \frac{R_s}{L_d} i_d + \frac{L_q}{L_d} p \omega_m i_q \quad (5.10)$$

$$\frac{di_q}{dt} = \frac{v_q}{L_q} - \frac{R_s}{L_q} i_q - \frac{L_d}{L_q} p \omega_m i_d - \frac{\psi_f p \omega_m}{L_q} \quad (5.11)$$

$$\psi_d = L_d i_d + \psi_f \quad (5.12)$$

$$\psi_q = L_q i_q \quad (5.13)$$

$$\frac{d\theta}{dt} = \omega_m \quad (5.14)$$

$$T_e = \frac{3}{2} p [\psi_f i_q + (L_d - L_q) i_d i_q] \quad (5.15)$$

where L_d and L_q are PMSM d- and q-axis inductance; p is the number of pole pairs; R_s is the stator resistance; ψ_f is the flux established by permanent magnet; ψ_d and ψ_q are stator flux components in d and q axis; v_d and v_q are the stator voltage components in the dq axis; θ is the rotor angular position and ω_m is the rotor speed. T_e is the electromagnetic motor torque. ω^* in the figures is the rotor speed reference. In the tested surface-mounted PMSM, $L_d = L_q = L$ because the permanent magnets are surface mounted and the reluctance in every position is same, which simplifies (5.15) to

$$T_e = \frac{3}{2} p \psi_f i_q \Rightarrow i_q = \frac{2}{3 p \psi_f} T_e \quad (5.16)$$

If $i_d = 0$ holds, the maximum torque per ampere control can be achieved for the tested non-salient pole PMSM. The electromagnetic torque generated by a PMSM can be controlled by the q-axis component of the stator current. To carry out the coordinate transformation ($dq \rightarrow abc$) in (5.9), the rotor position is obtained from an encoder. The torque reference T_e^* can be either specified by the operator or obtained from a closed-loop speed controller. Here a PI controller is used to generate the torque reference from the rotor speed error. The obtained i_q^* reference together with i_d^* are converted into i_{abc}^* in the abc frame and then sent to the MC HB controller.

(b). HB-FOC Controller Design

Based on the model derived above, the FOC controller combined with the HB controller can be designed for the MC based PMSM drive as shown in Fig. 5.4. The HB controller generates gating signals for the semiconductor devices and sensors are used to measure the motor speed and currents. The speed controller adopted in this work is a common PI controller whose parameters are given in Table 5.3.

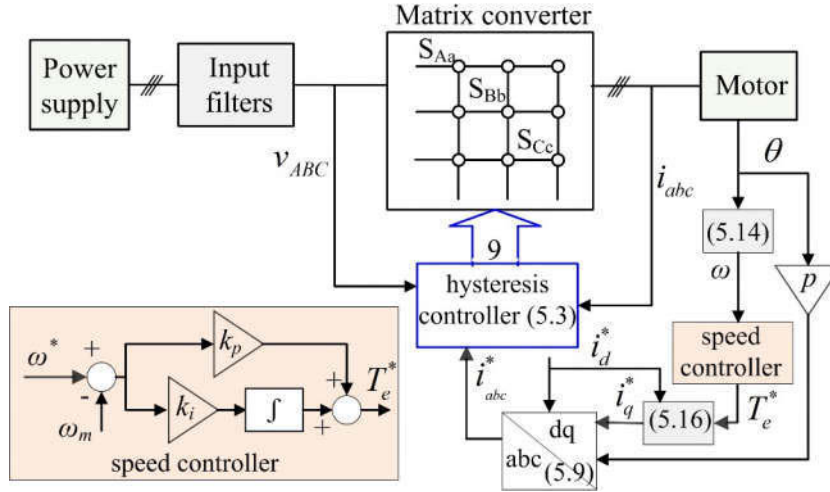


Fig. 5.4 HB-FOC controller diagram for MC based PMSM drive.

Table 5.2 MC input power supply, filter and load parameters.

V_{SA} (V)	f_s (Hz)	L_A (mH)	r_A (Ω)	C_{AB} (μ F)	R_L (Ω)	L_L (mH)
40	50	4.8	30	15	5	10

Table 5.3 PMSM system and controller parameters for F-HB based MC-PMSM drive.

$R_s (\Omega)$	L (mH)	p	J (kg·m ²)	ψ_f (Wb)	ω_N (rpm)	T_N (N·m)
1.8	15.05	3	0.002	0.1057	1500	4.5

Table 5.3 (continued).

K_p	K_i	h	T_s (s)
0.05	1	0.02	50×10^{-6}

5.1.5 Simulation and Experimental Results

(a). Simulation Results

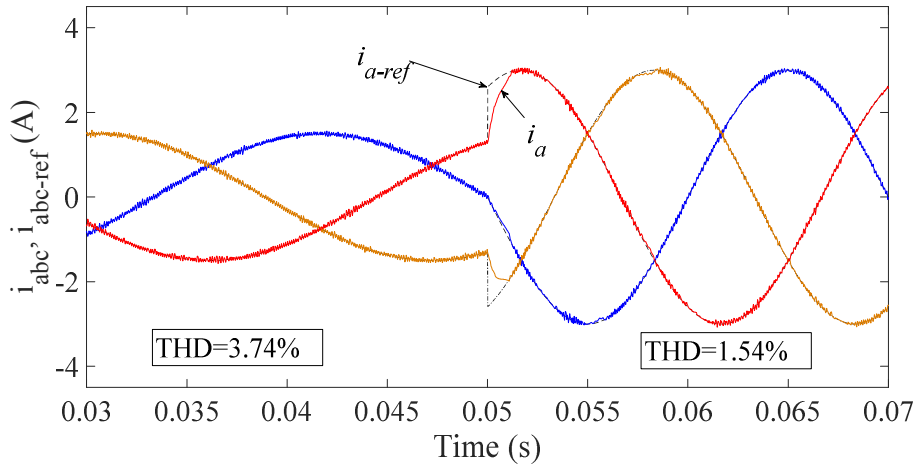
The simulated system and controller parameters, unless elsewhere specified, are tabulated in Tables 5.2 and 5.3. The loads under test are three-phase inductive loads. The steady-state simulation results of F-HB and S-HB tracking reference currents $i_{abc-ref} = [3\sin(120\pi t) \ 3\sin(120\pi t - 2\pi/3) \ 3\sin(120\pi t + 2\pi/3)]$ A under various sampling intervals and HB bands are tabulated in Table 5.4. As summarized in this table, S-HB exhibits improved THD performance, especially low-order harmonics, while the average switching frequencies are higher. These are only appreciably observable when sampling interval is sufficiently short.

Table 5.4 Comparative results for performances of F-HB and S-HB.

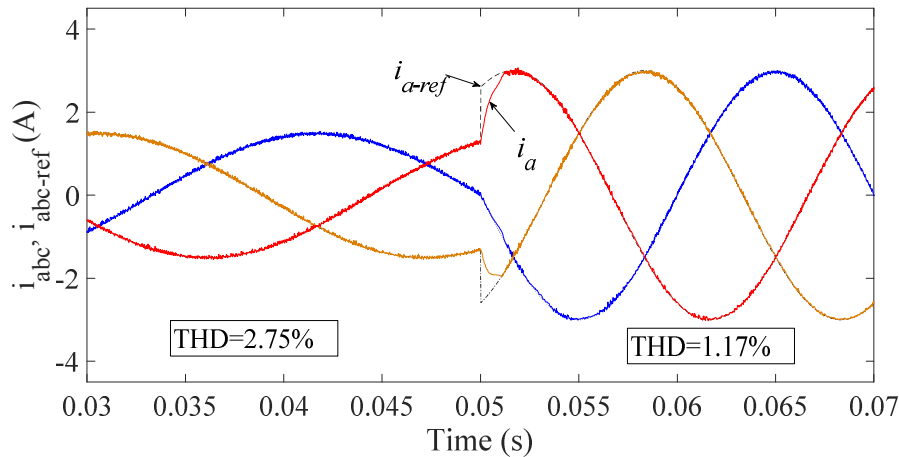
T_s (μ s)		10			30			50			100		
h (A)		0.02	0.05	0.1	0.02	0.05	0.1	0.02	0.05	0.1	0.02	0.05	0.1
THD (%)	F-HB	0.73	1.19	1.83	1.91	2.00	3.01	3.37	3.06	3.54	6.80	6.64	6.42
	S-HB	0.68	0.74	1.08	2.05	2.02	2.08	3.38	3.36	3.35	6.84	6.98	6.87
Average Switching frequency (kHz)	F-HB	9.85	6.95	4.52	3.93	3.54	2.75	2.43	2.33	2.03	1.25	1.21	1.17
	S-HB	10.4	8.9	8.75	3.95	3.59	3.17	2.44	2.33	2.11	1.23	1.22	1.19

The dynamic responses of the F-HB and S-HB controllers are shown and compared in Fig. 5.5. Here $h = 0.05$ A and $T_s = 20 \mu$ s. The current references are $i_{abc}^* = [1.5\sin(60\pi t)$

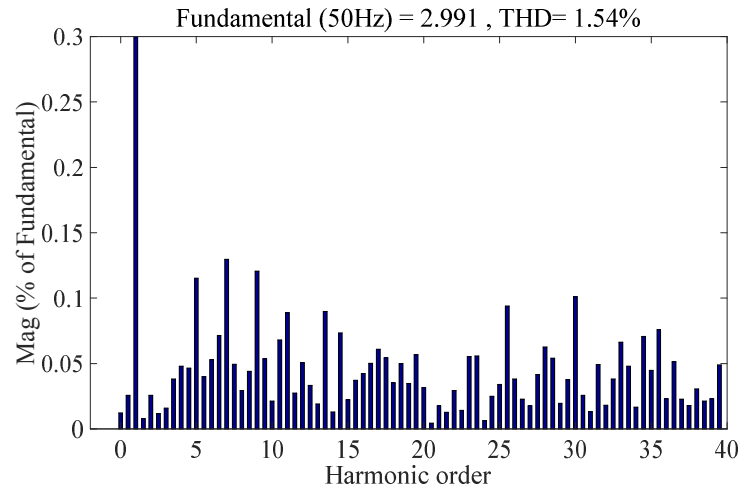
$1.5\sin(60\pi t - 2\pi/3)$ $1.5\sin(60\pi t + 2\pi/3)$] A before 0.025 s and $[3\sin(100\pi t)$ $3\sin(100\pi t - 2\pi/3)$ $3\sin(100\pi t + 2\pi/3)$] after 0.025 s. According to the simulation results shown in Figs. 5.5(a) and (b), it can be stated that both methods present excellent dynamic performance in regulating currents. Compared with F-HB, the THD values are reduced from 3.74 % and 1.54 % to 2.75 % and 1.17 % respectively in the S-HB while the average switching frequencies are relatively higher. This can be observed in Figs. 5.5(c) to (f). From the fast Fourier transform (FFT) analysis, in Figs. 5.5(c) and (d), for the second part of the current, a wide range of harmonics are suppressed. The average switching frequencies (shown in Figs. 5.5(e) and (f)) and consequential switching losses are not very high. The superior performance of S-HB is observable only when the sampling interval is small (high frequency). Therefore, for the practical implementation, it is not worth considering S-HB.



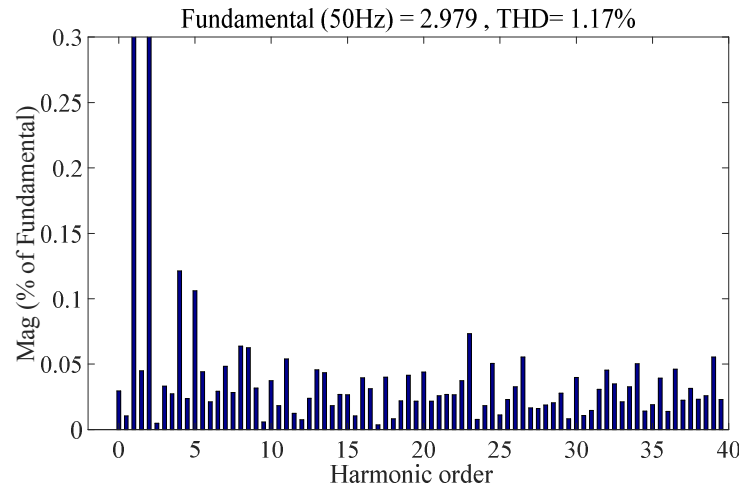
(a)



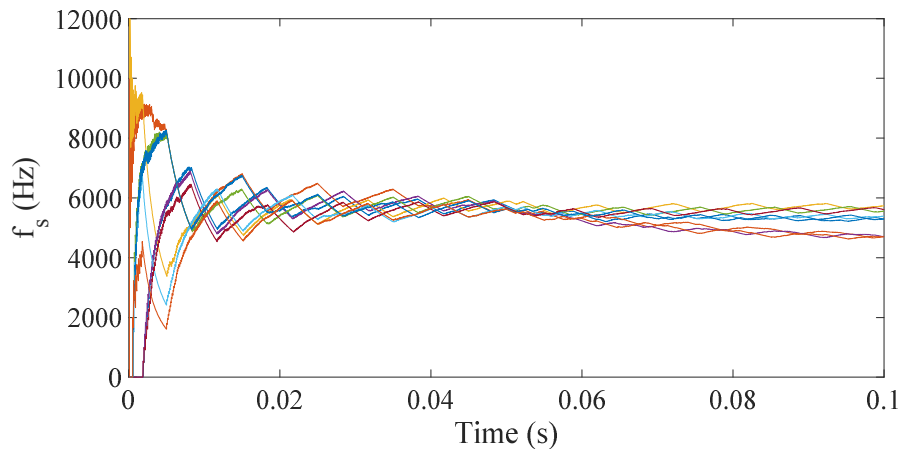
(b)



(c)



(d)



(e)

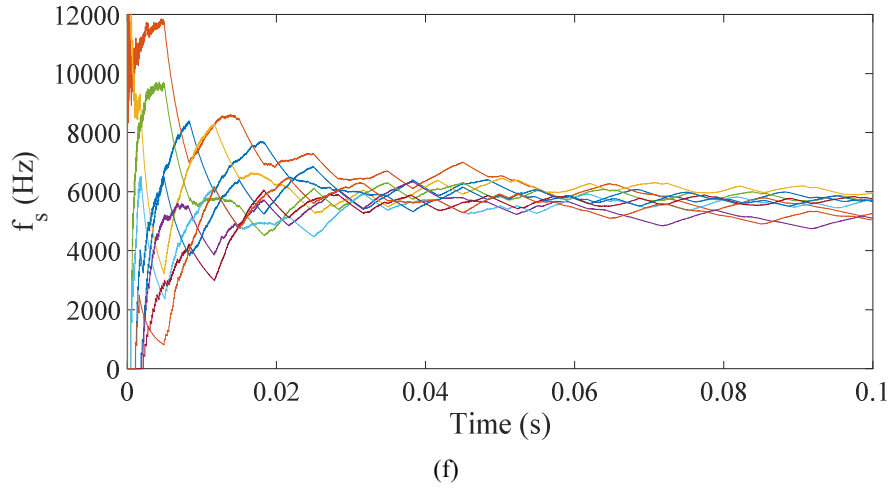
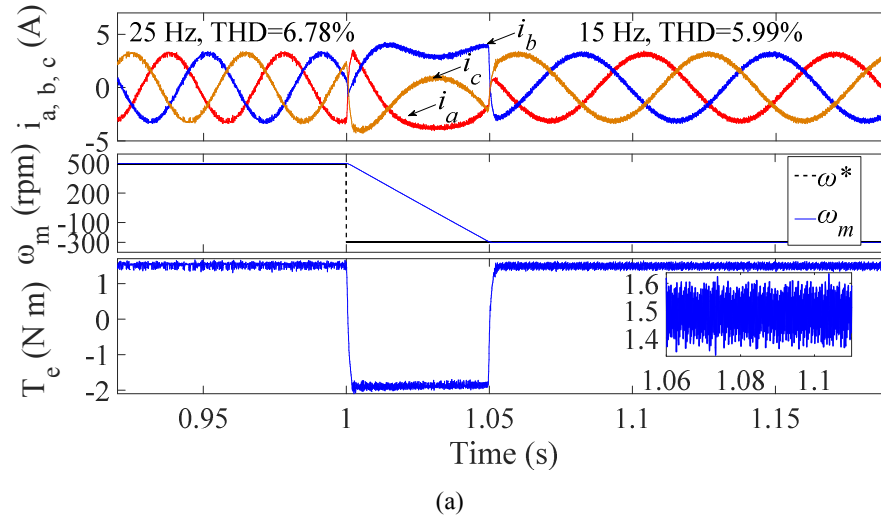


Fig. 5.5 Simulation results of HB current controller for MC: (a) F-HB controller currents dynamic performance, (b) S-HB controller currents dynamic performance, (c) FFT analysis of F-HB output current after 0.05 s, (d) FFT analysis of S-HB output current after 0.05 s, (e) F-HB average switching frequency, (f) S-HB average switching frequency.



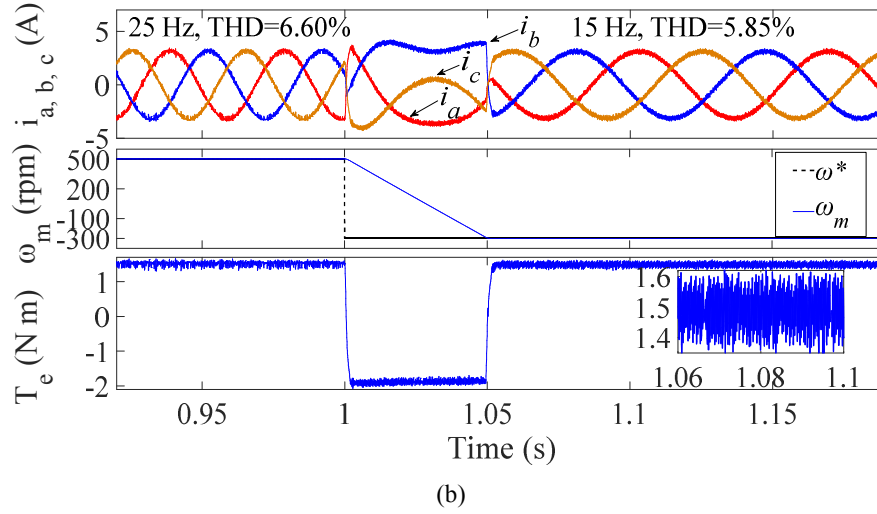


Fig. 5.6 Simulation results of HB-FOC for MC based PMSM drive system in response to the speed change from +500 rpm to -300 rpm at 1 s when $T_L = 1.5$ N m. (a) F-HB, (b) S-HB.

Simulation work of the proposed control strategy for an MC based PMSM drive was carried out, and the simulation results are presented in Fig. 5.6. The parameters of the rotor speed PI controller are $K_p = 0.5$ and $K_i = 0.55$. Transient behaviour of the PMSM stator currents, rotor speed and electromagnetic torque are shown under a speed change from 500 rpm to -300 rpm when the load torque $T_L = 1.5$ N·m. As observed from the figure, the proposed control strategy shows good regulation performance. S-HB has a slightly lower current THD (5.85 %) than F-HB (5.99 %). The torque ripples of the S-HB range from 1.336 N m to 1.626 N m while the torque ripples of the F-HB range from 1.333 N m to 1.639 N m. These demonstrate slightly better performance for S-HB.

(b). Experimental Verification

To verify the feasibility and effectiveness of the proposed strategy, the experimental work was implemented in a scaled-down MC based drive system. The experiment set up is shown in Fig. 5.7. The clamp circuit is not shown in the figure; however, it is used in the hardware to protect devices from overvoltage. Chapter 4 details the MC hardware. Further modification was required for the experimental work in this chapter. An enhanced quadrature encoder pulse was used to obtain the rotor angular position, thus the motor speed. The motor encoder used had 2000 lines which is a high-resolution encoder.

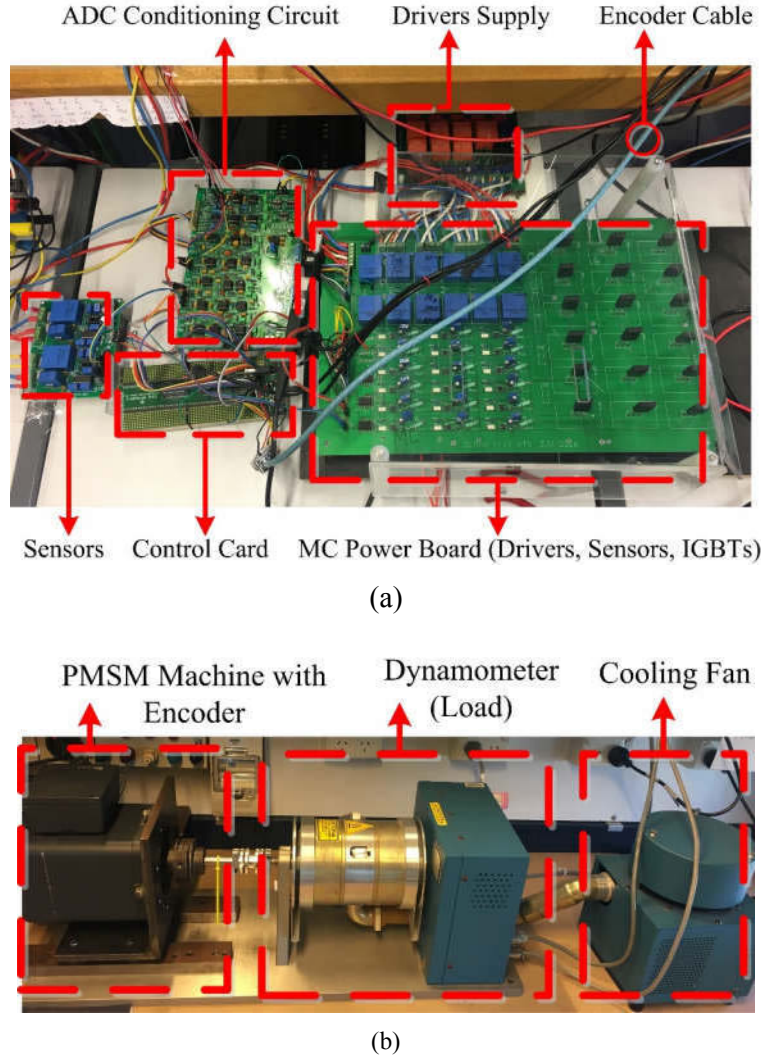
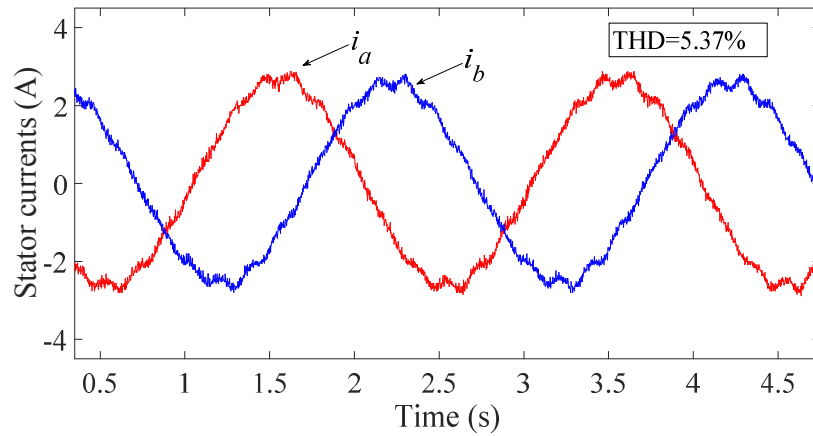


Fig. 5.7 The experimental set up: (a) MC hardware board, (b) PMSM test bench.

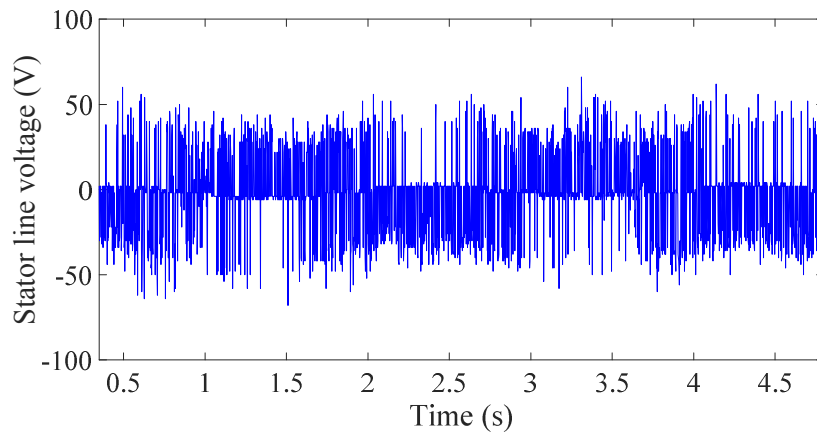
The tested surface-mounted PMSM parameters are tabulated in Table 5.3. Since the performances of F-HB and S-HB based controllers are very similar and S-HB renders heavier computation burden, here only F-HB is tested on hardware to demonstrate the controller effectiveness for the MC based drive. The code execution time was around 25 μs , which is a light computational burden. The sample time should be higher than the execution time so that the code has enough time to be executed during each sample interval.

In the experimental results, all THD values are shown for phase a current. The steady-state performances are presented in Figs. 5.8 and 5.9. Fig. 5.8 shows the steady-state results for low-speed operation (10 rpm and 50 rpm) with a load torque of 1.5 N m.

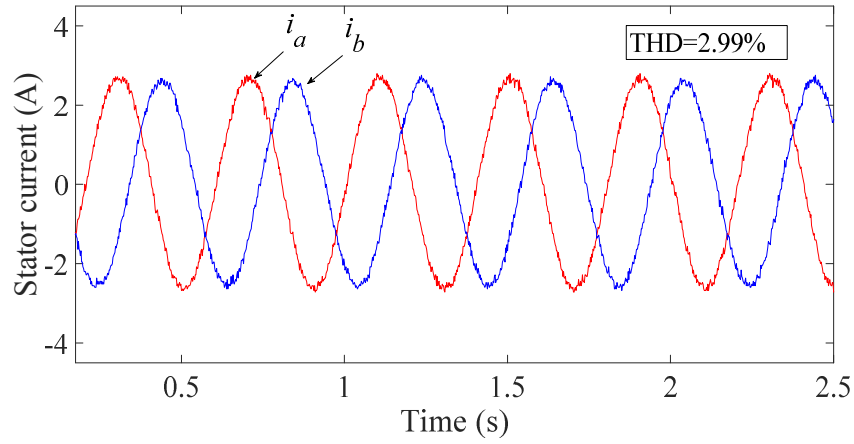
Sinusoidal stator currents were obtained with the proposed control strategy. The stator current THDs are relatively low, i.e., 5.37 % and 2.99 % for speeds of 10 rpm and 50 rpm respectively. These results validate that the proposed controller is effective in regulating low-speed operation. Fig. 5.9 shows the steady-state regulation performance of the proposed controller for relatively higher speeds. Fig. 5.9(a) shows the steady-state stator currents for 500 rpm with a 1.5 N m load applied. The THD for the stator current is 4.09 %. In Figs. 5.9(c) and (d), the rotor speed is 300 rpm and a load torque of 1.5 N m is applied. The input current is usually not a control objective in the VSI based motor drive system; however, with the proposed approach, the MC input currents were regulated, and the results are shown in Fig. 5.9(c). The input power factor is around unity in this case. The input current is distorted because it is conveniently regulated by the inherent line-commutated modulation of the proposed HB current controller. The PMSM electromagnetic torque is shown in Fig. 5.9(d).



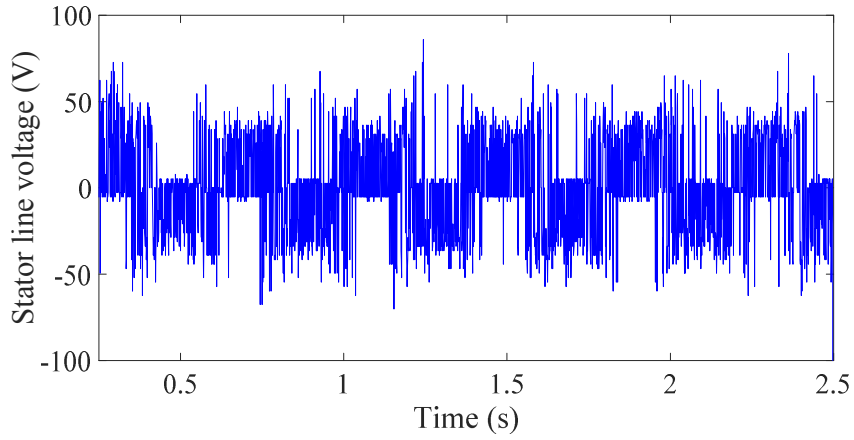
(a)



(b)

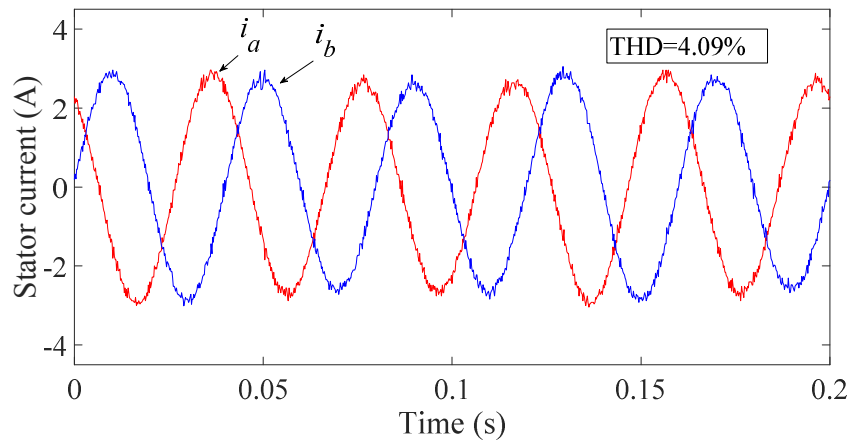


(c)

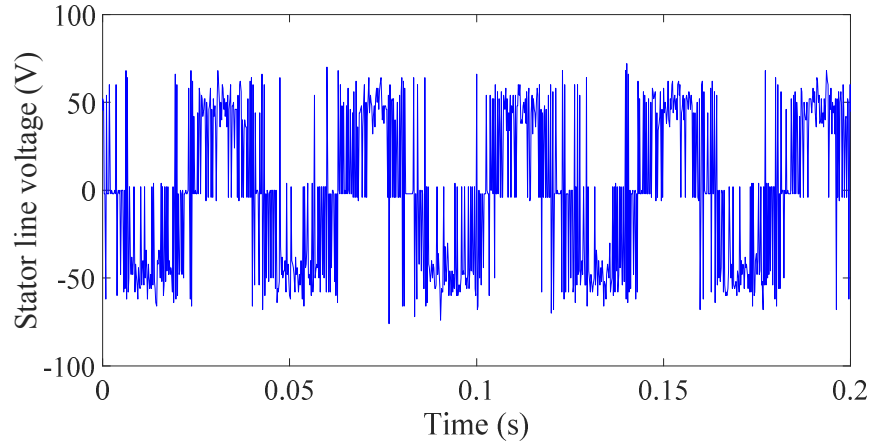


(d)

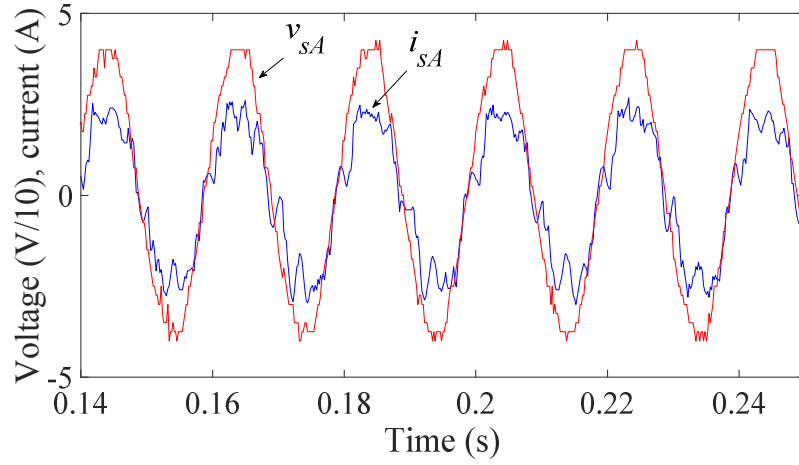
Fig. 5.8 Experimental results of HB-FOC controlled MC based PMSM drive (steady-state results 1): (a) PMSM stator currents when $\omega = 10$ rpm and $T_L = 1.5$ N m, (b) PMSM stator line voltage when $\omega = 10$ rpm and $T_L = 1.5$ N m, (c) PMSM stator currents when $\omega = 50$ rpm and $T_L = 1.5$ N m, (d) PMSM stator line voltage when $\omega = 50$ rpm and $T_L = 1.5$ N m.



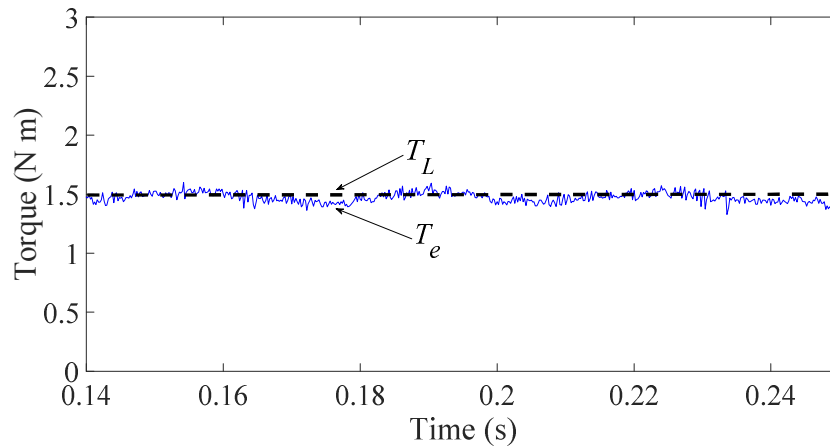
(a)



(b)



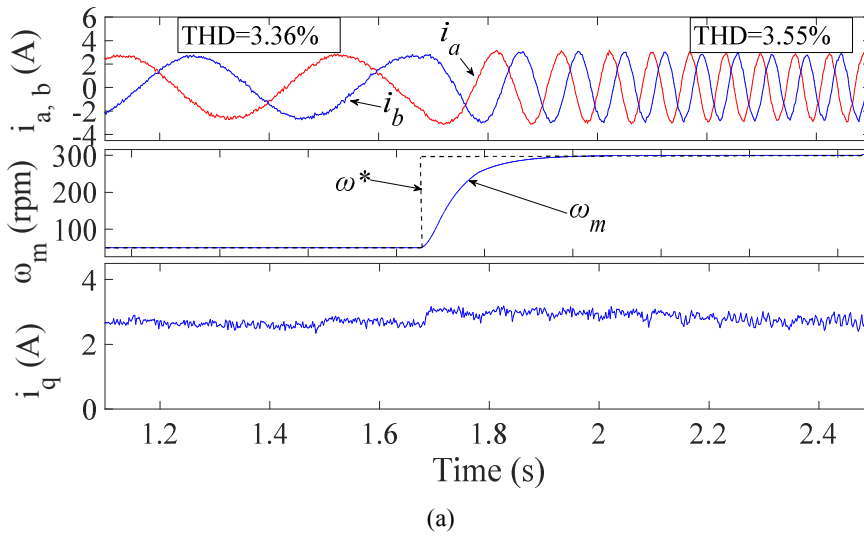
(c)



(d)

Fig. 5.9 Experimental results for HB-FOC controlled MC based PMSM drive (steady-state results 2): (a) PMSM stator currents when $\omega = 500$ rpm and $T_L = 1.5$ N m, (b) PMSM stator line voltage when $\omega = 500$ rpm and $T_L = 1.5$ N m, (c) MC input phase voltage and current when $\omega = 300$ rpm and $T_L = 1.5$ N m, (d) PMSM torque performance when $\omega = 300$ rpm and $T_L = 1.5$ N m.

The experimental results of transient behaviour are shown in Figs. 5.10 and 5.11. Fig. 5.10 shows the results when the output power is increased either by increasing the rotor speed or the applied load torque. Fig. 5.10(a) shows the PMSM stator currents, rotor speed and q-axis current responses to a speed change from 50 rpm to 300 rpm when a load $T_L = 1.5$ N m is applied. Fig. 5.10(b) demonstrates the PMSM stator currents, rotor speed, and q-axis current responses to the step load change from 0 N m to 1.5 N m when the rotor speed is maintained at 500 rpm. As seen from these figures, the proposed control strategy can track and maintain the target speed effectively, and fast dynamics are achieved. Fig. 5.11 shows the test results when the output power is decreased by reducing the rotor speed. In Fig. 5.11(a), the PMSM stator currents and MC input current are shown for a deceleration from 350 rpm to 250 rpm when the load torque is 1.5 N m. The rotor speed and q-axis current for this test are shown in Fig. 5.11(b). These results show good regulation of the proposed controller during deceleration.



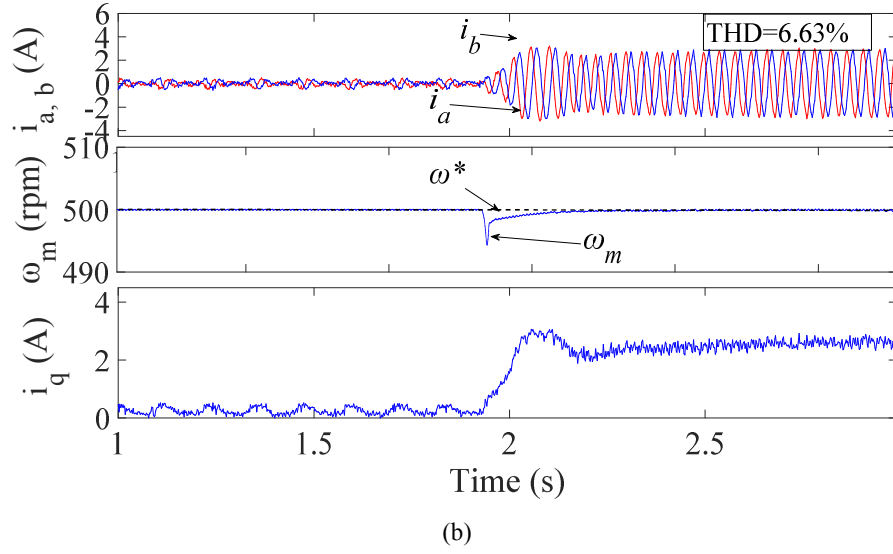
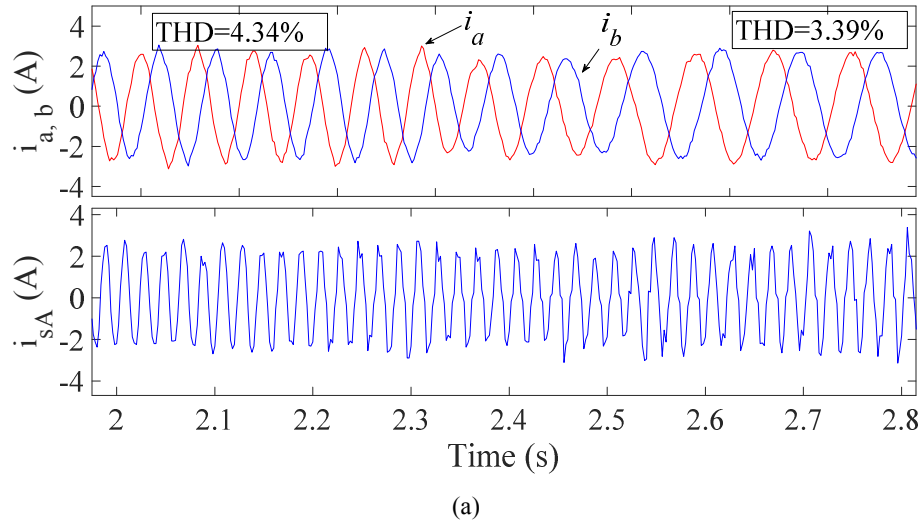


Fig. 5.10 Experimental results of HB-FOC controlled MC based PMSM drive (transient results 1): (a) PMSM stator currents, rotor speed and q -axis component current responses to command speed step change from 50 rpm to 300 rpm when $T_L = 1.5$ N m, (b) PMSM stator currents, rotor speed and q -axis current component to load torque step change from 0 to 1.5 N m when $\omega = 500$ rpm.



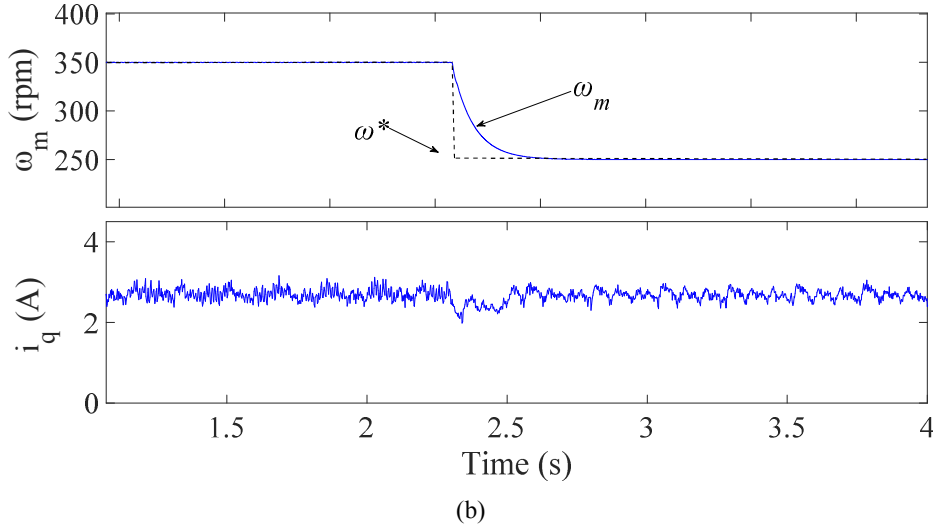


Fig. 5.11 Experimental results of HB-FOC controlled MC based PMSM drive (transient results 2): (a) PMSM stator current and MC input current response, (b) PMSM rotor speed and q -axis current component response to command speed step change from 350 rpm to 250 rpm (deceleration) when $T_L = 1.5$ N m.

From the above simulation and experimental results, the effectiveness of the MC based PMSM drive system under steady-state and transient tests is demonstrated. The THD of the stator current under various tests are low, ranging from 2.99 % to 6.63 %. The proposed control method is simple and practical.

5.1.6 Conclusions

HB control in FOC is popular in VSIs and motor drives based on VSIs; however, it has not been reported in the literature for a direct 3×3 MC or MC based drive system. This work introduces the HB current controller to the MC and MC based AC drive system. This method is simple, and the computation burden is light. Both the fixed and sinusoidal band HB controllers that are developed involve inherent modulation of the input currents, and the simulation results are evaluated comparatively. S-HB has better harmonic performance and higher average switching frequency. It is shown that S-HB has significantly superior performance over F-HB only at high sampling frequencies. The input current regulation is achieved through the line-commutated modulation. The better input currents regulation results can be achieved by integrating other methods, such as SVM, into the overall modulation. With an MC based drive, the braking chopper is not required. It is important to state that this scheme cannot only be applied

to the PMSM but also to other machines such as induction motors. The proposed scheme is explicit, effective and suitable for practical applications. Experimental results demonstrate the effectiveness of the proposed controller and MC in driving a PMSM.

5.2 DTC for the Matrix Converter-Fed Motor Drive

The direct MC is a promising AC/AC conversion topology and it is being researched. Motor drives are one of the main potential applications of the MC. This work carries forward the application of MCs in AC motor drives using DTC. In the common DTC scheme for MCs, two vectors with the maximum amplitudes are used to control the torque and flux. In the proposed approach, the input voltage vector sectors are redefined, and therefore a modified and simplified switching look-up table is obtained. In this case, the most appropriate vector to be applied is uniquely determined, and the number of switch actions is reduced. The excellent dynamic performance is obtained by selecting the maximum vector. Flux and speed are controlled effectively. Simulation work is carried out for an induction motor, and the results verify the effectiveness of the proposed DTC control in MC based AC drive systems.

5.2.1 Introduction

DTC was first presented in [28] for the high-performance control of an induction motor. As its name implies, DTC controls the torque and flux directly. It is a simple yet powerful control technique for motor drives, and it offers various benefits including fast torque response, robustness, no coordinate transformations (angle detection), no modulation stage, and no current controllers required [29], [30]. DTC does not require any other motor parameters except for the stator resistance; this enhances the controller robustness. DTC can also operate in sensorless mode (or torque control mode). These contribute to the fast development of DTC, in both research and industry, for the applications of high-performance drives [27].

However, there are some drawbacks associated with the DTC. One of the main issues is the high torque and flux ripples [22]. These are in addition to the variable switching frequency. In conventional DTC for a VSI based drive system, the flux locus is split into six sections and only eight vectors are available to generate the required vector. Therefore, the exact required vector is hard to produce to a high degree of accuracy,

which results in the flux and torque ripples. Much research has aimed to dealing with this problem [31][32]. These include applications of new converters such as multilevel inverters [33][34] and MCs [23][35] because they can produce more vectors for the DTC.

Combining the advantages of DTC and the MC, DTC controlled MC drivers were initially proposed in [29]. In [29], three hysteresis controllers were used to control the electromagnetic torque, stator flux and input power factor simultaneously by selecting the most suitable voltage vector available in the MC. Since MCs generate more voltage vectors that are suitable for DTC control, the control flexibility is enhanced. Most work utilizes this flexibility to control the MC input power factor [29][22]. This extra control objective introduces an extra hysteresis comparator contributing to heavier computation burden, more switching actions, and switching losses.

The work described in this chapter modifies and simplifies the traditional DTC switching table for the MC based driver such that the selected voltage vector for each stator flux sector is uniquely determined. The transition is smoother between switching actions, and thus switching losses are reduced. The speed control mode is based on a PI controller which is tested here.

5.2.2 Matrix Converter and Space Vectors

As obtained in Table 2.1 in Chapter 2, the MC space vectors are composed of eighteen active, three zero and six rotating vectors. Rotating vectors cannot be usefully applied because their locations (angles) keep changing. Active vectors are numbered (± 1 , ± 2 , ± 3 , ..., ± 9) and summarized in Table 2.1. These vectors have fixed locations and they form hexagons, as redrawn in Fig. 5.12 (Fig. 2.2 repeated), while their amplitudes vary with input voltages. In zero states, all the MC outputs are connected to the same input resulting in vectors with zero amplitudes while angles are arbitrary. In SVM, these active and zero vectors are applied to generate the desired output voltage and input current vectors at the same time. In DTC control, appropriate vectors are selected based on the prescribed switching look-up table according to the instantaneous stator flux and torque/speed information. This will be explained later.

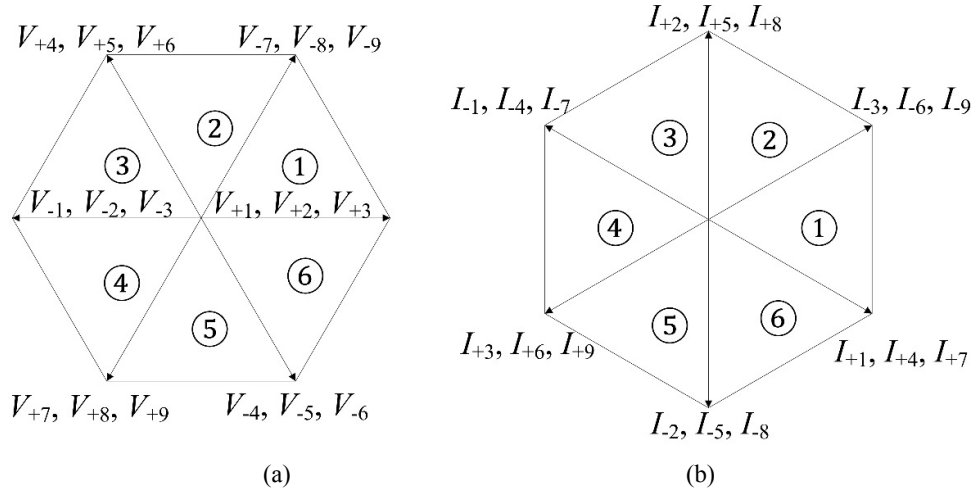


Fig. 5.12 MC (a) input voltage and (b) output current vectors hexagon (Fig. 2.2 repeated).

5.2.3 Induction Motor Model and DTC Theory

In DTC controlled induction machines, the stator flux and torque are controlled directly by selecting the appropriate voltage vectors available in the drive converter. The stator flux is obtained from

$$\psi_s = \int (V_s + R_s i_s) dt \quad (5.17)$$

If the voltage drop across the stator resistor R_s is neglected, then

$$\psi_s = \int V_s dt \quad (5.18)$$

where ψ_s is the stator flux and V_s is the voltage applied at the stator. Considering a short finite time t (control cycle period), (5.17) can be approximately written as

$$\Delta\psi_s = V_s \Delta t \quad (5.19)$$

which means that the stator flux will change accordingly in the direction of the applied voltage vector. Therefore, the stator flux can be regulated by selecting suitable voltage vectors. In the stationary reference frame (synchronized with stator), the electromagnetic torque developed in an induction machine is

$$T_e = \frac{3}{2} p \psi_s i_s \quad (5.20)$$

which can be rewritten as

$$T_e = \frac{3}{2} p |\psi_s| |i_s| \sin(\theta_{is} - \theta_{\psi s}) \quad (5.21)$$

where ψ_s is the stator flux vector; i_s is the stator current vector; and p is the pole pair number of the motor; and $|V|$ implies amplitude of the vector V . θ_{is} and $\theta_{\psi s}$ are the stator current angle and stator flux angle respectively, both of which are referred to the stationary reference frame as shown in Fig. 5.13. In (5.21), $|\psi_s|$ is normally set to a constant value in DTC. Since the rotor time constant is usually larger than the stator time constant, the rotor flux can be assumed constant (d -axis components of stator current) taking into consideration the fast control response. Therefore, the change of torque, at certain speeds, requires the change of stator flux angle $\theta_{\psi s}$ if the stator flux amplitude is maintained constant [27]. Therefore, if a voltage vector which is able to maintain the stator flux amplitude while changing the stator flux to the desired position is selected, the torque can be regulated instantaneously.

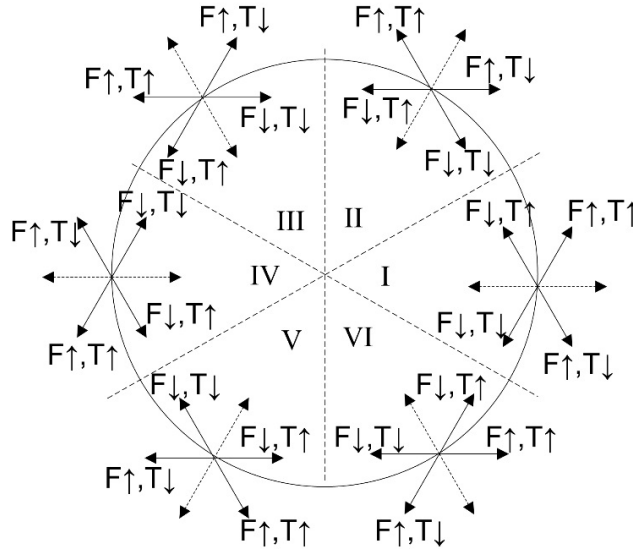


Fig. 5.13 DTC illustration diagram with the MC vectors.

DTC requires the estimation of stator flux and torque, which can be achieved using

$$\psi_{\alpha s} = \int (V_{\alpha s} - R_s i_{\alpha s}) dt \quad (5.22)$$

$$\psi_{\beta s} = \int (V_{\beta s} - R_s i_{\beta s}) dt \quad (5.23)$$

$$\psi_s = \sqrt{\psi_{\alpha s}^2 + \psi_{\beta s}^2} \quad (5.24)$$

$$\theta_{\psi s} = \tan^{-1} \left(\frac{\psi_{\beta s}}{\psi_{\alpha s}} \right) \quad (5.25)$$

$$T_e = \frac{3}{2} p (\psi_{\alpha s} i_{\beta s} - \psi_{\beta s} i_{\alpha s}) \quad (5.26)$$

These are developed in the stationary reference frame ($\alpha\beta$). As can be seen, the estimation only needs the rotor resistance, which is independent of other motor parameters.

5.2.4 DTC Control for Matrix Converter Drives

According to the above description, DTC can control the torque and flux directly via applying opposite voltage vectors available in drive converters. The voltage space vectors generated in an MC were presented earlier. The voltage vector selection is based on the flux and torque error information.

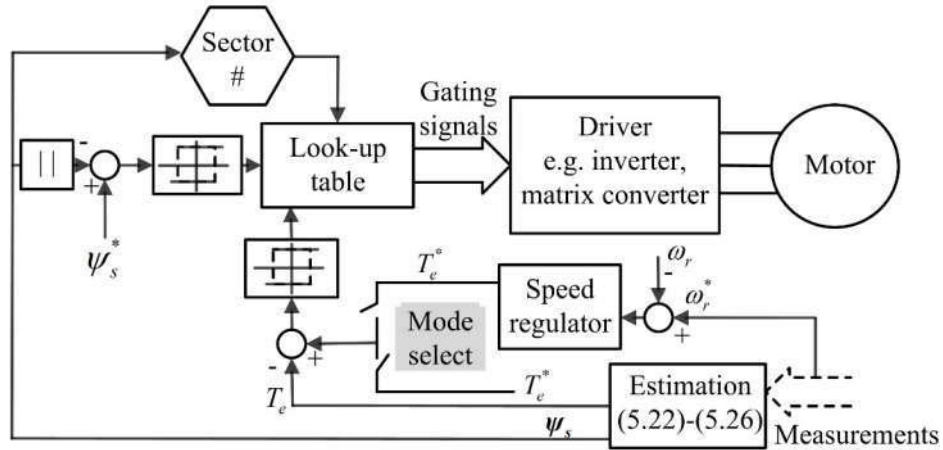


Fig. 5.14 Block diagram of DTC for motor drive with inverter or MC.

(a). Common DTC Scheme

The DTC controller diagram for MC is shown in Fig. 5.14. There are two operating modes: torque control and speed control. As shown in the figure, the hysteresis comparators produce signals in the DTC to select the voltage vectors. In each flux sector (I to VI), different voltage vectors will have different effects on both the flux and

torque, as illustrated in Fig. 5.13. In this figure, ($F\uparrow$, $T\downarrow$) indicates the flux and torque will be increased and decreased respectively if that voltage vector is selected, e.g., the voltage vectors (± 4 , ± 5 , ± 6) for sector I. Further selection of the voltage vectors depends on the input voltage vector locations. Some vectors are not used as they may have varying effects on torque and flux in the specific sector such as voltage vectors (± 1 , ± 2 , ± 3) in sector I.

A switching look-up table for the MC based DTC can be adapted from the VSI DTC scheme since their voltage vectors have the same layout (six directions with 60° apart from each other). However, in the MC, there are more active voltage vectors available corresponding to a specific voltage vector in the VSI DTC scheme. These vectors have different amplitudes although they may all be able to achieve the goals of controlling the stator flux and torque.

In the most common MC DTC, only two vectors with the maximum amplitude are considered to achieve fast-dynamic responses and simplicity. In fact, these two vectors have different effects on the input current, thus the input power factor. Therefore, the input power factor can be controlled by making use of this flexibility. However, this results in a heavier computation burden and higher switching frequency, thus higher switching losses.

(b). DTC with a Modified Switching Table

Since the amplitudes of voltage vectors are related to the input voltage vector location (sector number), the input voltage vector sector may be sub-divided or redefined so that only one maximum output voltage vector is available in each sector. In the proposed scheme, the input voltage vector sectors are moved forward by 30° compared with the conventional scheme as shown in Fig. 5.15. In this way, the maximum voltage vectors available in each sector is only one instead of two. For example, in the newly defined input voltage vector sector I, the output voltage vector -3 has the maximum amplitude. The selection of the maximum vector ensures a fast-dynamic response, and this further simplifies the switching table, thus the control implementation.

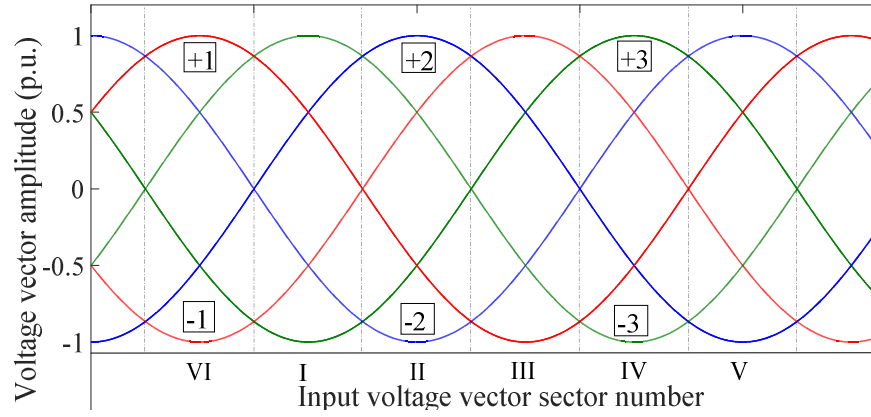


Fig. 5.15 Redefined input voltage vector sector for deciding the amplitudes of output voltage vectors.

The modified switching look-up table, as shown in Table 5.5, can be obtained in a straightforward manner from the VSI DTC look-up table. The appropriate selection of zero vectors is beneficial in reducing the switch actions and switching frequency. There are two zero vectors available in the last two columns of Table 5.5; however, only one will be applied depending on the previous switch state.

Table 5.5 Modified switching look-up table for MC DTC.

New input voltage sector #	Selected voltage vector # in VSI							
	V_{11}	V_{12}	V_{13}	V_{14}	V_{15}	V_{16}	V_{17}	V_{18}
I	V_{-3}	V_{+9}	V_{-6}	V_{+3}	V_{-9}	V_{+6}	V_{01}, V_{03}	V_{01}, V_{03}
II	V_{+2}	V_{-8}	V_{+5}	V_{-2}	V_{+8}	V_{-5}	V_{02}, V_{03}	V_{02}, V_{03}
III	V_{-1}	V_{+7}	V_{-4}	V_{+1}	V_{-7}	V_{+4}	V_{01}, V_{02}	V_{01}, V_{02}
IV	V_{+3}	V_{-9}	V_{+6}	V_{-3}	V_{+9}	V_{-6}	V_{01}, V_{03}	V_{01}, V_{03}
V	V_{-2}	V_{+8}	V_{-5}	V_{+2}	V_{-8}	V_{+5}	V_{02}, V_{03}	V_{02}, V_{03}
VI	V_{+1}	V_{-7}	V_{+4}	V_{-1}	V_{+7}	V_{-4}	V_{01}, V_{02}	V_{01}, V_{02}

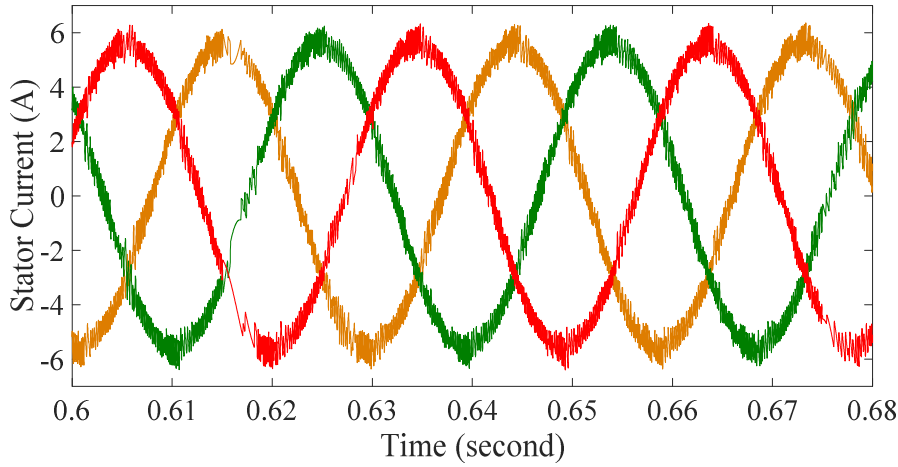


Fig. 5.16 Motor steady-state stator current when speed is 1000 rpm and load torque is 10 N m.

5.2.5 Simulation Results

Simulation results of the DTC MC drive are presented in this section. The speed control mode is examined, and the parameters used for the speed PI controller are $K_p = 30$ and $K_i = 0.05$. The hysteresis bands of hysteresis comparators for the stator flux and torque are 0.5 and 0.01 respectively. Other simulation parameters are tabulated in Table 5.6. The steady-state tests were performed first. Fig. 5.16 shows the motor steady-state stator current. The surge current is observed at the start of the motor. Fig. 5.17 presents the electromagnetic torque of the motor. The torque exhibits large ripple, which is a known weakness of DTC. Fig. 5.18 shows the stator flux locus. The flux can be controlled effectively (the reference is 0.9876 Wb).

Table 5.6 Induction machine simulation parameters.

$R_s (\Omega)$	$R_r (\Omega)$	$L_s (H)$	$L_r (H)$	$L_m (H)$	p	$T_s (s)$
3.126	1.879	0.23	0.23	0.221	2	1×10^{-5}

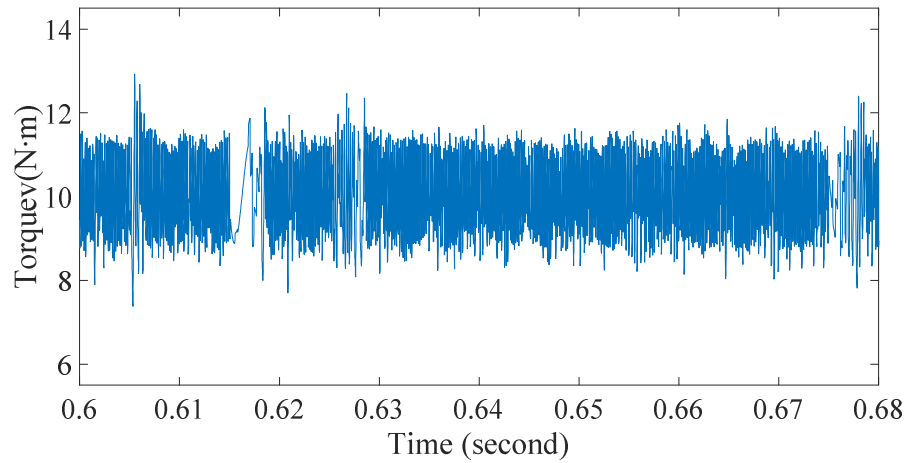


Fig. 5.17 Motor steady-state electromagnetic torque when speed is 1000 rpm and load torque is 10 N m.

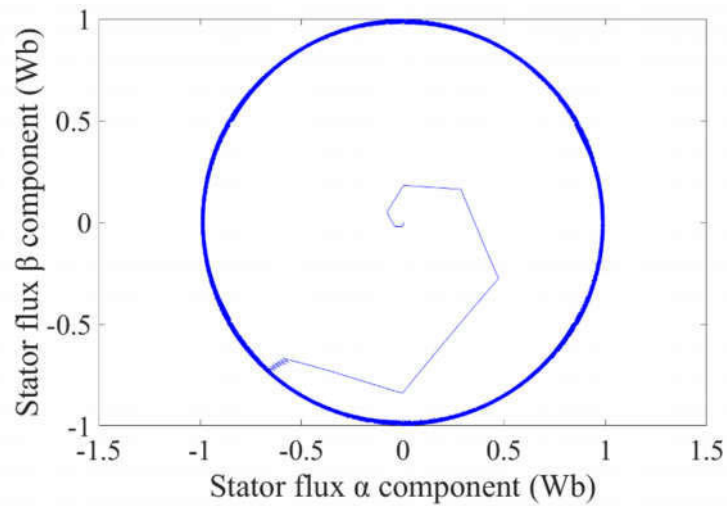


Fig. 5.18 Steady-state stator flux locus when speed is 1000 rpm and load torque is 10 N m.

Transient performance of the proposed controller is evaluated under a step change of the load torque from 5 N m to -5 N m at 0.65 s when the speed is 1000 rpm. Fig. 5.19 shows that the controller has a fast torque dynamic response. The transient stator currents are shown in Fig. 5.20. DTC performance is independent of the motor parameters except for the stator resistance. Simulation results verify that the proposed DTC controller is effective in controlling the MC based driver.

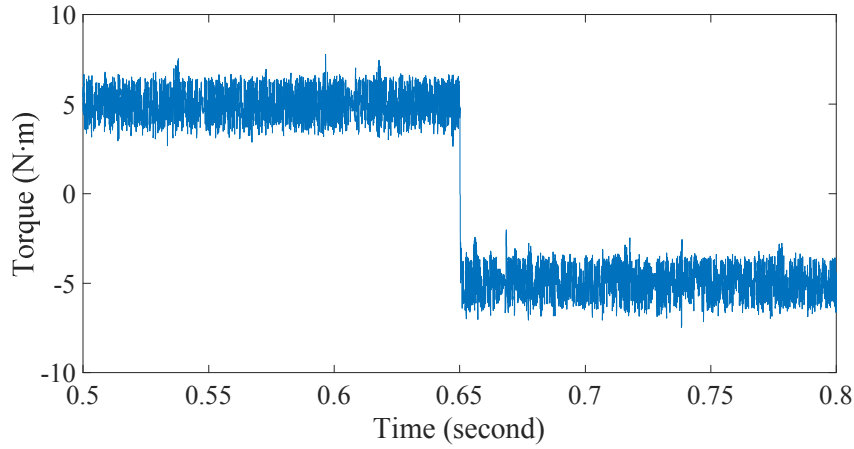


Fig. 5.19 Torque transient response to a step change at 0.65s.

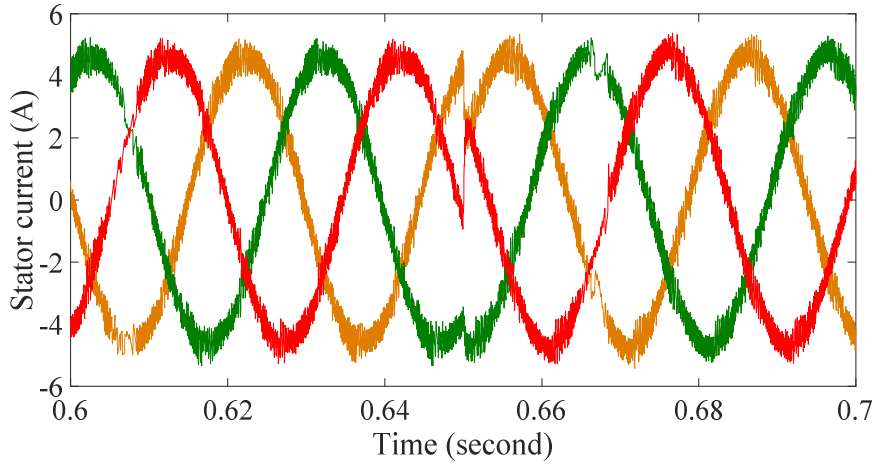


Fig. 5.20 Stator current for a torque step change at 0.65s.

5.2.6 Conclusions

DTC has developed very quickly in both research and industry because of direct torque and flux control, and fast torque dynamic response. DTC requires no coordinate transformations, current controller, or modulation stage. The implementation of DTC for an MC drive is explained in this chapter. The modified switching look-up table is obtained via redefining the input voltage vector sectors. As a result, only one maximum voltage space vector corresponding to each VSI voltage vector is available. In this way, a fast-dynamic response is maintained, and switch actions and switching losses are reduced. Simulation results for an induction machine with the proposed controller are

shown to verify the controller effectiveness. Future work will be carried out to implement the multi-band hysteresis comparators and to deal with the torque ripple.

5.3 Summary

The AC motor drive is a promising application area for the MC. This chapter covers the application of a direct MC in an AC motor drive and two control strategies are investigated. The first control method is the FOC based HB current controller for a PMSM. The second control strategy is the DTC with a modified switching look-up table. There is great research potential in the field of MC-fed AC motor drives.

The materials presented in this chapter have been published in [10], [24] and [36].

References

- [1] J. Rodriguez, R. M. Kennel, J. R. Espinoza, M. Trincado, C. A. Silva, C. A. Rojas, "High-performance control strategies for electrical drives: An experimental assessment," *IEEE Trans. Ind. Electron.*, vol. 59, no. 2, pp. 812-820, 2012.
- [2] A. Raisemche, M. Boukhniher, C. Larouci, D. Diallo, "Two active fault-tolerant control schemes of induction-motor drive in EV or HEV," *IEEE Trans. Veh. Technol.*, vol. 63, no. 1, pp. 19-29, 2014.
- [3] J. Guzinski, H. Abu-Rub, "Speed sensorless induction motor drive with predictive current controller," *IEEE Trans. Ind. Electron.* vol. 60, no. 2, pp. 699-709, 2013.
- [4] F. Wu, L. Zhang, and Q. Wu, "Simple unipolar maximum switching frequency limited hysteresis current control for grid-connected inverter," *IET Power Electronics*, vol. no. 7, pp. 933-945, 2013.
- [5] J. Peter, G. D. Marques, R. Ramchand, "Current error space vector based constant switching frequency hysteresis controller for VSI fed Induction Motor drives." 9th Int. Conf. Compatibility and Power Electron., pp. 246-251, 2015.
- [6] R. Ramchand, K. Gopakumar, C. Patel, K. Sivakumar, A. Das, H. Abu-Rub, "Online computation of hysteresis boundary for constant switching frequency current-error space-vector-based hysteresis controller for VSI-fed IM drives," *IEEE Trans. Power Electron.*, vol 27, no. 3, pp. 1521-1529, 2012.
- [7] F. Wu, F. Feng, L. Luo, J. Duan, L. Sun, "Sampling period online adjusting-based hysteresis current control without band with constant switching frequency," *IEEE Trans. Ind. Electron.*, vol. 62, no. 1, pp. 270-277, 2015.
- [8] R. Ramchand, K. Gopakumar, C. Patel, K. Sivakumar, A. Das, H. Abu-Rub, "Online computation of hysteresis boundary for constant switching frequency current-error space-vector-based hysteresis controller for VSI-fed IM drives," *IEEE Trans. Power Electron.*, vol 27, no. 3, pp. 1521-1529, 2012.

- [9] A. Tripathi, P. C. Sen, "Comparative analysis of fixed and sinusoidal band hysteresis current controllers for voltage source inverters," *IEEE Trans. Ind. Electron.*, vol. 39, no. 1, pp. 63-73, 1992.
- [10] J. Zhang, L. Li, L. Zhang, D. G. Dorrell, "Hysteresis Band Current Controller based Field-Oriented Control for an Induction Motor driven by a Direct Matrix Converter," 43rd Annual Conference of the IEEE Ind. Electron. Society (IECON 2017), Beijing, China, pp. 4633-4638, November 2017.
- [11] X. Li, M. Su, Y. Sun, H. Dan, and W. Xiong, "Modulation strategies based on mathematical construction method for matrix converter under unbalanced input voltages," *IET Power Electronics*, vol. 6, no. 3, pp.434-445, 2013.
- [12] S. M. Dabour, E. M. and Rashad, "Analysis and implementation of space-vector-modulated three-phase matrix converter," *IET Power Electronics*, vol. 5, no. 8, pp.1374-1378, 2012.
- [13] P. Wheeler, J. Rodriguez, J. Clare, L. Empringham, and A. Weinstein, "Matrix converters: a technology review," *IEEE Trans. Ind. Electron.*, vol. 49, no. 2, pp. 276-288, 2002.
- [14] S. F. Pinto, P. V. Mendes and J. Fernando Silva, "Modular matrix converter based solid state transformer for smart grids," *Electric Power Syst. Research*, vol. 136, pp. 189-200, 2016.
- [15] J. Zhang, L. Li, Z. Malekjamshidi, and D. G. Dorrell, "Predictive Voltage Control of Direct Matrix Converter with Reduced Number of Sensors for the Renewable Energy and Microgrid Applications," *IEEE Energy Conversion Congress and Exposition (ECCE)*, Cincinnati, USA, pp. 3309-3315, Oct. 2017.
- [16] J. Zhang, D. G. Dorrell and L. Li, "Applications of the Direct Space Vector Modulation Controlled Matrix Converter as the Unified Power Flow Controller," *The 8th Int. Conf. on Power Electron., Machines & Drives (PEMD 2016)*, Glasgow, pp. 1-6, 2016.
- [17] Y. Bak, E. Lee, and K. B. Lee, "Indirect matrix converter for hybrid electric vehicle application with three-phase and single-phase outputs," *Energies*, vol. 8, no. 5, pp. 3849-3866, 2015.
- [18] D. Casadei, G. Serra, A. Tani, "The use of matrix converters in direct torque control of induction machines," *IEEE Trans. Ind. Electron.*, vol. 48, no. 6, pp. 1057-1064, 2001.
- [19] C. Xia, J. Zhao, Y. Yan, T. Shi, "A novel direct torque control of matrix converter-fed PMSM drives using duty cycle control for torque ripple reduction," *IEEE Trans. Ind. Electron.*, vol. 61, no. 6, pp. 2700-2713, 2014.
- [20] R. Vargas, U. Ammann, B. Hudoffsky, J. Rodriguez, P. Wheeler, "Predictive torque control of an induction machine fed by a matrix converter with reactive input power control," *IEEE Trans. Power Electron.*, vol. 25, no. 6, pp. 1426-1438, 2010.
- [21] . Yan, J. Zhao, C. Xia, and T. Shi, "Direct torque control of matrix converter-fed permanent magnet synchronous motor drives based on master and slave vectors," *IET Power Electronics*, vol. 8, no. 2, pp.288-296, 2014.
- [22] C. Ortega, A. Arias, C. Caruana, J. Balcells, and G. M. Asher, "Improved waveform quality in the direct torque control of matrix-converter-fed PMSM drives," *IEEE Trans. Ind. Electron.*, vol. 57, no. 6, pp. 2101-2110, 2010.
- [23] K. B. Lee, and F. Blaabjerg, "Sensorless DTC-SVM for induction motor driven by a matrix converter using a parameter estimation strategy," *IEEE Trans. Ind. Electron.*, vol. 55, no. 2, pp. 512-521, 2008.

- [24] J. Zhang, L. Li, D. G. Dorrell, Y. Guo, "Direct Torque Control with a Modified Switching Table for a Direct Matrix Converter based AC Motor Drive System," 20th Int. Conf. on Electrical Machines and Systems (ICEMS 2017). Sydney, Australia, 2017.
- [25] K. B. Lee, and F. Blaabjerg, F.: "An improved DTC-SVM method for sensorless matrix converter drives using an overmodulation strategy and a simple nonlinearity compensation," IEEE Trans. Ind. Electron., vol. 54, no. 6, pp. 3155-3166, 2007.
- [26] R. Gupta, A. Ghosh, A. A. Joshi, A., "Multiband hysteresis modulation and switching characterization for sliding-mode-controlled cascaded multilevel inverter," IEEE Trans. Ind. Electron., vol. 57, no. 7, pp. 2344-2353, 2010.
- [27] H. Abu-Rub, A. Iqbal, J. Guzinski, High performance control of AC drives with MATLAB/Simulink models. John Wiley & Sons, 2012.
- [28] I. Takahashi, and T. Noguchi, "A new quick-response and high-efficiency control strategy of an induction motor," IEEE Trans. Ind. Appl., vol. IA-22, no. 5, pp. 820-827, 1986.
- [29] D. Casadei, G. Serra, A. Tani, "The use of matrix converters in direct torque control of induction machines," IEEE Trans. Ind. Electron., vol. 48, no. 6, pp. 1057-1064, 2001.
- [30] S. Sebtahmadi, H. Pirasteh, S. H. Kaboli, A. Radan, and S. Mekhilef, "A 12-sector space vector switching scheme for performance improvement of matrix-converter-based DTC of IM drive," IEEE Trans. Power Electron., vol. 30, no. 7, pp. 3804-3817, 2015.
- [31] D. Mohan, X. Zhang, and G. Foo, "Generalized DTC Strategy for Multilevel Inverter fed IPMSMs with Constant Inverter Switching Frequency and Reduced Torque Ripples," IEEE Trans. Energy Conversion, vol. pp, no. 99, pp. 1, 2017.
- [32] Y. S. Choi, H. H. Choi, and J. W. Jung, "Feedback linearization direct torque control with reduced torque and flux ripples for IPMSM drives," IEEE Trans. Power Electron., vol. 31, no. 5, pp. 3728-3737, 2016.
- [33] F. Khoucha, S. M. Lagoun, K. Marouani, A. Kheloui, and M. Benbouzid, "Hybrid cascaded H-bridge multilevel-inverter induction-motor-drive direct torque control for automotive applications," IEEE Trans. Ind. Electron., vol. 57, no. 3, pp. 892-899, 2010.
- [34] G. S. Buja, and M. P. Kazmierkowski, "Direct torque control of PWM inverter-fed AC motors-a survey," IEEE Trans. Ind. Electron., vol. 51, no. 4, pp. 744-757, 2004.
- [35] C. Xia, J. Zhao, Y. Yan, T. Shi, "A novel direct torque control of matrix converter-fed PMSM drives using duty cycle control for torque ripple reduction," IEEE Trans. Ind. Electron., vol. 61, no. 6, pp. 2700-2713, 2014.
- [36] J. Zhang, H. Yang, T. Wang, L. Li, D. G. Dorrell, D.D.C. Lu, "Field-Oriented Control based on Hysteresis Band Current Controller for a Permanent Magnet Synchronous Motor driven by a Direct Matrix Converter," IET Power Electronics, vol. 11, no. 7, pp. 1277-1285, 2018.

6 PREDICTIVE CONTROL FOR MICROGRID AND OTHER CONVERSION POSSIBILITIES

In this chapter, model predictive control (MPC) is employed to control the MC. The first part of this chapter investigates the predictive voltage control of MC for microgrid applications and the second part investigate other conversion possibilities of the MC.

6.1 Predictive Control for Microgrid

The work in this section proposes a predictive voltage control strategy for a direct MC used in a renewable energy distributed generation system. A direct MC with LC filters is controlled in order to work as a stable voltage supply for loads. This is especially relevant for stand-alone operation of a renewable energy microgrid where a stable sinusoidal voltage, with desired amplitude and frequency under various load conditions, is the main control objective. MPC is used to regulate the MC so that it produces stable sinusoidal voltages for different loads. With predictive control, many other control objectives, e.g., input power factor, common-mode voltage and switching frequency, can be achieved depending on the application. To reduce the number of required measurements and sensors, this work utilizes observers and makes use of the switch

matrices. In addition, the voltage transfer ratio can be improved with the proposed strategy. The controller is tested under various conditions including intermittent disturbance, non-linear loads and unbalanced loads. The proposed controller is effective, simple, and easy to implement. Simulation and experimental results verify the effectiveness of the proposed scheme and control strategy.

6.1.1 Introduction

A modern interconnected power system can contain hybrid AC and DC grids, with various power electronic converters interfacing different energy sources [1][2], as shown in Fig. 6.1. The distributed generators (DGs) are modern components in a grid network and they are interconnected via the point of common coupling (PCC). Energy generation issues are driving the development of microgrids and renewable energy based DGs and these have been the focus of great interest [3][4]. A microgrid can operate in a grid-connected mode or an islanded mode. When operated in the grid-connected mode, the main control objective is the current or power exchange with the utility grid. The main control objective during islanded operation is to maintain stable sinusoidal voltages for loads [5]-[8]. These operating modes depend on system operating conditions, user demand, availability of energy, and utility grid requirement. For both operating modes, a microgrid should be able to supply electricity in a reliable, secure and economical manner [9]-[11]. To this end, power electronic converters play a critical role [12]. Various power electronic converters, including multilevel converters [13], together with their corresponding control techniques, have been researched for controlling power flow, current and voltage for microgrid applications [14].

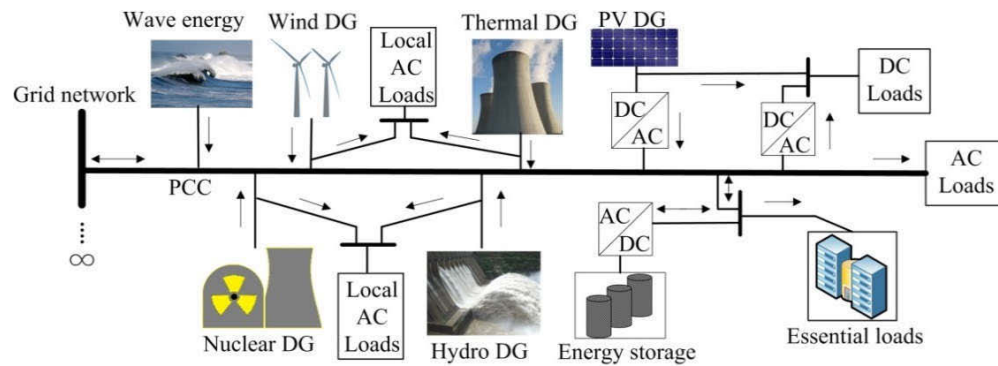


Fig. 6.1 Diagram of an interconnected power system example involving renewable DGs.

This work mainly focuses on the islanded mode of a renewable energy based microgrid. At present, a microgrid is an inverter-dominated system [7][15]. However, it is difficult to maintain feed to connected loads, particularly nonlinear loads, at the required voltage and frequency with an inverter [8]. In the literature, research projects on voltage source inverters (VSI) and neutral point clamped (NPC) inverters, with many control methods, have been carried out on uninterrupted power system-based (UPS) DGs in order to regulate the output voltage [16][17]. *LC* filters are commonly used in these applications. However, these strategies are only suitable for a microgrid with DC DGs. For AC DGs, the rectifier stage and DC-link capacitor are required together with an inverter for indirect AC/AC conversion. These will make the system bulky, reduce the lifetime and increase maintenance. In addition, there exists the necessity of the DC link voltage control. Other significant drawbacks of this structure include unidirectional power flow, difficulty in controlling the input power factor, and handling of the input unbalance and intermittent disturbance of the renewable energy sources.

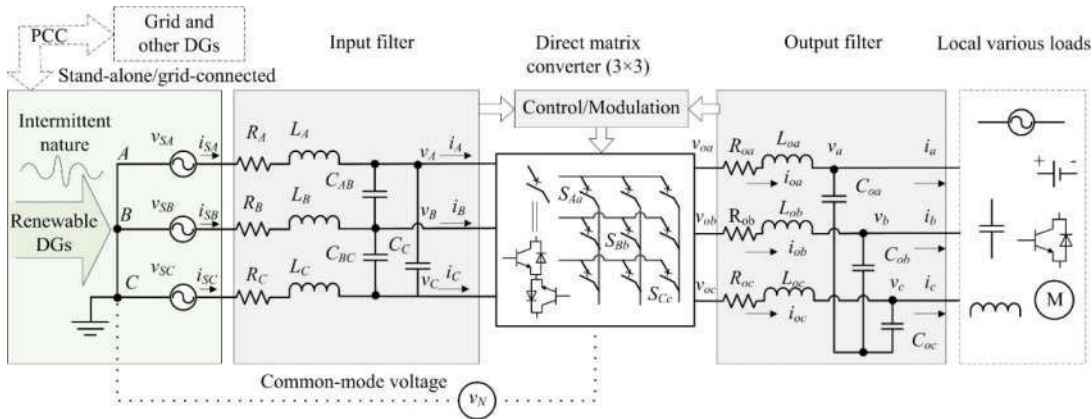


Fig. 6.2 AC microgrid with renewable DGs and MC.

Recent demand for the AC/AC conversion has grown in the field of DGs in microgrids [18][19]. A solution for direct AC/AC conversion is the MC [20]; this is an alternative to the established indirect AC/AC conversion method with a DC link. A direct three-phase MC features compact structure, bidirectional power flow, controllable input power factor (which can be set to unity), regeneration capability, and no energy-storage elements [20]–[22]. In addition, it was reported in [23] that the MC can be used for other conversions (i.e., AC/DC, DC/AC, and DC/DC) to feed various loads such as inductive,

capacitive, nonlinear, AC and even DC systems, as shown in Fig. 6.2. MCs have been assessed for suitability in many applications [24]-[26]. However, the use of a direct MC in a renewable energy based microgrid remains unexplored.

In terms of control approaches for direct MCs, classic modulation methods including scalar modulation and pulse width modulation (PWM) techniques usually are programmed offline; thus, these methods are vulnerable to the system and load variations causing steady-state errors [27]. Space vector modulation (SVM) has been widely researched and applied. However, the voltage transfer ratio (VTR) is limited to below $\sqrt{3}/2$ (≈ 0.866), which is a known drawback, like most of the other control methods. Most of the control methods are concerned with sinusoidal output currents, so they cannot provide sinusoidal voltages. Furthermore, they cannot handle common-mode voltage which can be detrimental, especially to motor loads. This is one of the main reasons for premature failures in a machine [28].

This work adopts MPC to control the output voltages of an MC for microgrid applications in the islanded mode. MPC is a simple and powerful control tool for power converters [29]. This method does not require a modulation stage but can utilize all 27 available MC switch states. MPC utilizes a system model to predict future system behaviour and select the optimum switch state by minimizing a predefined cost function. The cost function design in MPC is flexible as it can contain many factors and constraints depending on the specific application and requirements [30]. Some predictive control strategies have been proposed for MCs [31]-[33]; however, they are mainly concerned with sinusoidal output currents rather than output voltages. In addition, the issues of limited VTR persist.

The objectives of this work are: (1) To develop a scheme for an MC interfaced renewable energy DG system; (2) Instead of controlling output currents, to propose a predictive voltage control strategy for a direct MC to supply various loads in an islanded AC microgrid by utilizing *LC* filters; (3) With the proposed predictive voltage control, other control objectives and constraints can be readily considered, including common-mode voltage, input power factor and average switching frequency; (4) To improve the VTR with the proposed scheme, the number of required sensors is reduced by employing observers; and (5) To develop an MC prototype to validate the proposed scheme.

The proposed scheme is tested under various conditions including nonlinear loads, unbalanced loads and intermittent disturbance and unbalanced input. The regulated voltage meets the voltage quality set in the IEEE standard: IEEE Std-519-2014 [34].

6.1.2 Model Development

(a). Filter models for prediction

The implementation of MPC is based on a system model. According to Fig. 6.2, the output filters of the MC are modeled as

$$\begin{cases} v_{oa} - i_{oa} \cdot R_{oa} - L_{oa} \frac{di_{oa}}{dt} = v_a \\ v_{ob} - i_{ob} \cdot R_{ob} - L_{ob} \frac{di_{ob}}{dt} = v_b \\ v_{oc} - i_{oc} \cdot R_{oc} - L_{oc} \frac{di_{oc}}{dt} = v_c \end{cases} \quad (6.1)$$

$$\begin{cases} C_{oa} \frac{dv_a}{dt} = i_{oa} - i_a \\ C_{ob} \frac{dv_b}{dt} = i_{ob} - i_b \\ C_{oc} \frac{dv_c}{dt} = i_{oc} - i_c \end{cases} \quad (6.2)$$

The variables in (6.1) and (6.2) are shown in Fig. 6.2. The capacitors can be connected in star (C_A, B, C) or delta (C_{AB}, BC, CA). The feature of the star connection is that the required capacitance is three times ($C_A = 3C_{AB}$) while the voltage rating is $1/\sqrt{3}$ times ($V_{AB} = \sqrt{3}V_A$) of that of the delta connection for the equivalent ratings.

In order to simplify the modeling procedure, it is sufficient to consider a single-phase model due to the symmetry of three-phase system. Hence (6.1) and (6.2) can be rewritten in the state space model:

$$\begin{bmatrix} \dot{i}_{oa} \\ \dot{v}_a \end{bmatrix} = F \begin{bmatrix} i_{oa} \\ v_a \end{bmatrix} + G \begin{bmatrix} v_{oa} \\ i_a \end{bmatrix},$$

$$F = \begin{bmatrix} -R_{oa}/L_{oa} & -1/L_{oa} \\ 1/C_{oa} & 0 \end{bmatrix} \text{ and } G = \begin{bmatrix} 1/L_{oa} & 0 \\ 0 & -1/C_{oa} \end{bmatrix} \quad (6.3)$$

where the voltages (v_{oa} and v_a), currents (i_{oa} and i_a), and filters (L_{oa} , R_{oa} , and C_{oa}) are denoted in Fig. 6.2. F and G are the state space matrices. Based on (6.3), the zero-order-hold based discretized model can be derived as

$$\begin{bmatrix} i_{oa}[k+1] \\ v_a[k+1] \end{bmatrix} = A \begin{bmatrix} i_{oa}[k] \\ v_a[k] \end{bmatrix} + B \begin{bmatrix} v_{oa}[k] \\ i_a[k] \end{bmatrix}, \text{ where } A = e^{F \cdot T_s} \text{ and } B = \int_0^{T_s} e^{F \cdot \tau} d\tau \cdot G \quad (6.4)$$

Here T_s is the sampling time and the matrices A and B can be obtained from

$$A = \begin{bmatrix} A_{11} & A_{12} \\ A_{21} & A_{22} \end{bmatrix}, \quad A_{11} = \frac{a \cdot e^{a \cdot T_s} - b \cdot e^{b \cdot T_s}}{a - b}, \quad A_{12} = \frac{-(e^{a \cdot T_s} - e^{b \cdot T_s})}{L_{oa}(a - b)}, \quad A_{21} = \frac{e^{a \cdot T_s} - e^{b \cdot T_s}}{C_{ab}(a - b)},$$

$$A_{22} = \frac{a \cdot e^{a \cdot T_s} - b \cdot e^{b \cdot T_s}}{a - b} + \frac{R_{oa} \cdot (e^{a \cdot T_s} - e^{b \cdot T_s})}{L_{oa}(a - b)} \quad (6.5)$$

$$B = \begin{bmatrix} B_{11} & B_{12} \\ B_{21} & B_{22} \end{bmatrix}, \quad B_{11} = \frac{e^{a \cdot T_s} - e^{b \cdot T_s}}{L_{oa}(a - b)}, \quad B_{12} = \frac{[a \cdot (e^{b \cdot T_s} - 1) - b \cdot (e^{a \cdot T_s} - 1)]}{(L_{oa} \cdot C_{oa} \cdot a \cdot b) \cdot (a - b)},$$

$$B_{22} = \frac{-e^{a \cdot T_s} + e^{b \cdot T_s} + R_{oa} \cdot [a - b - a \cdot e^{b \cdot T_s} + b \cdot e^{a \cdot T_s}]}{(L_{oa} \cdot C_{oa} \cdot a \cdot b) \cdot (a - b)} \quad (6.6)$$

$$\text{with } a, b = \frac{-R_{oa} / L_{oa} \pm \sqrt{(R_{oa} / L_{oa})^2 - 4 / C_{oa} / L_{oa}}}{2}.$$

Therefore, the future behaviour of the output voltage v_a can be predicted using

$$v_a[k+1] = A_{21} \cdot i_{oa}[k] + A_{22} \cdot v_a[k] + B_{21} \cdot v_{oa}[k] + B_{22} \cdot i_a[k] \quad (6.7)$$

which is derived from the discretized model (6.4).

Similarly, the prediction model of input current i_{sA} using the input filter model can be obtained in (6.8) to predict the future behaviour of input current.

$$i_{sA}[k+1] = M_{11} \cdot i_{sA}[k] + M_{12} \cdot v_a[k] + N_{11} \cdot v_{sA}[k] + N_{12} \cdot i_a[k] \quad (6.8)$$

The matrices in (6.8) are derived in a similar manner.

The dimension of the models can be reduced from the three-phase model to an α - β or d - q model using frame transformations. Based on these predictions, the MPC evaluates each switch state and selects the optimum one to be applied at the next sampling instant. This switch state should result in a minimum value of the cost function. Some variables in (6.7) and (6.8) can be measured using voltage and current transducers while some can be estimated using observers or calculated using switch matrices (2.1) and (2.2). The

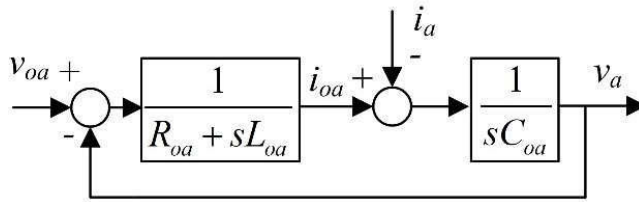
utilization of observers to estimate some variables can reduce the number of required sensors, thus the cost. The design of observers is described in the next section.

(b). Improved VTR

The output LC filter can also be modeled in the block diagram as shown in Fig. 6.3(a). Based on this figure, the transfer function of $v_a(s)$ to $v_{oa}(s)$ can be expressed as

$$H(s) = \frac{v_a(s)}{v_{oa}(s)} = \frac{1}{L_{oa}C_{oa}s^2 + R_{oa}C_{oa}s + 1} \quad (6.9).$$

Using (6.9), Bode plots are obtained for $H(s)$ with different values of L_{oa} and C_{oa} as shown in Fig. 6.3(b). Here R_{oa} is fixed to $0.5 \, \Omega$ while L_{oa} and C_{oa} are given in the legend, e.g., (2, 40) means $L_{oa} = 2 \, \text{mH}$ and $C_{oa} = 40 \, \mu\text{F}$. These Bode plots are related to Table 6.2 and Fig. 6.7 in Section 6.1.5. As observed in these Bode plots, the magnitude responses are greater than zero at the targeted frequency $2\pi \times 50 \, \text{rad/s}$, which means v_a can be larger than v_{oa} , and thus an improved VTR. For instance, if the magnitude in frequency domain is 0.5 dB, the real filter gain is 1.06; therefore, the improved VTR is expected to reach $1.06 \times 0.866 = 0.918$. It is worth noting that the main purpose of the output LC filters in this work is to provide sinusoidal voltages rather than improving the VTR.



(a)

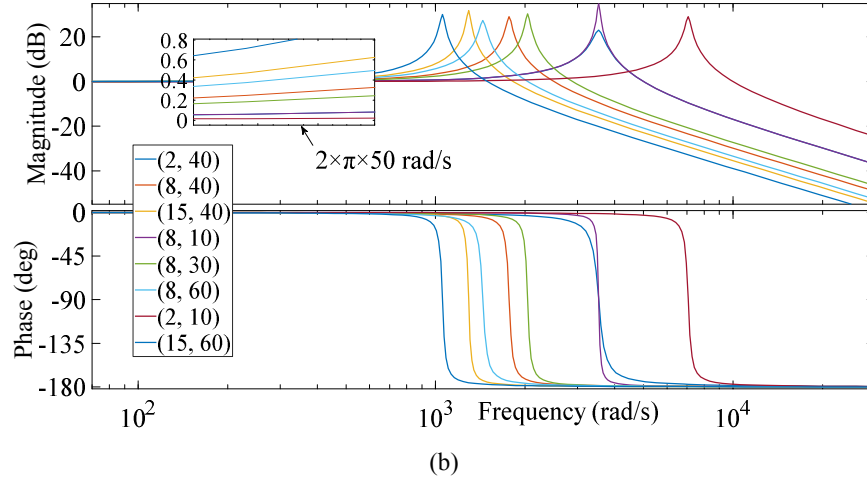


Fig. 6.3 Output filter model in block diagram and its Bode plots for different values of L_{oa} and C_{oa} (mH, μ F).

6.1.3 Observers Design

An observer is a dynamic system that can estimate the states of a system. For a system described in the state-space form

$$\dot{X} = FX + GU \quad (6.10)$$

$$Y = CX + DU \quad (6.11)$$

the Luenberger state observer can be designed to estimate the state X , as illustrated in

$$\dot{\hat{X}} = F\hat{X} + GU + L(Y - \hat{Y}) \quad (6.12)$$

$$\hat{Y} = C\hat{X} + DU \quad (6.13)$$

where \hat{X} and \hat{Y} are the estimation of state X and output Y . Substituting (6.13) into (6.12) leads to

$$\begin{aligned} \dot{\hat{X}} &= F\hat{X} + GU + L(Y - \hat{Y}) = F\hat{X} + GU + LY - LC\hat{X} - LDU \\ &= (F - LC)\hat{X} + (G - LD)U + LY \end{aligned} \quad (6.14)$$

where L is the observer gain matrix and can be computed by using Ackermann's formula based on the desired eigenvalues of observer. The estimation error is

$E = X - \hat{X}$ and its differential equation is $\dot{E} = \dot{X} - \dot{\hat{X}} = (F - LC)E$. The correct selection of gain matrix ensures that the error system is asymptotically stable so that the

estimation error will finally decay to zero. Using (6.14), the observer diagram shown in Fig. 6.4 can be developed.

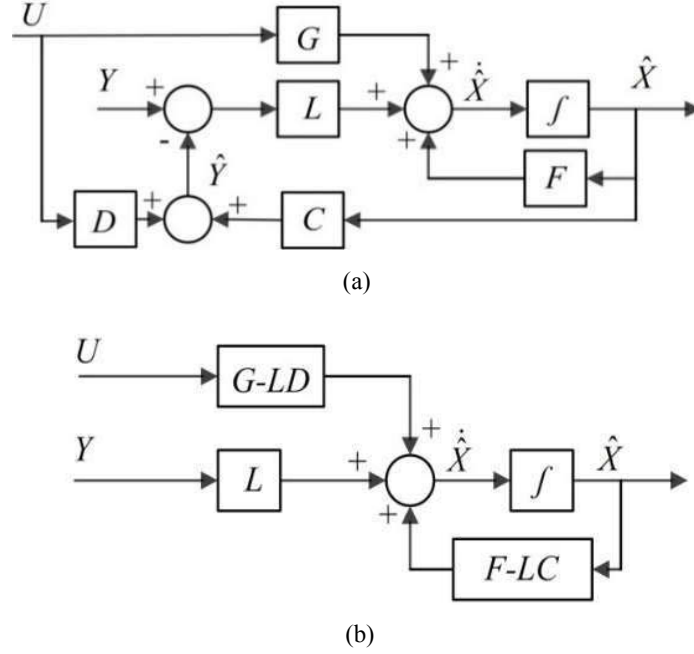


Fig. 6.4 Luenberger observer design diagram and the simplified diagram.

Depending on the specific observed state, the descriptions should be modified accordingly, and some assumptions may be necessary. In order to observe the load current i_a , for example, the assumption $di_a/dt = 0$ is made and added to the model (6.3) to make a 3-D observer. This assumption is based on the fact that the sampling interval of the algorithm is usually sufficiently short, so the load current barely changes. Therefore, a 3-D observer model based on the modified model is obtained where

$$\dot{X}_o = \begin{bmatrix} \dot{i}_{oa} \\ \dot{v}_a \\ \dot{i}_a \end{bmatrix} = F_o \begin{bmatrix} i_{oa} \\ v_a \\ i_a \end{bmatrix} + G_o U_o, \quad Y_o = C_o \begin{bmatrix} i_{oa} \\ v_a \\ i_a \end{bmatrix} + D_o U_o, \quad F_o = \begin{bmatrix} -R_{oa}/L_{oa} & -1/L_{oa} & 0 \\ 1/C_{oa} & 0 & -1/C_{oa} \\ 0 & 0 & 0 \end{bmatrix},$$

$$G_o = [1/L_{oa} \quad 0 \quad 0]^T, \quad U_o = v_{oa} \quad (6.15)$$

Here, the matrices C_o and D_o can be designed according to the desired outputs. Given that the system in (6.10) and (6.11) is observable, the gain matrix L in (6.14) can be designed correctly so that the eigenvalues of $F-LC$ are strictly on the left-hand side of

complex plane. Under this condition, the estimation error dynamics is asymptotically stable, which means the estimation error will decay to zero eventually. In this work, a 2-D observer is adopted because of simplicity and it can be derived in a manner similar to the 3-D observer. Load currents $i_{a,b,c}$ and source voltages $v_{sA,sB,sC}$ are estimated using the observers. The desired eigenvalues for estimating $i_{a,b,c}$ and $v_{sA,sB,sC}$ are set to $-2200 \pm 3800i$, and -80000 and -80001 respectively. It is worth mentioning that the sampling time influences the performance of the observer since a discrete integrator is used. The shorter sampling time results in more accurate estimation.

6.1.4 Predictive Voltage Controller Design

In the MPC, a cost function is used to optimize the selection of switch actions. The design of cost function reflects the control objectives and priorities. In this work, the main control objective is the stable sinusoidal output voltages, in addition to unit input power factor, elimination of the common-mode voltage, and low switching frequency. Different combinations can be used depending on the specific applications. Therefore, the cost function for selecting the optimum switch state consists of four sub-functions and they are described in sequence by

$$g = \lambda_1 \cdot \left\{ |v_a^* - v_a^p| + |v_b^* - v_b^p| + |v_c^* - v_c^p| \right\} + \lambda_2 \cdot |Q^* - Q^p| + \lambda_3 \cdot |v_N^* - v_N| + \lambda_4 \cdot \sum_{i=1}^9 |S_i - S_i^p| \quad (6.16)$$

where $v_{a,b,c}^*$ and Q^* are references for the three-phase output voltages and input reactive power, and their counterparts $v_{a,b,c}^p$ and Q^p are the predicted values; v_N represents the common-mode voltage shown in Fig. 6.2 and its desired reference v_N^* is normally zero; S_i is the current switch state and S_i^p is the potential switch state to be applied; and $\lambda_{1,2,3,4}$ are the weighting factors which determine priorities for each term. Terms with greater factors attract more control attention. The main control objective here is to have stable output sinusoidal voltages. If more control objectives are considered at the same time, each control performance will be compromised. Designing these factors is usually based on empirical methods [35]. The cost function is not limited to this form; other terms such as integral and squared terms can also be used for meeting the requirements of different applications. The operation of absolute values in (6.16) consumes a great amount of execution time, and therefore they can be replaced by the square operation.

Here the input power factor control is achieved by regulating the reactive power. The reactive power is calculated using

$$Q = \frac{3}{2}(v_{S-\beta} \cdot i_{S-\alpha} - v_{S-\alpha} \cdot i_{S-\beta}), \quad P = \frac{3}{2}(v_{S-\alpha} \cdot i_{S-\alpha} + v_{S-\beta} \cdot i_{S-\beta}) \quad (6.17)$$

where Q and P represent the reactive and active power. $v_{S-\alpha, \beta}$ and $i_{S-\alpha, \beta}$ represent the α and β components of source voltages $v_{SA, SB, SC}$ and currents $i_{SA, SB, SC}$, and they are obtained using abc to $\alpha\beta$ transformation

$$\begin{bmatrix} u_\alpha \\ u_\beta \end{bmatrix} = \begin{bmatrix} \frac{2}{3} & -\frac{1}{3} & -\frac{1}{3} \\ 0 & -\frac{1}{\sqrt{3}} & \frac{1}{\sqrt{3}} \end{bmatrix} \begin{bmatrix} u_a \\ u_b \\ u_c \end{bmatrix} \quad (6.18)$$

where $u_{\alpha, \beta}$ and $u_{a, b, c}$ stand for the variables in the $\alpha\beta$ and abc systems.

From the above descriptions, the model predictive voltage controller for the direct MC in an islanded microgrid can be illustrated by Fig. 6.5. In this figure, the measured variables are denoted by the solid arrow lines, while the dashed arrow lines represent the observed variables. The calculated variables are shown by the dot-dashed lines. It is worth noting that the algorithm sample delay can be compensated in this controller [36].

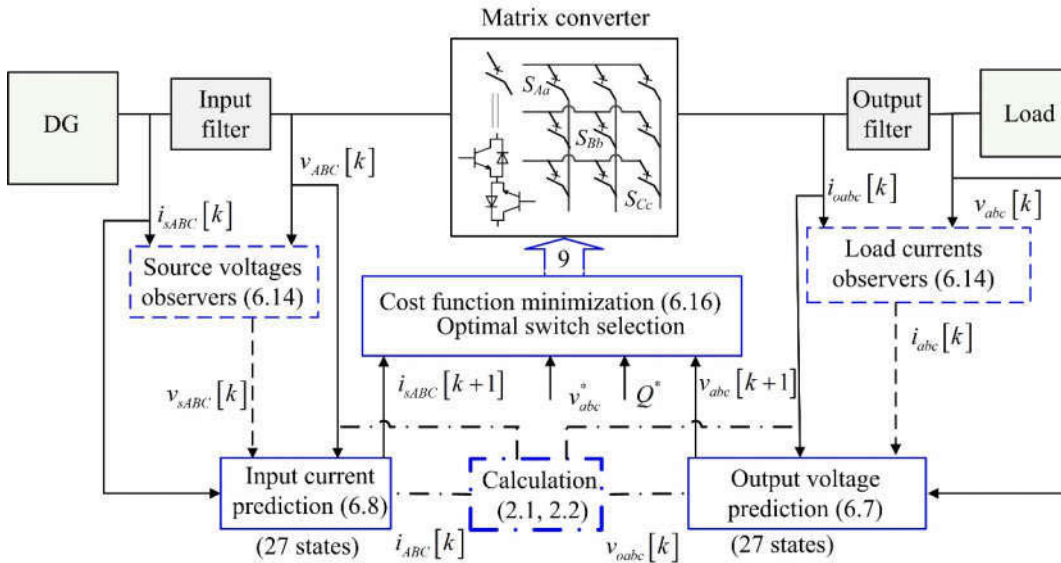


Fig. 6.5 The predictive voltage controller scheme for MC in an islanded microgrid.

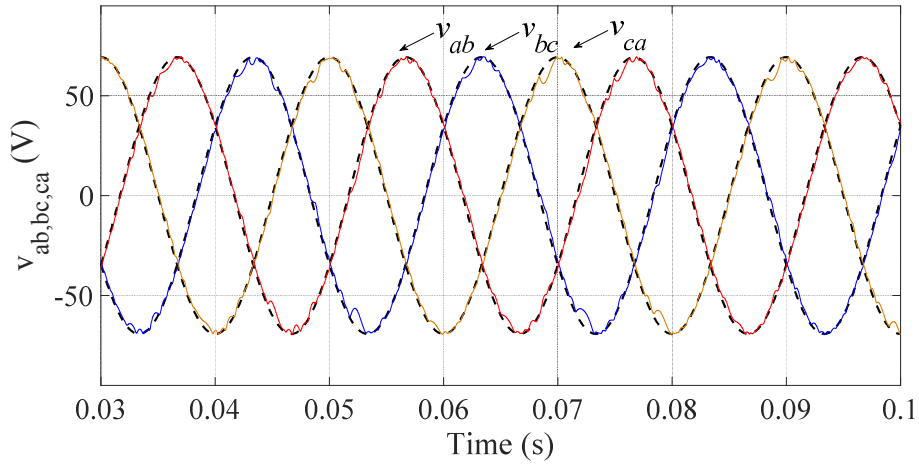
6.1.5 Simulation Results

In order to verify the proposed strategy, simulation tests were carried out and the results are shown in this section. The simulation parameters are tabulated in Table 6.1. The MPC controller parameters for each test are shown in the figure captions for clarity. Since this work focuses on the islanded operation mode, the stable voltages should be maintained under various load and input conditions. The execution time of the algorithm was around 61 μs and the sampling interval should be long enough for the code to be executed. As a result, a sampling time of 80 μs was used. In all the following figures, the black dashed voltage waveforms denote the voltage references.

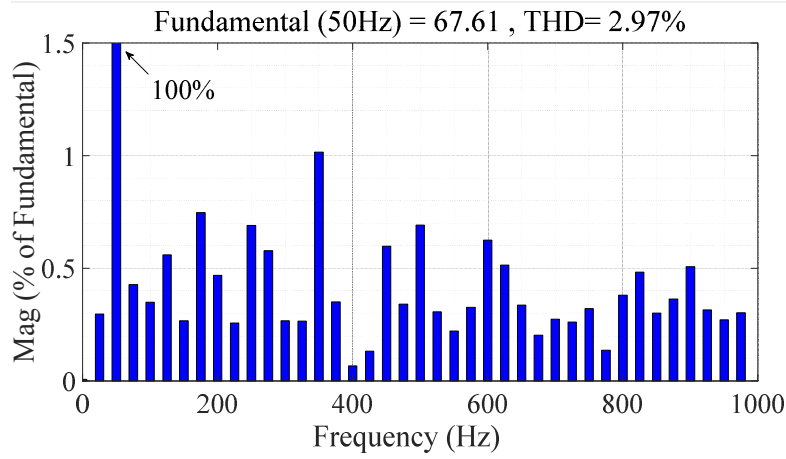
Table 6.1 Simulation system and controller parameters

v_s [V _{pk-pk}]	L_A [mH]	C_{AB} [μF]	R_A [Ω]	L_{oa} [mH]	C_{oa} [μF]	R_{oa} [Ω]	f_s [Hz]	f_o [Hz]	Q^* [VAr]	T_s [μs]
100	6.8	9.5	0.5	8	40	0.5	50	50	0	80

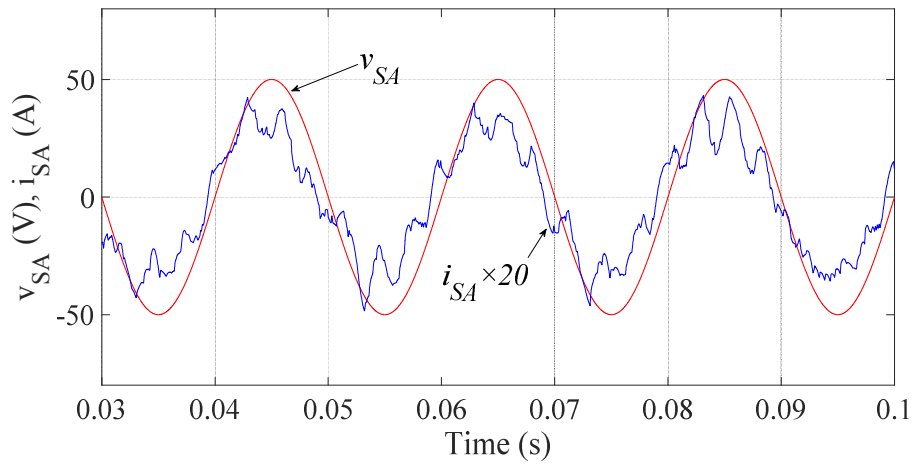
Fig. 6.6 shows the steady-state test results for an inductive load ($R_l = 20 \Omega$, $L_l = 14 \text{ mH}$). The amplitude and frequency of output line-to-line voltages were set to $40\sqrt{3} \text{ V}$ and 50 Hz. Fig. 6.6(a) shows the regulated three-phase output voltages, and the fast Fourier transform (FFT) analysis is shown in Fig. 6.6(b). As seen in the figure, the output voltages can be regulated to track the prescribed references effectively. In IEEE standard Std-519, the recommended harmonic voltage limits are 5 % for the individual harmonic and 8 % for the total harmonic distortion (THD). As seen in Fig. 6.6(b), the regulated voltage satisfies these requirements. Fig. 6.6(c) shows the system source voltage and current. The input power factor is not regulated in this test, and therefore there exists an obvious phase difference between the voltage and current. The result of controlled input power factor will be shown later. Fig. 6.6(d) compares the estimated load currents ($i_{ae, be, ce}$ - solid lines) and measured loads currents ($i_{a, b, c}$ - dashed lines). A good match between the estimated and measured curves is achieved.



(a)



(b)



(c)

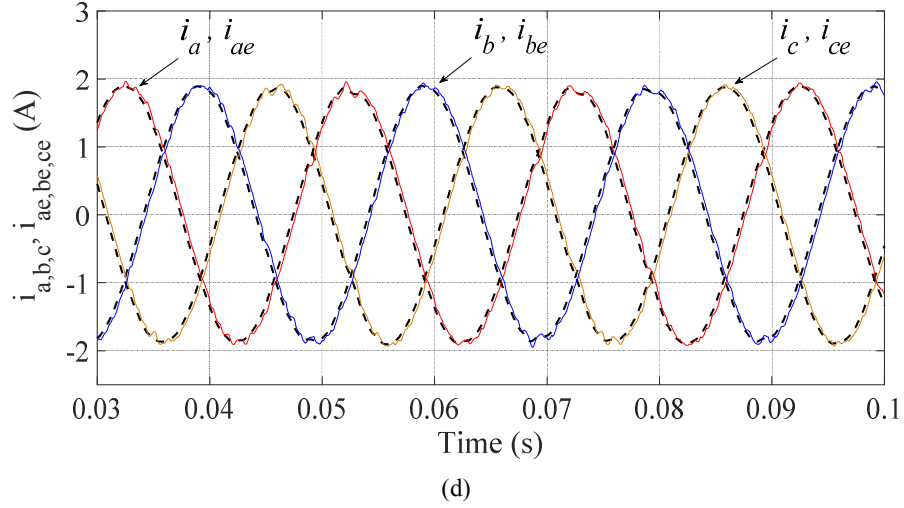


Fig. 6.6 Simulation results: (a) regulated output line-to-line voltages, (b) FFT analysis result and harmonic spectrum for v_{ab} , (c) source voltage and current waveforms, (d) estimated and measured load currents. ($\lambda_1=1$, $\lambda_2=0$, $\lambda_3=0$, $\lambda_4=0$).

Table 6.2 Investigation of VTR versus output filter parameters

Case	L_{oa} [mH]	C_{oa} [μ F]	Fundamental	VTR	THD [%]
1	2	40	46.23	0.9246	4.79
2	8	40	45.82	0.9164	5.55
3	15	40	44.98	0.8996	5.43
4	8	10	44.75	0.8950	6.56
5	8	30	45.52	0.9104	5.98
6	8	60	46.23	0.9246	4.27
7	2	10	46.01	0.9202	8.77
8	15	60	45.94	0.9188	3.89

As analysed in the previous section, an output filter can help improve the VTR. Table 6.2 demonstrates the VTR performance for different values of L_{oa} and C_{oa} as studied in the previous section. As seen in Table 6.2, the VTR is larger than 0.866 for all the cases presented in the table. Here the reference amplitudes are the same as the source voltage amplitudes. The fundamental output voltage amplitude is used when investigating the VTR. It is worth noting that the fundamental amplitude is normally lower than the peak amplitude. Therefore, the consideration of peak amplitude can lead to a slightly higher VTR. Increasing voltage references can also result in an increase in VTR while the distortions will deteriorate. The voltage waveforms corresponding to these cases are

shown in Fig. 6.7. From these results, it is concluded that good voltage regulation performance with improved VTR can be achieved with the proposed strategy by selecting appropriate filter parameters.

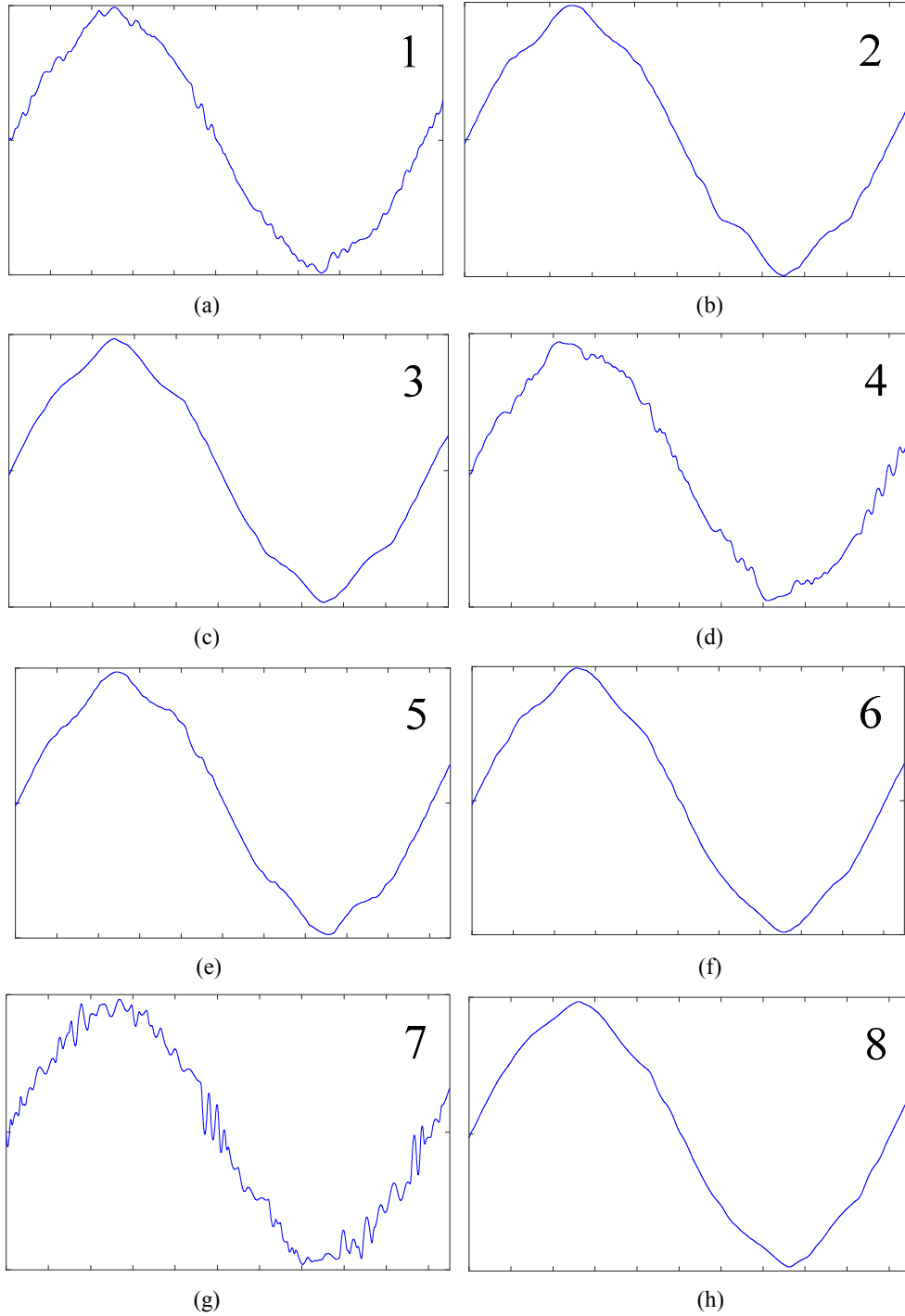
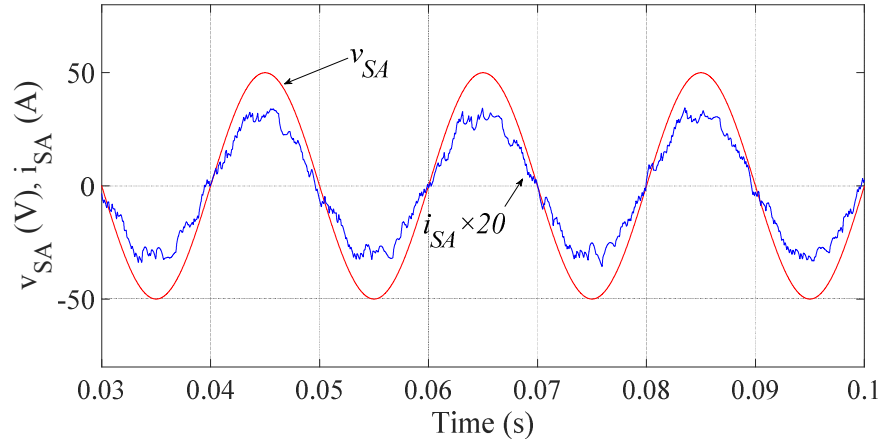
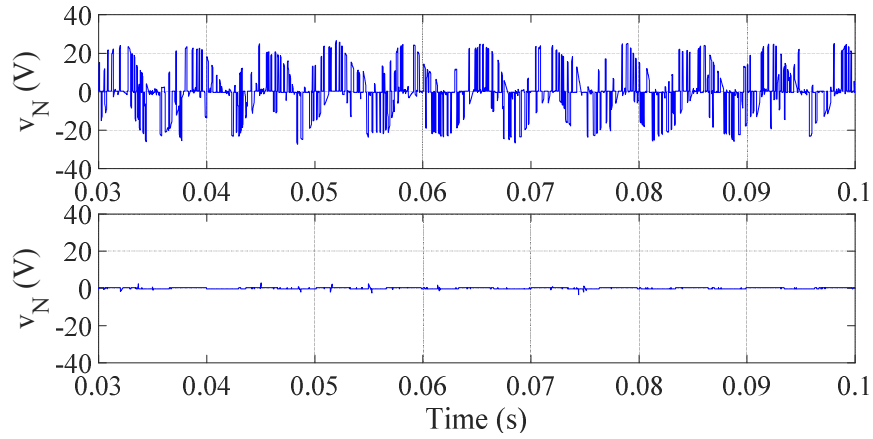


Fig. 6.7 Simulation results: output voltage waveforms corresponding to the parameter combinations listed in Table 6.2.

In addition to the voltage regulation, the predictive control can also control the input power factor, common-mode voltage and the switching frequency. These results are presented in Fig. 6.8. The source voltage and current with the controlled input power factor are shown in Fig. 6.8(a). As observed in this figure, the current is nearly in phase with the voltage. A unity power factor is achieved with the proposed controller. Fig. 6.8(b) demonstrates the common-mode voltage reduction performance. From this figure, it is observed that the common-mode voltage is heavily suppressed. The common-mode voltage reduction is especially beneficial to motor loads. Fig. 6.8(c) compares the unregulated and regulated averaging switching frequencies of the switches. As seen, the average switching frequency can be regulated effectively. The lower switching frequency can result in lower switching losses.



(a)



(b)

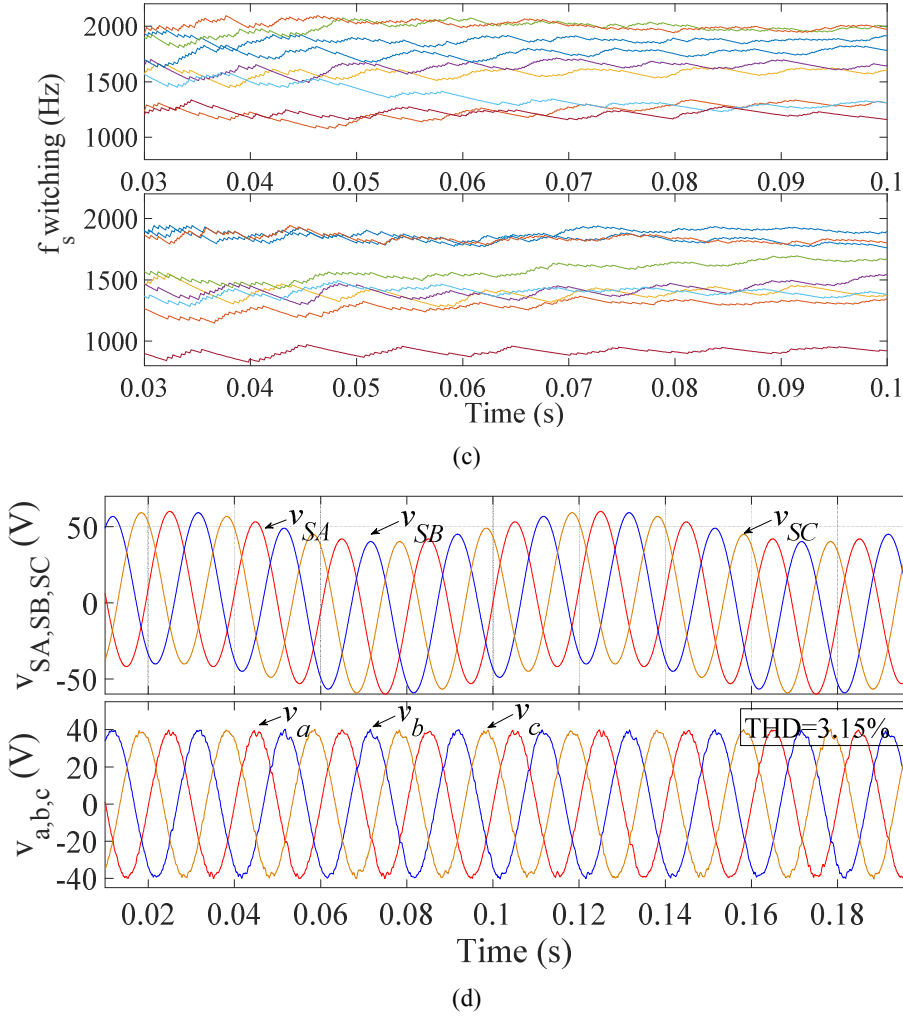
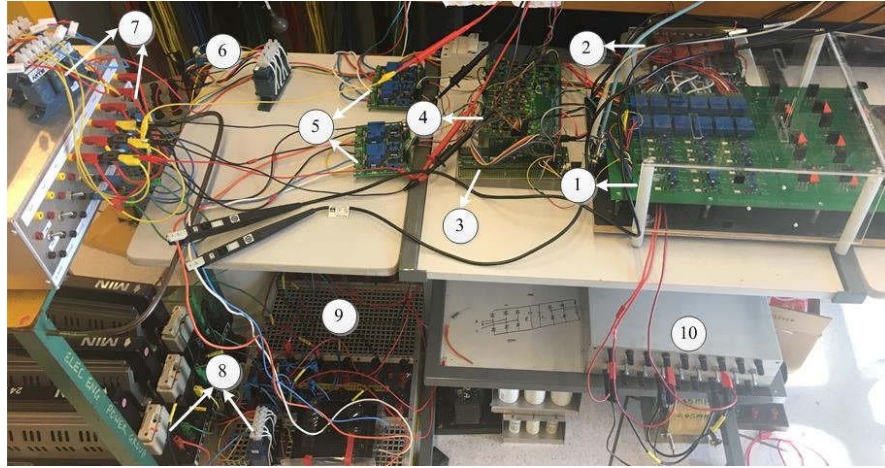


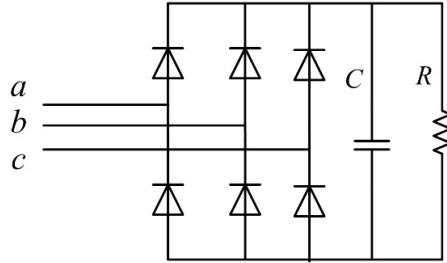
Fig. 6.8 Simulation results: (a) source voltage and current with controlled power factor with $\lambda_2=0.0067$, (b) uncontrolled and controlled common mode voltage with $\lambda_3=25$, (c) uncontrolled and controlled average switching frequencies with $\lambda_4=0.09$, (d) simulated intermittent source voltages and controlled output voltages.

In a renewable DG based microgrid, the source voltage may suffer from an intermittent disturbance because of the discontinuity of a renewable energy source. This was simulated by adding the disturbance signal of $10 \times \sin(20\pi t)$ V to the source voltages. The source voltages and regulated output voltages are displayed in Fig. 6.8(d). It can be concluded from this figure that the output voltage can be controlled effectively, although the source voltages are unbalanced and have disturbances. The proposed scheme was also tested under an unbalanced load and a nonlinear load. However, these results are not presented here because the regulated voltage waveforms are very similar to the results shown in Figs. 6.6(a) and 6.8(d). Instead, the corresponding experimental

results will be shown in the next section. The simulation results in this section verify the feasibility of the proposed scheme and effectiveness of the proposed controller.



(a)



(b)

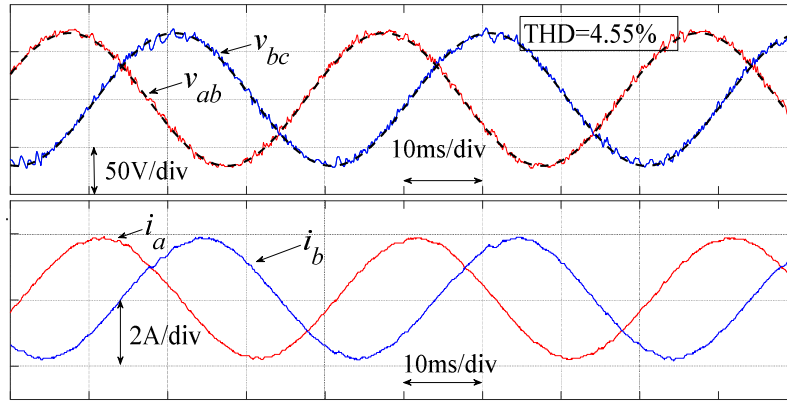
Fig. 6.9 Hardware setup for verifying the proposed scheme: (a) MC system comprising ① MC prototype, ② IGBT drivers power supply, ③ microprocessor control card, ④ ADC conditioning circuits, ⑤ sensors boards, ⑥ input filter inductors, ⑦ output LC filters, ⑧ inductive loads, ⑨ clamp circuit, ⑩ input filter capacitors, (b) nonlinear load with $R=30\Omega$ and $C=1700\mu\text{F}$.

6.1.6 Experimental Validation

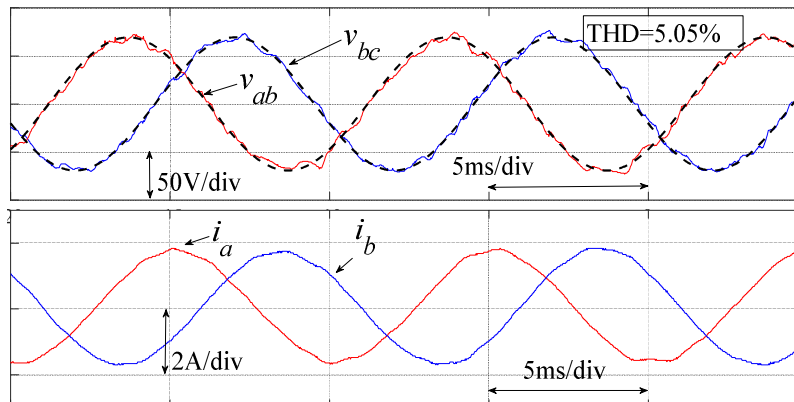
In order to further validate the feasibility and effectiveness of the proposed strategies, the MC set-up previously described was modified and the experimental work was carried out. The experimental set up is shown in Fig. 6.9(a). Fig. 6.9(b) shows the nonlinear load used to perform the nonlinear load test. A serial communications interface was used for the communication between the host computer and DSP card for sending command and receiving data. The analog to digital conversion (ADC) and

peripheral circuits were employed to process the signals from voltage and current sensors. The enhanced pulse width modulator blocks were used to generate the control pulses.

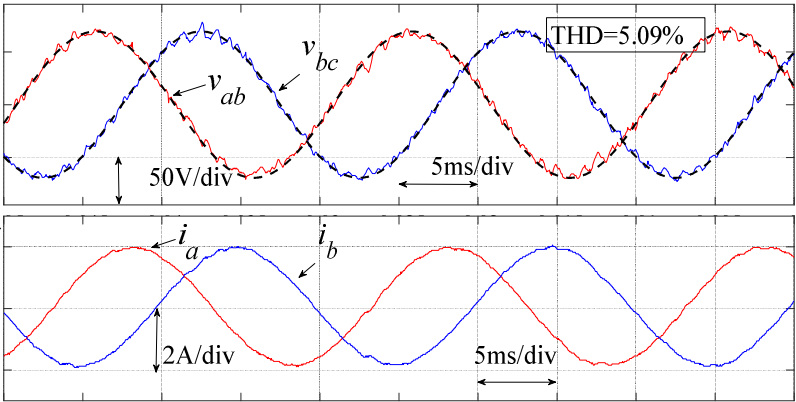
In the experimental tests, the amplitude and frequency of output line-to-line voltages were set to $40 \times \sqrt{3}$ V and 50 Hz. The reference voltages are denoted by the dashed lines in the following figures. Other system parameters are shown in Table 6.1 which are same as the simulation parameters unless elsewhere specified. Figs. 6.10(a)-(c) show the regulated output voltage waveforms tracking reference voltages of different frequencies (25, 100 and 50 Hz). The corresponding currents are shown in the bottom part of each figure. Here only two phases (v_{ab} , v_{bc} and i_a , i_b) are shown for clarity, and the THD values are shown at the top-right corner for v_{ab} . These results demonstrate the effectiveness of proposed controller in regulating the output voltage with a wide frequency range. The MC can be employed to interface two systems that are greatly different in frequencies.



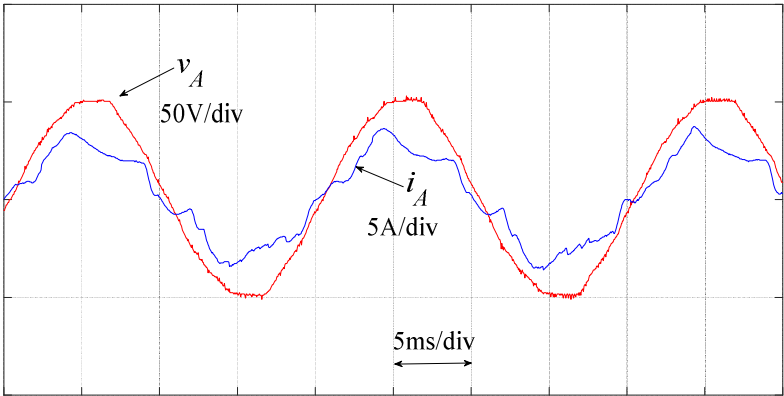
(a)



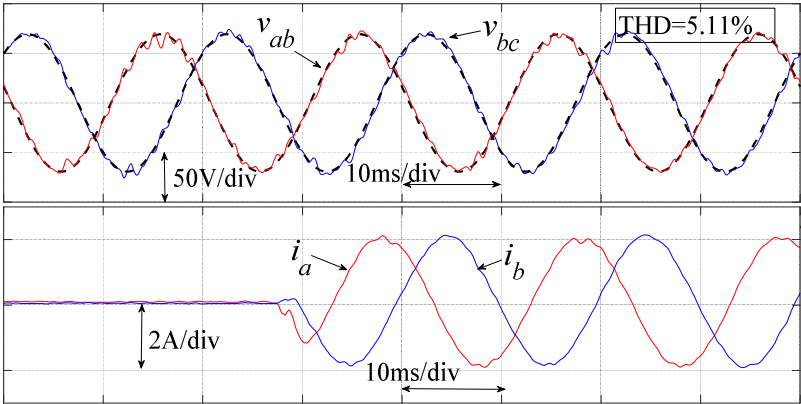
(b)



(c)



(d)



(e)

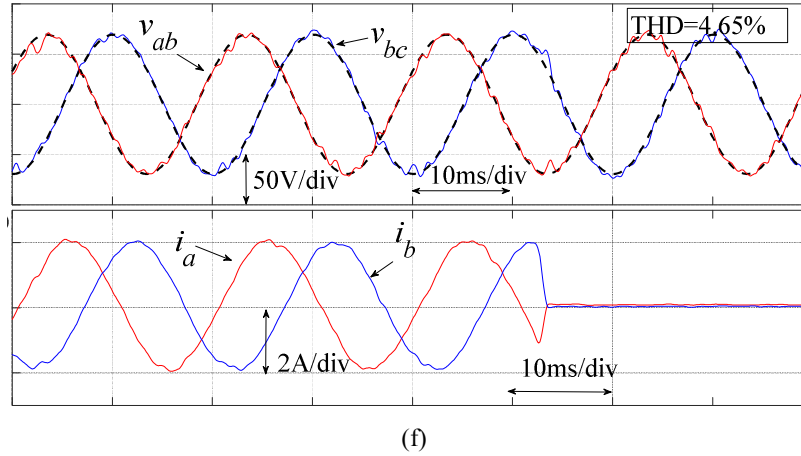


Fig. 6.10 Experimental waveforms: (a) output voltage and currents when $f_o=25$ Hz, (b) output voltage and currents when $f_o=100$ Hz, (c) output voltage and currents when $f_o=50$ Hz, (d) source voltage and current when $f_o=50$ Hz, (e) output voltage and current responses to load connection, (f) output voltage and current responses to load disconnection. ($\lambda_1=1$, $\lambda_2=0$, $\lambda_3=0$, $\lambda_4=0$).

Fig. 6.10(d) shows the experimental waveforms of the source voltage and current with uncontrolled input power factor. An obvious phase difference exists between the voltage and current. The results with the controlled input power factor will be shown in the later part of this section. Fig. 6.10(e) displays the output voltage and currents responses to load connection. At the beginning, there is no load connected to the output terminals, so the load currents are zero. There is no obvious perturbation in the regulated voltages when the load is applied. In contrast, Fig. 6.10(f) shows the responses to load disconnection. This figure verifies when the load is shed, the output voltage can be regulated effectively. The THD values in these results are low, ranging from 4.55 % to 5.11 %. The voltage quality in terms of harmonics distortion complies with the requirements in IEEE standard Std-519.

In Fig. 6.11, the experimental results for the regulated input power factor and common-mode voltage are shown and compared with the unregulated waveforms. In Fig. 6.11(a), the regulated input power factor is increased to 0.981 from 0.943. The power factor was obtained from a FLUKE clamp meter. The power factor values shown in the figure are the averaged values based on several readings. This is because of the varying power factor caused by the current distortions. From Fig. 6.11(b), it is evident that the common-mode voltage is suppressed dramatically.

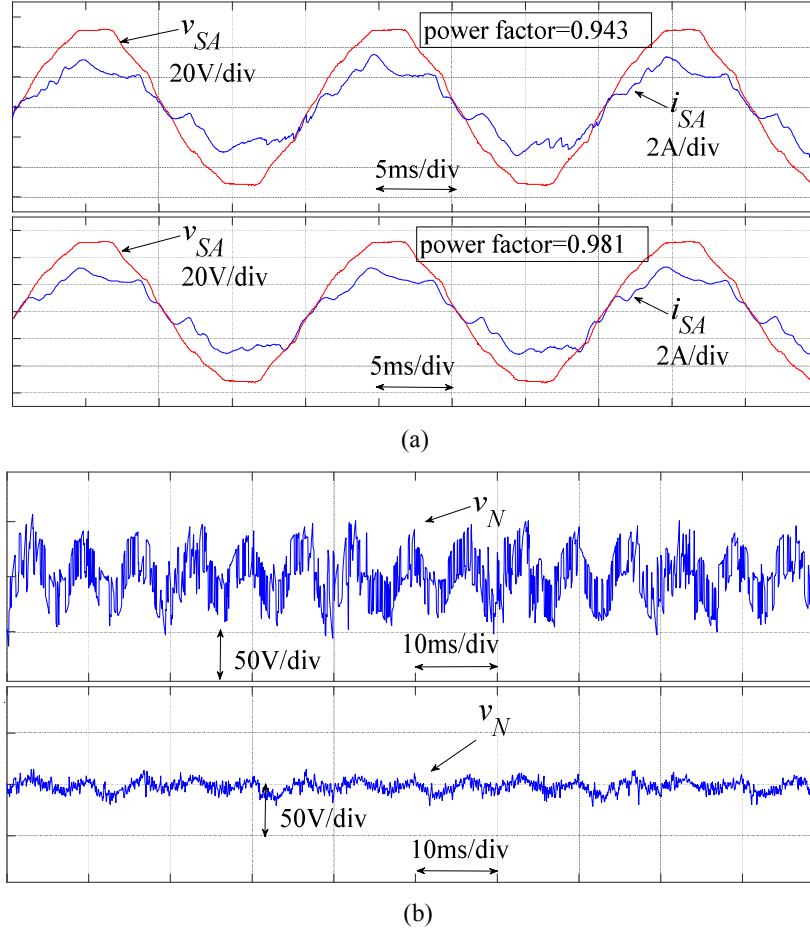
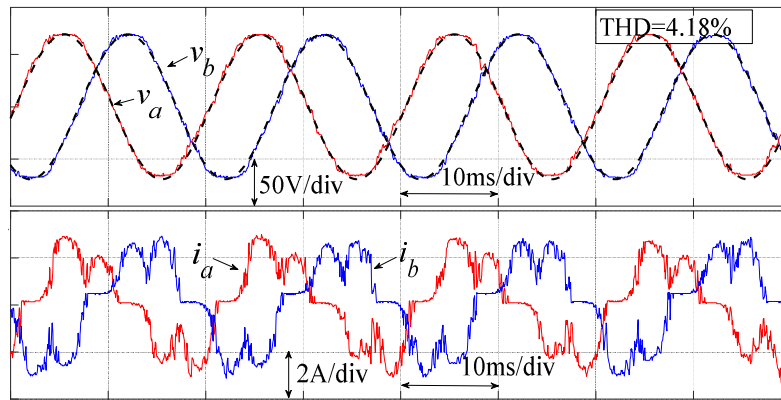
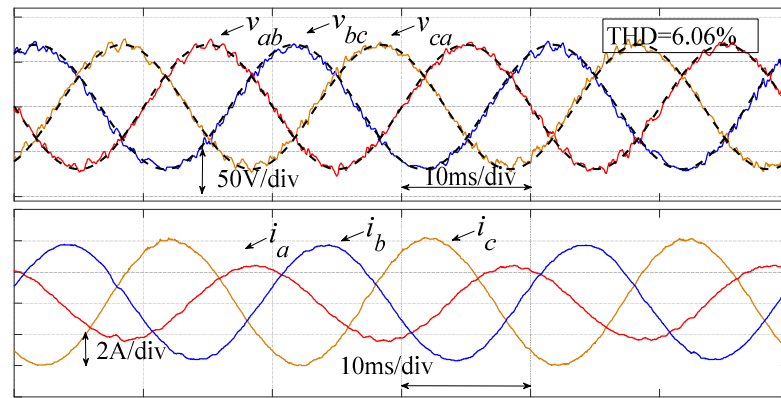


Fig. 6.11 Experimental waveforms: (a) uncontrolled and controlled input power factor with $\lambda_2=0.0067$, (b) uncontrolled and controlled common mode voltage with $\lambda_3=25$.

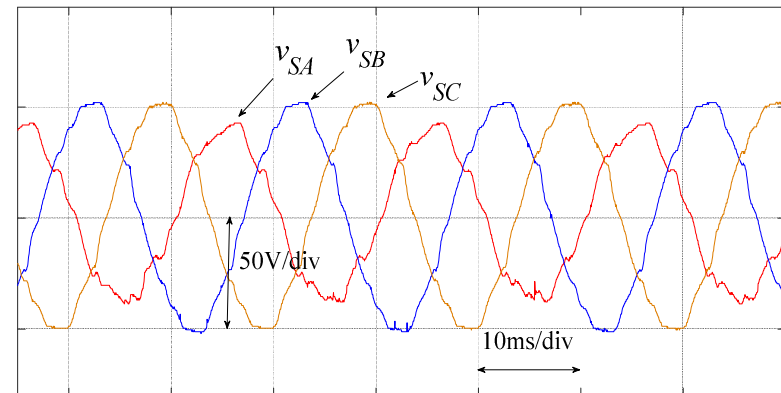
Fig. 6.12 presents the experimental results for the nonlinear load, unbalanced load and unbalanced input tests. The nonlinear load used for Fig. 6.12(a) was a three-phase diode bridge rectifier with a capacitive load, as shown in Fig. 6.9(b). As shown in Fig. 6.12(a), the output voltage can be regulated effectively under the nonlinear load test. The output current is distorted in a manner similar to the current in common rectifier applications (even with ideal voltage supplies). The current can be improved with extra filters. Fig. 6.12(b) shows the results of unbalanced load test. For the unbalanced load test, the resistors for each phase were changed to 20, 12 and 8 Ω respectively while the inductors were kept at 14 mH.



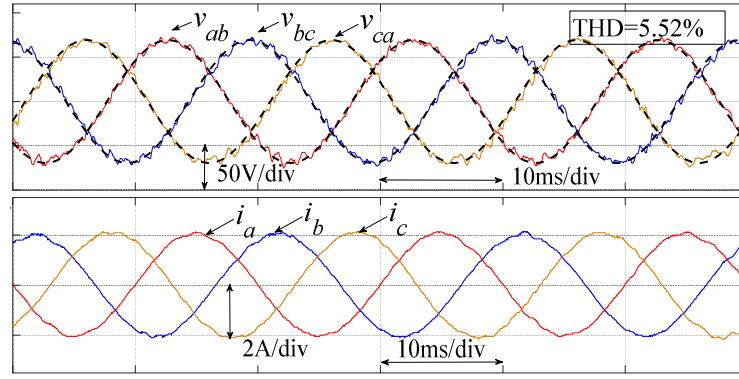
(a)



(b)



(c)



(d)

Fig. 6.12 Experimental waveforms: (a) output voltages and currents for nonlinear load test, (b) output voltages and currents for unbalanced load test, (c) input voltages and currents for unbalanced input test, (d) output voltages and currents for unbalanced input test.

Since it was not practical to implement the intermittent tests, tests under unbalanced input were performed instead. This is achieved by inserting a $5\ \Omega$ resistor in phase A , between the source supply and the MC. The resulted supply voltages are shown Fig. 6.12(c) while the regulated output voltages and load currents are shown in Fig. 6.12(d). As can be seen, a stable voltage is maintained even when the source is unbalanced.

The proposed scheme has been tested under various load and input conditions as described above. The experimental results verify that the output voltage can be effectively controlled to provide a stable voltage supply with good quality to different loads. The voltage harmonic distortions are under the limits set in IEEE Std-519.

6.1.7 Conclusions

An MC can fulfill direct AC/AC conversion and it can be used to interface different systems with appropriate control strategies. The work in this section proposes a renewable energy based microgrid involving a direct MC. The LC filters are connected to the output terminals to provide a stable sinusoidal voltage supply to the load. The predictive voltage control is developed, and this involves various control objectives including sinusoidal output voltages, unit input power factor, common-mode voltage and averaging switching frequency reduction. The main control objective is to supply the stable voltage to various loads under various input and load conditions including unbalanced and nonlinear loads. A renewable energy based DG may suffer from the intermittent disturbance and unbalance which are also investigated in this work. Various

tests validate the effectiveness of MC when applied in an islanded microgrid. The VTR is improved and it is supported by the theoretical analysis. Luenberger observers are adopted in the work to reduce the required number of sensors, thus the cost. Their effectiveness is verified when used in a predictive voltage controller. The simulation and experimental results verify the feasibility and effectiveness of the proposed strategy.

6.2 Predictive Control for Other Conversion Possibilities

The three-phase direct MC has been researched exclusively as a direct AC/AC converter, being an alternative to the conventional AC/DC/AC converter. Other possibilities of the MC such as AC/DC, DC/AC and DC/DC conversion still remain unexplored. This section firstly explores these possibilities and puts forward a concept of versatile converter. With one MC, different conversion purposes can be accomplished as required. The MC based conversion has some advantages compared with other converters. MPC is applied in this work to control the MC to perform the required conversion goals. A generalized model is obtained for all types of conversion. With MPC, different objectives and constraints can be easily included in the control scheme. In addition, the observers are used to reduce the number of voltage and current sensors. Simulation results verify the effectiveness and feasibility of AC/DC, DC/AC and DC/DC conversion with the MC.

6.2.1 Introduction

Smart grids and eco-friendly distributed generation systems are growing in popularity [37]. Power electronic converters are becoming common components in the power industry and they are becoming more important especially in the context of modern smart grids involving various renewable energy sources and energy storage systems. They play a vital role in various areas such as renewable energy integration, grid synchronization, energy conversion and power control [38-40]. Power electronic converters can be generally classified into following four types: AC/AC, AC/DC, DC/AC and DC/DC converters. Almost all power electronic converters are employed for one unique purpose of conversion only, such as a rectifier for the AC/DC conversion, an inverter for the DC/AC conversion and a Buck-Boost converter for the

DC/DC conversion. However, the modern power industry requires more flexibility in power conversion and control strategies [41][42]. Different converters are required in different situations. Therefore, it is beneficial if one converter can perform any conversion function when required. The concept of versatile conversion with the MC was put forward in [19] where a three-phase direct MC was proposed for the stand-alone operation of an AC microgrid to supply stable and sinusoidal voltages to local loads.

The direct three-phase MC has been considered as an alternative to the traditional AC/DC/AC converter. It is suitable for a wide range of applications including renewable energy and aerospace systems [43]. It has advantages such as compact volume, bidirectional power flow, controllable input power factor, sinusoidal waveform, direct conversion and longer life cycle [20]. Its derivatives have been proposed for many applications [44]. However, the MC has only really been researched as an AC/AC converter. This section investigates some interesting possibilities of the MC for other types of conversion, i.e., AC to DC, DC to AC and DC to DC conversion, which leads to a versatile converter. This illustrates some open research and potential application areas of the MC, such as electric vehicles, AC and/or DC grid interface, renewable energy systems, UPS and aircraft systems. Some features of different types of conversion with the MC are compared with their traditional counterparts. Different possibilities, except for AC/AC conversion which is already well known, are discussed here.

- AC to DC conversion: in MC based conversion, the capacitance required at the DC side is reduced markedly compared with common rectifiers [45], from hundreds or thousands of microfarads to several tens of microfarads. As there are three terminals at the output side, three levels of DC voltage can be obtained, which results in the increased flexibility. Interestingly, the MC based AC/DC converter can be used as either the boost or buck type of converter to supply DC loads with a wide voltage range. The output DC voltages can cover a wide range (being able to reach zero), and the input power factor can be regulated to reach unity. This is advantageous considering more stringent requirements on the current THD and power factor. Unity input power factor can be maintained even under low DC output voltage operations. This conversion topology can handle the issues of unbalanced input AC supplies.

- DC to AC conversion: with the MC, up to three independent DC voltages can be connected to the input side. This structure can handle the common mode voltage which is intractable with traditional DC/AC inverter drives [46]. In this structure, the large electrolytic capacitors are not required at the DC side. Other benefits of the traditional DC/AC inverter are still retained with this structure.
- DC to DC conversion: it is worth noting that DC to DC conversion is possible with the MC although it is not very practical to do so because of the high number of switches. However, both input and output have three terminals which can enable the best use of switches and flexible use of DC sources. High power capacity can be achieved.

MPC is a simple yet powerful control for power electronic converters [30]. It is used in this work to achieve the desired control objectives. Various control objectives and system constraints can be easily included in this control strategy. It is very easy to understand and implement. A generalized MPC is employed in this work to control all types of conversion.

6.2.2 Versatile Conversion and Simulation Results

Simulation results are presented in this section for AC/AC, AC/DC, DC/AC and DC/DC conversions. The system parameters are shown in Table 6.3. The sampling time T_s is set to 1×10^{-5} s. The weighting factors vary from case to case depending on the control objectives. The power sources and filter parameters should be appropriately adjusted according to the requirement of each type of conversion. The loads for AC/AC and DC/AC conversion are inductive loads, while the loads for AC/DC and DC/DC conversion are capacitive loads.

Table 6.3 Simulation system parameters.

V_s (V)	R_A (Ω)	L_A (mH)	C_{AB} (μ F)	R_{oa} (Ω)	L_{oa} (mH)	C_{ab} (μ F)	R_L (Ω)	L_L (mH)	C_L (μ F)
220	0.5	3.2	2	0.5	4.8	10	50	10	20

(a). AC-AC Conversion

AC to AC conversion using the MC (shown in Fig. 6.13) has been researched, mainly focusing on the output current control. However, the output voltage control of an MC is rarely investigated. The stand-alone operation of an MC based AC microgrid was proposed in [46] to supply stable and sinusoidal voltages to the loads. In [46], the input power factor, common-mode voltage and switching frequency are considered in the MPC; therefore, they are not presented here.

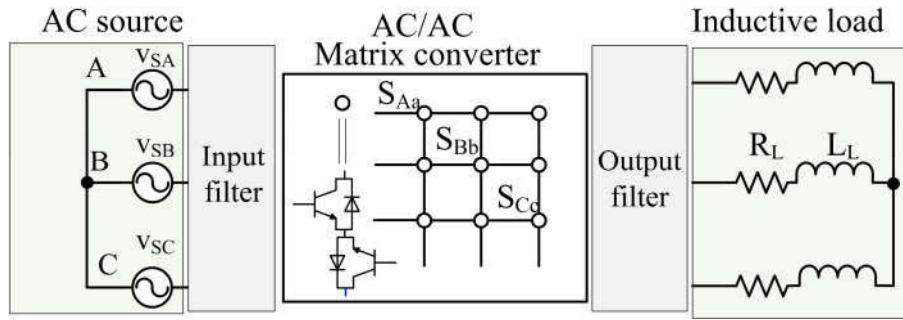


Fig. 6.13 Diagram for AC/AC conversion using MC.

(b). AC-DC Conversion

Regarding AC to DC conversion shown in Fig. 6.14, the output voltage and input power factor are regulated. Reference voltages for three DC output terminals are $[100 -33.33 -66.67]$ V before 0.05 s and $[100 -33.33 -66.67] \times 1.5$ V after 0.05 s. The output DC voltages can be obtained either from each terminal (level) or from two terminals to get the difference between two levels. Simulation results are shown in Fig. 6.15. From Fig. 6.15(b), it is evident that the dynamic response is fast and zero steady state error is maintained. The voltage and current of phase A input are shown in Fig. 6.15(c) and they are in phase (unity power factor operation).

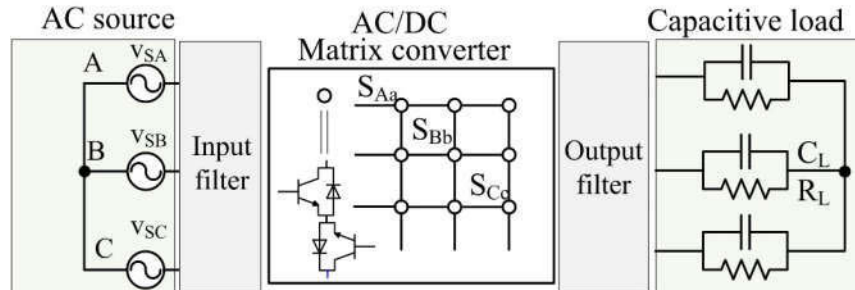


Fig. 6.14 Diagram for AC/DC conversion using MC.

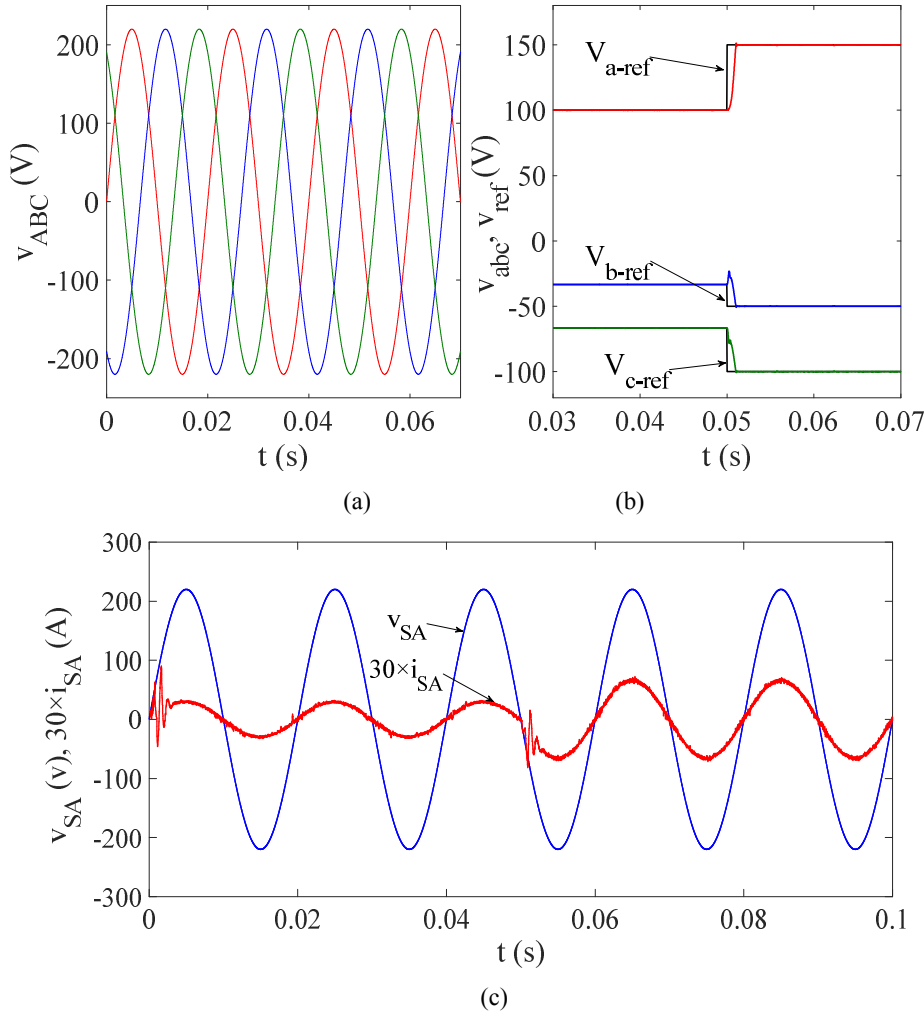


Fig. 6.15 AC/DC conversion (a) input voltages, (b) output voltages and (c) unity input power factor operation for the input phase A .

(c). DC-AC Conversion

One of the main applications of DC/AC converters is the AC motor drive where a rectifier is usually needed to generate a DC voltage supply. In this case, AC/AC conversion using the MC can be applied, eliminating the DC link in the traditional AC/DC/AC drive structure [47]. Another main application of DC/AC converters is the integration of DC energy sources into an AC grid. This is the main interest of this work. Although up to 3 independent DC supplies can be utilized at the input as shown in Fig. 6.16, only one DC source is considered here to make it comparable with traditional DC/AC converters. Therefore, the DC voltage supplies v_{SB} and v_{SC} are short circuited to the negative pole of v_{SA} (not just removed). The reference output AC voltages are

$[50\sin(100\pi t) \ 50\sin(100\pi t-2\pi/3) \ 50\sin(100\pi t+2\pi/3)]$ V before 0.05 s and $[90\sin(100\pi t) \ 90\sin(100\pi t-2\pi/3) \ 90\sin(100\pi t+2\pi/3)]$ V after 0.05 s. The output voltage is shown in Fig. 6.17(a). It is evident that the voltage tracking performance is good and dynamic response is fast. With only one DC source, the common-mode voltage cannot be handled effectively. The common-mode voltage reduction for the case of two DC sources is shown in Figs. 6.17(b) and (c). The common-mode voltage is suppressed significantly.

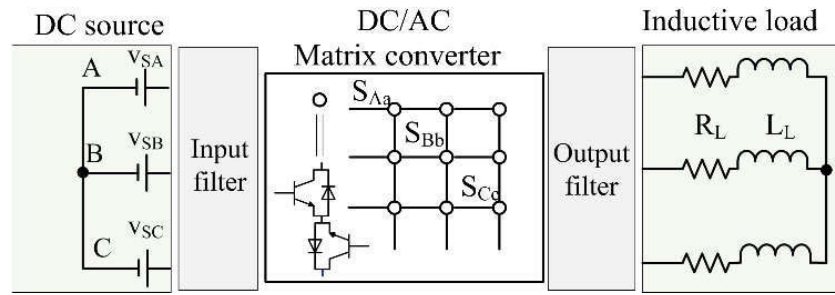
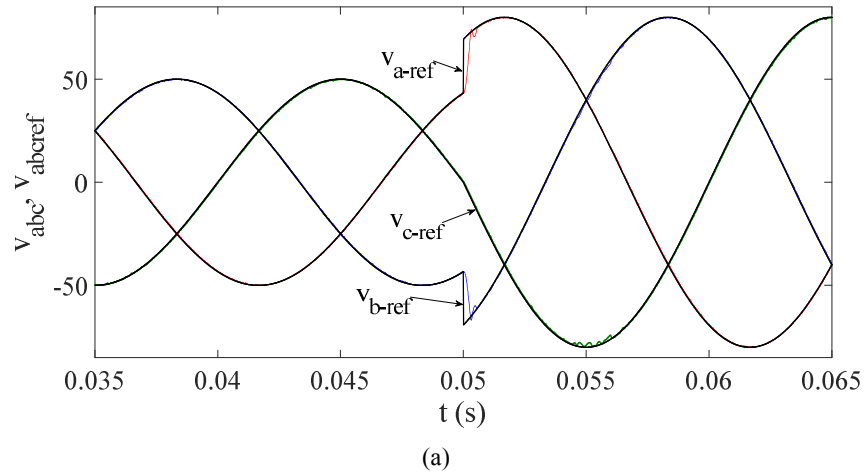


Fig. 6.16 Diagram for DC/AC conversion using MC.



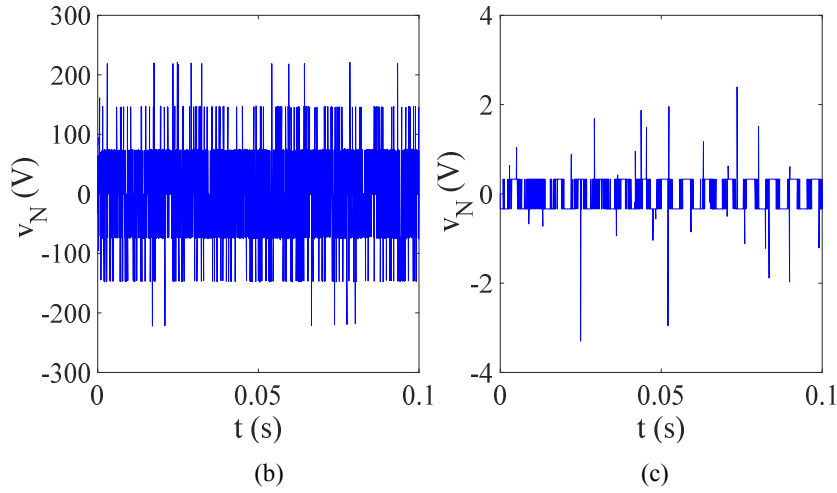


Fig. 6.17 DC/AC conversion (a) output voltages, (b) unregulated common-mode voltage and (c) regulated common-mode voltage.

(d). DC-DC Conversion

DC/DC conversion using an MC requires too many semiconductor devices compared to traditional DC/DC converters [46][48]. However, both input and output have three terminals enabling the input and output to be connected to three DC sources and three loads respectively as shown in Fig. 6.18. The power capacity can be improved with this structure. In this type of conversion, some of the 9 switches will be underutilized and this depends on the input and output arrangements. Simulation results are shown for single DC input and three DC output. Output voltage references are [60 0 -60] V before 0.05 s and [100 0 -100] V after 0.05 s. Output voltages are shown in Fig. 6.19(a) and their performance is acceptable. Large electrolytic capacitors are not required in this topology. The average switching frequency of 9 switches in the MC is shown in Fig. 6.19(b). As seen from this figure, some of the switches are underutilized and this is related to the input and output connections.

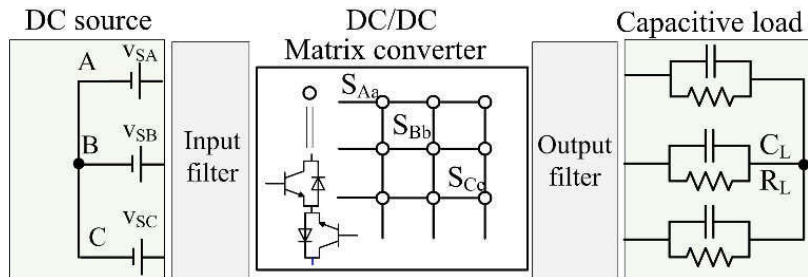
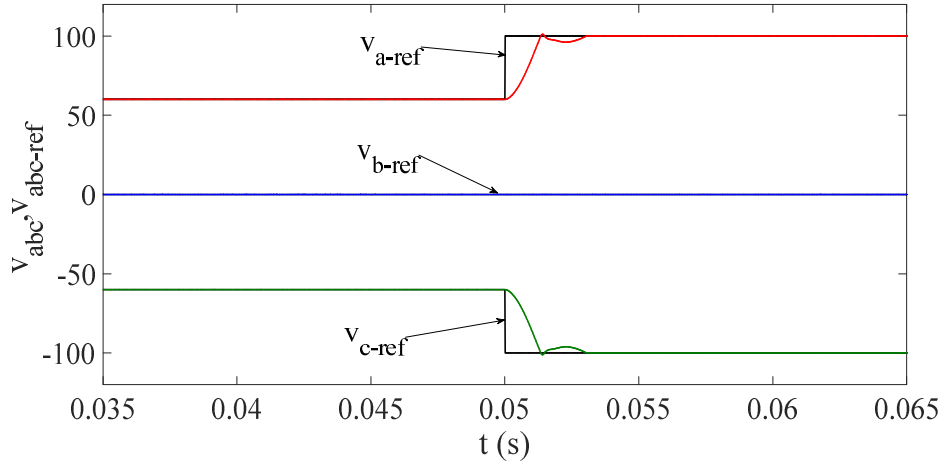
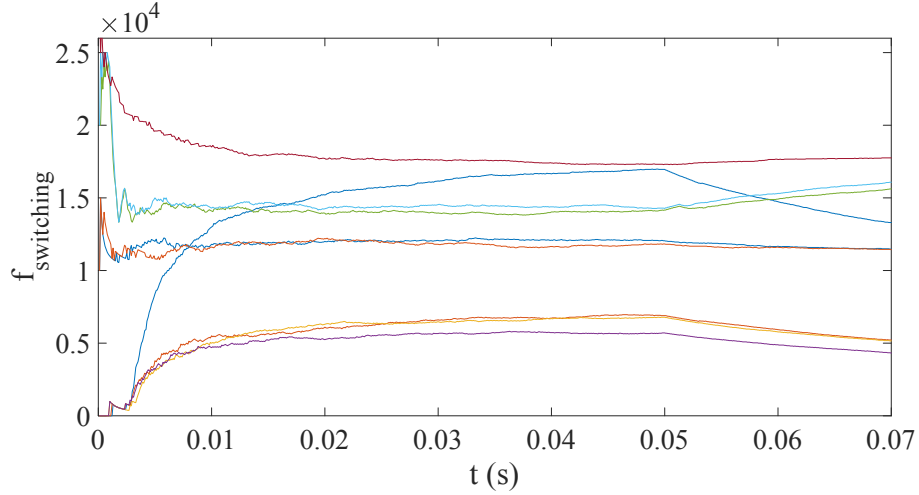


Fig. 6.18 Diagram for DC/DC conversion using MC.



(a)



(b)

Fig. 6.19 DC/DC conversion (a) output voltages and (b) average switching frequencies of 9 switches in the MC.

6.2.3 Conclusions

This section puts forward a discussion of a versatile converter based on the direct three-phase MC. Different types of conversion, i.e., AC/AC, AC/DC, DC/AC and DC/DC can be performed as required. MPC is adopted to control the MC based on a generalized model. Various control objectives and system constraints can be considered in the MPC controller. Power can flow bidirectionally through the MC. Simulation results verify the feasibility of the proposed scheme and demonstrate the features for each type of conversion. Other aspects regarding this topic such as PWM techniques and control

methods development, switching losses investigation and application exploration are open for research. Further work needs to be done to fully investigate the working mechanism of each type of conversion with the MC. The operation of different scenarios under various input and load conditions needs to be further investigated too. To conclude, the MC cannot only be used as an AC/AC converter, but also as AC/DC, DC/AC and DC/DC converters.

6.3 Summary

In this chapter, predictive control is used to explore the application of direct MCs in microgrids. The MC is regulated to supply stable three-phase sinusoidal output voltages for the load in the islanded microgrid. The grid-connected operation will be investigated in the future work. The MC's potential conversion possibilities for AC/DC, DC/AC and DC/DC are also investigated in this chapter.

The materials presented in this chapter have been published in [19] and [23].

References

- [1] Y. Xia, W. Wei, M. Yu, X. Wang, and Y. Peng, "Power Management for a Hybrid AC/DC Microgrid with Multiple Subgrids," *IEEE Trans. Power Electron.*, vol. 33, no. 4, pp. 3520-3533, 2018.
- [2] H. Xiao, A. Luo, Z. Shuai, G. Jin, and Y. Huang, "An improved control method for multiple bidirectional power converters in hybrid AC/DC microgrid," *IEEE Trans. Smart Grid*, vol. 7, no. 1, pp. 340-347, 2016.
- [3] J. Pegueroles-Queralt, F. D. Bianchi, and O. Gomis-Bellmunt, "A power smoothing system based on supercapacitors for renewable distributed generation," *IEEE Trans. on Ind. Electron.*, vol. 62, no. 1, pp. 343-350, 2015.
- [4] S. A. Saleh, E. Ozkop, and A. S. Aljankawey, "The Development of a Coordinated Anti-Islanding Protection for Collector Systems With Multiple Distributed Generation Units," *IEEE Trans. Ind. Appl.* vol. 52, no. 6, pp. 4656-4667, 2016.
- [5] D. E. Olivares, A. Mehrizi-Sani, A. H. Etemadi, C. A. Canizares, R. Iravani, M. Kazerani, A. H. Hajimiragha et al., "Trends in microgrid control," *IEEE Trans. smart grid*, vol. 5, no. 4, pp. 1905-1919, 2014.
- [6] X. Dou, K. Yang, X. Quan, Q. Hu, Z. Wu, B. Zhao, P. Li, S. Zhang and Y. Jiao. "An Optimal PR Control Strategy with Load Current Observer for a Three-Phase Voltage Source Inverter," *Energies* 8, no. 8, pp. 7542-7562, 2015.

- [7] J. Huang, C. Jiang and R. Xu, "A review on distributed energy resources and MicroGrid," *Renewable and Sustainable Energy Reviews*, vol. 12, no. 9, pp. 2472-2483, 2008.
- [8] A. Trivedi and M. Singh, "Repetitive Controller for VSIs in Droop Based AC-Microgrid," *IEEE Trans. Power Electron.*, vol. 32, no. 8, pp. 6595-6604, 2017.
- [9] N. Hatziaegyriou, H. Asano, R. Iravani, and C. Marnay, "Microgrids," *IEEE power and energy mag.*, vol. 5, no. 4, pp. 78-94, 2007.
- [10] B. Kroposki, R. Lasseter, T. Ise, S. Morozumi, S. Papatlianassiou, and N. Hatziaegyriou, "Making microgrids work," *IEEE power and energy mag.*, vol. 6, no. 3, pp. 41-53, 2008.
- [11] N. Merritt, C. Chakraborty, and P. Bajpai, "New Voltage Control Strategies for VSC based DG Units in an Unbalanced Microgrid," *IEEE Trans. Sustainable Energy*, vol. 8, no. 3, pp., 1762-1770, 2017.
- [12] J. Justo, F. Mwasilu, J. Lee and J. Jung, "AC-microgrids versus DC-microgrids with distributed energy resources: A review." *Renewable and Sustainable Energy Reviews*, vol. 24, pp.387-405, 2013.
- [13] L. Wang, D. Zhang, Y. Wang, B. Wu, and H. S. Athab, "Power and voltage balance control of a novel three-phase solid-state transformer using multilevel cascaded H-Bridge inverters for microgrid applications," *IEEE Trans. Power Electron.*, vol. 31, no. 4, pp. 3289-3301, 2016.
- [14] F. Bosio, L. Ribeiro, F. Freijedo, M. Pastorelli and J. Guerrero, "Discrete-Time Domain Modelling of Voltage Source Inverters in Standalone Applications: Enhancement of Regulators Performance by Means of Smith Predictor," *IEEE Trans. Power Electron.*, DOI 10.1109/TPEL.2016.2632527, 2016.
- [15] I. J. Balaguer, Q. Lei, S. Yang, U. Supatti, and F. Z. Peng, "Control for grid-connected and intentional islanding operations of distributed power generation," *IEEE Trans. Ind. Electron.*, vol. 58, no. 1, pp. 147-157, 2011.
- [16] P. Cortés, G. Ortiz, J. Yuz, J. Rodríguez, S. Vazquez and L. G. Franquelo, "Model predictive control of an inverter with output filter for UPS applications," *IEEE Trans. on Ind. Electron.*, vol. 56, no. 6, pp. 1875-1883, 2009.
- [17] A. Pirooz and R. Noroozian, "Predictive voltage control of three-phase voltage source inverters to supply nonlinear and unbalanced loads," *6th Drives Systems & Technologies Conf. (PEDSTC)*, pp. 389-394, 2015.
- [18] X. Liu, P. Loh, P. Wang, F. Blaabjerg, Y. Tang, and E. A. Al-Ammar, "Distributed generation using indirect matrix converter in reverse power mode," *IEEE Trans. on Power Electron.*, vol. 28, no. 3, pp. 1072-1082, 2013.
- [19] J. Zhang, L. Li, Z. Malekjamshidi, and D. G. Dorrell, "Predictive Voltage Control of Direct Matrix Converter with Reduced Number of Sensors for the Renewable Energy and Microgrid Applications," *IEEE Energy Conversion Congress and Exposition (ECCE)*, Cincinnati, USA, pp. 3309-3315, Oct. 2017.
- [20] P. Wheeler, J. Rodriguez, J. C. Clare, L. Empringham, and A. Weinstein, "Matrix converters: A technology review," *IEEE Trans. on Ind. Electron.*, vol. 49, no. 2, pp. 276-288, 2002.
- [21] J. Zhang, L. Li, D. Dorrell, and Yo. Guo, "A PI controller with current feedforward to improve the steady-state error performance for a current controlled direct matrix converter," *20th Int. Conf. Electrical Machines and Syst. (ICEMS)*, IEEE, pp. 1-6., 2017.

- [22] G. Zhang, M. Su, Q. Zhu, and F. Blaabjerg, "A Predictive-Control-Based Over-Modulation Method for Conventional Matrix Converters," *IEEE Trans. Power Electron.*, vol. 33, no. 4, pp. 3631 – 3643, 2018.
- [23] J. Zhang, L. Li, and D. Dorrell, "Investigation of Direct Matrix Converter Working as a Versatile Converter (AC/AC, AC/DC, DC/AC, DC/DC Conversion) with Predictive Control," In 43rd Annual Conference Industrial Electronics Society, IEEE IECON 2017, Beijing, China, pp. 4644-4649, 2017.
- [24] J. Zhang, D. G. Dorrell and L. Li, "Applications of the Direct Space Vector Modulation Controlled Matrix Converter as the Unified Power Flow Controller," *The 8th Int. Conf. on Power Electron., Machines & Drives (PEMD 2016)*, Glasgow, pp. 1-6, 2016.
- [25] S. Arevalo, P. Zanchetta, P. W. Wheeler, A. Trentin, and L. Empringham, "Control and implementation of a matrix-converter-based AC ground power-supply unit for aircraft servicing," *IEEE Trans. Ind. Electron.*, vol. 57, no. 6, pp. 2076-2084, 2010.
- [26] P. Zanchetta, P. W. Wheeler, J. C. Clare, M. Bland, L. Empringham, and D. Katsis, "Control design of a three-phase matrix-converter-based ac-ac mobile utility power supply." *IEEE Trans. on Ind. Electron.*, vol. 55, no. 1, pp. 209-217, 2008.
- [27] M. Hamouda, F. Fnaiech, K. Al-Haddad and H. Y. Kanaan, "Matrix converter control: A sliding mode approach." *30th Ann. Conf. Ind. Electron. Society (IECON 2004)*, vol. 3, pp. 2295-2300, 2004.
- [28] S. M. Ahmed, H. Abu-Rub and Z. Salam, "Common-Mode Voltage Elimination in a Three-to-Five-Phase Dual Matrix Converter Feeding a Five-Phase Open-End Drive Using Space-Vector Modulation Technique," *IEEE Trans. Ind. Electron.*, vol. 62, no. 10 pp. 6051-6063, 2015.
- [29] J. Rodriguez, M. P. Kazmierkowski, J. R. Espinoza, P. Zanchetta, H. Abu-Rub, H. A. Young and C. A. Rojas, "State of the art of finite control set model predictive control in power electronics," *IEEE Trans. Ind. Informatics*, vol. 9, no. 2 pp. 1003-1016, 2013.
- [30] S. Kouro, P. Cortés, R. Vargas, U. Ammann and J. Rodríguez, "Model predictive control—A simple and powerful method to control power converters," *IEEE Trans. Ind. Electron.*, Vol. 56, no. 6, pp. 1826-1838, 2009.
- [31] M. Rivera, C. Rojas, J. Rodríguez, P. Wheeler, B. Wu, and J. R. Espinoza, "Predictive current control with input filter resonance mitigation for a direct matrix converter," *IEEE Trans. Power Electron.*, vol. 26, no. 10, pp. 2794-2803, 2011.
- [32] M. Rivera, A. Wilson, C. A. Rojas, J. Rodriguez, J. R. Espinoza, P. W. Wheeler, and L. Empringham, "A comparative assessment of model predictive current control and space vector modulation in a direct matrix converter." *IEEE Trans. on Ind. Electron.*, vol. 60, no. 2, pp. 578-588, 2013.
- [33] S. Vazquez, J. I. Leon, L. G. Franquelo, J. Rodriguez, H. A. Young, A. Marquez, and P. Zanchetta, "Model predictive control: A review of its applications in power electronics," *IEEE Ind. Electron. Magazine*, vol. 8, no. 1, pp. 16-31, 2014.
- [34] IEEE Recommended Practice and Requirements for Harmonic Control in Electric Power Systems, IEEE Standard: IEEE Std 519™-2014 (Revision of IEEE Std 519-1992).

- [35] P. Cortés, S. Kouro, B. L. Rocca, R. Vargas, J. Rodríguez, J. I. León, S. Vazquez and L. G. Franquelo, "Guidelines for weighting factors design in model predictive control of power converters and drives," *Int. Conf. Ind. Tech. (ICIT 2009)*, pp. 1-7, 2009.
- [36] P. Cortes, J. Rodríguez, C. Silva and A. Flores, "Delay compensation in model predictive current control of a three-phase inverter," *IEEE Trans. Ind. Electron.*, vol. 59, no. 2, pp. 1323-1325, 2012.
- [37] F. Blaabjerg, R. Teodorescu, M. Liserre, and A. V. Timbus, "Overview of control and grid synchronization for distributed power generation systems," *IEEE Trans. Ind. Electron.*, vol. 53, no. 5, p. 1398-1409, 2006.
- [38] P. Rodriguez, A. Luna, R. Santiago Munoz-Aguilar, I. Etxeberria-Otadui, R. Teodorescu, and F. Blaabjerg, "A stationary reference frame grid synchronization system for three-phase grid-connected power converters under adverse grid conditions," *IEEE Trans. Power Electron.*, vol. 27, no. 1, pp. 99-112, 2012.
- [39] J. M. Carrasco, L. G. Franquelo, J. T. Bialasiewicz, E. Galván, R. C. PortilloGuisado, M. M. Prats, J. I. León, and N. Moreno-Alfonso, "Power-electronic systems for the grid integration of renewable energy sources: A survey," *IEEE Trans. Ind. Electron.*, vol. 53, no. 4, pp. 1002-1016, 2006.
- [40] J. Rocabert, A. Luna, F. Blaabjerg, and P. Rodriguez, "Control of power converters in AC microgrids," *IEEE Trans. Power Electron.*, vol. 27, no. 11, pp. 4734-4749, 2012.
- [41] J. A. Momoh, "Smart grid design for efficient and flexible power networks operation and control," In *Power Systems Conference and Exposition*, IEEE, pp. 1-8, 2009.
- [42] A. Camacho, M. Castilla, J. Miret, J. C. Vasquez, and E. Alarcón-Gallo, "Flexible voltage support control for three-phase distributed generation inverters under grid fault," *IEEE Trans. Ind. Electron.*, vol. 60, no. 4, pp. 1429-1441, 2013.
- [43] S. F. Pinto, P. V. Mendes and J. Fernando Silva, "Modular matrix converter based solid state transformer for smart grids," *Electric Power Syst. Research*, vol. 136, pp. 189-200, 2016.
- [44] J. Zhang, L. Li, D. G. Dorrell, "Dq coupling suppressed PID controller for the transmission line power flow control using a matrix converter." In *42nd Annual Conference Industrial Electronics Society, IECON 2016*, IEEE, pp. 6249-6254, 2016.
- [45] A. K. Singh, Elango Jeyasankar, Pritam Das, and Sanjib Kumar Panda, "A Matrix-Based Nonisolated Three-Phase AC–DC Rectifier With Large Step-Down Voltage Gain," *IEEE Trans. Power Electron.*, vol. 32, no. 6, pp. 4796-4811, 2017.
- [46] L. Concari, D. Barater, C. Concar, and G. Buticchi, "A novel three-phase inverter for common-mode voltage reduction in electric drives," In *Energy Conversion Congress and Exposition (ECCE 2017)*, IEEE, pp. 2980-2987, 2015.
- [47] J. Zhang, L. Li, D. G. Dorrell, Y. Guo, "Direct Torque Control with a Modified Switching Table for a Direct Matrix Converter based AC Motor Drive System," *20th Int. Conf. on Electrical Machines and Systems (ICEMS 2017)*. Sydney, Australia, 2017.
- [48] J. Zhang, D. G. Dorrell, L. Li, and A. Argha, "A novel sliding mode controller for DC-DC boost converters under input/load variations," In *41st Annual Conf. Ind. Electron. Society (IECON 2015)*, IEEE, pp. 1698-1703, 2015.

7 CONCLUSIONS

This chapter concludes this thesis and outlines further work that can be carried out in the future.

7.1 Conclusions

The direct matrix converter (MC) offers many advantages such as bidirectional power flow, controllable power factor, high power density, increased system reliability and the potential to serve as a versatile converter. However, there are some drawbacks associated with this converter. This thesis tries to find solutions to some of these issues and key findings have been reported in other chapters. These include: (1) a simple control method of an MC based unified power flow controller (MC-UPFC); (2) improvement of the steady-state performance; (3) a simple hysteresis band controller for an MC-fed AC drive; (4) applications of the MC in smart grids and distributed generations; and (5) improvement of voltage transfer ratio with an LC filter and predictive control.

In this thesis, some control strategies and potential application areas of the three-phase direct MC were investigated. Conclusions for each work were summarized at the end of each chapter. Most research objectives have been achieved. It is concluded that the MC is a promising converter that can be applied in various areas especially in motor drives and microgrids due to many benefits that this converter can provide.

The control strategies including space vector modulation, proportional-integral control, proportional-resonant control, hysteresis-band (HB) current control, direct torque control, and model predictive control. Some derivatives were investigated in this thesis for the three-phase direct MC. These control strategies can be applied in different fields depending on specific applications. Some of the control strategies proposed in this thesis can be readily extended to other converters.

In terms of application areas, the work in this thesis illustrates that the MC can be used as a unified power flow controller in transmission systems, motor drives, distributed generation systems and both islanded and grid-connected microgrids. These demonstrate the potential areas where the MC can be applied.

7.2 Future Work

Research work has been carried out and some objectives have been achieved as presented in this thesis. However, more research still needs to be done to develop MC technology. Based on the work presented in this thesis and other work reported in the literature, further potential areas of investigation are summarized as follows.

- (1) The application of the MC in regulating power flow of a transmission system needs to be further investigated especially in the experimental environment. Here the MC is employed to interface two AC systems that have the same frequency, which is an important field.
- (2) The HB controlled MC has been investigated for motor drives in Chapter 4. However, the MC input current is not controlled effectively. SVM can be combined with the proposed HB controller to control a motor drive and the MC input current at the same time. In addition, constant switching frequency can be achieved with this strategy.
- (3) When used in a microgrid, the MC can be utilized in both islanded and grid-connected modes. The control of the MC in the islanded mode has been investigated. The effectiveness of the MC in islanded mode has been validated experimentally. However, the effectiveness of the MC in grid-connected mode is not validated experimentally.

(4) The MC can carry out AC/DC, DC/AC and DC/DC conversion in addition to AC/AC conversion. This proposal needs further investigation in terms of specific modulation techniques, as well as the advantages and disadvantages when compared with traditional converters. This should be done through theoretical investigation and experimental work. Potential application areas need to be investigated as well.

(5) Model predictive control is a simple and powerful tool for power electronic converters including MCs. However, due to the heavy computational burden caused by a large number of control actions in MCs, and design of weighting factors for different objectives, model predictive control is not very practical to implement. Sequential model predictive control is a modified control strategy that does not require weighting factors and reduces the computational burden. This method can be exploited in MCs and other converters as well used to simplify the design process and improve the performance. This area is expected to attract more research attention.

APPENDICES

APPENDIX A	168
APPENDIX B	172

APPENDIX A

DERIVING EQUATIONS FOR DIRECT SVM

In order to obtain the equations (2.9) to (2.14) in Chapter 2, the following steps can be followed.

According to Fig. 2.3(a) in Chapter 2, the following equations are obtained for the voltage vectors,

$$|V_\beta| = t_{x1}|V_{x1}| + t_{x2}|V_{x2}| = T_s \frac{2V_o \sin(\theta)}{\sqrt{3}} \quad (\text{A.1})$$

$$|V_\alpha| = t_{y1}|V_{y1}| + t_{y2}|V_{y2}| = T_s \frac{2V_o \sin(\pi/3 - \theta)}{\sqrt{3}} \quad (\text{A.2})$$

where V_{x1} , V_{x2} and V_{y1} , V_{y2} are the appropriate active vectors chosen to form V_α and V_β respectively. $|V|$ denotes the amplitude of the vector V . t_{x1} , t_{x2} and t_{y1} , t_{y2} are their corresponding working time as expressed by

$$t_\beta = t_{x1} + t_{x2} \quad (\text{A.3})$$

$$t_\alpha = t_{y1} + t_{y2} \quad (\text{A.4})$$

$$t_{01} = T_s - (t_\alpha + t_\beta) \quad (\text{A.5})$$

where T_s is the cycle period (also the switching period); t_α , t_β and t_{01} are the time for V_α , V_β and zero vectors. Their corresponding duty cycles are:

$$D_\alpha = \frac{t_\alpha}{T_s}, \quad D_\beta = \frac{t_\beta}{T_s}, \quad D_{01} = \frac{t_{01}}{T_s}, \quad 0 \leq D_\alpha, D_\beta, D_{01} \leq 1, \quad D_\alpha + D_\beta + D_{01} = 1$$

Although the amplitudes of active vectors vary with the input voltages, their instantaneous values can be replaced by the sampled value during a sampling period since the sampling time is usually very short. When both the output voltage and input current vector lie in sector ① of their hexagons, vector numbers ± 1 , ± 3 , ± 7 and ± 9 should be selected. However, the selection of $+1$, -3 , -7 and $+9$ renders lowest switching actions. According to Fig. 2.3(a), the following equations are obtained:

$$-t_{x1}|V_{+9}| + t_{x2}|V_{-7}| = T_s \frac{2V_o \sin(\theta)}{\sqrt{3}} \quad (\text{A.6})$$

$$-t_{y1}|V_{-3}| + t_{y2}|V_{+1}| = T_s \frac{2V_o \sin(\pi/3 - \theta)}{\sqrt{3}} \quad (\text{A.7})$$

Similar to the above analysis, based on Fig. 2.3(b), the relationships pertaining to the current vectors are obtained:

$$|I_\delta| = -t_{x1}|I_{+9}| + t_{y1}|I_{-3}| = T_s \frac{2I_i \sin(\rho)}{\sqrt{3}} \quad (\text{A.8})$$

$$|I_\gamma| = -t_{x2}|I_{-7}| + t_{y2}|I_{+1}| = T_s \frac{2I_t \sin(\pi/3 - \rho)}{\sqrt{3}} \quad (\text{A.9})$$

$$t_\delta = t_{x1} + t_{y1} \quad (\text{A.10})$$

$$t_\gamma = t_{x2} + t_{y2} \quad (\text{A.11})$$

$$t_{02} = T_s - (t_\gamma + t_\delta) \quad (\text{A.12})$$

$$D_\gamma = \frac{t_\gamma}{T_s}, \quad D_\delta = \frac{t_\delta}{T_s}, \quad D_{02} = \frac{t_{02}}{T_s}, \quad 0 \leq D_\gamma, D_\delta, D_{02} \leq 1, \quad D_\gamma + D_\delta + D_{02} = 1$$

According to (A.6) to (A.9), t_{x1} , t_{x2} , t_{y1} , and t_{y2} can be solved. However, it is easier to use the following equations.

$$\frac{t_{x1}|I_{+9}|}{\sin(\rho)} = \frac{t_{x2}|I_{-7}|}{\sin(\pi/3 - \rho)} \quad (\text{A.13})$$

$$\frac{t_{y1}|I_{-3}|}{\sin(\rho)} = \frac{t_{y2}|I_{+1}|}{\sin(\pi/3 - \rho)} \quad (\text{A.14})$$

Here (A.13) and (A.14) are obtained based on the Sine law. According to (A.6), (A.7), (A.13) and (A.14), t_{x1} , t_{x2} and t_{y1} , t_{y2} are derived:

$$t_{x1} = \frac{2}{\sqrt{3}} T_s \frac{V_o \sin(\theta) \sin(\rho) |I_{-7}|}{|V_{-7}| |I_{+9}| \sin(\pi/3 - \rho) - |V_{+9}| |I_{-7}| \sin(\rho)} \quad (\text{A.15})$$

$$t_{x2} = \frac{2}{\sqrt{3}} T_s \frac{V_o \sin(\theta) \sin(\pi/3 - \rho) |I_{+9}|}{|V_{-7}| |I_{+9}| \sin(\pi/3 - \rho) - |V_{+9}| |I_{-7}| \sin(\rho)} \quad (\text{A.16})$$

$$t_{y1} = \frac{2}{\sqrt{3}} T_s \frac{V_o \sin(\pi/3 - \theta) \sin(\rho) |I_{+1}|}{|V_{+1}| |I_{-3}| \sin(\pi/3 - \rho) - |V_{-3}| |I_{+1}| \sin(\rho)} \quad (\text{A.17})$$

$$t_{y2} = \frac{2}{\sqrt{3}} T_s \frac{V_o \sin(\pi/3 - \theta) \sin(\pi/3 - \rho) |I_{-3}|}{|V_{+1}| |I_{-3}| \sin(\pi/3 - \rho) - |V_{-3}| |I_{+1}| \sin(\rho)} \quad (\text{A.18})$$

As I_{+1} and I_{-3} , I_{-7} and I_{+9} have the same absolute amplitude, (A.15) to (A.16) are simplified to:

$$t_{x1} = \frac{2}{\sqrt{3}} T_s \frac{V_o \sin(\theta) \sin(\rho)}{|V_{-7}| \sin(\pi/3 - \rho) - |V_{+9}| \sin(\rho)} \quad (\text{A.19})$$

$$t_{x2} = \frac{2}{\sqrt{3}} T_s \frac{V_o \sin(\theta) \sin(\pi/3 - \rho)}{|V_{-7}| \sin(\pi/3 - \rho) - |V_{+9}| \sin(\rho)} \quad (\text{A.20})$$

$$t_{y1} = \frac{2}{\sqrt{3}} T_s \frac{V_o \sin(\pi/3 - \theta) \sin(\rho)}{|V_{+1}| \sin(\pi/3 - \rho) + |V_{-3}| \sin(\rho)} \quad (\text{A.21})$$

$$t_{y2} = \frac{2}{\sqrt{3}} T_s \frac{V_o \sin(\pi/3 - \theta) \sin(\pi/3 - \rho)}{|V_{+1}| \sin(\pi/3 - \rho) + |V_{-3}| \sin(\rho)} \quad (\text{A.22})$$

Substituting the amplitudes of V_{+1} , V_{-3} , V_{-7} and V_{+9} (expressed in Table 2.1) into (A.19) to (A.22) results in:

$$t_{x1} = \frac{2}{\sqrt{3}} T_s \frac{V_o \sin(\theta) \sin(\rho)}{V_i \cos(\omega_i t - \rho - \pi/3)} \quad (\text{A.23})$$

$$t_{x2} = \frac{2}{\sqrt{3}} T_s \frac{V_o \sin(\theta) \sin(\pi/3 - \rho)}{V_i \cos(\omega_i t - \rho - \pi/3)} \quad (\text{A.24})$$

$$t_{y1} = \frac{2}{\sqrt{3}} T_s \frac{V_o \sin(\pi/3 - \theta) \sin(\rho)}{V_i \cos(\omega_i t - \rho - \pi/3)} \quad (\text{A.25})$$

$$t_{y2} = \frac{2}{\sqrt{3}} T_s \frac{V_o \sin(\pi/3 - \theta) \sin(\pi/3 - \rho)}{V_i \cos(\omega_i t - \rho - \pi/3)} \quad (\text{A.26})$$

Based on the phase angle relationship between the input voltage and current, (A.23) to (A.26) can be simplified into:

$$t_{x1} = q \frac{2}{\sqrt{3}} T_s \frac{\sin(\theta) \sin(\rho)}{\cos(\varphi_i)} \quad (\text{A.27})$$

$$t_{x2} = q \frac{2}{\sqrt{3}} T_s \frac{\sin(\theta) \sin(\pi/3 - \rho)}{\cos(\varphi_i)} \quad (\text{A.28})$$

$$t_{y1} = q \frac{2}{\sqrt{3}} T_s \frac{\sin(\pi/3 - \theta) \sin(\rho)}{\cos(\varphi_i)} \quad (\text{A.29})$$

$$t_{y2} = q \frac{2}{\sqrt{3}} T_s \frac{\sin(\pi/3 - \theta) \sin(\pi/3 - \rho)}{\cos(\varphi_i)} \quad (\text{A.30})$$

$$t_{x1} + t_{x2} + t_{y1} + t_{y2} \leq T_s \quad (\text{A.31})$$

$$t_0 = T_s - (t_{x1} + t_{x2} + t_{y1} + t_{y2}) \quad (\text{A.32})$$

$$q = \frac{V_o}{V_i} \leq \left| \frac{\sqrt{3} \cos(\varphi_i)}{2 \sin(\theta + \pi/3) \sin(\rho + \pi/3)} \right| \geq \frac{\sqrt{3}}{2} \cos(\varphi_i) = 0.866 \cos(\varphi_i) \quad (\text{A.33})$$

If any of the times is less than zero, the corresponding reverse vector should be selected instead of the assumed vector. For example, if $t_{x1} < 0$, I_{+1} and V_{+1} should be selected rather than I_{-1} and V_{-1} . The maximum VTR can reach $\sqrt{3}/2$ (≈ 0.866) when the input power factor is unity and θ and ρ are equal to $\pi/6$ simultaneously.

In Table 2.3, only the positive vectors are assumed to be applied. Considering this assumption and the lowest switching actions, the general equations for all the situations in Table 2.3 can be obtained in

$$t_{x1} = (-1)^{m+n} \frac{2}{\sqrt{3}} T_s q \frac{\sin(\theta) \sin(\rho)}{\cos(\varphi_i)} \quad (\text{A.34})$$

$$t_{x2} = (-1)^{m+n+1} \frac{2}{\sqrt{3}} T_s q \frac{\sin(\theta) \sin(\pi/3 - \rho)}{\cos(\varphi_i)} \quad (\text{A.35})$$

$$t_{y1} = (-1)^{m+n+1} \frac{2}{\sqrt{3}} T_s q \frac{\sin(\pi/3 - \theta) \sin(\rho)}{\cos(\varphi_i)} \quad (\text{A.36})$$

$$t_{y2} = (-1)^{m+n} \frac{2}{\sqrt{3}} T_s q \frac{\sin(\pi/3 - \theta) \sin(\pi/3 - \rho)}{\cos(\varphi_i)} \quad (\text{A.37})$$

$$|t_{x1}| + |t_{x2}| + |t_{y1}| + |t_{y2}| \leq T_s \quad (\text{A.38})$$

$$t_0 = T_s - (|t_{x1}| + |t_{x2}| + |t_{y1}| + |t_{y2}|) \quad (\text{A.39})$$

where θ and ρ are:

$$\theta = \text{mod}(\omega_o t + \varphi, 2\pi) - \frac{(m-1)\pi}{3} \quad (\text{A.40})$$

$$\rho = \text{mod}(\omega_i t - \varphi_i + \pi/6, 2\pi) - \frac{(n-1)\pi}{3} \quad (\text{A.41})$$

Here m and n ($m, n = 1, 2, 3, 4, 5, 6$) are the m^{th} output voltage vector sector and the n^{th} input current vector sector. m and n can be calculated based on the phase angle of output voltage and the phase angle of input current respectively using

$$m = \text{int} \left[\frac{\text{mod}(\omega_o t + \varphi, 2\pi)}{\pi/3} \right] + 1 \quad (\text{A.42})$$

$$n = \text{int} \left[\frac{\text{mod}(\omega_i t - \varphi_i + \pi/6, 2\pi)}{\pi/3} \right] + 1 \quad (\text{A.43})$$

where $\text{int}(k)$ is a function to get the nearest integer that is smaller than k and $\text{mod}(h, k)$ is a function to get the remainder of h/k .

APPENDIX B

LOOK-UP TABLES FOR SYMMETRIC SWITCHING

This appendix presents the exhaustive look-up table of symmetric switching sequence for the indirect SVM. The first row shows the sequential time slots in a sampling interval, and the first column indicates the switches in a direct matrix converter. Here a value of ‘1’ means the corresponding switch is turned on and ‘0’ means off. The time slots are distributed symmetrically throughout the sampling interval.

Table B.1 look-up table of the symmetric switching sequence for the indirect SVM. ($k_v = 1$; $k_i = 1$)

	$t_{v\alpha}/2$	$t_{\delta\alpha}/2$	$t_{\delta\beta}/2$	$t_{v\beta}/2$	$t_0/2$	$t_0/2$	$t_{v\beta}/2$	$t_{\delta\beta}/2$	$t_{\delta\alpha}/2$	$t_{v\alpha}/2$
S_{Aa}	1	1	1	1	0	0	1	1	1	1
S_{Ba}	0	0	0	0	0	0	0	0	0	0
S_{Ca}	0	0	0	0	1	1	0	0	0	0
S_{Ab}	0	1	1	0	0	0	0	1	1	0
S_{Bb}	1	0	0	0	0	0	0	0	0	1
S_{Cb}	0	0	0	1	1	1	1	0	0	0
S_{Ac}	0	0	0	0	0	0	0	0	0	0
S_{Bc}	1	1	0	0	0	0	0	0	1	1
S_{Cc}	0	0	1	1	1	1	1	1	0	0

Table B.1. *Continued.* ($k_v = 1$; $k_i = 2$)

	$t_{v\alpha}/2$	$t_{\delta\alpha}/2$	$t_{\delta\beta}/2$	$t_{v\beta}/2$	$t_0/2$	$t_0/2$	$t_{v\beta}/2$	$t_{\delta\beta}/2$	$t_{\delta\alpha}/2$	$t_{v\alpha}/2$
S_{Aa}	1	1	0	0	0	0	0	0	1	1
S_{Ba}	0	0	1	1	1	1	1	1	0	0
S_{Ca}	0	0	0	0	0	0	0	0	0	0
S_{Ab}	1	0	0	0	0	0	0	0	0	1
S_{Bb}	0	0	0	1	1	1	1	0	0	0
S_{Cb}	0	1	1	0	0	0	0	1	1	0
S_{Ac}	0	0	0	0	0	0	0	0	0	0
S_{Bc}	0	0	0	0	1	1	0	0	0	0
S_{Cc}	1	1	1	1	0	0	1	1	1	1

Table B.1. *Continued.* ($k_v = 1$; $k_i = 3$)

	$t_{\gamma\alpha}/2$	$t_{\delta\alpha}/2$	$t_{\delta\beta}/2$	$t_{\gamma\beta}/2$	$t_0/2$	$t_0/2$	$t_{\gamma\beta}/2$	$t_{\delta\beta}/2$	$t_{\delta\alpha}/2$	$t_{\gamma\alpha}/2$
S_{Aa}	0	0	0	0	1	1	0	0	0	0
S_{Ba}	1	1	1	1	0	0	1	1	1	1
S_{Ca}	0	0	0	0	0	0	0	0	0	0
S_{Ab}	0	0	0	1	1	1	1	0	0	0
S_{Bb}	0	1	1	0	0	0	0	1	1	0
S_{Cb}	1	0	0	0	0	0	0	0	0	1
S_{Ac}	0	0	1	1	1	1	1	1	0	0
S_{Bc}	0	0	0	0	0	0	0	0	0	0
S_{Cc}	1	1	0	0	0	0	0	0	1	1

Table B.1. *Continued.* ($k_v = 1$; $k_i = 4$)

	$t_{\gamma\alpha}/2$	$t_{\delta\alpha}/2$	$t_{\delta\beta}/2$	$t_{\gamma\beta}/2$	$t_0/2$	$t_0/2$	$t_{\gamma\beta}/2$	$t_{\delta\beta}/2$	$t_{\delta\alpha}/2$	$t_{\gamma\alpha}/2$
S_{Aa}	0	0	0	0	0	0	0	0	0	0
S_{Ba}	1	1	0	0	0	0	0	0	1	1
S_{Ca}	0	0	1	1	1	1	1	1	0	0
S_{Ab}	0	1	1	0	0	0	0	1	1	0
S_{Bb}	1	0	0	0	0	0	0	0	0	1
S_{Cb}	0	0	0	1	1	1	1	0	0	0
S_{Ac}	1	1	1	1	0	0	1	1	1	1
S_{Bc}	0	0	0	0	0	0	0	0	0	0
S_{Cc}	0	0	0	0	1	1	0	0	0	0

Table B.1. *Continued.* ($k_v = 1$; $k_i = 5$)

	$t_{\gamma\alpha}/2$	$t_{\delta\alpha}/2$	$t_{\delta\beta}/2$	$t_{\gamma\beta}/2$	$t_0/2$	$t_0/2$	$t_{\gamma\beta}/2$	$t_{\delta\beta}/2$	$t_{\delta\alpha}/2$	$t_{\gamma\alpha}/2$
S_{Aa}	0	0	0	0	0	0	0	0	0	0
S_{Ba}	0	0	0	0	1	1	0	0	0	0
S_{Ca}	1	1	1	1	0	0	1	1	1	1
S_{Ab}	1	0	0	0	0	0	0	0	0	1
S_{Bb}	0	0	0	1	1	1	1	0	0	0
S_{Cb}	0	1	1	0	0	0	0	1	1	0
S_{Ac}	1	1	0	0	0	0	0	0	1	1
S_{Bc}	0	0	1	1	1	1	1	1	0	0
S_{Cc}	0	0	0	0	0	0	0	0	0	0

Table B.1. *Continued.* ($k_v = 1$; $k_i = 6$)

	$t_{\gamma\alpha}/2$	$t_{\delta\alpha}/2$	$t_{\delta\beta}/2$	$t_{\gamma\beta}/2$	$t_0/2$	$t_o/2$	$t_{\gamma\beta}/2$	$t_{\delta\beta}/2$	$t_{\delta\alpha}/2$	$t_{\gamma\alpha}/2$
S_{Aa}	0	0	1	1	1	1	1	1	0	0
S_{Ba}	0	0	0	0	0	0	0	0	0	0
S_{Ca}	1	1	0	0	0	0	0	0	1	1
S_{Ab}	0	0	0	1	1	1	1	0	0	0
S_{Bb}	0	1	1	0	0	0	0	1	1	0
S_{Cb}	1	0	0	0	0	0	0	0	0	1
S_{Ac}	0	0	0	0	1	1	0	0	0	0
S_{Bc}	1	1	1	1	0	0	1	1	1	1
S_{Cc}	0	0	0	0	0	0	0	0	0	0

Table B.1. *Continued.* ($k_v = 2$; $k_i = 1$)

	$t_{\gamma\alpha}/2$	$t_{\delta\alpha}/2$	$t_{\delta\beta}/2$	$t_{\gamma\beta}/2$	$t_0/2$	$t_o/2$	$t_{\gamma\beta}/2$	$t_{\delta\beta}/2$	$t_{\delta\alpha}/2$	$t_{\gamma\alpha}/2$
S_{Aa}	0	1	1	0	0	0	0	1	1	0
S_{Ba}	1	0	0	0	0	0	0	0	0	1
S_{Ca}	0	0	0	1	1	1	1	0	0	0
S_{Ab}	1	1	1	1	0	0	1	1	1	1
S_{Bb}	0	0	0	0	0	0	0	0	0	0
S_{Cb}	0	0	0	0	1	1	0	0	0	0
S_{Ac}	0	0	0	0	0	0	0	0	0	0
S_{Bc}	1	1	0	0	0	0	0	0	1	1
S_{Cc}	0	0	1	1	1	1	1	1	0	0

Table B.1. *Continued.* ($k_v = 2$; $k_i = 2$)

	$t_{\gamma\alpha}/2$	$t_{\delta\alpha}/2$	$t_{\delta\beta}/2$	$t_{\gamma\beta}/2$	$t_0/2$	$t_o/2$	$t_{\gamma\beta}/2$	$t_{\delta\beta}/2$	$t_{\delta\alpha}/2$	$t_{\gamma\alpha}/2$
S_{Aa}	1	0	0	0	0	0	0	0	0	1
S_{Ba}	0	0	0	1	1	1	1	0	0	0
S_{Ca}	0	1	1	0	0	0	0	1	1	0
S_{Ab}	1	1	0	0	0	0	0	0	1	1
S_{Bb}	0	0	1	1	1	1	1	1	0	0
S_{Cb}	0	0	0	0	0	0	0	0	0	0
S_{Ac}	0	0	0	0	0	0	0	0	0	0
S_{Bc}	0	0	0	0	1	1	0	0	0	0
S_{Cc}	1	1	1	1	0	0	1	1	1	1

Table B.1. *Continued.* ($k_v = 2$; $k_i = 3$)

	$t_{\gamma\alpha}/2$	$t_{\delta\alpha}/2$	$t_{\delta\beta}/2$	$t_{\gamma\beta}/2$	$t_0/2$	$t_0/2$	$t_{\gamma\beta}/2$	$t_{\delta\beta}/2$	$t_{\delta\alpha}/2$	$t_{\gamma\alpha}/2$
S_{Aa}	0	0	0	1	1	1	1	0	0	0
S_{Ba}	0	1	1	0	0	0	0	1	1	0
S_{Ca}	1	0	0	0	0	0	0	0	0	1
S_{Ab}	0	0	0	0	1	1	0	0	0	0
S_{Bb}	1	1	1	1	0	0	1	1	1	1
S_{Cb}	0	0	0	0	0	0	0	0	0	0
S_{Ac}	0	0	1	1	1	1	1	1	0	0
S_{Bc}	0	0	0	0	0	0	0	0	0	0
S_{Cc}	1	1	0	0	0	0	0	0	1	1

Table B.1. *Continued.* ($k_v = 2$; $k_i = 4$)

	$t_{\gamma\alpha}/2$	$t_{\delta\alpha}/2$	$t_{\delta\beta}/2$	$t_{\gamma\beta}/2$	$t_0/2$	$t_0/2$	$t_{\gamma\beta}/2$	$t_{\delta\beta}/2$	$t_{\delta\alpha}/2$	$t_{\gamma\alpha}/2$
S_{Aa}	0	1	1	0	0	0	0	1	1	0
S_{Ba}	1	0	0	0	0	0	0	0	0	1
S_{Ca}	0	0	0	1	1	1	1	0	0	0
S_{Ab}	0	0	0	0	0	0	0	0	0	0
S_{Bb}	1	1	0	0	0	0	0	0	1	1
S_{Cb}	0	0	1	1	1	1	1	1	0	0
S_{Ac}	1	1	1	1	0	0	1	1	1	1
S_{Bc}	0	0	0	0	0	0	0	0	0	0
S_{Cc}	0	0	0	0	1	1	0	0	0	0

Table B.1. *Continued.* ($k_v = 2$; $k_i = 5$)

	$t_{\gamma\alpha}/2$	$t_{\delta\alpha}/2$	$t_{\delta\beta}/2$	$t_{\gamma\beta}/2$	$t_0/2$	$t_0/2$	$t_{\gamma\beta}/2$	$t_{\delta\beta}/2$	$t_{\delta\alpha}/2$	$t_{\gamma\alpha}/2$
S_{Aa}	1	0	0	0	0	0	0	0	0	1
S_{Ba}	0	0	0	1	1	1	1	0	0	0
S_{Ca}	0	1	1	0	0	0	0	1	1	0
S_{Ab}	0	0	0	0	0	0	0	0	0	0
S_{Bb}	0	0	0	0	1	1	0	0	0	0
S_{Cb}	1	1	1	1	0	0	1	1	1	1
S_{Ac}	1	1	0	0	0	0	0	0	1	1
S_{Bc}	0	0	1	1	1	1	1	1	0	0
S_{Cc}	0	0	0	0	0	0	0	0	0	0

Table B.1. *Continued.* ($k_v = 2$; $k_i = 6$)

	$t_{\gamma\alpha}/2$	$t_{\delta\alpha}/2$	$t_{\delta\beta}/2$	$t_{\gamma\beta}/2$	$t_0/2$	$t_0/2$	$t_{\gamma\beta}/2$	$t_{\delta\beta}/2$	$t_{\delta\alpha}/2$	$t_{\gamma\alpha}/2$
S_{Aa}	0	0	0	1	1	1	1	0	0	0
S_{Ba}	0	1	1	0	0	0	0	1	1	0
S_{Ca}	1	0	0	0	0	0	0	0	0	1
S_{Ab}	0	0	1	1	1	1	1	1	0	0
S_{Bb}	0	0	0	0	0	0	0	0	0	0
S_{Cb}	1	1	0	0	0	0	0	0	1	1
S_{Ac}	0	0	0	0	1	1	0	0	0	0
S_{Bc}	1	1	1	1	0	0	1	1	1	1
S_{Cc}	0	0	0	0	0	0	0	0	0	0

Table B.1. *Continued.* ($k_v = 3$; $k_i = 1$)

	$t_{\gamma\alpha}/2$	$t_{\delta\alpha}/2$	$t_{\delta\beta}/2$	$t_{\gamma\beta}/2$	$t_0/2$	$t_0/2$	$t_{\gamma\beta}/2$	$t_{\delta\beta}/2$	$t_{\delta\alpha}/2$	$t_{\gamma\alpha}/2$
S_{Aa}	0	0	0	0	0	0	0	0	0	0
S_{Ba}	1	1	0	0	0	0	0	0	1	1
S_{Ca}	0	0	1	1	1	1	1	1	0	0
S_{Ab}	1	1	1	1	0	0	1	1	1	1
S_{Bb}	0	0	0	0	0	0	0	0	0	0
S_{Cb}	0	0	0	0	1	1	0	0	0	0
S_{Ac}	0	1	1	0	0	0	0	1	1	0
S_{Bc}	1	0	0	0	0	0	0	0	0	1
S_{Cc}	0	0	0	1	1	1	1	0	0	0

Table B.1. *Continued.* ($k_v = 3$; $k_i = 2$)

	$t_{\gamma\alpha}/2$	$t_{\delta\alpha}/2$	$t_{\delta\beta}/2$	$t_{\gamma\beta}/2$	$t_0/2$	$t_0/2$	$t_{\gamma\beta}/2$	$t_{\delta\beta}/2$	$t_{\delta\alpha}/2$	$t_{\gamma\alpha}/2$
S_{Aa}	0	0	0	0	0	0	0	0	0	0
S_{Ba}	0	0	0	0	1	1	0	0	0	0
S_{Ca}	1	1	1	1	0	0	1	1	1	1
S_{Ab}	1	1	0	0	0	0	0	0	1	1
S_{Bb}	0	0	1	1	1	1	1	1	0	0
S_{Cb}	0	0	0	0	0	0	0	0	0	0
S_{Ac}	1	0	0	0	0	0	0	0	0	1
S_{Bc}	0	0	0	1	1	1	1	0	0	0
S_{Cc}	0	1	1	0	0	0	0	1	1	0

Table B.1. *Continued.* ($k_v = 3; k_i = 3$)

	$t_{\gamma\alpha}/2$	$t_{\delta\alpha}/2$	$t_{\delta\beta}/2$	$t_{\gamma\beta}/2$	$t_0/2$	$t_0/2$	$t_{\gamma\beta}/2$	$t_{\delta\beta}/2$	$t_{\delta\alpha}/2$	$t_{\gamma\alpha}/2$
S_{Aa}	0	0	1	1	1	1	1	1	0	0
S_{Ba}	0	0	0	0	0	0	0	0	0	0
S_{Ca}	1	1	0	0	0	0	0	0	1	1
S_{Ab}	0	0	0	0	1	1	0	0	0	0
S_{Bb}	1	1	1	1	0	0	1	1	1	1
S_{Cb}	0	0	0	0	0	0	0	0	0	0
S_{Ac}	0	0	0	1	1	1	1	0	0	0
S_{Bc}	0	1	1	0	0	0	0	1	1	0
S_{Cc}	1	0	0	0	0	0	0	0	0	1

Table B.1. *Continued.* ($k_v = 3; k_i = 4$)

	$t_{\gamma\alpha}/2$	$t_{\delta\alpha}/2$	$t_{\delta\beta}/2$	$t_{\gamma\beta}/2$	$t_0/2$	$t_0/2$	$t_{\gamma\beta}/2$	$t_{\delta\beta}/2$	$t_{\delta\alpha}/2$	$t_{\gamma\alpha}/2$
S_{Aa}	1	1	1	1	0	0	1	1	1	1
S_{Ba}	0	0	0	0	0	0	0	0	0	0
S_{Ca}	0	0	0	0	1	1	0	0	0	0
S_{Ab}	0	0	0	0	0	0	0	0	0	0
S_{Bb}	1	1	0	0	0	0	0	0	1	1
S_{Cb}	0	0	1	1	1	1	1	1	0	0
S_{Ac}	0	1	1	0	0	0	0	1	1	0
S_{Bc}	1	0	0	0	0	0	0	0	0	1
S_{Cc}	0	0	0	1	1	1	1	0	0	0

Table B.1. *Continued.* ($k_v = 3; k_i = 5$)

	$t_{\gamma\alpha}/2$	$t_{\delta\alpha}/2$	$t_{\delta\beta}/2$	$t_{\gamma\beta}/2$	$t_0/2$	$t_0/2$	$t_{\gamma\beta}/2$	$t_{\delta\beta}/2$	$t_{\delta\alpha}/2$	$t_{\gamma\alpha}/2$
S_{Aa}	1	1	0	0	0	0	0	0	1	1
S_{Ba}	0	0	1	1	1	1	1	1	0	0
S_{Ca}	0	0	0	0	0	0	0	0	0	0
S_{Ab}	0	0	0	0	0	0	0	0	0	0
S_{Bb}	0	0	0	0	1	1	0	0	0	0
S_{Cb}	1	1	1	1	0	0	1	1	1	1
S_{Ac}	1	0	0	0	0	0	0	0	0	1
S_{Bc}	0	0	0	1	1	1	1	0	0	0
S_{Cc}	0	1	1	0	0	0	0	1	1	0

Table B.1. *Continued.* ($k_v = 3$; $k_i = 6$)

	$t_{\gamma\alpha}/2$	$t_{\delta\alpha}/2$	$t_{\delta\beta}/2$	$t_{\gamma\beta}/2$	$t_0/2$	$t_0/2$	$t_{\gamma\beta}/2$	$t_{\delta\beta}/2$	$t_{\delta\alpha}/2$	$t_{\gamma\alpha}/2$
S_{Aa}	0	0	0	0	1	1	0	0	0	0
S_{Ba}	1	1	1	1	0	0	1	1	1	1
S_{Ca}	0	0	0	0	0	0	0	0	0	0
S_{Ab}	0	0	1	1	1	1	1	1	0	0
S_{Bb}	0	0	0	0	0	0	0	0	0	0
S_{Cb}	1	1	0	0	0	0	0	0	1	1
S_{Ac}	0	0	0	1	1	1	1	0	0	0
S_{Bc}	0	1	1	0	0	0	0	1	1	0
S_{Cc}	1	0	0	0	0	0	0	0	0	1

Table B.1. *Continued.* ($k_v = 4$; $k_i = 1$)

	$t_{\gamma\alpha}/2$	$t_{\delta\alpha}/2$	$t_{\delta\beta}/2$	$t_{\gamma\beta}/2$	$t_0/2$	$t_0/2$	$t_{\gamma\beta}/2$	$t_{\delta\beta}/2$	$t_{\delta\alpha}/2$	$t_{\gamma\alpha}/2$
S_{Aa}	0	0	0	0	0	0	0	0	0	0
S_{Ba}	1	1	0	0	0	0	0	0	1	1
S_{Ca}	0	0	1	1	1	1	1	1	0	0
S_{Ab}	0	1	1	0	0	0	0	1	1	0
S_{Bb}	1	0	0	0	0	0	0	0	0	1
S_{Cb}	0	0	0	1	1	1	1	0	0	0
S_{Ac}	1	1	1	1	0	0	1	1	1	1
S_{Bc}	0	0	0	0	0	0	0	0	0	0
S_{Cc}	0	0	0	0	1	1	0	0	0	0

Table B.1. *Continued.* ($k_v = 4$; $k_i = 2$)

	$t_{\gamma\alpha}/2$	$t_{\delta\alpha}/2$	$t_{\delta\beta}/2$	$t_{\gamma\beta}/2$	$t_0/2$	$t_0/2$	$t_{\gamma\beta}/2$	$t_{\delta\beta}/2$	$t_{\delta\alpha}/2$	$t_{\gamma\alpha}/2$
S_{Aa}	0	0	0	0	0	0	0	0	0	0
S_{Ba}	0	0	0	0	1	1	0	0	0	0
S_{Ca}	1	1	1	1	0	0	1	1	1	1
S_{Ab}	1	0	0	0	0	0	0	0	0	1
S_{Bb}	0	0	0	1	1	1	1	0	0	0
S_{Cb}	0	1	1	0	0	0	0	1	1	0
S_{Ac}	1	1	0	0	0	0	0	0	1	1
S_{Bc}	0	0	1	1	1	1	1	1	0	0
S_{Cc}	0	0	0	0	0	0	0	0	0	0

Table B.1. *Continued.* ($k_v = 4$; $k_i = 3$)

	$t_{\gamma\alpha}/2$	$t_{\delta\alpha}/2$	$t_{\delta\beta}/2$	$t_{\gamma\beta}/2$	$t_0/2$	$t_0/2$	$t_{\gamma\beta}/2$	$t_{\delta\beta}/2$	$t_{\delta\alpha}/2$	$t_{\gamma\alpha}/2$
S_{Aa}	0	0	1	1	1	1	1	1	0	0
S_{Ba}	0	0	0	0	0	0	0	0	0	0
S_{Ca}	1	1	0	0	0	0	0	0	1	1
S_{Ab}	0	0	0	1	1	1	1	0	0	0
S_{Bb}	0	1	1	0	0	0	0	1	1	0
S_{Cb}	1	0	0	0	0	0	0	0	0	1
S_{Ac}	0	0	0	0	1	1	0	0	0	0
S_{Bc}	1	1	1	1	0	0	1	1	1	1
S_{Cc}	0	0	0	0	0	0	0	0	0	0

Table B.1. *Continued.* ($k_v = 4$; $k_i = 4$)

	$t_{\gamma\alpha}/2$	$t_{\delta\alpha}/2$	$t_{\delta\beta}/2$	$t_{\gamma\beta}/2$	$t_0/2$	$t_0/2$	$t_{\gamma\beta}/2$	$t_{\delta\beta}/2$	$t_{\delta\alpha}/2$	$t_{\gamma\alpha}/2$
S_{Aa}	1	1	1	1	0	0	1	1	1	1
S_{Ba}	0	0	0	0	0	0	0	0	0	0
S_{Ca}	0	0	0	0	1	1	0	0	0	0
S_{Ab}	0	1	1	0	0	0	0	1	1	0
S_{Bb}	1	0	0	0	0	0	0	0	0	1
S_{Cb}	0	0	0	1	1	1	1	0	0	0
S_{Ac}	0	0	0	0	0	0	0	0	0	0
S_{Bc}	1	1	0	0	0	0	0	0	1	1
S_{Cc}	0	0	1	1	1	1	1	1	0	0

Table B.1. *Continued.* ($k_v = 4$; $k_i = 5$)

	$t_{\gamma\alpha}/2$	$t_{\delta\alpha}/2$	$t_{\delta\beta}/2$	$t_{\gamma\beta}/2$	$t_0/2$	$t_0/2$	$t_{\gamma\beta}/2$	$t_{\delta\beta}/2$	$t_{\delta\alpha}/2$	$t_{\gamma\alpha}/2$
S_{Aa}	1	1	0	0	0	0	0	0	1	1
S_{Ba}	0	0	1	1	1	1	1	1	0	0
S_{Ca}	0	0	0	0	0	0	0	0	0	0
S_{Ab}	1	0	0	0	0	0	0	0	0	1
S_{Bb}	0	0	0	1	1	1	1	0	0	0
S_{Cb}	0	1	1	0	0	0	0	1	1	0
S_{Ac}	0	0	0	0	0	0	0	0	0	0
S_{Bc}	0	0	0	0	1	1	0	0	0	0
S_{Cc}	1	1	1	1	0	0	1	1	1	1

Table B.1. *Continued.* ($k_v = 4$; $k_i = 6$)

	$t_{\gamma\alpha}/2$	$t_{\delta\alpha}/2$	$t_{\delta\beta}/2$	$t_{\gamma\beta}/2$	$t_0/2$	$t_o/2$	$t_{\gamma\beta}/2$	$t_{\delta\beta}/2$	$t_{\delta\alpha}/2$	$t_{\gamma\alpha}/2$
S_{Aa}	0	0	0	0	1	1	0	0	0	0
S_{Ba}	1	1	1	1	0	0	1	1	1	1
S_{Ca}	0	0	0	0	0	0	0	0	0	0
S_{Ab}	0	0	0	1	1	1	1	0	0	0
S_{Bb}	0	1	1	0	0	0	0	1	1	0
S_{Cb}	1	0	0	0	0	0	0	0	0	1
S_{Ac}	0	0	1	1	1	1	1	1	0	0
S_{Bc}	0	0	0	0	0	0	0	0	0	0
S_{Cc}	1	1	0	0	0	0	0	0	1	1

Table B.1. *Continued.* ($k_v = 5$; $k_i = 1$)

	$t_{\gamma\alpha}/2$	$t_{\delta\alpha}/2$	$t_{\delta\beta}/2$	$t_{\gamma\beta}/2$	$t_0/2$	$t_o/2$	$t_{\gamma\beta}/2$	$t_{\delta\beta}/2$	$t_{\delta\alpha}/2$	$t_{\gamma\alpha}/2$
S_{Aa}	0	1	1	0	0	0	0	1	1	0
S_{Ba}	1	0	0	0	0	0	0	0	0	1
S_{Ca}	0	0	0	1	1	1	1	0	0	0
S_{Ab}	0	0	0	0	0	0	0	0	0	0
S_{Bb}	1	1	0	0	0	0	0	0	1	1
S_{Cb}	0	0	1	1	1	1	1	1	0	0
S_{Ac}	1	1	1	1	0	0	1	1	1	1
S_{Bc}	0	0	0	0	0	0	0	0	0	0
S_{Cc}	0	0	0	0	1	1	0	0	0	0

Table B.1. *Continued.* ($k_v = 5$; $k_i = 2$)

	$t_{\gamma\alpha}/2$	$t_{\delta\alpha}/2$	$t_{\delta\beta}/2$	$t_{\gamma\beta}/2$	$t_0/2$	$t_o/2$	$t_{\gamma\beta}/2$	$t_{\delta\beta}/2$	$t_{\delta\alpha}/2$	$t_{\gamma\alpha}/2$
S_{Aa}	1	0	0	0	0	0	0	0	0	1
S_{Ba}	0	0	0	1	1	1	1	0	0	0
S_{Ca}	0	1	1	0	0	0	0	1	1	0
S_{Ab}	0	0	0	0	0	0	0	0	0	0
S_{Bb}	0	0	0	0	1	1	0	0	0	0
S_{Cb}	1	1	1	1	0	0	1	1	1	1
S_{Ac}	1	1	0	0	0	0	0	0	1	1
S_{Bc}	0	0	1	1	1	1	1	1	0	0
S_{Cc}	0	0	0	0	0	0	0	0	0	0

Table B.1. *Continued.* ($k_v = 5$; $k_i = 3$)

	$t_{\gamma\alpha}/2$	$t_{\delta\alpha}/2$	$t_{\delta\beta}/2$	$t_{\gamma\beta}/2$	$t_0/2$	$t_0/2$	$t_{\gamma\beta}/2$	$t_{\delta\beta}/2$	$t_{\delta\alpha}/2$	$t_{\gamma\alpha}/2$
S_{Aa}	0	0	0	1	1	1	1	0	0	0
S_{Ba}	0	1	1	0	0	0	0	1	1	0
S_{Ca}	1	0	0	0	0	0	0	0	0	1
S_{Ab}	0	0	1	1	1	1	1	1	0	0
S_{Bb}	0	0	0	0	0	0	0	0	0	0
S_{Cb}	1	1	0	0	0	0	0	0	1	1
S_{Ac}	0	0	0	0	1	1	0	0	0	0
S_{Bc}	1	1	1	1	0	0	1	1	1	1
S_{Cc}	0	0	0	0	0	0	0	0	0	0

Table B.1. *Continued.* ($k_v = 5$; $k_i = 4$)

	$t_{\gamma\alpha}/2$	$t_{\delta\alpha}/2$	$t_{\delta\beta}/2$	$t_{\gamma\beta}/2$	$t_0/2$	$t_0/2$	$t_{\gamma\beta}/2$	$t_{\delta\beta}/2$	$t_{\delta\alpha}/2$	$t_{\gamma\alpha}/2$
S_{Aa}	0	1	1	0	0	0	0	1	1	0
S_{Ba}	1	0	0	0	0	0	0	0	0	1
S_{Ca}	0	0	0	1	1	1	1	0	0	0
S_{Ab}	1	1	1	1	0	0	1	1	1	1
S_{Bb}	0	0	0	0	0	0	0	0	0	0
S_{Cb}	0	0	0	0	1	1	0	0	0	0
S_{Ac}	0	0	0	0	0	0	0	0	0	0
S_{Bc}	1	1	0	0	0	0	0	0	1	1
S_{Cc}	0	0	1	1	1	1	1	1	0	0

Table B.1. *Continued.* ($k_v = 5$; $k_i = 5$)

	$t_{\gamma\alpha}/2$	$t_{\delta\alpha}/2$	$t_{\delta\beta}/2$	$t_{\gamma\beta}/2$	$t_0/2$	$t_0/2$	$t_{\gamma\beta}/2$	$t_{\delta\beta}/2$	$t_{\delta\alpha}/2$	$t_{\gamma\alpha}/2$
S_{Aa}	1	0	0	0	0	0	0	0	0	1
S_{Ba}	0	0	0	1	1	1	1	0	0	0
S_{Ca}	0	1	1	0	0	0	0	1	1	0
S_{Ab}	1	1	0	0	0	0	0	0	1	1
S_{Bb}	0	0	1	1	1	1	1	1	0	0
S_{Cb}	0	0	0	0	0	0	0	0	0	0
S_{Ac}	0	0	0	0	0	0	0	0	0	0
S_{Bc}	0	0	0	0	1	1	0	0	0	0
S_{Cc}	1	1	1	1	0	0	1	1	1	1

Table B.1. *Continued.* ($k_v = 5$; $k_i = 6$)

	$t_{\gamma\alpha}/2$	$t_{\delta\alpha}/2$	$t_{\delta\beta}/2$	$t_{\gamma\beta}/2$	$t_0/2$	$t_0/2$	$t_{\gamma\beta}/2$	$t_{\delta\beta}/2$	$t_{\delta\alpha}/2$	$t_{\gamma\alpha}/2$
S_{Aa}	0	0	0	1	1	1	1	0	0	0
S_{Ba}	0	1	1	0	0	0	0	1	1	0
S_{Ca}	1	0	0	0	0	0	0	0	0	1
S_{Ab}	0	0	0	0	1	1	0	0	0	0
S_{Bb}	1	1	1	1	0	0	1	1	1	1
S_{Cb}	0	0	0	0	0	0	0	0	0	0
S_{Ac}	0	0	1	1	1	1	1	1	0	0
S_{Bc}	0	0	0	0	0	0	0	0	0	0
S_{Cc}	1	1	0	0	0	0	0	0	1	1

Table B.1. *Continued.* ($k_v = 6$; $k_i = 1$)

	$t_{\gamma\alpha}/2$	$t_{\delta\alpha}/2$	$t_{\delta\beta}/2$	$t_{\gamma\beta}/2$	$t_0/2$	$t_0/2$	$t_{\gamma\beta}/2$	$t_{\delta\beta}/2$	$t_{\delta\alpha}/2$	$t_{\gamma\alpha}/2$
S_{Aa}	1	1	1	1	0	0	1	1	1	1
S_{Ba}	0	0	0	0	0	0	0	0	0	0
S_{Ca}	0	0	0	0	1	1	0	0	0	0
S_{Ab}	0	0	0	0	0	0	0	0	0	0
S_{Bb}	1	1	0	0	0	0	0	0	1	1
S_{Cb}	0	0	1	1	1	1	1	1	0	0
S_{Ac}	0	1	1	0	0	0	0	1	1	0
S_{Bc}	1	0	0	0	0	0	0	0	0	1
S_{Cc}	0	0	0	1	1	1	1	0	0	0

Table B.1. *Continued.* ($k_v = 6$; $k_i = 2$)

	$t_{\gamma\alpha}/2$	$t_{\delta\alpha}/2$	$t_{\delta\beta}/2$	$t_{\gamma\beta}/2$	$t_0/2$	$t_0/2$	$t_{\gamma\beta}/2$	$t_{\delta\beta}/2$	$t_{\delta\alpha}/2$	$t_{\gamma\alpha}/2$
S_{Aa}	1	1	0	0	0	0	0	0	1	1
S_{Ba}	0	0	1	1	1	1	1	1	0	0
S_{Ca}	0	0	0	0	0	0	0	0	0	0
S_{Ab}	0	0	0	0	0	0	0	0	0	0
S_{Bb}	0	0	0	0	1	1	0	0	0	0
S_{Cb}	1	1	1	1	0	0	1	1	1	1
S_{Ac}	1	0	0	0	0	0	0	0	0	1
S_{Bc}	0	0	0	1	1	1	1	0	0	0
S_{Cc}	0	1	1	0	0	0	0	1	1	0

Table B.1. *Continued.* ($k_v = 6$; $k_i = 3$)

	$t_{\gamma\alpha}/2$	$t_{\delta\alpha}/2$	$t_{\delta\beta}/2$	$t_{\gamma\beta}/2$	$t_0/2$	$t_0/2$	$t_{\gamma\beta}/2$	$t_{\delta\beta}/2$	$t_{\delta\alpha}/2$	$t_{\gamma\alpha}/2$
S_{Aa}	0	0	0	0	1	1	0	0	0	0
S_{Ba}	1	1	1	1	0	0	1	1	1	1
S_{Ca}	0	0	0	0	0	0	0	0	0	0
S_{Ab}	0	0	1	1	1	1	1	1	0	0
S_{Bb}	0	0	0	0	0	0	0	0	0	0
S_{Cb}	1	1	0	0	0	0	0	0	1	1
S_{Ac}	0	0	0	1	1	1	1	0	0	0
S_{Bc}	0	1	1	0	0	0	0	1	1	0
S_{Cc}	1	0	0	0	0	0	0	0	0	1

Table B.1. *Continued.* ($k_v = 6$; $k_i = 4$)

	$t_{\gamma\alpha}/2$	$t_{\delta\alpha}/2$	$t_{\delta\beta}/2$	$t_{\gamma\beta}/2$	$t_0/2$	$t_0/2$	$t_{\gamma\beta}/2$	$t_{\delta\beta}/2$	$t_{\delta\alpha}/2$	$t_{\gamma\alpha}/2$
S_{Aa}	0	0	0	0	0	0	0	0	0	0
S_{Ba}	1	1	0	0	0	0	0	0	1	1
S_{Ca}	0	0	1	1	1	1	1	1	0	0
S_{Ab}	1	1	1	1	0	0	1	1	1	1
S_{Bb}	0	0	0	0	0	0	0	0	0	0
S_{Cb}	0	0	0	0	1	1	0	0	0	0
S_{Ac}	0	1	1	0	0	0	0	1	1	0
S_{Bc}	1	0	0	0	0	0	0	0	0	1
S_{Cc}	0	0	0	1	1	1	1	0	0	0

Table B.1. *Continued.* ($k_v = 6$; $k_i = 5$)

	$t_{\gamma\alpha}/2$	$t_{\delta\alpha}/2$	$t_{\delta\beta}/2$	$t_{\gamma\beta}/2$	$t_0/2$	$t_0/2$	$t_{\gamma\beta}/2$	$t_{\delta\beta}/2$	$t_{\delta\alpha}/2$	$t_{\gamma\alpha}/2$
S_{Aa}	0	0	0	0	0	0	0	0	0	0
S_{Ba}	0	0	0	0	1	1	0	0	0	0
S_{Ca}	1	1	1	1	0	0	1	1	1	1
S_{Ab}	1	1	0	0	0	0	0	0	1	1
S_{Bb}	0	0	1	1	1	1	1	1	0	0
S_{Cb}	0	0	0	0	0	0	0	0	0	0
S_{Ac}	1	0	0	0	0	0	0	0	0	1
S_{Bc}	0	0	0	1	1	1	1	0	0	0
S_{Cc}	0	1	1	0	0	0	0	1	1	0

Table B.1. *Continued.* ($k_v = 6$; $k_t = 6$)

	$t_{\gamma\alpha}/2$	$t_{\delta\alpha}/2$	$t_{\delta\beta}/2$	$t_{\gamma\beta}/2$	$t_0/2$	$t_0/2$	$t_{\gamma\beta}/2$	$t_{\delta\beta}/2$	$t_{\delta\alpha}/2$	$t_{\gamma\alpha}/2$
S_{Aa}	0	0	1	1	1	1	1	1	0	0
S_{Ba}	0	0	0	0	0	0	0	0	0	0
S_{Ca}	1	1	0	0	0	0	0	0	1	1
S_{Ab}	0	0	0	0	1	1	0	0	0	0
S_{Bb}	1	1	1	1	0	0	1	1	1	1
S_{Cb}	0	0	0	0	0	0	0	0	0	0
S_{Ac}	0	0	0	1	1	1	1	0	0	0
S_{Bc}	0	1	1	0	0	0	0	1	1	0
S_{Cc}	1	0	0	0	0	0	0	0	0	1